The Impact of Organic Ligand Complexation on the Stabilization and Transport of Dissolved Iron

Laura Moore

A dissertation

submitted in partial fulfillment of the

requirements for the degree of

Doctor of Philosophy

University of Washington

2023

Reading Committee:

Randelle M. Bundy, Chair

Joseph A. Resing, Chair

Robert M. Morris

Program Authorized to Offer Degree:

Oceanography

University of Washington

Abstract

The Impact of Organic Ligand Complexation on the Stabilization and Transport of Dissolved Iron

Laura Moore

Chairs of the Supervisory Committee:
Randelle M. Bundy
Joseph A. Resing
School of Oceanography

Iron is an essential nutrient for life, but it is only present in low concentrations in the ocean. Dissolved Fe (dFe) is the most biologically labile fraction of Fe in seawater, the majority of which is bound to a heterogeneous pool of organic ligands. These organic ligands stabilize dFe against precipitative loss and mediate the bioavailability and biogeochemical cycling of this critical element. Characterizing the organic ligand pool is primarily done using one of two independent approaches. The first, competitive ligand exchange-adsorptive cathodic stripping voltammetry (CLE-ACSV), is an electrochemical technique used to measure the concentration and average Fe-binding strength of the total ligand pool. The second, liquid chromatography-mass spectrometry (LC-MS), is used to identify specific iron-binding ligands and most frequently targets a class of strongly Fe-binding molecules known as siderophores. My dissertation combines LC-MS and CLE-ACSV techniques in order to characterize Fe-binding ligands at multiple levels and examine ligand impact on the stabilization and transport of dissolved Fe. I identified the ubiquitous presence of siderophores in novel oceanographic environments, including within the Eastern Tropical North Pacific oxygen deficient zone and near diverse hydrothermal venting systems along the Southern East Pacific Rise. In both study regions, I explored the critical role of organic ligands and siderophores in stabilizing dFe and facilitating Fe transport into the ocean interior. This dissertation expands ligand characterization studies to environments near key Fe sources to the deep ocean, including continental margins and hydrothermal vents, and identifies siderophores across a much wider range of chemical and dFe gradients than has previously been observed. This dissertation presents some of the first combined LC-MS and CLE-ACSV ligand characterization studies and offers unprecedented insight into the dynamics of the organic ligand pool near critical Fe sources.

TABLE OF CONTENTS

LIST OF FIGURES

LIST OF TABLES

ACKNOWLEDGEMENTS

This dissertation was only possible through the support, mentorship, and encouragement of so many special people in my life. Thank you for helping me to become the oceanographer I always dreamed of and for making the journey memorable.

It is with tremendous gratitude that I thank my advisors, Randie Bundy and Joe Resing, for guiding me through my PhD. Thank you, Randie, for your unwavering support and infectious enthusiasm. Your encouragement to explore and experiment, question and adventure made this experience unforgettable. Thank you for helping me to grow not only as a scientist, but also as mentor and person. It has been a privilege being your first student. Thank you, Joe, for introducing me to the hydrothermal community and opening the doors to so many opportunities that have shaped my PhD experience. Thank you for helping me to grow as a field scientist through at-sea experiences and helping me to expand my chemical expertise. Your knowledge and support have made this dissertation possible. I am also grateful to my committee, Bob Morris, Anitra Ingalls, and Bo Zhang for their support, ideas, and encouragement. Thank you also to the oceanography graduate school community and particularly my cohort, a remarkable group of people who helped make the graduate school experience a positive one.

To all of my advisors and mentors who guided me along my scientific journey towards graduate school: You are the ones who opened the first doors and gave me the tools I needed to succeed. To Ilja Siepmann and Becky Lindsey: thank you for opening that first door and entrusting me with my first project. To Miguel Goñi: thank you for welcoming me to oceanography and for helping me explore the many facets of oceanographic research, from fieldwork to data analysis. You inspired me to become a chemical oceanographer. To Becky Alexander, thank you for introducing me to the University of Washington and polar research, which led me to apply here. And to Gary Miessler: thank you for all your guidance throughout undergrad and for always believing in me.

The members of the Bundy lab are an absolutely spectacular group of people and working with them has been a privilege and a delight. Thank you to Susanna Michael, Travis Mellett, Angel Ruacho and Laramie Jensen for helping me navigate graduate school and always providing advice and encouragement. Thank you to Patrick Monreal and Jess Davis for exciting adventures at sea and to the coffee shop, and for all of the amazing conversations both academic and otherwise. Thank you to Colleen Hoffman, your mentorship and encouragement have helped me grow as a scientist, and I learned so much over our 75 days of at-sea research escapades. Thank you to Jiwoon Park, for an amazing 5 years of being your officemate, your friendship and support that have helped me through graduate school, and all of the adventures, from obtaining bubble tea on the Ave to visiting the most powerful mass spectrometer in the world.

To Erin Brault, Andrea Kittleson, Davis Grilley, and my neighbor family: thank you for believing in me and supporting my dreams even as they led me away from Minnesota. To Elsa Kunz, Kristine Patzer and Meryl Nath, thank you for being my first lab partners and for your friendship and inspiration. To Alex Goldstein, Kalen Robeson, and Bebhinn Gilbert, thank you for making living in Seattle wonderful, for all the dinners and conversations, and most of all, for laughter. To Rita Aylward: thank you for our many coffee breaks, chemistry and geology discussions, and for always being up for a fun conversation or quick hello. Thank you to Nora Gilbertson, for your amazing friendship and the adventures in skiing, climbing, walks and exciting science conversations that make a PhD not only possible, but also fun. Thank you to my partner Nathan, for your support and encouragement throughout the final years of graduate school and for reminding me of the joys both within and outside the world of science.

Finally, thank you to my family, who have supported by scientific dreams from the very beginning. Thank you for encouraging me to explore the world around me and ask questions, even as those questions led me far away. Thank you for your curiosity when I explained my work, and your reassurance during the times of frustration. Your love and support have gotten me to where I am today. Thank you.

DEDICATION

To my grandmothers Ellen and Karol, for your curiosity, creativity, and inspiration.

Chapter 1. INTRODUCTION

1.1 BACKGROUND

Iron (Fe) is an essential element for life, facilitating key cellular processes such as nitrogen fixation, respiration, and photosynthesis (Morel and Price, 2003). Yet, despite being the fourth most abundant element in Earth's crust, Fe is a limiting nutrient in over 30% of the global ocean (Boyd and Ellwood, 2010; Moore et al., 2013). The low Fe concentrations in the ocean are largely driven by the low solubility of inorganic Fe in seawater (~0.01 nM), such that Fe must be stabilized either physically or chemically to maintain significant and biologically viable dissolved Fe (dFe) concentrations (Liu and Millero, 2002). Most dFe in the ocean (> 99%) is chemically stabilized by organic Fe(III)-binding ligands (Gledhill and Buck, 2012; Gledhill and van den Berg, 1994; Rue and Bruland, 1995) that increase Fe concentrations from the small inorganic solubility limit to upwards of 20 nM near some Fe sources such as hydrothermal plumes and margin sediments (e.g. Hawkes et al., 2013a; Vedamati et al., 2014). These organic ligands exert important controls on the stability and bioavailability of Fe, making ligands an essential component of the global oceanic Fe biogeochemical cycle. Indeed, global biogeochemical models that incorporate organic ligand parameters have demonstrated that a doubling of oceanic ligand concentrations has a greater impact on total primary productivity, and thus atmospheric CO_2, than does increasing the external sources of Fe to the ocean (Tagliabue et al., 2014). Modeling studies such as these demonstrate how the biogeochemical cycling of Fe and the overall oceanic Fe inventory have the potential to both directly and indirectly impact primary productivity, atmospheric CO_2 uptake, and climate (Moore et al., 2013; Tagliabue et al., 2017, 2014). Thus, characterizing Fe-binding ligands and their role in the global oceanic Fe cycle is an essential task.

Organic Fe-binding ligands are a complex and heterogeneous mixture of microbially-synthesized compounds that are actively or passively released as microbial by-products with Fe-binding capabilities that can maintain dFe at biologically viable concentrations (Christel S. Hassler et al., 2011; Shaked et al., 2020). Individual compounds within the ligand pool have a diverse range of structures and Fe affinities, ranging from weakly binding exopolysaccharides (e.g. Norman et al., 2015) or humic-like substances (e.g. Laglera et al., 2011) to the extremely high Fe-affinity siderophores (Boiteau et al., 2016a; Bundy et al., 2018). Siderophores are low molecular weight organic compounds produced by microbes to obtain scarce or inaccessible Fe resources (Gledhill and Buck, 2012; Sandy and Butler, 2009; Vraspir and Butler, 2009). This diversity in compounds encompasses several operationally defined size fractions with siderophores at the smallest end of the soluble size fraction (< 0.02 μm) and larger substances like humic substances and exopolysaccharides in the colloidal size fraction (0.02-0.2 μm) (Gledhill and Buck, 2012). Ligand concentrations are similarly variable, ranging from < 1 nM in some regions of the surface ocean to over 1 μM near hydrothermal vents (Caprara et al., 2016; Kleint et al., 2016).

Despite the complexity in ligand identities and concentrations, understanding ligand distributions is essential for accurately modeling dissolved Fe distributions (Tagliabue et al. 2016). Most models that include ligands parameterize them as a single ligand class that behaves uniformly across all oceanic environments, while more advanced models have a dynamic ligand system controlled by universally applied cycling processes (Tagliabue et al., 2016; Völker and Tagliabue, 2015). The high variability in ligand concentrations and binding strengths suggest that a variable and dynamic ligand pool will more accurately model Fe biogeochemistry, particularly in regions with distinct ligand sources and/or high ligand turnover (Tagliabue et al., 2016, 2014). All ligands are ultimately biologically produced (Gledhill and Buck, 2012), but the composition and Fe stabilization capacity of the ligand pool can vary based on both environmental source and internal cycling processes. Distinct sources such as continental margins, sediments, coastal riverine input, ice shelves, and hydrothermal systems can all contribute unique ligands to the ocean interior (e.g. Bennett et al., 2008; Bundy et al., 2015; Hopkinson and Barbeau, 2007; Norman et al., 2015). These ligands also undergo complex internal cycling processes including removal via biological uptake or photochemical degradation and regeneration via additional microbial production, cell lysis or macromolecule degradation (Gledhill and Buck, 2012; Hunter and Boyd, 2007). Both ligand sources and internal cycling are poorly constrained, which limits understanding of their role in Fe biogeochemical cycling and modeling accuracy.

Studies have shown that ligand concentrations exceed dFe in most of the global ocean except in areas of extremely high Fe inputs such as hydrothermal vents (Buck et al., 2018, 2015; Caprara et al., 2016; Gerringa et al., 2015; J. A. Hawkes et al., 2013; Kleint et al., 2016). The near ubiquitous excess of ligands over Fe supports the large control ligands exert on Fe biogeochemical cycling. However, there remain critical gaps in scientific understanding of Fe-ligand interactions, particularly in areas with higher Fe concentrations (Caprara et al., 2016). Although Fe-rich environments make up only a small proportion of the ocean, these areas are generally situated near critical Fe sources that exert important controls on Fe distribution. For instance, continental margins and hydrothermal vents are the two largest sources of Fe to the global ocean, controlling Fe concentrations in an estimated 74% and 23% percent of the ocean’s area, respectively (Tagliabue et al., 2014). The composition and concentration of organic Fe binding ligands is anticipated to have large effects on the physical and chemical speciation of Fe near these key sources, with critical impacts on the overall stability and transport of Fe away from these regions and into the ocean interior (Bennett et al., 2008; Lam et al., 2020). The diversity in ligand sources, size, identity, Fe-affinity, and concentration makes measuring ligands a formidable analytical challenge, despite widespread acknowledgement of the major impact of ligands on Fe biogeochemistry and the necessity of including ligand parameters to accurately model Fe distributions (Tagliabue et al., 2017, 2016, 2014).

1.2 MEASURING IRON-BINDING ORGANIC LIGANDS

Most organic ligand studies have focused on bulk electrochemical measurements such as competitive ligand exchange-adsorptive cathodic stripping voltammetry (CLE-ACSV) that quantify the concentration and average Fe-binding strength of the total ligand pool (Caprara et al., 2016; Gledhill and Buck, 2012; Gledhill and van den Berg, 1994; Rue and Bruland, 1995). These methods have confirmed the ubiquity of Fe-binding ligands in the ocean and brought recognition to ligand importance as a dFe stabilization mechanism. CLE-ACSV operates by establishing a competitive equilibrium between the natural ligands in seawater and an artificial added ligand. By titrating the sample with added Fe, the concentration and average binding strength of the natural ligand pool can then be calculated (Gledhill and van den Berg, 1994; Rue and Bruland, 1995). CLE-ACSV is a highly sensitive technique that has the advantages of small sample volumes, minimal pre-analysis sample manipulation (e.g. no preconcentration step), and a relatively low-cost equipment set-up. As a result, this method has been widely used by the international GEOTRACES program and has been intercalibrated between multiple labs (Buck et al., 2018, 2015; Gerringa et al., 2015; Pižeta et al., 2015). However, CLE-ACSV measurements do not allow for identifying specific Fe-binding molecules beyond operational definitions derived from binding strength. Advances in CLE-ACSV such as using multiple analytical window techniques have been able to better constrain binding strength classes (Bundy et al., 2014), and modifications to the original CLE-ACSV method allow for the identification of certain broad classes of ligands such as exopolysaccharides (Norman et al., 2015) and humic substances (Laglera et al., 2007). However, specific compound identification is still unattainable using electrochemistry.

More recent ligand identification studies rely on liquid chromatography-mass spectrometry (LC-MS) methods to identify specific Fe-binding ligands based on mass to charge ratios, with a specific focus on siderophores (Boiteau et al., 2019; Bundy et al., 2018; Mawji et al., 2008; Park et al., 2023). LC-MS analyses start by pre-concentrating a large volume of seawater (≥ 4L) in a solid phase extraction step to isolate siderophores in sufficient quantities for analytical detection. Sample concentrate is then separated using liquid chromatography coupled to two mass spectrometer detectors. Inductively coupled plasma-mass spectrometry (ICP-MS) is used to quantify Fe-binding compounds, and electrospray ionization-mass spectrometry (ESI-MS) is used to identify specific mass to charge (m/z) ratios that can either be matched to a database of known siderophores or be used to identify new compounds. By matching the results from the two detectors, individual siderophores can be identified and quantified (Boiteau et al., 2016b; Bundy et al., 2018). This technique is analytically intensive, requiring large sample volumes, several expensive specialized pieces analytical equipment and complex data analysis. As a newer technique, it also lacks the large body of comparative analyses and intercalibration efforts of CLE-ACSV. However, this technique offers unprecedented insight into the specific compounds that make up the Fe-binding ligand pool, which can be used to elucidate how Fe-binding ligands relate to the microbial community, particularly with regards to siderophores.

Siderophores have some of the strongest Fe binding affinities of natural molecules and as a result are thought to disproportionally impact dFe complexation and stabilization within the wider ligand pool (Bundy et al., 2018, 2015; Gledhill and Buck, 2012; Vraspir and Butler, 2009). Over 500 siderophores have been identified to date, most of which have been isolated from terrestrial bacterial and fungal cultures, with some siderophores identified from marine heterotrophic bacteria cultures (Hider and Kong, 2010; Sandy and Butler, 2009). Studies identifying siderophores in the ocean are sparse but have shown the importance of siderophores to dFe stabilization, solubilization, and bioavailability (Bundy et al., 2015; Kraemer et al., 2005; Kügler et al., 2020; Manck et al., 2022; Vraspir and Butler, 2009). Importantly, the composition of siderophores can be used to link Fe-binding ligands to the specific microbes that produced them, offering unprecedented insight into the Fe acquisition pathways used by diverse microbial communities in nature (Boiteau et al., 2016a).

1.3 APPLICATION AND SYNTHESIS OF MULTIPLE LIGAND MEASUREMENT TECHNIQUES

The CLE-ACSV and LC-MS methods offer complementary insights into the critical roles of ligands in Fe biogeochemistry. However, these techniques are rarely combined within a single dataset (Bundy et al., 2018) and have limited spatial coverage, even when applied independently. Siderophore measurements are particularly sparse and have been restricted primarily to the Fe-poor surface (0-200 m) and mesopelagic (200-1,000 m) waters in the ocean (Boiteau et al., 2019, 2016a; Bundy et al., 2018; Mawji et al., 2011, 2008; Park et al., 2023; Velasquez et al., 2011), with only one published dataset from below 1,500 m (Hoffman et al. 2023). CLE-ACSV ligand studies are more widespread, owing in large part to the international GEOTRACES program (Buck et al., 2018, 2015; Caprara et al., 2016; Gerringa et al., 2015). Even so, these measurements focused on the open ocean, with limited application to coastal regions and other areas with elevated Fe concentrations (> 1 nM) (Caprara et al., 2016). Ligand data is underrepresented in important areas near key Fe sources to the ocean. Relatively few CLE-ACSV studies have examined ligand concentrations and binding strengths near the margins (Ardiningsih et al., 2021; Bundy et al., 2015; Gerringa et al., 2008; Hopkinson and Barbeau, 2007) and hydrothermal environments (Bennett et al., 2008; J. A. Hawkes et al., 2013; Hoffman et al., 2023; Kleint et al., 2016; Wang et al., 2021, 2019), and these studies have limited spatial coverage. Siderophore data is even more sparse, and only two studies to date have identified siderophores in Fe-rich regions including a benthic boundary layer (Boiteau et al., 2019) and one study that examined siderophores in several hydrothermal vent sites along the Mid-Atlantic Ridge (Hoffman et al., 2023).

This thesis expands organic Fe-binding ligand studies to include a broader range of oceanic environments that encompass a larger Fe gradient. By choosing study regions near important Fe sources, including continental margins and hydrothermal vents, these ligand measurements can be used to examine the effects of ligands on Fe speciation and subsequent transport of Fe from the source and into the ocean interior. This thesis combines LC-MS and CLE-ACSV methods to offer unprecedented insight into the complex dynamics of the ligand pool near important Fe sources to the deep Pacific Ocean, including the continental margin bordering the Eastern Tropical North Pacific oxygen deficient zone and the hydrothermal systems along the Southern East Pacific Rise. Furthermore, this is one of the first times that combined LC-MS and CLE-ACSV techniques have successfully been applied to a large dataset. Finally, this thesis expands LC-MS siderophore identification studies into the deep ocean (>

1,500 m) and presents some of the first evidence for microbial siderophore production in oxygen deficient zones and hydrothermal vents.

1.4 THESIS ORGANIZATION

Chapter 2 focuses on combining CLE-ACSV measurements of the total ligand pool and LC-MS identification of siderophores to characterize the Fe-binding ligand pool at an inshore-offshore transect of the Eastern Tropical North Pacific Oxygen Deficient Zone (ODZ) near the Mexican margin. This chapter has been published in *Marine Chemistry* in 2021 (Moore et al. 2021).

Chapter 3 describes the spatial and temporal chemical variability of hydrothermal venting systems along the 16-18ºS sector of the Southern East Pacific Rise (SEPR). CLE-ACSV measurements of the total ligand pool are combined with dissolved Fe (dFe) size fractionation data to assess the impact of organic ligands on the physicochemical stabilization of dFe.

Chapter 4 uses LC-MS techniques to identify and quantify siderophores across a diverse array of venting systems along the SEPR and combines these data with CLE-ACSV measurements from Chapter 2 to assess the impact of siderophores on the total Fe-binding ligand pool.

Chapter 5 summarizes the findings of this thesis on the roles of organic ligands in facilitating Fe transport near Fe sources to the deep Pacific Ocean and the novel insights provided by combining CLE-ACSV and LC-MS analyses. The potential for future research endeavors is then discussed within the context of these results.

Chapter 2. ORGANIC COMPLEXATION OF IRON BY STRONG LIGANDS AND SIDEROPHORES IN THE EASTERN TROPICAL NORTH PACIFIC OXYGEN DEFICIENT ZONE

*This chapter is modified from the version published in *Marine Chemistry* (Moore et al. 2021). Author list below. See 2.8 for detailed author contributions.

Laura E. Moore, Maija I. Heller, Katherine A. Barbeau, James W. Moffett, Randelle M. Bundy

2.1 ABSTRACT

Continental margins are an important external source of dissolved iron to the marine environment. However, the mechanisms responsible for the offshore transport of dissolved iron is impacted by the resulting iron speciation. We characterized the iron speciation in the Eastern Tropical North Pacific (ETNP) oxygen deficient zone (ODZ), including dissolved iron, organic iron-binding ligands, and reduced iron. Organic iron-binding ligands were measured using both competitive ligand exchange adsorptive cathodic stripping voltammetry (CLE-ACSV) and liquid chromatography electrospray ionization mass spectrometry (LC-ESI-MS) in order to explore the impact of organic ligands on dissolved iron and iron(II) biogeochemistry in the region. Organic ligands were present in high concentrations (1.06-5.30 nmol L^{-1}) and exceeded dissolved iron concentrations (0.36-4.52 nmol L^{-1}) at all locations. Iron-binding strengths (log $K_{FeL,Fe'}^{cond}$) ranged 11.22 to 12.75 and were elevated in the ODZ layer relative to the oxygenated water column. LC-ESI-MS revealed the presence of siderophores, or bacterially-produced organic ligands with high Fe-affinity, in all samples analyzed, suggesting these compounds may be produced by microbes in the ODZ despite high ambient dFe_T concentrations. This study is the first to characterize siderophores in an ODZ environment to date, and the three siderophores found (amphibactin B,

synechobactin c9, synechobactin c10) could contribute to the observed elevated log $K^{cond}_{FeL,Fe'}$ of ligands in the ODZ. Comparative analysis of organic ligand log $K^{cond}_{FeL,Fe'}$ values in other low oxygen environments suggests that strong ligands, including siderophores, could be present in other low oxygen regions. In a simple model of the shelf-to-offshore iron transport mechanism, strong organic iron-binding ligands had a large impact on the longevity and transport of iron in the ODZ. These results suggest that organic ligand composition can have an impact on iron distributions in the ETNP ODZ and regulate the offshore transport of iron to the open ocean.

2.2 INTRODUCTION

Iron (Fe) is an essential life-supporting element across the global ocean. As an important cofactor in cellular processes ranging from photosynthesis to nitrogen fixation, Fe exerts control on CO_2 uptake, macronutrient availability, and primary production (Morel and Price, 2003). Although one of the most abundant elements on earth, Fe is a limiting nutrient in an estimated 30-40% of the ocean and rarely exceeds 1 nmol L^{-1} in concentration (Moore et al., 2013). Characterizing Fe biogeochemistry is therefore crucial for understanding and predicting biomass distributions and climate impacts. Despite large advances in scientific understanding of the Fe cycle (Tagliabue et al., 2017), the key sources and sinks of Fe are still not well understood. For example, a comparison across thirteen global biogeochemical models that include Fe biochemistry show almost a two order of magnitude range in the total Fe inputs in the models (Tagliabue et al., 2016). The thirteen models also have dissolved Fe residence times ranging from 5 to greater than 500 years, and three of the models do not contain any sediment Fe sources despite the documented impact of margins on Fe biogeochemistry (Johnson et al., 1999; Lam et al., 2006; Lam and Bishop, 2008).

Models that do include sediment sources estimate that sediments are the most important Fe source in approximately 74% of the ocean by area (Tagliabue et al., 2014). This sedimentary Fe can be upwelled at eastern boundary margins and help to drive the high productivity commonly associated with coastal regions (Johnson et al., 1999). However, the effects of the sedimentary Fe flux extend far beyond local impacts. Sediment-sourced Fe has been tracked as far as 1,000 km from the nearest margin, and this Fe contributes to phytoplankton blooms in the North Pacific HNLC region (Lam et al., 2006; Lam and Bishop, 2008), highlighting the downstream biological impacts of this important Fe source. Relatively higher concentrations of Fe have been found in the pore waters of sediment cores underlying oxygen minimum zones (OMZs; < 90 µM O_2), corresponding with higher observed benthic Fe fluxes and elevated concentrations of reduced Fe (Fe(II)) (Elrod et al., 2004; Lohan and Bruland, 2008). Margins with low bottom water oxygen content, but are not yet sulfidic, have been shown to have the most efficient export of Fe from the margin (Scholz et al., 2014). These studies suggest that continental margins associated with OMZs, and by extension oxygen deficient zones (ODZs; < 2 µM O_2), might play a disproportionally large role in Fe supply to the ocean and may further enhance the export of Fe from margin sediments to the open ocean.

The Eastern Tropical North Pacific (ETNP) near the southwestern Mexican coast, is one potentially important coastal margin. Here, highly productive surface waters resulting from strong coastal upwelling drive the formation of the world's largest permanent ODZ (Horak et al., 2016). Organic matter degradation combined with low water column ventilation result in layers of suboxic (< 20 µM O_2) and anoxic (< 2 µM O_2) waters (Fiedler and Talley, 2006). Under these conditions, Fe can exist in both its oxidized (Fe(III)) and reduced (Fe(II)) states (e.g. Moffett et al., 2007), unlike the oxygenated ocean in which Fe is almost exclusively Fe(III) (Millero et al., 1995). The presence of Fe(II) introduces additional reaction pathways for both biotic and abiotic processes and likely plays an important role in Fe biogeochemistry in the ODZ. For instance, anaerobic Fe-oxidizing bacteria have been proposed as an important mediator of Fe oxidation reactions in ODZs (Croot et al., 2019). On a global scale, ODZs in particular may facilitate the transport of Fe from the continental shelf to the open ocean (Scholtz et al., 2014). In shelf systems with an oxygenated water column, soluble Fe(II) is released from reducing sediments into the water column, and is then rapidly oxidized to insoluble Fe(III), effectively "trapping" Fe on the shelf (Vedamati et al., 2014). In an ODZ, low O_2 increases the longevity of Fe(II) released from the margin (Kondo and Moffett, 2013), possibly providing a mechanism by which Fe can escape the shelf. Observations along the Peru margin in the ODZ suggest that the long-range transport of Fe off the shelf is not in the core of the ODZ, but below the Fe(II) max on the shelf slope (Lam et. al 2020). Therefore, the mechanism for transport of total dissolved Fe (dFe_T) off the shelf in low oxygen systems remains unclear. It appears that inorganic and redox properties of Fe alone, are insufficient to describe the complicated dynamics of off shelf transport of dFe_T in these systems.

Although Fe redox reactions in the ODZ are suspected to be the primary driver for Fe transformations in the ODZ, an estimated > 99% of the dFe_T in the ocean is bound to organic ligands (Rue and Bruland, 1995), an observation that has been supported in ODZ environments as well (Glass et al., 2015; Hopkinson and Barbeau, 2007; Kondo and Moffett, 2015; Witter et al., 2000b). These organic Fe-binding ligands increase the solubility of Fe(III) in seawater and help govern the bioavailability, reactivity and transport of dFe_T (Buck et al., 2018; Gledhill and Buck, 2012; Hunter and Boyd, 2007; Rose and Waite, 2003). Previous studies in the ETNP, Eastern Tropical South Pacific (ETSP), and the Arabian Sea found elevated organic ligand concentrations in the ODZ and noted the high conditional binding strengths (log $K_{FeL,Fe'}^{cond}$) of these ligands (Hopkinson and Barbeau, 2007; Kondo and Moffett, 2015; Witter et al., 2000b). It has been hypothesized that the high ligand concentrations and strong stability constants in low oxygen regions result from the increased remineralization of organic matter, which is suspected to be a source of ligands (Boyd and Ellwood, 2010; Witter et al. 2001). Hopkinson and Barbeau (2007) suggested that the strong ligands observed in the ODZ are potentially the result of ligand production by organisms living in low oxygen regimes, some of which may have high iron requirements (e.g. Saito et al., 2020). However, the source of these ligands and the specific roles they play in Fe biogeochemistry in the ODZ environment remain elusive, largely because ligand identities are unknown. Recent advances in liquid chromatography coupled to inductively coupled plasma mass spectrometry and electrospray ionization-mass spectrometry (LC-ICP/ESI-MS) have enabled the ability to identify Fe-binding organic ligands (Boiteau and Repeta, 2015; Mawji et al., 2011, 2008; Velasquez et al., 2011). These analyses target the identification of siderophores, or small Fe-binding ligands with extremely high Fe-binding affinities. Siderophores are thought to be most often produced by bacteria under Fe-limiting conditions as a competitive method of Fe acquisition and solubilization (Kramer et al., 2019). The stability constants of siderophores generally overlap with the conditional binding strengths of the L_1 class of natural ligands that have been broadly observed in the marine environment via voltammetric methods, and with the ligands found in previous studies in the ETNP ODZ (Glass et al., 2015; Gledhill and Buck, 2012; Hopkinson and Barbeau, 2007). This suggests the possibility of siderophores contributing to the ligand pool in this region, though their presence may be surprising given the generally high Fe concentrations. To our knowledge however, no organic ligand characterization analyses targeting siderophores have been performed in any ODZ environments to date. The presence of such strong ligands in ODZs may have important implications for Fe reactivity and bioavailability in these regions, and may also play a role in the off-shelf transport of Fe from coastal margins.

In this paper, we investigate the speciation of dFe_T in the ETNP ODZ to elucidate the complex processes impacting Fe biogeochemistry in this and other similar regions. We combine measurements of dFe_T, Fe(II) and organic Fe-binding ligands using both targeted mass spectrometry approaches and traditional voltammetric characterization of the organic ligand pool. Together, these approaches provide an important step forward in understanding the role and identities of organic ligands in ODZs, and the role of organic ligands in ODZ Fe biogeochemistry.

2.3 METHODS

2.3.1 *Sample collection and storage*

Samples in this study were collected from two Lagrangian stations and one regular station in March and April 2012 aboard the R/V *Thomas G. Thompson*. Lagrangian stations were sampled by deploying a free-floating surface-tethered sediment net trap array and tracking the array for the duration of the station (5 days each) to ensure sampling of the same water mass. Samples were collected using 5 L Teflon-coated external-spring Niskin-type bottles (Ocean Test Equipment) mounted on a trace metal clean rosette (Sea-Bird Electronics). The trace metal rosette was lowered over the side of the ship on a Kevlar line and the bottles were preprogrammed to trip on the upcast at specified depths with an autofire module (Sea-Bird Electronics). The trace metal rosette was equipped with temperature, conductivity, and fluorescence sensors, while the ship's rosette was additionally equipped with oxygen and transmissivity sensors. Once on board, Niskin bottles were quickly retrieved and mounted on a rack within a positive pressure Class-100 clean van. Bottles were pressurized with filtered N_2 gas, and samples were filtered through acid-cleaned 0.2 μm Acropak 200 capsule filters (Pall Corporation). All sample bottles were cleaned according to GEOTRACES “cookbook” protocols (Cutter et al., 2017). Samples were collected in 250 mL low-density polyethylene bottles (LDPE) bottles (Nalgene) for total dissolved metals, 500 mL fluorinated LDPE bottles for speciation analyses, and Teflon bottles for Fe(II) measurements. Total dissolved Fe (dFe_T) samples were acidified to pH < 1.7 via the addition of trace metal grade HCl (Optima, Fisher) then stored for at least one month prior to analysis. Speciation samples were stored at -20°C until analysis in the lab. Nutrient samples were directly collected from the Niskin bottles deployed from the ship’s CTD rosette and subsequently filtered through GF/F glass fiber filters and refrigerated prior to analysis.

2.3.2 *O_2, nitrate and nitrite measurements*

The ship’s CTD was equipped with a standard Seabird oxygen sensor (SBE43) that was calibrated using Winkler titrations carried out during the first leg of the cruise. All CTD data was then corrected using this calibration. The limit of detection was ~1 μmol kg^{-1} and was frequently reached in the ODZ. A Switchable Trace Oxygen (STOX) amperometric microsensor was then used to make additional oxygen measurements in the ODZ (Revsbech et al., 2011, 2009; Tiano et al., 2014) to define the anoxic layer. Details on these measurements are explained in detail elsewhere (Tiano et al., 2014). NO_3^- and NO_2^- concentrations were measured following standard JGOFs (United Nations Educational Scientific and Cultural Organization, 1994) protocols onboard with a Technicon Autoanalyzer using the Griess-Ilosvay colorimetric method (Strickland and Parsons, 1972) modified from the Armstrong procedure (Armstrong et al., 1967).

Briefly, NO_2^- in water samples was diazotized with sulfanilamide and reacted with N-(1-naphthyl)-ethylenediamine to form an azo dye with a maximum absorbance at 540 nm. A spectrophotometer equipped with a 15 mm flow cell was used to measure absorbance and quantify NO_2^-. Samples for NO_3^- analysis were first passed through a cadmium column to reduce NO_3^- to NO_2^- then analyzed in the same manner. The NO_3^- concentration is defined as the excess of NO_2^- determined from the cadmium column method over the original NO_2^- measurement.

2.3.3 *Reagents*

All reagents were prepared in a HEPA-filtered laminar-flow space or a Class-100 clean room. All samples and standards for Fe(II) analysis were stored in acid-cleaned Teflon bottles. For Fe(II) measurements, a 0.004 mol L^{-1} luminol stock solution was prepared in a 4 mol L^{-1} NH_4 and 0.5 mol L^{-1} HCl (Optima, Fisher Scientific) with luminol sodium salt (Sigma Aldrich). The stock solution was diluted to a working solution concentration of 0.001 mol L^{-1} and the pH was adjusted to 10.25-10.34. Working solutions were stored in the refrigerator and were allowed to sit for a minimum of 10 hours prior to use. All luminol solutions were prepared in 1 L amber high-density polyethylene (HDPE) bottles (Nalgene). Ferrous sulfate (Sigma Aldrich) was dissolved in pH 2 MilliQ (Optima HCl, Fisher Scientific) to prepare a 0.01 mol L^{-1} Fe(II) primary standard solution. 100 nmol L^{-1} secondary solutions were then prepared daily by diluting the primary standard in pH 2 MilliQ. For total dissolved Fe analysis, a 0.1 mol L^{-1} ammonium acetate buffer was prepared using equivalent parts 0.1 mol L^{-1} ammonium hydroxide (NH_4OH; Optima, Fisher Scientific) and 0.1 mol L^{-1} acetic acid (CH3COOH; Optima, Fisher Scientific). Nitrilotriacetatic acid (NTA) Superflow chelating resin (Qiagen) was cleaned and conditioned prior to use according to Lee et al. (2011). Briefly, the NTA resin (25 mL) was first washed five times with MilliQ, followed by five washes of 1.5 mol L^{-1} trace metal grade HCl (Optima, Fisher

Scientific), concluding with several more MilliQ washes to ensure the removal of HCl from the solution. Following cleaning, the resin was then conditioned with 0.5 mol L^{-1} trace metal grade HCl and refrigerated for 4-5 days at ~4°C. As a final cleaning step, the resin was then washed five times with 0.5 mol L^{-1} trace metal grade HNO_3 (Optima, Fisher Scientific) and five times with MilliQ water to ensure removal of HNO_3. The resin was then diluted two-fold with 25 mL MilliQ and stored in the refrigerator as the primary resin. Working resin suspensions were prepared using a 1:50 dilution of primary resin to MilliQ. All voltammetry reagents (salicylaldoxime, boric acid buffer, and Fe standards) were prepared in acid-cleaned Teflon bottles. A 4 mmol L^{-1} salicylaldoxime (SA) solution was prepared by dissolving SA (Fluka, > 98% assay) in methanol (CH_3OH, Optima Fisher). Boric acid (Alfa Aesar, 99.99% metals basis) was dissolved in 0.4 N NH_4OH (Optima, Fisher) to prepare a 1.5 M boric acid buffer. A 2 mM Fe primary standard was prepared by diluting Fe AA standard with pH 2 MilliQ. Four secondary Fe standards were made from the primary standard to final concentrations 100 nmol L^{-1}, 200 nmol L^{-1}, 1µmol L^{-1}, and 2 µmol $^{L-1}$ in pH 2 MilliQ.

2.3.4 *Fe(II) measurements*

Fe(II) concentrations were determined shipboard using a luminol-based chemiluminescence technique adapted from (King et al., 1995) and modified according to Vedamati et al., (2014). An FeLume flow injection analysis (FIA) system (Waterville Analytical) was set up in continuous flow mode (see Hopkinson and Barbeau, 2007; Kondo and Moffett, 2013) such that sample and luminol were mixed at a constant 1:1 ratio in the flow cell. Both the luminol and sample were maintained at a pH between 10.25 and 10.34. The FIA system was calibrated using Fe(II) standard additions (0.5-1 nmol L^{-1}) to seawater taken at depth and stored for several days in the dark. The detection limit, defined as 3 times the standard deviation of blank seawater measurements ($n = 3$), was 16 pmol L^{-1}. All Fe(II) measurements were completed immediately after sampling to avoid oxidative loss of Fe(II).

2.3.5 *Total dissolved Fe analyses*

Using a method adapted from (Lee et al., 2011), dFe_T concentrations were determined using a single batch NTA resin extraction followed by isotope dilution and subsequent ICP-MS analysis on an Element 2 (Thermo Scientific). Samples were prepared in 15 mL polypropylene (VWR) acid-cleaned tubes. Prior to analysis, tubes were rinsed seven times with MilliQ and at least once with the sample. Tubes were filled with ~7.5 mL sample (exact volume determined gravimetrically) and spiked with a sufficient ^{57}Fe-enriched spike (BDH Aristar Plus, VWR) to bring the final [^{57}Fe] to ~1 nM (exact concentrations were calculated using the gravimetrically determined volume for each sample). The pH was increased to at least 4 with the addition of 1.5 mL of 0.1 mol L^{-1} ammonium acetate buffer (Lee et al., 2011). For the dFe_T measurements, 0.1 mL of 1.5 mol L^{-1} trace metal grade hydrogen peroxide (Optima, Fisher Scientific) was also added to each sample (Lohan et al., 2005). Samples were then left to equilibrate for at least an hour at room temperature to ensure the complete oxidation of Fe(II) to Fe(III) (Lee et al., 2011).

Following equilibration, 200 µL of the working resin suspension was added to each sample and the tubes were placed on a shaker for 4-5 days. The samples were then centrifuged for 10 min at 4000 rpm, and the seawater was carefully decanted to leave only the resin beads at the bottom. The beads were washed with 3 mL MilliQ to remove salts and the tubes were once again centrifuged using the same settings. This step was repeated twice more to ensure total salt removal. After the final wash, 1 mL of 5% HNO_3 (Optima, Fisher Scientific) was added to each tube and samples were left on the shaker for 1-2 days, after which they were centrifuged and the carefully decanted sample was ready for analysis.

The isotope ratio (^{56}Fe:^{57}Fe) was determined on an Element 2 in medium resolution mode. Procedural seawater blanks were prepared the same way using ~0.2 mL low-metal surface seawater from the 2009 Pacific GEOTRACES intercomparison cruise. All samples were analyzed in triplicate. The Sampling and Analysis of Iron (SAFe) reference standards S1 and D1 (Johnson et al., 2007) were measured alongside the samples to assess the accuracy of the method. The resulting concentrations were 0.091± 0.007 nmol L^{-1} ($n = 3$) and 0.595 ± 0.029 nmol L^{-1} ($n = 3$) for S1 and D1, respectively. These values are within the range of consensus values for S1 (0.093 ± 0.008 n nmol L^{-1}) and somewhat lower than D1 consensus values (0.67 ± 0.04 nmol L^{-1}); http://www.geotraces.org/science/intercalibration).

2.3.6 *Voltammetric determination of the ligand pool*

Competitive ligand exchange adsorptive cathodic stripping voltammetry (CLE-ACSV) was used to determine the concentration and strength of natural Fe-binding organic ligands. The theory is described in detail elsewhere (Abualhaija and van den Berg, 2014; Rue and Bruland, 1995). Briefly, an artificial ligand, in this case salicylaldoxime (SA), of known Fe-binding and equilibrium properties was added to samples to compete with the natural ligands. The Fe(SA) complex is electroactive and adsorbs onto the mercury drop during the deposition step. Then, a voltammetric signal is generated proportional to the amount of Fe that is stripped from the surface of the mercury drop during a linear cathodic voltage sweep. By titrating the sample with increasing Fe at a constant artificial ligand concentration, the concentration and binding strengths of natural ligands can be calculated via chemical equilibria and mass balance. We assume that all dFe_T in the samples is exchangeable with SA over the timescale of equilibration (overnight), although we acknowledge that some species of particularly strong ligands or inorganic colloids may not be consistent with this assumption. In addition, all dFe_T was assumed to be present as

Fe(III) because samples were collected and stored under oxic conditions; any Fe(II) present would have oxidized prior to the time of analysis.

For CLE-ACSV analyses, 15 separate 10 mL aliquots of each sample were transferred to acid-cleaned and conditioned Teflon vials (Savillex Corporation). Each aliquot was buffered to a pH of 8.2 (NBS scale) via addition of 50 µL of 1.5 mol L^{-1} boric acid-ammonia buffer. 25 µL of 4 mmol L^{-1} SA was pipetted into each aliquot for a final concentration of 10 µmol L^{-1}. Linear Fe additions were added to the aliquots ranging from 0 to 10 nmol L^{-1}. Samples were equilibrated overnight prior to analysis on a BASi hanging mercury drop electrode with a platinum auxiliary electrode and Ag/AgCl reference electrode (Bioanalytical Systems Incorporated). Samples were analyzed using differential pulse stripping voltammetry with a linear sweep of 0 to -800 mV, following a deposition step of 120 s at 0 volts (with stirring), and 15s of quiet time. Peak heights were calculated in ECD-SOFT using a curved baseline and ligand concentrations and strengths were then fitted using ProMCC (Omanović et al., 2015). The conditional stability constants used were $\log K_{FeSA,Fe'}^{cond} = 6.5$ and $\log B_{FeSA_2,Fe'}^{cond} = 10.2$ for the respective mono and bis complexes of SA, along with an inorganic side reaction coefficient $\log\alpha_{Fe'} = 10$ (Abualhaija and van den Berg, 2014). The conditional stability constants refer to the binding strength of Fe to SA relative to inorganic Fe (Fe′) while $\alpha_{Fe'}$ refers to the relative abundance of inorganically complexed Fe to free Fe. Only one ligand class was detected in the samples, based on visual inspection and error analysis in ProMCC. An initial internal sensitivity was calculated using the last 3 points of the titration curve and then adjusted based on visual inspection of the data.

2.3.7 *Characterization of the ligand pool with mass spectrometry*

In order to determine the identity of the Fe-binding organic ligands, the organic matter in our samples was extracted using solid phase extraction techniques followed by mass spectrometric analysis. To provide sufficient volume for these analyses, samples were pooled from the volume remaining from the voltammetric samples, resulting in pooled sample volumes ranging from 750 – 1650 mL. Samples were pooled according to 7 groups named for their location and average depth: LS1-33m, S107-137m, S107-325m, LS2-85m, LS2-350m, LS2-600m, and LS2-1217m. A MilliQ process blank was also extracted and analyzed to account for potential bottle effects from fluorinated LDPE bottles. To extract organic molecules from our samples, Bond-Elut ENV solid phase extraction (SPE) columns (1000 mg, 6mL; Agilent Technologies) were activated with 2 column volumes of distilled MeOH and rinsed with two column volumes of MilliQ prior to use. The pooled samples were then pumped onto the SPE columns and columns were then rinsed with MilliQ for 2-3 minutes following sample extraction to remove salts. Following preconcentration, columns were frozen at -20°C until analysis. Columns were later thawed and eluted using 13 mL of distilled or Optima grade methanol into acid-cleaned 15 mL falcon tubes. Sample extracts were dried down on a Speed-Vac concentrator (Thermo Scientific) system to ~0.5 mL and frozen until analysis. Extracts were weighed to determine extraction volume.

To identify organic ligands in our extracts, the samples were analyzed via liquid chromatography coupled to electrospray ionization mass spectrometry (LC-ESI-MS). Samples were injected and separated on a polyetheretherketone (PEEK)-lined C18 column using a Dionex Ultimate 3000 RSLCnano system in nanopump mode. We used a 5 mmol L^{-1} ammonium formate dissolved in both distilled methanol (solvent B) and in MilliQ water (Solvent A) gradient with a flow rate of 50 μL/min. The gradient starts at 5% B for 1 minute, followed by a 20 minute ramp from 5% to 90% B, then a 10 minute isocratic elution at 90% B, a 5 minute ramp from 90% to 95% B, a 5 minute isocratic elution at 95% B, before an 11 minute column conditioning step of 5% B for a total run time of 52 minutes. The LC flow was connected directly to a Q-Exactive

HR mass spectrometer (Thermo Scientific). The sample was introduced using a HESI ion source with spray voltage of 3.5 kV, temperature of 320 °C, sheath gas of 16, sweep gas of 1, and auxiliary gas of 3 (arbitrary units). The auxiliary gas heater was set to 90 °C, and the S-lens RF level to 65.0. Scans were collected in positive ion mode with a *m/z* range of 200-2000 at 120,000 resolution and a maximum injection time of 50 ms. High-energy collision-induced dissociation MS^2 data were collected at 30,000 resolution targeting the most abundant ions and specific known siderophores (Baars et al., 2014a) with an inclusion list using an isolation window of 1.0 m/z. A collision energy of 35% was used for fragmentation.

2.3.8 *Siderophore identification*

The LC-ESI-MS data were analyzed using an in-house R-code modified from that of Boiteau et al. (2016) and Bundy et al., (2018). First, ESI data was converted to an open source format (mzXML) using MS Convert (Proteowizard). The ESI-MS data was then mined for “targeted” compounds using a database of more than 300 known siderophores (Baars et al., 2014a). Extracted ESI traces corresponding to the masses of the unbound “apo” form, ^{54}Fe form, and ^{56}Fe-bound form of each siderophore were then plotted for visual inspection. Only siderophores showing aligned peaks for all three forms were considered as putatively identified siderophores. Putative siderophores were then further examined based on MS^2 fragmentation data. Only putative siderophores with available MS^2 data and consistent fragmentation patterns across samples were continued to be considered putative siderophores. MS^2 spectra were compared to the literature when possible, but fragmentation data is often unavailable for these compounds. In the absence of existing MS^2 data, and to increase our confidence in the putative identification, in-silico fragmentation experiments were also performed on the likely siderophore candidates using publicly available CFM-ID 3.0 (https://cfmid.wishartlab.com).

2.4 RESULTS

2.4.1 *Regional hydrography*

Two Lagrangian stations (*see section 2.3.1*) were examined in this study: one coastal near shore station (LS1) and an offshore station (LS2) (Figure 2.1A). Two casts from an additional station (S107) were also examined (Figure 2.1A). LS1, located 40 km off of the Southwestern coast of Mexico, was primarily influenced by warm (~21 °C), high-salinity (~35) Subtropical Underwater (STUW) at depths below 20 m, while surface samples were dominated by high-temperature (> 24°C), relatively salty (> 34) Equatorial Surface Water (ESW) (Figure 2.1B). The oxygen deficient layer, as defined by $[O_2] < 2$ μmol kg^{-1}, spanned from 35 m to 800 m depth in the nearshore LS1 (Figure 2.1C). A primary NO_2^- maximum of 4.9 μmol kg^{-1} was detected at the top of the oxygen deficient layer (50 m), and a secondary maximum of 4.9 μmol kg^{-1} occurred at 150 m depth (Figure 2.1E). The surface chlorophyll maximum (2.5 μmol kg^{-1}) was observed along with a secondary chlorophyll maximum (15.7 μmol kg^{-1}) at 15 m (Figure 2.1E). S107 was located 5 km Northeast of LS1 and shared similar features. STUW dominated below 20 m at S107, while ESW was the dominant water mass in the surface (Figure 2.1B). The oxygen deficient layer at S107 stretched from 50 m to 800 m and contained a single NO_2^- maximum of 6.2 μmol/kg at 100 m along with a single chlorophyll maximum (14.1 μmol kg^{-1}) at 10 m (Figure 2.1C-D). LS2 was located approximately 400 km offshore and slightly southwest of the nearshore stations. STUW dominated below 50 m, while surface waters were influenced by a band of high-temperature (> 25°C), low-salinity (< 34) Tropical Surface Water (Figure 2.1B). The oxygen deficient layer at LS2 began at 100 m and extended to 800 m, and the primary NO_2^-

maximum was located at 65 m (1.6 μmol kg^{-1}), and the secondary NO_2^- maximum (6.0 μmol kg^{-1}) was present at 150 m (Figure 2.1C,F). The chlorophyll maxima were present at 60 m (3.0 μmol kg^{-1}) and at 110 m (3.6 μmol kg^{-1}; Figure 2.1F). All three stations are dominated by STUW below 50 m depth and share identical oxygen profiles below 100 m depth.

2.4.2 *Dissolved iron distributions*

The dFe_T at LS1 ranged from 1.42 nmol L^{-1} to 4.45 nmol L^{-1} with a prominent maximum at 30 m directly above the top of the ODZ, and a minimum of 1.42 nmol L^{-1} at 150 m coincident with the secondary NO_2^- maximum (Figure 2.2A, Figure 2.1E). Despite its close proximity to LS1, S107 had a much narrower range of dFe_T (1.08-1.48 nmol L^{-1}) and showed little to no change with depth (Figure 2.2B). LS2 had dFe_T concentrations ranging from 0.62 nmol L^{-1} to 3.66 nmol L^{-1} with a primary dFe_T maximum of 2.06 nmol L^{-1} at 90 m coincident with the top of the ODZ and a secondary maximum of 3.66 nmol L^{-1} at 400 m (Figure 2.2C). The dFe_T concentrations were found to be higher inshore at stations LS1 and S107 relative to the offshore LS2 station (Table 2.1). Offshore, average [dFe_T] was elevated in the ODZ relative to the oxygenated water column, while average inshore [dFe_T] was to be higher in the oxygenated region as a result of the primary dFe_T maximum at LS1 (Table 2.1). Although LS1 and LS2 were Lagrangian, there was considerable variability between casts (Figure 2.2A, C), suggesting a dynamic environment. S107 did not exhibit noticeable variability between casts (Figure 2.2B).

2.4.3 *Fe(II) distributions*

Fe(II) at LS1 had an Fe(II) maximum of 1.83 nmol L^{-1} at 30 m (range 0.01-1.83 nmol L^{-1}) (Figure 2.2D), while LS2 had a maximum of 0.53 nmol L^{-1} at the surface and a secondary maximum of 0.16 nM between 150 and 200 m (range 0.06-0.53 nmol L^{-1}) (Figure 2.2E). Unlike

dFe_T, Fe(II) showed relatively little variability between casts at LS2. Fe(II) at LS1, however, exhibited similar variability between casts as dFe_T. The Fe(II) maximum at LS1 was coincident with the primary NO_2^- maximum, while the Fe(II) maximum at LS2 was coincident with the secondary NO_2^- maximum (Figure 2.2D-E, Figure 2.1E-F). Fe(II) was enriched in LS1 relative to LS2 for the majority of sampling depths. Similarly, the percentage of total Fe(II) (%Fe(II) = ([Fe(II)]/[dFe_T]) x 100) was higher inshore (range < 1 – 78%) compared to offshore (range 3 – 48%) for the majority of sampling depths (Figure 2.2F). Below the Fe(II) maximum and within the ODZ (from 200-800 m at LS1 and 400-800 m at LS2), %Fe(II) remained relatively stable, averaging 10.2±2.4% for LS1 and 4.7±1.6% for LS2 (Figure 2.2F). For both stations, %Fe(II) was greatest in the NO_2^- maxima. Fe(II) was not measured at S107.

2.4.4 *Voltammetric determination of Fe-binding organic ligands*

All samples contained a single ligand class whose concentration exceeded that of dFe_T at all sampling depths (Figure 2.3F), resulting in a pool of excess ligands ([eL] = [L] – [dFe_T]) throughout the water column. Although only a single ligand class was resolved per sample, the ligand binding strengths (log $K_{FeL,Fe'}^{cond}$) across the three stations ranged from a binding strength typical of the moderately strong L_2 class (log $K_{FeL,Fe'}^{cond}$= 11.0-12.0), to the strong L_1 class (log $K_{FeL,Fe'}^{cond}$> 12.0) based on the definitions suggested by Gledhill and Buck (2012) (Figure 2.3). Samples from LS1, the station closest to shore, contained only L_1 type ligands (log $K_{FeL,Fe'}^{cond}$= 12.09-12.75) (Figure 2.3G). S107 samples contained slightly weaker ligands (log $K_{FeL,Fe'}^{cond}$= 11.42-12.13), likely comprising a mixture of L_1 and L_2 ligands (Figure 2.3H). Samples from LS2 also contained ligands with log $K_{FeL,Fe'}^{cond}$ spanning the range encompassed by both L_1 and L_2-type ligands (log $K^{cond}_{FeL,Fe'}$= 11.22-12.26). The strongest ligands at LS2 occurred within the oxygen deficient layer coincident with both elevated dFe_T and ligand concentrations (Figure 2.3C, I).

Ligand concentrations ([L]) at LS1 (2.75-5.04 nmol L^{-1}), S107 (2.17-3.23 nmol L^{-1}), and LS2 (1.06-5.30 nmol L^{-1}) closely resembled the depth distributions for dFe_T (1.63-4.45, 1.08-1.49, 0.62-3.66 nmol L^{-1} respectively; Figure 2.3A-C). Excess ligand ([eL]) at LS1 (0.52-1.61 nmol L^{-1}) and LS2 (0.17-3.13 nmol L^{-1}) displayed a maximum at the upper ODZ boundary, while [eL] at S107 (1.09-1.88 nmol L^{-1}) showed a maximum somewhat below the ODZ boundary (Figure 2.3D-F). Table 2.1 describes ligand characteristics for four different environments: Inshore ODZ, Inshore Oxygenated, Offshore ODZ, and Offshore Oxygenated. Offshore station LS2 had higher average [L] in both the oxygenated and ODZ environments when compared to the corresponding inshore (LS1, S107) environments. Oxygenated areas had comparatively higher average [L] overall than their ODZ counterparts, but the [L] in the ODZ exhibited considerably more variability. Inshore [eL] were elevated in the oxygenated environment relative to the ODZ, while the opposite occurred offshore. The log $K^{cond}_{FeL,Fe'}$ similarly demonstrated opposing patterns inshore and offshore, with higher log $K^{cond}_{FeL,Fe'}$ values in the inshore oxygenated environment and lower log $K^{cond}_{FeL,Fe'}$ values in the offshore oxygenated environment relative to the corresponding ODZ values.

2.4.5 *Characterization of the ligand pool using LC-ESI-MS*

LC-ESI-MS analyses revealed the presence of identifiable siderophores, or Fe-binding organic ligands, in all samples. These samples were only searched for known siderophores, with a total of 3 putative siderophores being identified: Amphibactin B, synechobactin c9, and synechobactin c10. All samples contained one or more of the putatively identified siderophores (Table 2.2). The retention time and neutral losses corresponding with amphibactin B match those found in a suite of closely related amphibactins (Bundy et al., 2018). Synechobactin c10 displayed one matching fragment (*m/z* 288) to an existing published spectrum and a retention time close to that published using a similar experimental procedure (Boiteau and Repeta, 2015). In addition, good MS^1 peak alignment for the three forms of synechobactin c10 (Fe-free "apo" form, ^{54}Fe-bound, and ^{56}Fe-bound) was demonstrated in all samples containing this putative siderophore. Based on similar MS^1 peak alignment, we also putatively identified synechobactin c9 but MS^2 spectra were inconclusive.

Due to limited sample volumes, we were unable to quantify the identified siderophores using LC-ICP-MS as in previous work (Boiteau et al., 2013; Bundy et al., 2018). Instead, siderophore relative abundances are expressed in terms of the intensity (peak height) of the MS^1 peak normalized to sample volume (Table 2.2, Figure 2.4). Amphibactin B was detected in LS1-33 m, S107-325 m, LS2-350 m and LS2-1217 m, which included environments both inshore and offshore, and within and outside the ODZ (Figure 2.4). Synechobactin c10 was detected in LS1-33 m, S107-137 m, LS2-350 m, LS2-600 m, and LS2-1217 m. While synechobactin c10 did not have any apparent pattern inside or outside the ODZ, it had a higher relative abundance inshore (Figure 2.4A). Synechobactin c9 was detected in all seven samples and its relative abundance increased with depth offshore (LS2) and peaked in abundance near the top of the ODZ inshore. No putatively identified siderophore demonstrated a distinct pattern based on oxygen concentrations. The small sampling volumes and the conservative definition of putative siderophores employed in this study suggest that these data are minimum estimates for the diversity of siderophores in this region.

2.5 DISCUSSION

2.5.1 *Dissolved iron dynamics inside and outside the ODZ*

Both dFe_T and Fe(II) followed patterns typical in ODZ environments, with higher concentrations closer to shore and lower concentrations offshore (Johnson et al., 1997). The region was also highly dynamic, as evidenced by large differences between casts within a single Lagrangian station (Figure 2.2). Comparisons of hydrography within a single Lagrangian station show no indication of changing water masses between casts. Therefore, the observed inter-cast variability is likely due to internal processes in the region, rather than an error in Lagrangian sampling. This is consistent with other observations from the ETNP, which also show a high degree of variability (K. Bolster pers. comm.). Both the dFe_T and Fe(II) displayed maxima at the top of the ODZ and near the NO_2^- max, which is consistent with other ODZ studies (Kondo and Moffett, 2015; Moffett et al., 2007). While the mechanisms producing the Fe maxima in the ODZ remain uncertain, possibilities include microbial Fe(III) reduction, remineralization of Fe on or incorporated into particles, or lateral advection from sediments (Kondo and Moffett, 2015; Vedamati et al., 2014). Although both Fe(II) and dFe_T displayed maxima in similar locations in the water column, the ratio of Fe(II) to dFe_T decreased offshore, suggesting the processes acting on the two Fe pools are decoupled (Figure 2.2). Here, we address three hypotheses to explain the patterns between inshore and offshore seen in our study site, as well as the origin of the dFe_T and Fe(II) maxima within the top of the ODZ. The first hypothesis (1) is that Fe(II) is primarily produced *in situ* via reduction of the dFe_T pool. The second hypothesis (2) is that Fe(II) and dFe_T patterns in the ODZ are driven by remineralization of sinking organic matter. Finally, the third hypothesis (3) is that the majority of the observed Fe(II) and/or Fe(III) is released from the sediments and are gradually oxidized via inorganic or organic reaction pathways, biologically removed, or abiotically scavenged as waters are advected offshore.

According to hypothesis 1, if we assume *in situ* reduction of the dFe_T pool is the source of Fe(II), we would expect [Fe(II)] to be proportional to its [dFe_T] source. However, the Fe(II):dFe_T ratio decreased between the inshore and offshore stations. Furthermore, redox conditions in the ODZ were not sufficiently reducing to inorganically reduce Fe(III) to Fe(II) on a reasonable timescale, particularly in the presence of the known Fe oxidizers NO_2^-, NO_3^-, and organic ligands (Hopkinson and Barbeau, 2007). As such, any reduction of the dFe_T pool must be microbially mediated. While anammox performing bacteria such as *Candidatus* Scalindua profunda demonstrate Fe(III) reduction in culture (Van de Vossenberg et al., 2013), the majority of known microbial Fe reducers are associated with anoxic sediments (Crosby et al., 2007; Thamdrup, 2000). It is possible that dFe_T is sourced from margin sediments and is slowly reduced as it is advected away from the margin, but due to the reducing nature of the sediments in this region it is more likely that a diffusive flux of dFe_T from sediments would be in the form of Fe(II). Therefore, it is unlikely that hypothesis 1 is the primary driver for the dFe_T and Fe(II) distributions observed in this study.

Hypothesis 2 is more difficult to address because we lack some important data in order to fully explore this hypothesis (e.g. particulate Fe and carbon measurements). However, evidence from isotope studies in the OMZ associated with the Senegalese margin found a heavy isotopic dFe_T signature, suggesting that remineralization is a significant processes in controlling dFe_T, particularly further away from the margin (Klar et al., 2018). To examine this mechanism, we used apparent oxygen utilization (AOU) as a proxy for remineralization. If the majority of dFe_T is being produced via remineralization, [dFe_T] should exhibit a positive linear correlation to

AOU. Examination of this proxy indicated that AOU and dFe_T are correlated below the oxycline, and an alternative process must be driving dFe_T distributions at the surface. Below the oxycline, AOU can account for between 38% (LS1) and 74% (S107) of the variance in dFe_T (data not shown), suggesting that remineralization of organic matter provides an important, but variable source of dFe_T in the ODZ. AOU, however, cannot account for Fe(II) distributions. AOU exhibits no correlation to Fe(II) at LS1 and can only account for 28% of the variance in Fe(II) below the oxycline at LS2 (data not shown). Therefore, we propose that hypothesis 2 can partially explain vertical dFe_T distributions, but that remineralization of organic matter is unlikely to be the source of the observed Fe(II) distributions both within and above the ODZ.

Hypothesis 3 suggests that the majority of the Fe observed in this region, and particularly the reduced Fe, is advected offshore from reducing sediments within the ODZ. This hypothesis has been proposed in the ETSP, and several lines of evidence suggest its importance. Lam et al. (2020) found that advection offshore was responsible for Fe transport from the sediments to open ocean off the Peru margin particularly from the slope, but that much of the dFe_T was lost via precipitation. Heller et al. (2017) proposed that Fe(II) maxima in the ETSP ODZ arose from an advected sedimentary source, based on Fe and radium isotope patterns (Heller et al., 2017). Unfortunately, no isotopic data is available for the present study, but the offshore decrease in [dFe_T] and [Fe(II)] is consistent with an advected signal. In addition, the decreasing Fe(II):dFe_T ratio between inshore and offshore can be accounted for if we assume an initial sediment source for the two species and different rates of loss as they are advected offshore. The anoxic conditions in the ODZ would help to stabilize Fe(II) against oxidation, while conversely the high concentrations of strong organic ligands (such as siderophores) that we identified in the region would likely enhance Fe(II) oxidation. Additionally, the organic ligands present are expected to prevent Fe(III) from precipitating. The presence of inert colloidal forms of Fe(III), although not measured in this study, would also likely stabilize Fe(III) against precipitation. As such, we propose that Fe(II) released by the sediments (hypothesis 3) is the driving mechanism behind lateral changes in Fe(II) and dFe_T, while the vertical patterns of dFe_T in the two profiles are a result of remineralization (hypothesis 2). The vertical patterns in Fe(II) may also be primarily explained via hypothesis 3. The hypothesis governing horizontal variations in Fe distributions from inshore to offshore will be further explored in section 2.5.4 in the context of the observed patterns in organic Fe-binding ligands, as the reactivity and redox behavior of Fe is likely strongly impacted by ligand processes in these coastal margins.

2.5.2 *Evidence for in-situ siderophore production in high Fe environments*

The voltammetry results indicated that strong Fe-binding ligands are present both inside and outside the ODZ, based on the observed log $K_{FeL,Fe'}^{cond}$ (Figure 2.3G-I). Strong L_1 Fe-binding ligands have been found throughout the global ocean, both in high and low Fe environments (Gledhill and Buck, 2012). The similar conditional stability constants of siderophores and L_1 ligands suggests that siderophores could possibly be present in many regions of the ocean. Siderophores were observed in all of our pooled samples from this work, despite the relatively high ambient dFe_T concentrations (Figure 2.4). Siderophores are common in terrestrial soil environments (Baakza et al., 2004; Guerinot, 1994; Kraemer, 2004; Sandy and Butler, 2009), and one study found siderophores in the marine benthic boundary layer (Boiteau et al., 2019). The measured siderophores in our samples therefore may have been advected along with the Fe from coastal sediments, or they may have been produced *in situ*. However, the types of siderophores we identified suggest they were likely produced by microbes in the water column rather than advected from the reducing sediments. All three identified siderophores were amphiphilic, or containing a polar headgroup and fatty acid tail (Figure 2.4C). Amphiphilic siderophores are found almost exclusively in aquatic environments, where the tail is thought to anchor the molecule to the cell and prevent diffusive loss (Kramer et al., 2019). This contrasts to soil environments where diffusive loss is minimal and most local siderophores lack the fatty acid tail. The amphiphilic characteristics of the siderophores found in the ODZ therefore support active *in situ* production. *In situ* production of siderophores could be a result of high Fe requirements for organisms living in low oxygen environments (Saito et al., 2020), intense competition for Fe resources (Boiteau et al., 2016a), or the presence of a relatively strong inert pool of FeL or particulate Fe such that siderophores are needed to access bioavailable Fe (Hogle et al. 2016; Bundy et al., 2018). Previous work shows that amphiphilic siderophores are generally found in regions where Fe is limiting, in contrast to suites of hydrophilic siderophores (not detected in this study) that have been found in more Fe-replete environments (Boiteau et al., 2016a; Mawji et al., 2011). It is important to note, however, that the LC-ESI-MS method used to characterize siderophores is somewhat biased toward the detection of amphiphilic compounds based on the chromatography and solid phase extraction methods used (McCormack et al., 2003). As such, there remains the possibility of uncharacterized hydrophilic siderophores in this region. The presence of siderophores in our samples is perhaps surprising, and suggests there is either competition for Fe or Fe has limited bioavailability in this region despite its high total concentrations. Boiteau et al. (2019) noted that amphibactins in particular have only been found in environments with low [dFe_T] (<0.3 nmol L^{-1}) despite the presence of known amphibactin-producing bacteria in Fe-rich regions. The presence of amphibactin B in our samples therefore suggests that Fe stress might have triggered the production of this siderophore. Siderophore contribution to the ligand pool in ODZ environments may also contribute to the elevation in log

$K^{cond}_{FeL,Fe'}$ values in this region. In addition, the oxidizing capacity of siderophores will result in rapid oxidation of Fe(II) despite low oxygen concentrations, thereby shortening the half-life of Fe(II) in the ODZ environment. The presence of such strong microbially-produced ligands in the ODZ has implications for Fe cycling and bioavailability in these important regions and will be important to explore further in future studies.

2.5.3 *Distinct ligand characteristics in worldwide ODZs*

Our data show that ligand strengths in the ODZ are stronger than those outside the ODZ in oxygenated waters (Figure 2.3). The presence and likely *in situ* production of siderophores within the ODZ suggest that siderophores might be contributing to the elevated log $K^{cond}_{FeL,Fe'}$ observed. Although siderophores have not been previously measured in any ODZs or OMZs to our knowledge, a comparative examination of ligand parameters inside and outside of low-oxygen regions in other studies suggest that siderophores or other very strong ligands might be ubiquitous in these environments (Figure 2.5). We chose to use OMZ regions for our comparative study as these data are more widely available than for ODZs. Data were compiled for the three largest permanent OMZs in the ocean: Arabian Sea (Witter et al., 2000b), ETNP (present study, Hopkinson and Barbeau, 2007), and Eastern Tropical South Pacific (ETSP) (Buck et al., 2018; Kondo and Moffett, 2015). Additional results from two smaller OMZs, the Western Atlantic (Gerringa et al., 2015) and Cape Verde (Buck et al., 2015), were included as well. A summary of voltammetry variables for the seven studies used in the comparison can be found in Table 2.3. In order to compare regions, an oxygen cutoff of 20 μmol kg^{-1} was applied as the OMZ boundary for the three major OMZs, while the Western Atlantic OMZ was defined as depths ranging 150-1000 m (consistent with original paper) and the Cape Verde OMZ had a 40 μmol kg^{-1} oxygen cutoff. With the exception of the Arabian Sea, the data indicate that the average log $K^{cond}_{FeL,Fe'}$ could be stronger in low oxygen regions of the water column when compared to the oxygenated regions (Figure 2.5). However, the relative changes in log $K^{cond}_{FeL,Fe'}$ between the two oxygen regimes are small enough that random variability in the ligand pool cannot be ruled out. The relatively small elevation in log $K^{cond}_{FeL,Fe'}$ might be expected for our siderophore hypothesis, however, because measured siderophore concentrations are typically low (~10 pmol L^{-1}) compared to the concentrations of the total ligand pool (1-5 nmol L^{-1}; Boiteau et al., 2016, 2019; Bundy et al., 2018). Even a small additional input of very strong ligands such as siderophores could plausibly be responsible for the slightly elevated log $K_{FeL,Fe'}^{cond}$ found in the majority of OMZ regions. It is important to note, however, that the studies compared here all use slightly different methods for characterizing the ligand pool (e.g. variation in analytical window and equilibration parameters), thereby making the comparison challenging. To address this, the analytical window and added ligand used by each study considered in this paper are reported in Table 2.4.

The analytical window influences the type of ligands detected by CLE-ACSV, such that higher windows are more likely to capture strong ligands, while lower windows are more likely to capture weaker ligands (Bundy et al., 2014; Laglera and Filella, 2015). As such, caution must be applied when comparing studies performed under different analytical windows. While there is large variation in analytical window applied in the studies compared here, there is no correlation between the analytical window and log $K_{FeL,Fe'}^{cond}$. Furthermore, we compare log $K_{FeL,Fe'}^{cond}$ values within each study such that the analytical window is consistent for each oxygenated/OMZ pair (e.g. oxygenated log $K_{FeL,Fe'}^{cond}$ and OMZ log $K_{FeL,Fe'}^{cond}$ for Western Atlantic derive from same analytical window). Therefore, we conclude that the results are unlikely to be an artefact of CLE-ACSV methodological variation. An additional challenge in interpretation arises from variation in [dFe_T] between studies and oxygen conditions. While OMZs tend to have higher [dFe_T] than their oxygenated counterparts (Table 2.3), log $K_{FeL,Fe'}^{cond}$ for the compiled dataset shows no dependence on [dFe_T]. Therefore, log $K_{FeL,Fe'}^{cond}$ differences between oxygenated and OMZ regions cannot be attributed simply to dFe_T variation.

In addition to the subtle differences in log $K_{FeL,Fe'}^{cond}$ between OMZs and oxygenated environments, other distinct characteristics of the ligand pool were observed between regions in this work (Figure 2.6). Apparent clusters in the ligand parameters were observed between the offshore and inshore ODZ, and the inshore and offshore oxygenated water column (Figure 2.6). Overall though, the data exhibit trends consistent with data found in the majority of open ocean ligand studies (Caprara et al., 2016). While [dFe$_T$] in our study is higher than the majority of samples in the ligand database, log $K_{FeL,Fe'}^{cond}$ and [eL] still fall within the average range encountered for the majority of ligand studies (Figure 2.6). This consistency suggests that ligands in the ODZ share fundamental similarities in terms of their composition and behavior to those in the rest of the ocean, despite the higher [dFe$_T$] environment. Thus, theoretical models about ligand cycling derived from open ocean samples can likely be broadly applied to the ODZ region. However, the four environments sampled in our study occupy distinct regions within the overall trend, suggesting subtle differences in their respective ligand pools. The environmental variation becomes important for addressing smaller-scale ligand dynamics and the role they play in regional Fe speciation. While it is important to acknowledge that biases in the CLE-ACSV technique could contribute to these small differences, the observed variation is potentially an indicator of ligand pool distinctions between environments that are worth exploring further.

2.5.4 *Understanding the role of ligands in Fe cycling in the ODZ margin environment*

The ligand pool in the ODZ margin environment has been shown to both have characteristics that are similar to other ligands present globally, and to also have unique features within the ODZ such as an elevated presence of particularly strong ligands, or siderophores. Previous work has explored Fe cycling in low oxygen regions largely in the context of inorganic redox processes, but this work has identified the potentially important role of ligands in facilitating off-shelf transport of dFe$_T$. To explore the impact of ligands on the observed Fe distributions and test the advection hypothesis (hypothesis 3), we developed a simple one-dimensional model of key processes involved in ODZ Fe speciation. The model is designed to predict changes in the speciation of Fe during lateral transport away from the shelf in the ODZ environment as a function of time. The model includes three species of Fe such that $dFe_T = FeL + Fe' + Fe(II)$ where FeL is organically-bound Fe and Fe′ is all inorganic species of Fe(III). These species are exchanged according to four major processes: oxidation of Fe(II), scavenging of Fe′, complexation of oxidizing Fe(II) by L, and biological uptake of FeL (Figure 2.7A). Colloidal processes were omitted from the model, despite a possible role in dFe_T transport, because these data were not collected for this study. Additional processes (dust deposition and FeL reduction) were deemed insignificant on the timescale of interest and as such were left out. Vertical mixing processes were also omitted from the model in the interest of simplicity and a focus on lateral transport.

The model (2.1) takes initial inputs of Fe(II) and FeL, the two dominant Fe species in this region based on the measurements of Fe(II) and the presence of excess ligands. Fe′ was excluded from the initial conditions because of its short residence time in the ODZ (~9-77 hrs; Witter et al., 2000) relative to transport offshore (~200 days, Margolskee et al., 2019) and its low concentrations in seawater (< 1% of [dFe_T]; Rue and Bruland, 1995). Therefore, initial FeL conditions were calculated as $dFe_T – Fe(II) = FeL$. Fe(II) oxidizes to Fe(III) in the model according to an adjustable half-life, $t_{1/2}$. Fe that leaves the Fe(II) pool as Fe(III) is partitioned into either the FeL pool or the Fe′ pool according to an adjustable fraction, γ. The γ is a simplified proxy for the capacity of organic ligands to bind additional inputs of Fe(III), ranging from 0 (cannot bind any additional Fe(III)) to 1 (binds all additional Fe(III)). The large measured excess ligand (eL) concentrations and high binding strengths (log $K^{cond}_{FeL,Fe'}$) of the ligand pool in the region (Figure 2.3) indicate that most, if not all of the free Fe(III) should be immediately bound to ligands, therefore bringing the predicted γ closer to 1. However, the model allows for variation in γ to account for oxidation pathways that bypass the stage in which ligands can easily bind Fe(III) such that some Fe(III) may go into the Fe′ pool. Examples of this mechanism would be the formation of insoluble Fe(III) oxyhydroxides or nanoparticles. Any Fe(III) that is passed to the Fe′ pool is assumed to be scavenged and leave the dissolved phase (Heller et al., 2017; Liu and Millero, 2002). Fe(III) that enters the FeL pool is modified according to a biological uptake rate, η, that affects the entire FeL pool. Because FeL in the ODZ has a residence time on the order of 23-250 yrs (Witter et al., 2000b), FeL decay is not considered an important sink in this model. The equations guiding this model (2.1) are written recursively to facilitate more complex modifications in the future (e.g concentration dependent loss rates).

The FeL and Fe(II) profiles from inshore station LS1 were used as inputs in the model and run for t = 5,000 hours to generate theoretical LS2 profiles. 5,000 hours is the predicted transport time from LS1 to LS2 based on modeled zonal velocities for the region (Margolskee et al., 2019). Results were depth-adjusted to account for deepening isopycnals offshore and then compared to the measured LS2 data. While it is unknown the extent to which LS1 and LS2 can be considered representative profiles of the region, they provide an important foundation for examining transport processes occurring there.

$$\begin{cases} t_1 = 0 \\ [Fe(II)]_1 = [Fe(II)]_{init} \\ [FeL]_1 = [FeL]_{init} \\ t_n = t_{n-1} + 1 \\ [Fe(II)]_n = [Fe(II)]_{init} \times \left(\left(0.5^{t_n / t_{1/2}} \right) - \left(0.5^{t_{n-1} / t_{1/2}} \right) \right) + [Fe(II)]_{n-1} \\ [FeL]_n = [FeL]_{n-1} + [Fe(II)]_{init} \times \gamma \times \left(\left(0.5^{t_{n-1} / t_{1/2}} \right) - \left(0.5^{t_n / t_{1/2}} \right) \right) - \eta \end{cases} \tag{2.1}$$

In order to test the hypothesis that Fe distributions can be explained by release of Fe from sediments within the ODZ combined with the oxidation of Fe(II) as waters were advected offshore, we tested different theoretical Fe(II) half-lives and compared the predicted profiles with the data (Figure 2.7B). Half-life measurements for Fe(II) under several different ambient conditions were used. Two theoretical half-lives measured under 30 nmol L^{-1} O_2 (Millero et al., 1987) and 30 µmol L^{-1} NO_3^- (Ottley et al., 1997) were compared with half-lives predicted from *in situ* measurements in the Peruvian OMZ (Croot et al., 2019). The theoretical half-lives for the 30 nmol L^{-1} O_2 and the 30 µmol L^{-1} NO_3^- experiments (16,000 hrs and 130,000 hrs respectively) were much longer than those predicted from *in situ* measurements (200-2,900 hrs). The shorter *in situ* half-lives suggest that something other than simple inorganic oxidation is occurring in ODZ environments. In our model, the 2,900 hour half-life was best able to predict the ODZ LS2 profile, consistent with *in situ* measurements in the ETSP and indicating the presence of additional oxidation pathways—possibly microbially-mediated Fe(II) oxidation or organic ligand-assisted oxidation. Above 200 m but still within the ODZ, a 1500 hr half-life best fits the LS2 profile, suggesting that Fe(II) in the upper part of the ODZ has an almost 50% shorter half-life compared to the heart of the ODZ, although it is still consistent with measured half-lives in the region (K. Bolster pers. comm.). This change in half-life is coincident with the onset of the oxycline and both the Fe(II) and dFe_T maxima. Additional factors that may be responsible for the predicted half-life discrepancy between upper and lower parts of the ODZ are pH and temperature. Cooler temperatures will result in slower Fe(II) oxidation, which is consistent with the slower half-life predicted for the deeper ODZ. Lack of pH measurements associated with our samples make it harder to account for this variable, but ODZs have lower pH, which will also slow Fe(II) oxidation, perhaps partially explaining the slower oxidation rates observed there (Millero et al., 1987).

The second stage of the model was to assign a reasonable FeL uptake rate, η (Figure 2.7C) in order to test whether changes in Fe speciation during advection could be due to biological uptake of Fe. Although Fe uptake rates in ODZ environments are not well known, microbes in these regions are thought to have high Fe requirements compared to their counterparts in oxygenated regions (Glass et al., 2015; Hutchins et al., 2002). A range of FeL uptake rates were estimated based on literature values, and microbes were assumed to be able to access organically-bound Fe (FeL), but the mechanism was not specified. An Fe uptake rate measured in heterotrophic bacterial isolates under Fe-limiting conditions, 27 fmol Fe L^{-1} hr^{-1}, was established as the lower limit (Tortell et al., 1996). An upper limit of 500 fmol L^{-1} hr^{-1} was calculated using an average steady-state Fe uptake rate from six bacterial strains under Fe-limiting conditions, 3.37×10^{-23} mol Fe $cell^{-1}$ min^{-1} (Granger and Price, 1999) and applying the uptake rate to cell abundances found in the ETSP OMZ core ($1\text{-}25 \times 10^5$ cells mL^{-1}) (Maßmig et al., 2020). An uptake rate of 200 fmol L^{-1} hr^{-1} generated the best modeled prediction of the LS2 profile as indicated by analysis of least squares of the predicted data compared to the observed profile.

In order to determine the impact of organic Fe-binding ligands on Fe speciation of the ODZ, the final stage of model testing was to examine the effects of the organic ligand pool on the observed FeL concentrations (Figure 2.7D). This was done by adjusting the ligand binding capacity, γ, while maintaining the 2,900 hour Fe(II) half-life and a constant 200 fmol L^{-1} hr^{-1} FeL uptake rate, determined from the preceding model results. Variability in γ is used to reflect differences in ligand strength and concentration, as well as the manner by which Fe(II) is oxidized. For instance, Fe-oxidizing bacteria, known to reside in OMZs, oxidize Fe(II) and precipitate Fe(III) in the same step (Emerson et al., 2010; Scholz et al., 2016), thereby effectively sequestering the resultant Fe(III) from rapid ligand uptake. In addition, γ may also reflect pH variability in the region as lower pH values are associated with a lower ligand binding capacity. While γ adjustments did not alter the predicted LS2 profile to the degree that the Fe uptake rate and Fe(II) half-life did, it did significantly change the proportion of the dFe_T that was comprised of [FeL]. At individual depths, the difference in FeL between $\gamma=0$ and $\gamma=1$ range from 0 to 1.3 nmol L^{-1}, changing the [FeL] by up to 60 % on average. Thus, changes to the ability of natural ligands to bind additional Fe inputs can have a large impact on the observed dFe_T. The effectiveness of ligand binding in the ODZ can therefore significantly impact the longevity, and potentially the ultimate bioavailability, of Fe sourced from margins within the ODZ. The ligand binding capacity, or γ, that best fit the measured profile changed with depth, suggesting a dynamic environment consistent with the inter-cast variability in dFe_T. Differences in γ, and by extension the ligand pool, may account for some of the observed variability in dFe_T. This was also supported by the Fe(II) profiles, since Fe(II) was unaffected by γ in our model, and the Fe(II) profiles were not nearly as variable as the dFe_T.

Overall, the simple model results (Figure 2.7) demonstrated a reasonable qualitative and quantitative prediction of the offshore depth profiles below 200 m and within the ODZ, thereby suggesting that the simple Fe speciation in our model accounts for the major processes affecting dFe_T as waters are advected from the margin offshore. Although it is probable that many processes are occurring to some degree, our model indicates that advection and ligand-mediated oxidation of Fe(II) are among the driving forces behind the observed Fe distributions offshore. The facility with which ligands can complex this oxidized Fe(II) is likely key to understanding the transport efficiency of Fe from the margin offshore. Variability in the ligand pool is shown in the model to have a large impact on observed dFe_T, and, by extension, the efficiency of shelf to offshore Fe transport. When examining characteristics of the ODZ ligand pool, analysis of log $K_{FeL,Fe'}^{cond}$ differences between oxygenated and OMZ regions (*section 2.5.3*) suggests the presence of a “background” ligand pool in the ODZ that is similar to ligands globally. This is supported by the similarities between this study’s dataset and the global ligand database (Figure 2.6) and suggests that the fundamentals of this model can be applied to other OMZ or nearshore environments. However, the log $K_{FeL,Fe'}^{cond}$ for ligands in the ETNP ODZ and other OMZ locations is consistently higher than that of corresponding oxygenated areas, possibly as a result of siderophore production in the low oxygen regions (Figure 2.7). This manifests as an environmentally-specific ligand signature (Figure 2.6) that could be a source of variability in the ligand pool as the production rates and residence times of siderophores are poorly constrained. Thus, small changes in the ligand pool, particularly in the strong ligand pool, may have large impacts on dFe_T transport.

2.6 CONCLUSIONS

Organic Fe-binding ligands play a fundamental role in Fe cycling in the ETNP ODZ. Our model shows that the degree to which ligands bind Fe after oxidation of Fe(II) modulates the size of the offshore dFe_T pool. Furthermore, based on the modeled half-life of Fe(II), it is likely that organic ligands facilitate Fe(II) oxidation, shortening its half-life from predicted inorganic oxidant based values. The identity of organic ligands in the ODZ has additional implications for Fe biogeochemistry in the region. Here, we present the first evidence for siderophore production in an ODZ environment. Their presence suggests the possibility of Fe competition in the ODZ, despite high ambient [dFe_T]. Siderophore production may also be a source of the stronger ligand signatures found in ODZs/OMZs relative to oxygenated areas, possibly elevating the average ODZ/OMZ ligand binding strengths beyond a universal background pool of ligands and increasing the longevity of dFe_T. Overall, the presence and composition of organic Fe-binding ligands in the ETNP ODZ facilitate offshore Fe transport and can account for many of the observed patterns in dFe_T and Fe(II).

2.7 ACKNOWLEDGEMENTS

We thank the captain and crew of the R/V *Thomas G.Thompson* and Chief Scientist Allan Devol. Thank you to Rachel Horak and Carolyn Buchwald for nutrient analyses and to Yang Han for shipboard work. Thank you to Charles C. Lanfear for assistance in coding the model. We also thank Joe Resing and Kenny Bolster for their helpful comments on the manuscript. This work was supported by NSF-OCE #1029316 to Allan Devol and NSF-OCE #1756402 to Laura Moore and Randelle M. Bundy.

2.8 AUTHOR CONTRIBUTIONS

LM did the ligand measurements and analyses, developed the model and drafted the manuscript. RB designed the study, performed shipboard analyses and helped draft the manuscript. MH performed dFe_T and Fe(II) analyses and edited the manuscript. JM and KB edited the manuscript.

2.9 FIGURES AND TABLES

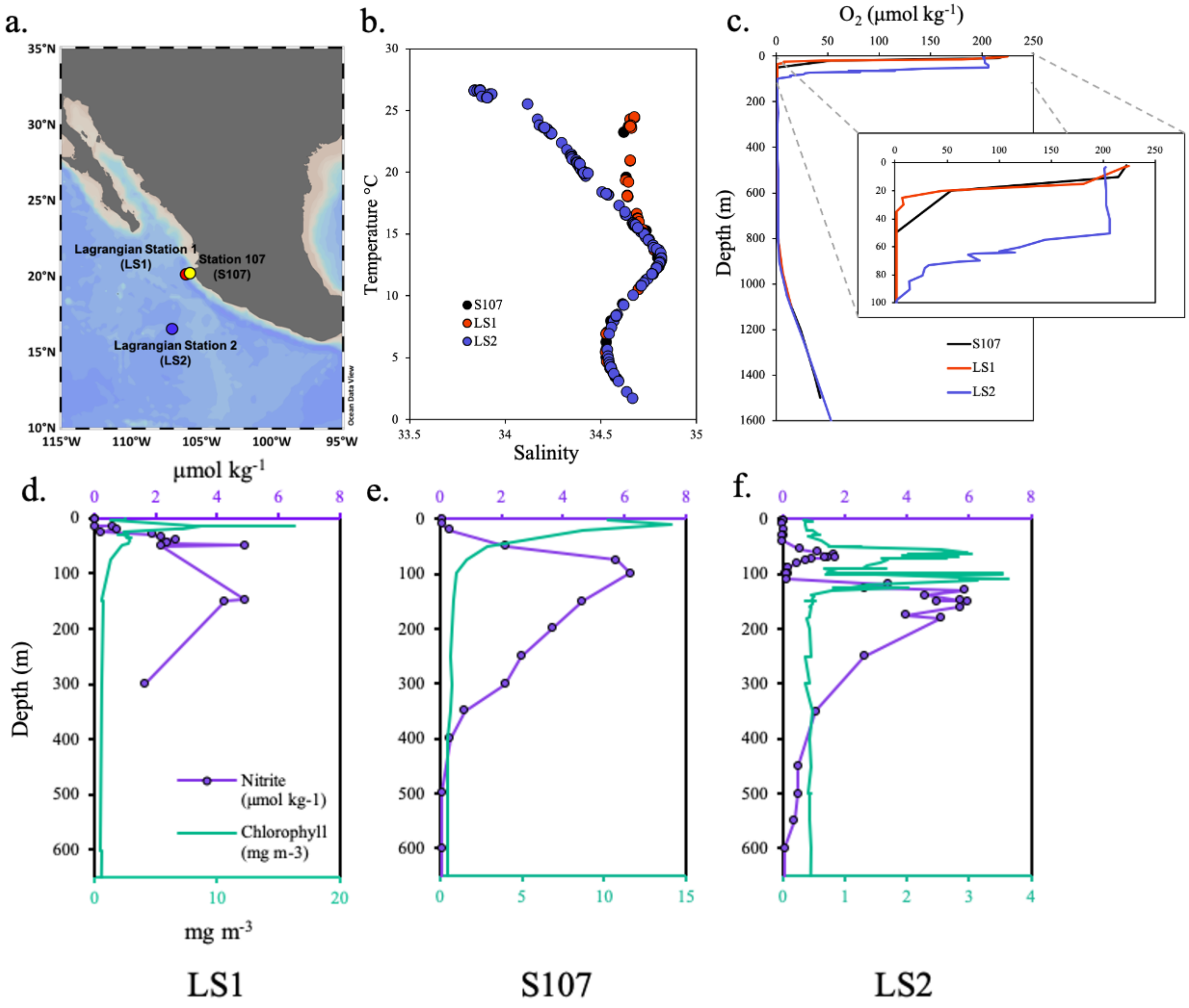

Figure 2.1. Station map and chemical characteristics.

A) The three major stations are LS1 (red) located 40 km off of the Mexican coast, S107 (yellow) located 5 km Northeast of LS1, and LS2 (blue) located 400 km off of the Mexican coast. B) Temperature-Salinity plot for S107 (black), LS1 (red), and LS2 (blue). C) Oxygen profiles for S107 (black), LS1 (red) and LS2 (blue). Inset zooms in on upper 100 m. D-F) Nitrite (purple) and chlorophyll (green) profiles for D) LS1, E) S107, and F) LS2.

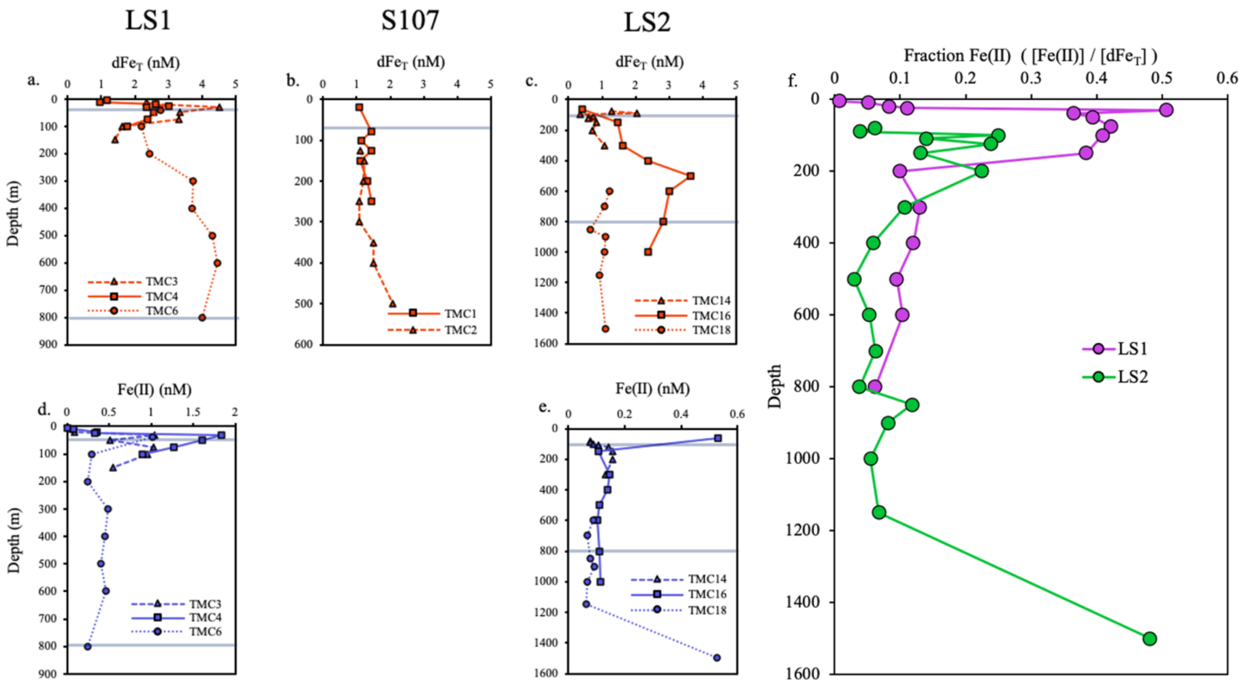

Figure 2.2. Dissolved iron redox speciation.

A-C) dFe_T profiles at A) LS1, B) S107, and C) LS2. Line styles and symbols refer to different casts in a Lagrangian station. Grey bars denote ODZ boundaries. D-E) Fe(II) profiles for D) LS1 and E) LS2. Fe(II) was not collected for S107. Line styles indicate different casts in a Lagrangian station. Grey bars denote ODZ boundaries. F) Fe(II) : dFe_T ratio for LS1 (purple) and LS2 (green).

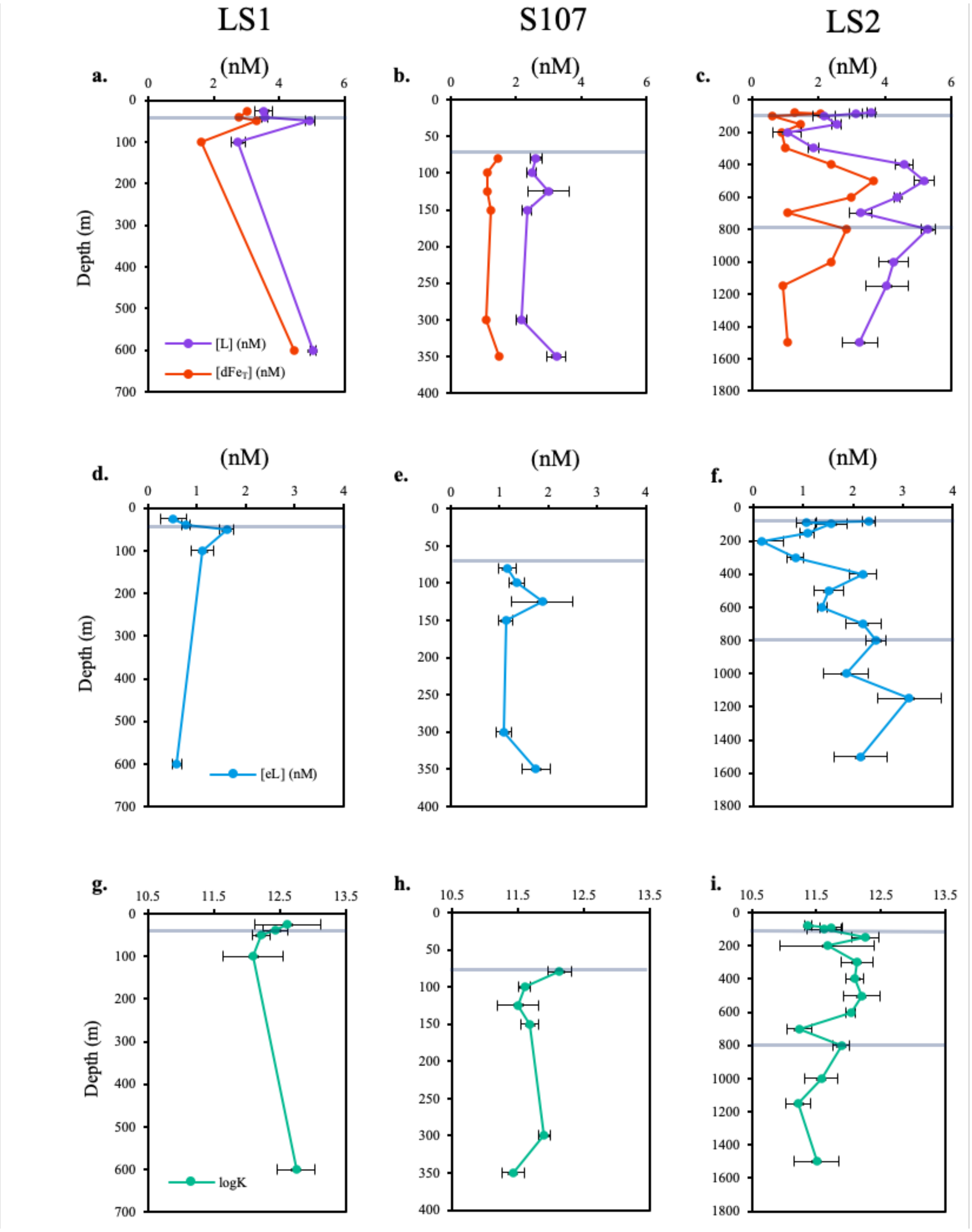

Figure 2.3. Dissolved iron-binding ligands.

A-C) dFe_T (red) and L (purple) profiles at A) LS1, B) S107, and C) LS2. D-F) Excess ligand ($[eL] = [L] - [Fe]$) profiles at D) LS1, E) S107, and F) LS2. G-I) Ligand binding strength (log $K^{cond}_{FeL,Fe'}$) profiles at G) LS1, H) S107, and I) LS2. Grey bars denote ODZ boundaries.

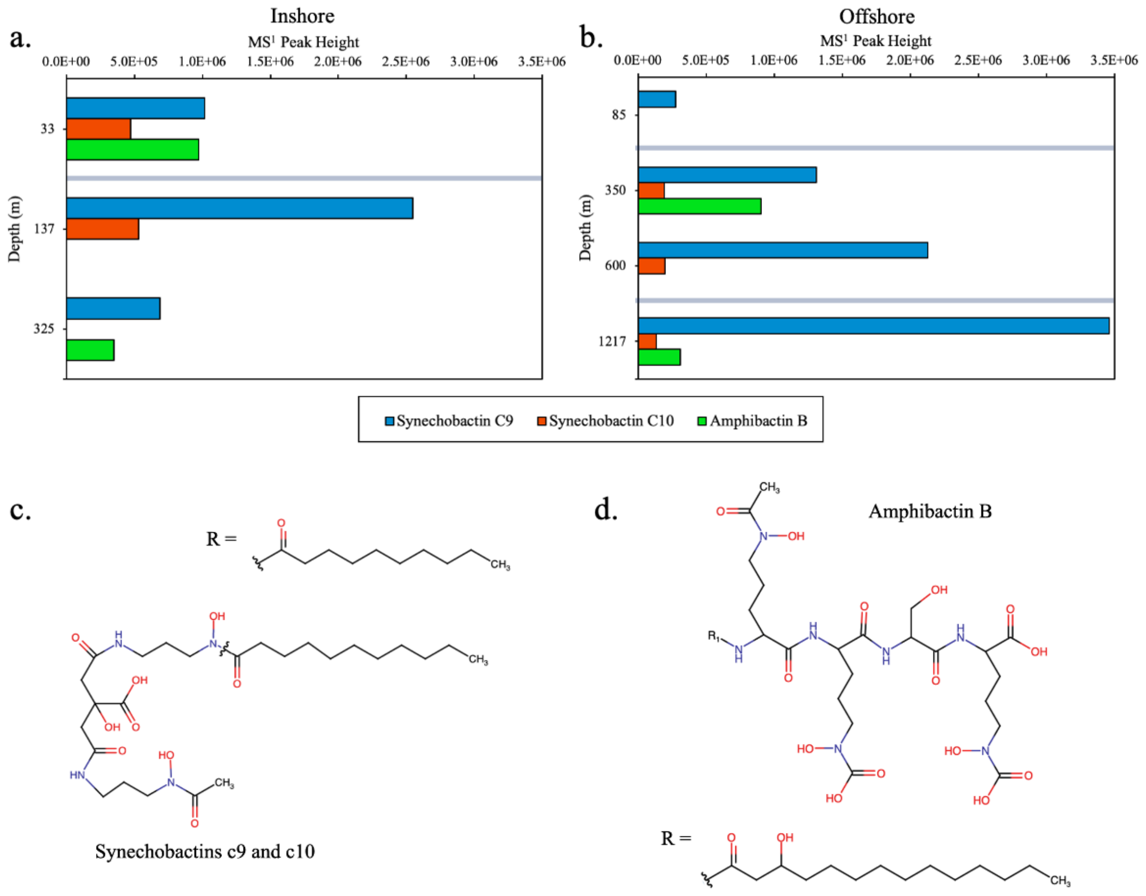

Figure 2.4. Siderophore abundances.

A) Inshore stations and B) offshore stations. Abundance is calculated as the height of the MS^1 peak corresponding to the siderophore. Grey bars denote ODZ boundaries. C) Synechobactin c9, c10 structures. D) Amphibactin B structure.

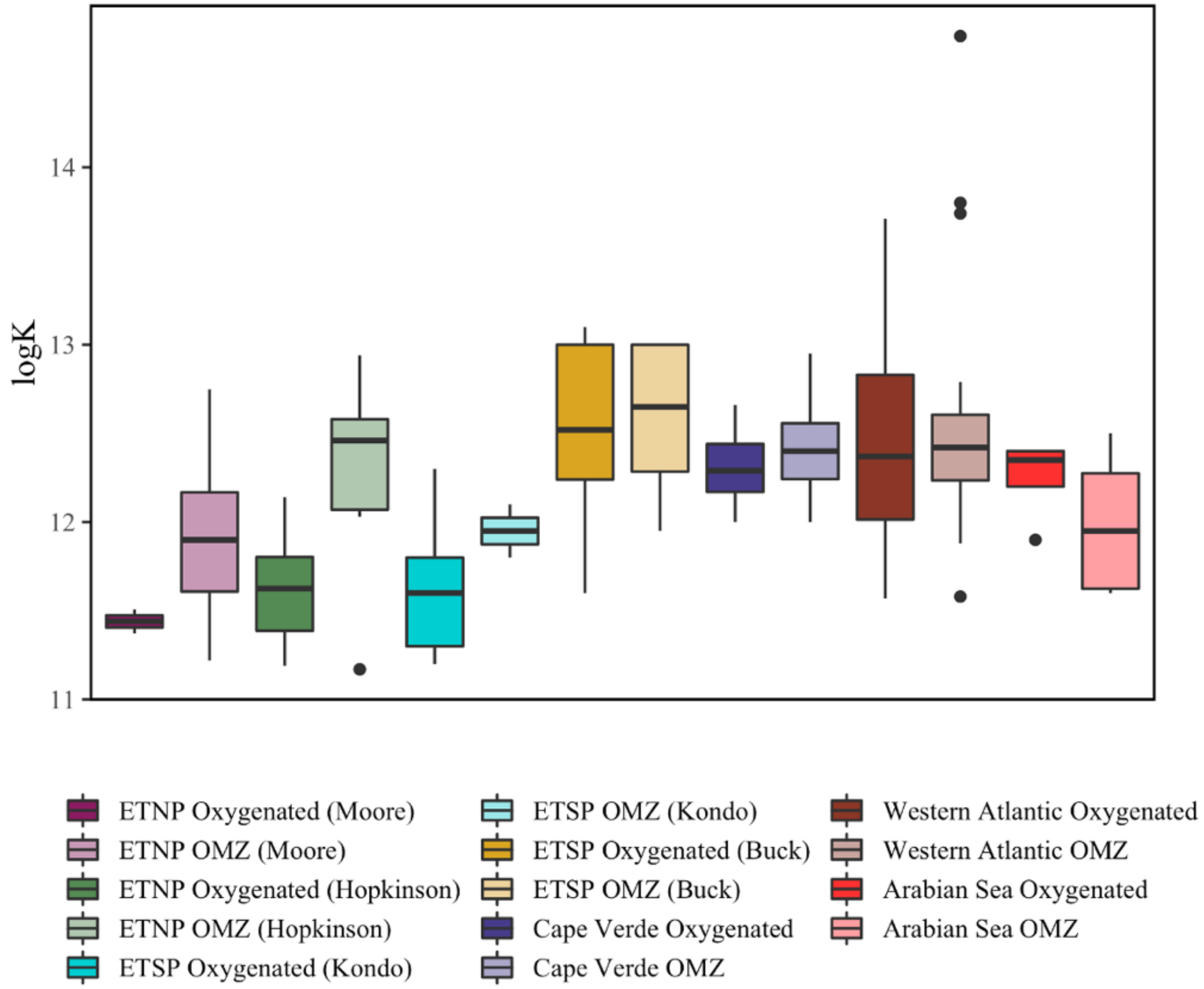

Figure 2.5. Comparison of ligand binding strengths ($\log K^{cond}_{FeL,Fe'}$) between oxygenated and oxygen deficient portions of the water column.

The seven different OMZ studies, include: Two studies from the ETNP (this study; magenta, and Hopkinson and Barbeau; green), two studies from the ETSP (Kondo and Moffett 2015; light blue, and Buck et al. 2018; yellow), an Eastern Atlantic (Cape Verde) study (Buck et al. 2015; blue), a Western Atlantic study (Gerringa et al. 2015; brown), and a study from the Arabian Sea (Witter et al. 2000; coral).

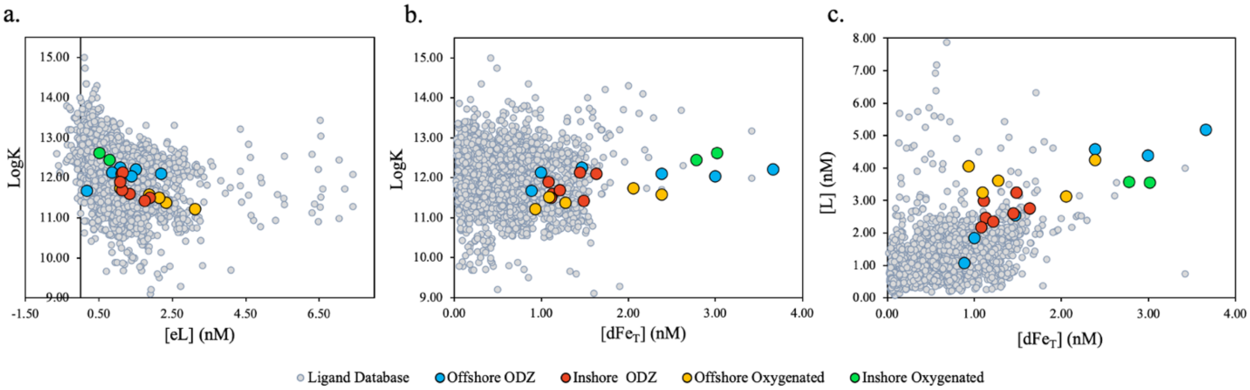

Figure 2.6. Comparison of this study to global iron-binding ligand datasets.

A) Ligand binding strength (log $K^{cond}_{FeL,Fe'}$) plotted against excess ligand concentrations ([eL] = [L] – [dFe$_T$]). B) log $K^{cond}_{FeL,Fe'}$ plotted against total iron concentration ([dFe$_T$]). C) Total ligand concentration ([L]) plotted against [dFe$_T$]. Colors refer to sampling environment: yellow = offshore oxygenated, green = inshore oxygenated, blue = offshore ODZ, red = inshore ODZ. Grey symbols are from the compiled ligand database (Caprara et al., 2016).

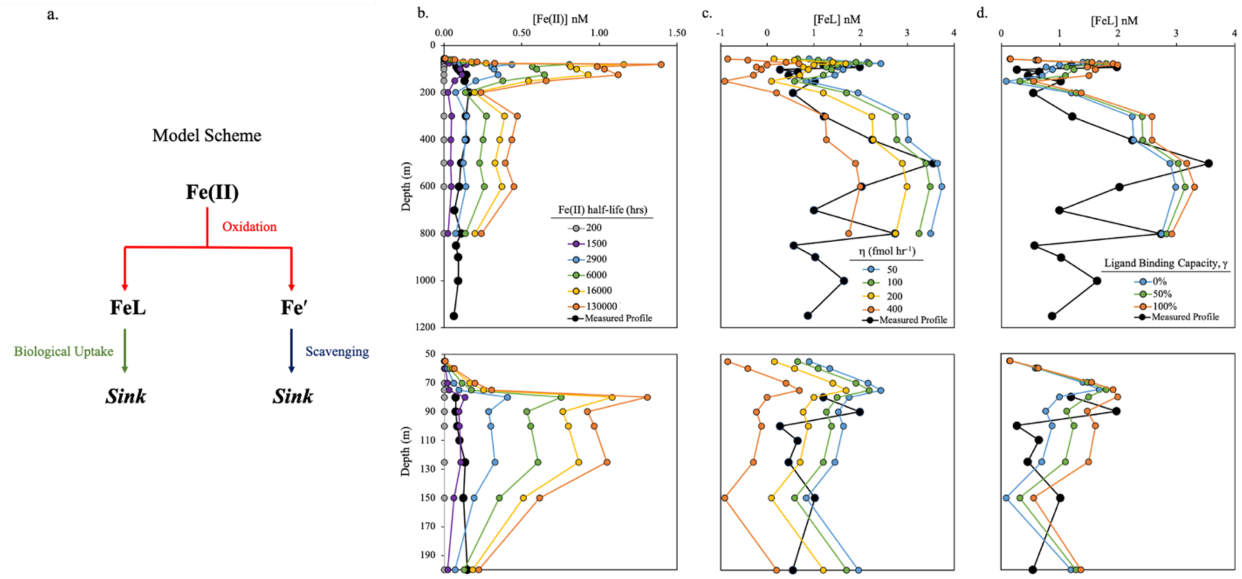

Figure 2.7. Iron transport model.

A) Model Scheme. B) Variation in modeled Fe(II) offshore profiles as a function of half-life. Compared to measured LS2 profile (black). C) Variation in modeled FeL offshore profiles as a function of FeL uptake rate, η. Compared to measured LS2 profile (black). D) Variations in modeled FeL offshore profiles as a function of the ligand binding capacity, γ (the percent of oxidizing Fe(II) entering the FeL pool). Compared to measured LS2 profile (black).

Table 2.1. Voltammetry data summary by sampling environment, including [dFe$_T$], [Fe(II)], [L], [eL], and log $K^{cond}_{FeL,Fe'}$. Errors are shown as ± 1 standard deviation.

	Inshore ODZ	**Inshore Oxygenated**	**Offshore ODZ**	**Offshore Oxygenated**
[dFe$_T$] (nmol kg^{-1})	2.93±0.98 (n=15)	2.45±1.11 (n=8)	1.54±1.04 (n=15)	1.09±0.51 (n=9)
[Fe(II)] (nmol kg^{-1})	0.69±0.41 (n=15)	0.47±0.64 (n=8)	0.12±0.03 (n=15)	0.18±0.20 (n=9)
[L] (nmol kg^{-1})	2.65±0.37 (n=7)	3.55±0.01 (n=2)	3.27±1.67 (n=6)	3.66±0.49 (n=5)
[eL] (nmol kg^{-1})	1.35±0.33 (n=7)	0.65±0.18 (n=2)	1.20±0.68 (n=6)	2.11±0.74 (n=5)
log $K^{cond}_{FeL,Fe'}$	11.76±0.28 (n=7)	12.53±0.13 (n=2)	12.07±0.21 (n=6)	11.48±0.20 (n=5)

Table 2.2. Siderophore identifications, with siderophore name, neutral mass, precursor ion, average retention time, apo peak mass (iron free), ^{56}Fe bound mass, and major MS^2 fragments.

Siderophore	**Neutral Mass (g/mol)**	**Precursor Ion ^{56}Fe monoisotopic $[M + H]^+$ *m/z***	**Retention Time (min)**	**Apo Mass *m/z***	**^{56}Fe mass *m/z***	**Dominant fragments *m/z***
Synechobactin C9	518.295	572.21	22.55	519.303	572.214	133.09, 205, 317.12, 361.07, 405.02
Synechobactin C10	532.311	586.23	27.03	533.318	586.229	117.07, 229.02, 289, 291.02, 307.01, 327.15
Amphibactin B	847.490	901.41	19.14	848.498	901.409	596, 624, 683

Table 2.3. Summary of voltammetry variables used in the interstudy comparison, including [dFe$_T$], [L], [eL], and log $K^{cond}_{FeL,Fe'}$. Errors are shown as ± 1 standard deviation.

	Current study		**Hopkinson and Barbeau 2007**		**Kondo and Moffett 2015**		**Buck et al. 2018**		**Buck et al. 2015**		**Gerringa et al. 2015**		**Witter et al. 2000**	
	Oxygenated (n = 2)	*OMZ (n = 23)*	*Oxygenated (n = 8)*	*OMZ (n = 9)*	*Oxygenated (n = 8)*	*OMZ (n = 4)*	*Oxygenated (n = 77)*	*OMZ (n = 63)*	*Oxygenated (n=65)*	*OMZ (n=38)*	*Oxygenated (n = 54)*	*OMZ (n = 21)*	*Oxygenated (n = 4)*	*OMZ (n = 6)*
[dFe$_T$] (nmol L^{-1})	1.18 ± 0.13	1.95 ± 1.05	0.15 ± 0.08	0.80 ± 0.25	0.28 ± 0.46	0.70 ± 0.51	0.78 ± 0.64	1.36 ± 1.81	0.95 ± 0.38	1.26 ± 0.24	0.57 ± 0.29	0.80 ± 0.31	1.70 ± 0.63	1.74 ± 0.35
[L] (nmol L^{-1})	3.42 ± 0.25	3.37 ± 1.17	0.80 ± 0.31	1.13 ± 0.28	1.03 ± 0.48	1.20 ± 0.89	1.30 ± 0.77	2.30 ± 2.53	1.74 ± 0.45	1.84 ± 0.40	1.14 ± 0.38	1.36 ± 0.47	2.92 ± 1.64	4.48 ± 1.08
[eL] (nmol L^{-1})	2.24 ± 0.12	1.41 ± 0.68	0.65 ± 0.29	0.32 ± 0.31	0.75 ± 0.34	0.50 ± 0.50	0.52 ± 0.48	0.95 ± 0.92	0.79 ± 0.26	0.59 ± 0.30	0.57 ± 0.42	0.56 ± 0.52	1.22 ± 1.58	2.73 ± 1.13
log $K^{cond}_{FeL,Fe'}$	11.44 ± 0.10	11.91 ± 0.41	11.62 ± 0.30	12.31 ± 0.54	11.66 ± 0.37	11.95 ± 0.13	12.55 ± 0.39	12.62 ± 0.36	12.30 ± 0.18	12.41 ± 0.22	12.44 ± 0.50	12.47 ± 0.52	12.25 ± 0.24	11.98 ± 0.40

Table 2.4. Summary of added ligands (identity and concentration) and analytical windows ($\alpha_{Fe'AL}$) used by the studies in the log $K_{FeL,Fe'}^{cond}$, and α_L intercomparison.

SA refers to salicylaldoxime, TAC refers to 2-(2-Thiazolylazo)-p-cresol, and NN refers to 1-nitroso-2-napthol.

	Current study	Hopkinson and Barbeau 2007	Kondo and Moffett 2015	Buck et al. 2018	Buck et al. 2015	Gerringa et al. 2015	Witter et al. 2000
Added Ligand	SA	TAC	TAC	SA	SA	TAC	NN
Concentration Added Ligand (μmol L^{-1})	10	10	7.3	25	25	10	20
Analytical window $\alpha_{Fe'AL}$	33	250	134	60	60	250	1096
Added Ligand Equilibration Time	Overnight	1 hr	12 - 17 hrs	≥ 15 min	≥ 15 min	> 6 hrs	16 hrs

Chapter 3. HYDROTHERMAL VENTING ALONG THE 16-18ºS SECTOR OF THE SOUTHERN EAST PACIFIC RISE: SPATIAL AND TEMPORAL VARIABILITY CONTRIBUTE TO COMPLEX PHYSICOCHEMICAL IRON STABILIZATION MECHANISMS

*This chapter will be submitted to a journal with the following author list. See 3.8 for detailed author contributions.

Laura E. Moore, Joseph A. Resing, Peter N. Sedwick, Christopher R. German, Bettina M. Sohst, Nathaniel J. Buck, Colleen L. Hoffmann, Tamara Baumberger, Tara E. Williams, Anson M. Antriasian, Matthew A. Charette, Sharon Walker, Randelle M. Bundy

3.1 ABSTRACT

The Southern East Pacific Rise (SEPR) is the fastest spreading ridge in the world with the highest spatial frequency of hydrothermal venting yet recorded. This ridge is responsible for an exceptionally stable neutrally-buoyant plume that stretches for thousands of kilometers into the western Pacific Basin. Due to its remote location, hydrothermal activity along the SEPR ridge axis is highly understudied. We visited the 16º-18ºS sector of the SEPR for the first time since 1995 to explore the diversity of venting systems along the ridge axis and examine their contributions to the stabilization of the essential micronutrient dissolved iron (dFe). We found the ridge crest to be dominated by low-temperature or “diffuse” venting with occasional high-temperature chimneys and fresh lavas. The diffuse venting sites varied chemically, but could best be distinguished by enrichments in total particulate sulfur, total dissolvable manganese, dissolved methane, and dissolved hydrogen, and a high proportion of the dissolved iron in the truly soluble size fraction (< 0.02 μm). Above the seafloor, the study region was covered by a

near-continuous yet chemically heterogenous neutrally buoyant plume that varied spatially and temporally. Overall, the venting systems along this sector appear to have aged and moved northwards since 1995, as evidenced by the comparatively low dCH_4:tdMn ratios in this study, particularly in the southern stations. The variety of venting sites resulted in a large range of dissolved iron concentrations (0.5-345 nM) with complex physical and chemical speciation that varied by sampling site. Most of the dissolved iron in the neutrally buoyant plume (~90%) was in the colloidal (0.02 μm < cFe < 0.2μm) size fraction, while dissolved iron from diffuse venting and background environments contained on average 50% colloidal iron. Measurements of the total organic iron-binding ligand pool showed that ligands near both high temperature and low temperature vents were relatively weak ($\log K_{Fe',FeL}^{cond} < 12$) and variable between sampling locations. Thermodynamic calculations suggest that all of the soluble iron and most (> 75%) of the colloidal iron is chemically stabilized by organic ligands irrespective of sampling environment, suggesting that organically-bound colloids are important for stabilizing dissolved iron from hydrothermal systems along the SEPR, and that they may help facilitate long-distance transport of dissolved iron into the ocean interior.

3.2 INTRODUCTION

Hydrothermal circulation is an important process that impacts global seawater chemistry via the exchange of elements between oceanic crust and overlying seawater (Tivey, 2007). There are a diverse array of seafloor hydrothermal venting systems along plate boundaries that emit chemically altered fluid at temperatures ranging from just above ambient seawater to over 400ºC (Baker et al., 2016; Beaulieu et al., 2015). These systems are associated with several geologic features, including underwater volcanoes and back arc systems, but the most common hydrothermal setting is along mid-ocean ridge (MOR) spreading centers (Beaulieu et al., 2015).

It has been shown that the spatial frequency of hydrothermal activity along MOR tectonic boundaries is proportional to their spreading rates, which range from ultraslow (10 mm/yr) to ultrafast (150 mm/yr) (Baker and German, 2004; Beaulieu et al., 2015). The fastest spreading ridge in the world, the Southern East Pacific Rise (SEPR), is predicted to have vents spaced as closely as one site per 25 km (Beaulieu et al., 2015).

Despite being the most hydrothermally active ridge, the SEPR is largely understudied due to its remote location. The few previous expeditions to the region however, confirmed the high spatial frequency of hydrothermal sites and identified a wide diversity of venting types along a relatively small section of ridge crest near 17ºS (Auzende et al., 1996; Charlou et al., 1996; Embley et al., 1998; Renard et al., 1985). Notably, most of these sites were characterized as low-temperature "diffuse" flow, although several high-temperature chimneys were also found. Concurrent with the high incidence of seafloor venting, was a pervasive neutrally buoyant plume that covered nearly 100% of the ridge axis between 17º25' and 18º40' S (Baker and Urabe, 1996; Feely et al., 1996; Ishibashi et al., 1997; Urabe et al., 1995). The relative contributions of diffuse and high-temperature fluids to the neutrally buoyant plume are unknown, but important to constrain. For example, although individual diffuse sites have lower metal concentrations like iron (Fe) and lower fluid fluxes than their high-temperature counterparts (Baker et al., 2016; Bemis et al., 2012), the majority of axial flow and heat flux passes through diffuse systems (Elderfield and Schultz, 1996; German et al., 2016). Therefore, a ridge sector primarily comprised of diffuse venting sites may have a disproportionate impact on the formation of the neutrally buoyant plume. The neutrally buoyant plumes produced along the SEPR are particularly notable because due to the bathymetry, they escape the ridge axis and deliver hydrothermally altered seawater into the Western Pacific Basin (Lupton and Craig, 1981; Resing et al., 2015). Unlike slow- to intermediate- spreading ridges, the SEPR does not have a pronounced axial valley (Charlou et al., 1996), allowing the plumes to spread laterally instead of being solely funneled along the ridge crest.

The observation of laterally spreading plumes from the SEPR into the western Pacific Basin has long been recorded. A large hydrothermal plume centered on 15ºS and stretching over 2,000 km from the ridge was first documented in 1981 based on ^{3}He anomalies (Lupton and Craig, 1981). Later, in 2013 this same plume was traced further, and found to extend over 4,000 km from the axis (Resing et al., 2015). Notably, this second study found that bioactive dissolved metals of hydrothermal origin, such as Fe and manganese (Mn), also persisted for thousands of kilometers in the plume. The transport of hydrothermal Fe is of particular interest because Fe is an essential nutrient for biological activity, facilitating nitrogen fixation, DNA synthesis, cellular respiration, and other key cellular processes (Morel and Price, 2003). Furthermore, Fe is a limiting nutrient in much of the surface ocean (Johnson et al., 1997; Moore et al., 2013), so understanding how sources of hydrothermal Fe impact the inventory of dissolved Fe (dFe) in the ocean is important for understanding long term changes in productivity and therefore atmospheric CO_2.

Although hydrothermal Fe is an important source for the global Fe inventory, the mechanism that stabilizes Fe in the dissolved phase to allow for long distance transport into the ocean interior is uncertain. Inorganic Fe is very insoluble in seawater (Liu and Millero, 2002) and must be stabilized either physically or chemically to maintain significant dissolved concentrations. Most dFe in the ocean is chemically stabilized via complexation by organic ligands (Gledhill and Buck, 2012; Gledhill and van den Berg, 1994; Rue and Bruland, 1995). These organic ligands are a heterogeneous mixture of microbially-synthesized compounds likely produced to maintain dFe in solution at biologically viable concentrations (Christel S. Hassler et al., 2011; Shaked et al., 2020). The Fe affinities of these compounds vary widely (Gledhill and Buck, 2012), from weakly binding humic-like substances (Laglera et al., 2011) and exopolysaccharides (Norman et al., 2015), to extremely strong siderophores produced specifically for microbial Fe acquisition (Boiteau et al., 2016a; Bundy et al., 2018). The composition and concentration of ligands play a large role in governing Fe biogeochemistry, and in most of the open ocean, organic ligands are thought to bind up to 99.9% of dFe (Rue and Bruland, 1995).

Although complexation to organic ligands is very important in the open ocean, their role in vent systems is understudied (Bennett et al., 2008; Hawkes et al., 2013; Hoffman et al., 2023; Kleint et al., 2016). Hydrothermal vents input Fe at concentrations up to one million times that of background seawater (Von Damm, 1990), far exceeding the available background organic ligand concentrations. Thus, it is thought that near venting systems, most of the Fe rapidly precipitates (Mottl and McConachy, 1990) and only a small portion remains as physically stabilized inorganic colloidal nanoparticles in the dissolved phase (Fitzsimmons et al., 2014; Gartman et al., 2014; Yücel et al., 2011) or is chemically stabilized by organic ligands (Bennett et al., 2008; Lough et al., 2019; Sander and Koschinsky, 2011). These colloids and ligand-bound Fe may be stable enough to escape the ridge and persist for long distance transport away from the vent source (Fitzsimmons et al., 2017; Resing et al., 2015; Tagliabue et al., 2016; Tagliabue and Resing, 2016). The relative contributions of inorganic colloids and ligand-bound Fe however, largely remain unknown and the complex interactions between the physical and chemical speciation of dFe in venting systems are still being disentangled (Lough et al., 2019).

While dFe stabilization has been studied in the distal plume of the SEPR, it has not been examined directly at hydrothermal sites along the ridge. This is a critical gap, because the chemistry of the distal plume and Fe stabilization mechanisms likely depend on immediate on-axis processes (Gartman and Findlay, 2020). Furthermore, understanding Fe stabilization at the SEPR is made especially challenging due to the diversity of venting systems and the prevalence of diffuse venting, which are more difficult to locate and are therefore more poorly understood (Baker et al., 2016; Chen et al., 2021). In this paper we tested two sets of hypotheses. In the first, we focused on diffuse venting and tested the assumptions that (1) diffuse venting systems are widespread on the SEPR and stable over decadal timescales and (2) diffuse venting contributes meaningfully to the pervasive neutrally buoyant plume in the region. Next, we focused on the stabilization of dFe and tested whether (3) organic dFe-binding ligands are an essential piece of the physical-chemical stabilization of dFe in venting environments and whether (4) Fe stabilization mechanisms vary between different types of venting (e.g. high-temperature vs. diffuse). To examine the variety of venting systems along the SEPR and their impact on Fe stabilization and plume formation, we visited the 17ºS sector of the SEPR. We chemically characterized nine on-axis sites and, when possible, compared them to the systems observed thirty years ago. We particularly focused on the identification of diffuse venting systems to better constrain their chemistry and to assess their impact on the pervasive neutrally buoyant hydrothermal plume in the region. Finally, we examined the physical and chemical speciation of dFe at each of the vent sites visited. We sought to determine how the size fractionation and chemical stabilization mechanisms of dFe on the ridge connect to the mechanisms controlling the stabilization of the larger plume in the western Pacific.

3.3 METHODS

3.3.1 *Seawater collection*

Samples were collected during the PLUME RAIDERS cruise (RR2106) on the *R/V* Roger Revelle from 18 September – 6 November 2021. The main study area was located along the 16-18ºS section of the Southern East Pacific Rise (SEPR, Figure 2.1), with additional crossover stations at 9ºN and U.S. GEOTRACES GP16 Station 18. Seawater was collected using 12 L Teflon-coated GO-Flo bottles (General Oceanics) on the U.S. GEOTRACES trace metal rosette (Cutter and Bruland, 2012). The rosette was additionally outfitted with a miniature autonomous plume recorder (MAPR;(Baker, 1997) from the National Oceanic and Atmospheric Administration Pacific Marine Environmental Laboratory (NOAA PMEL) including oxidation reduction potential (ORP) and light scattering sensors, and an ultra-short baseline (USBL) transponder to ensure precise site locations on repeat casts. Two bottles were tripped at every depth to ensure adequate volumes of seawater were obtained for sample analysis. Samples for dissolved gases, total dissolvable Fe (dtFe) and total dissolvable Mn (tdMn), dFe and dissolved Mn (dMn), soluble Fe (sFe) and soluble Mn (sMn) and total suspended particle analysis were collected from even numbered bottles, while dissolved aluminum (dAl) and total organic dFe-binding ligand samples were collected from odd numbered bottles. All cleaning and sampling procedures were modeled off of the GEOTRACES cookbook protocols (Cutter et al., 2017; Cutter and Bruland, 2012).

Dissolved gases hydrogen (dH_2) and methane (dCH_4) were sampled on deck by collecting 100 mL bubble-free seawater in a syringe via trace metal clean tubing connected to the GO-Flo bottle. GO-Flo bottles were then transported into a class 100 clean container and pressurized to 10 psi with High Efficiency Particulate Air (HEPA) filtered compressed air for further subsampling. Samples for tdFe, tdMn, dFe, dMn, dAl, sFe, and organic ligands were filtered through a 0.2 µm polyethersulfone (Supor) membrane filter (Acropak 200, Pall Corporation). Acropak filters were cleaned with dilute ultrapure HCl (10% trace metal grade, Fisher Scientific) prior to use and rinsed with sample three times before subsample collection. The tdFe, tdMn, dFe, dMn, and dAl samples were collected into 100 mL acid-washed low-density polyethylene (LDPE) bottles then acidified within one hour of sampling with 0.5 mL sub-boiled quartz distilled 6 N HCl to pH 1.7. Organic ligand samples were collected into acid-washed 500 mL fluorinated high-density polyethylene (FLPE) bottles and stored frozen at -20ºC. The sFe and sMn samples were collected in 125 mL acid washed bottles then filtered a second time through a 0.02 µm Anotop syringe filter (Ussher et al., 2010) prior to acidification to pH 1.7 and storage in 60 mL LDPE bottles. Unfiltered samples for tdMn and tdFe analyses were collected into 125 mL acid-washed LDPE bottles and acidified to pH 1.7 with ultrapure HCl. Remaining seawater was then filtered onto 47 mm, 0.2 µm polycarbonate track etched filters (Whatman) backed with cellulose ester filters (Whatman) to obtain total suspended particulate samples. Filters were then rinsed under low vacuum with approximately 15 mL of MilliQ water adjusted to pH 8 with ultrapure ammonium hydroxide (Optima, Fisher Scientific) to remove excess sea salt. Samples were then stored in a desiccator until the end of the cruise.

3.3.2 *Dissolved methane and hydrogen analyses*

Samples for dH_2 and dCH_4 were measured shipboard following the method of Kelley et al., (1998) and Baumberger et al., (2014). Following sample collection, 40 mL of ultrapure helium (He) was added to the syringe of 100 mL bubble-free seawater. Syringes were then shaken vigorously and left to warm at room temperature for approximately 30 minutes to allow the gases to equilibrate between the seawater and headspace. The headspace was then injected into an

SDRI 8610 gas chromatograph equipped with a 30 m long 50 µm Molecular Sieve 5A column to separate the dCH_4 and dH_2 using ultrapure He as a carrier gas. The dH_2 was detected with a He-pulsed discharge detector and dCH_4 was detected with a flame ionization detector powered by ultra-zero air from a gas cylinder and hydrogen from a Vici DMS PG Plus hydrogen generator. Standards were diluted from 100 ppm CH_4 in N_2 and 100 ppm H_2 in N_2. Analytical precision was determined by replicate draws and was the greater of > 2.5% of measured concentrations or ± 0.1 nM (Baumberger et al., 2014). The detection limit for both dCH_4 and dH_2 was 0.2 nM and 0.3 nM, respectively.

3.3.3 *Dissolved and total dissolvable iron and manganese analyses*

All samples for tdFe, dFe, tdMn, dMn, and dAl were measured shipboard using flow injection analysis (FIA) and analyzed within 6-8 hours of sample collection. The dFe, tdFe, dMn, and tdMn samples were measured using direct injection FIA with spectrophotometric detection modified from Measures et al., (1995) and detailed in Sedwick et al., (2008) for Fe and from Resing and Mottl, (1992) for Mn. Detection limits for Mn and Fe were 1 nM and 1.5 nM, respectively. The percentage of tdFe in the dissolved phase was then calculated (%dFe = 100 X dFe/tdFe)

3.3.4 *Dissolved aluminum analyses*

The dAl sample concentrations were measured at-sea by Tara Williams (Old Dominion University) using direct flow-injection analysis with micelle enhanced fluorometric detection with Brij-35 as the surfactant (Resing and Measures 1994, Brown and Bruland 2008), with a detection limit of 0.24 nM (based on 3-sigma for repeat analyses of reference seawater GSP). The accuracy of the FIA methods were assessed via separate periodic analyses of GEOTRACES reference seawater GSP, which yielded a concentration of 1.3 ± 0.08 nM (n = 11). There is currently no consensus value for dAl in the GSP seawater, however the measured average concentration is similar to the consensus value reported for SAFe S, which was collected at the same location as GSP.

3.3.5 *Soluble iron and manganese analyses*

The 0.02 µm-filtered, acidified samples for sFe and sMn were analyzed at Old Dominion University by Bettina Sohst using a sector-field inductively-coupled plasma mass spectrometer (Thermo Fisher Scientific ElementXR) with an in-line separation-preconcentration system (Elemental Scientific SeaFAST SP3). Calibration standards were prepared in filtered, acidified low-iron and low-manganese seawater, for which initial Fe and Mn concentrations were determined using the method of standard additions, using yttrium as an internal standard. Analytical blank concentrations were assessed by applying the in-line separation-preconcentration procedure including all reagents and loading air in place of the seawater sample (air blank), yielding mean blank concentrations of 0.06 ± 0.01 nM Fe and 0.004 ± 0.001 (n = 13).

The mean Fe concentration for separate determinations of the SAFe D2 and GEOTRACES GSP seawater consensus materials were 0.98 ± 0.04 nM (n = 5) and 0.15 ± 0.06 nM (n = 2), respectively, which are within the one-sigma analytical uncertainty of the current consensus values of 0.93 ± 0.02 nM dFe for SAFe D2 and 0.16 ± 0.05 nM dFe for GSP. The mean Mn concentration for separate determinations of the GEOTRACES GSP seawater consensus materials was 0.79 ± 0.01 nM (n = 4), which is within the one-sigma analytical uncertainty of the current consensus value of 0.78 ± 0.03 nM dMn for GSP. These results yield detection limits of 0.15 nM Fe and 0.03 nM Mn, based on 3-sigma for repeat analyses of reference seawater GSP. The colloidal fraction (0.02-0.2 µm) of dFe and dMn were calculated by difference from the dissolved and soluble measurements. In a few cases, sFe > dFe, likely a result of the more sensitive ICP-MS method when compared to FIA. For these cases, all dFe is assumed to be soluble with no colloidal contributions. The percentages of dFe in the soluble phase and colloidal phase were then calculated (%sFe = 100 X sFe/dFe; %cFe = 100 – %sFe).

3.3.6 *Total suspended particulate analyses*

Analyses for suspended particulate matter were performed at NOAA PMEL by Nathaniel Buck following the method of Buck et al., (2021) using energy dispersive X-ray fluorescence (ED-XRF) on a Quant'X (Thermo Fisher) fitted with a rhodium target X-ray tube and lithium-drifted solid-state detector. Sample filters were run using thin film techniques due to the low quantities of suspended matter in the deep ocean. Elements analyzed included sodium (Na), magnesium (Mg), aluminum (Al), silica (Si), sulfur (S), chlorine (Cl), potassium (K), calcium (Ca), titanium (Ti), vanadium (V), chromium (Cr), Mn, Fe, nickel (Ni), copper (Cu), zinc (Zn), arsenic (As), bromine (Br), strontium (Sr), tungsten (W), and lead (Pb). Calibrations were performed using commercially available thin-film standards (MicroMatter). Additional standards of Fe and Mn, prepared by quantitatively precipitating metals from a solution of known concentration (Holyńska and Bisiniek, 1976) and loading onto a filter, were utilized to lower the detection limits for these elements. Reference standard NIST 2798 was periodically analyzed to monitor elemental recovery and acid washed blank filters were analyzed to determine background elemental concentrations. Detection limits for all elements were ≤ 0.1 nM, except Al, which had a detection limit of 0.54 nM.

3.3.7 *Organic iron-binding ligand analyses*

Samples for dFe-binding organic ligands were measured using competitive ligand exchange adsorptive cathodic stripping voltammetry (CLE-ACSV) (Abualhaija and van den Berg, 2014; Rue and Bruland, 1995). All titrations were performed on a controlled growth drop mercury electrode (CGME, Bioanalytical Systems Incorporated) equipped with an Ag/AgCl reference electrode and platinum auxiliary electrode, with a mercury drop size of 14 and acid-cleaned Teflon analytical cell (Bioanalytical Systems Incorporated). Samples for which dFe concentrations were less than 10 nM were first analyzed using the forward titration method using a 5 µM salicyladoxime analytical window (Abualhaija and van den Berg, 2014). Briefly, samples were thawed, and 10 mL were aliquoted into each of 15 acid-cleaned and conditioned Teflon vials (Savillex Corporation). Then, 10 µL of 1.5 M boric acid buffer (boric acid, Alfa Aesar 99.99% metals basis, in 0.4 N Optima NH_4OH, Fisher Scientific) was added to each vial for a final concentration of 5 µM to achieve a pH of 8.2. Next, 12.5 µL of 4M salicylaldoxime (Fluka > 98% assay in Optima MeOH, Fisher Scientific) was then added to each vial for a final concentration of 5µM. The dFe standards (Diluted from SpexCertiPrep in pH 2 HCl) were then added to each vial, ranging 0-10 nM for final concentrations. Aliquots were then equilibrated overnight prior to electrochemical analysis using differential pulse stripping voltammetry (0 to -800 mV), with a 120-180s deposition period with stirring at 0 mV. After the final aliquot was analyzed, 5 nM of dFe standard was added and the aliquot was re-measured to ensure complete titration of the ligands. Peak heights were obtained using ECD-Soft and ligand concentrations and binding strengths were calculated using ProMCC (Omanović et al., 2015) with an inorganic side reaction coefficient of $\log\alpha_{Fe'} = 10$ (Abualhaija and van den Berg, 2014).

For samples where forward titrations showed no curvature, indicating no excess ligands were present or in the case where dFe in the sample was > 10 nM, reverse titrations were completed, employing 1-nitroso-2-naphthol (NN) as the competing ligand. The procedure and theory are described in detail elsewhere (Hawkes et al., 2013; Hawkes et al., 2013). Briefly, samples were thawed, and 10 mL were aliquoted into each of 10, 30 mL acid-cleaned and conditioned Teflon vials (Savillex Corporation). Then, 10 μL of boric acid buffer was added to each vial for a final concentration of 5 μM and pH of 8.2. NN standard (Sigma Aldrich) prepared in methanol (Optima, Fisher Scientific) was then added to each vial to achieve final concentrations ranging 0-40 μM, and aliquots were left to equilibrate overnight. After equilibration, samples were analyzed electrochemically using linear sweep voltammetry (-150 to -650 mV) after a 5-minute nitrogen purge (ultra high purity, Airgas) and a 120 s deposition time at -50 mV. Three standard additions of dFe standard were added to the final aliquot and analyzed to calculate the amount of dFe that was exchangeable with NN under the analytical conditions. The estimates of exchangeable dFe often exceeded the ambient dFe concentrations in the samples. In these cases, all ambient dFe was assumed to be exchangeable. Peak heights were obtained using ECD-Soft, and ligand concentrations and binding strengths were calculated using publicly available R code (Hawkes et al., 2013) with the unsaturated Fe fit with $\log\alpha_{Fe'} = 9.8$ as the inorganic side reaction coefficient.

Thirteen samples were analyzed using both forward and reverse titrations, and estimated ligand concentrations calculated between the two titration types agreed within 15 ± 9% and were not statistically different (Grubbs test outlier 116%, $p < 1E-5$). In the case where both a forward and reverse titration were completed on a given sample, the reverse titration data was assumed to be more reliable in the case where dFe was very similar to the calculated ligand concentrations, and therefore the reverse titration results were used. A total of 79 organic dFe-binding ligand samples were analyzed, 34 of which were analyzed shipboard and 45 were analyzed in the lab. Intercomparisons of fresh versus frozen analyses for CLE-ACSV show that the results compare very well (Buck et al., 2016, 2012).

3.3.8 *Characterization of sampling environments*

Samples were grouped by sampling environments in order to explore geochemical characteristics across different sites. Samples were grouped by first performing a principal component analysis (PCA) of all the particulate variables on the entire dataset (Supplementary Figure 3.11, Supplementary Table 3.1-Supplementary Table 3.2). The particulate dataset was chosen for PCA analysis because it had the best sampling coverage and because plumes have historically been structurally characterized using particle intensity (dNTU). A subset of five major particulate variables that were found to explain the majority of the variance in the dataset (pFe, pP, pSi, pMn, and pS_{tot}) were then chosen (Supplementary Figure 3.11). These variables were chosen carefully such that the sample variance in the PCA was largely unchanged and the explanation power of the combination of the variables was greatly improved. For example, elements that are major components of seawater were removed (Na, Mg, Ca, K, Br, Cl) as were elements that were only abundant (> 1 nM) in less than 25% of samples (Cu, Ni, Cr, Ti, Pb, W, Sr, Zn, As, V, Al). Using the five chosen particle variables, a separate PCA was performed on each of the 10 major sampling stations to assess sample groupings within each site.

Samples were then assigned to a specific environment by comparing visual sample grouping results within the initial PCA analysis to plume structures characterized by dNTU data (Figure 3.2). Samples at least 40 m above the seafloor were assigned to four different environments: shallow, deep background, center neutrally buoyant plume, and fringe neutrally buoyant plume. Briefly, “shallow” refers to samples from a depth between 2,090 and 2,350 m. “Deep background” samples were those that contained no noticeable particles (a particle anomaly (dNTU) < 0.0075). “Neutrally buoyant plume” samples were those that also had noticeable particles (dNTU ≥ 0.0075). The neutrally buoyant plume was further divided into the “center plume” and “fringe plume” based on further criteria. Samples with a dNTU ≥ 50% of the maximum dNTU value for their corresponding station were considered part of the center of the neutrally buoyant plume, while those with dNTU < 50% of the maximum dNTU value were considered to be on the “fringe” or edge of the neutrally buoyant plume. In 91% of the samples (71 out of the 78 samples > 40 m above seafloor), the visual PCA groupings could be accurately assigned to environments defined by the dNTU criteria. The remaining six samples were grouped according to the nearest samples in the PCA analysis (sample #: M0081, M0083, M0137, M0165, M0183, M0245 and M0249).

Samples within 40 m of the seafloor were first grouped based on the PCA and then were assessed on a station-by-station basis using additional geochemical data and categorized into further environmental groupings as needed, because particulate data were insufficient for defining near-seafloor environments. We sampled a rising high-temperature buoyant plume at stations Lava and Macro based on temperature and ORP anomalies, and high dMn concentrations (Supplementary Table 3.1). These samples within the buoyant plume were classified as “buoyant high temperature.” Station Bio had high particulate and dissolved metals signatures, but no associated ORP or temperature anomalies (Supplementary Table 3.1). This, combined with the dNTU plume structure, indicated that the neutrally buoyant plume extended all the way to the seafloor and samples were classified as “fringe neutrally buoyant.” Stations North, Purple Haze, and Flo all had ORP anomalies, elevated pS_{tot}, low particulate metals, and/or elevated dissolved gases (Supplementary Table 3.1). All samples from these stations were classified as low-temperature "diffuse" venting. Based on the temperature anomaly observed at North, it is likely that some amount of buoyant fluid was sampled here, but the dissolved metal concentrations were not high enough to characterize North as "high temperature venting". Stations Bart, 16º43', and Micro did not show the ORP anomalies and elevated pS_{tot} that characterized the diffuse flow in North, Purple Haze, and Flo (Supplementary Table 3.1). However, they did have low particle concentrations and other features characteristic of diffuse flow. Station Bart and Micro has elevated dMn concentrations and 16º43' had a high percentage of dFe relative to tdFe. One of the samples at Micro also had an unusually high dH_2 concentration. These samples were therefore classified as "diffuse". Additional PCA analyses were then performed on individual environmental groupings, to explore further how additional variables (e.g. dissolved metals and gases) explained the variance between samples within groupings (*see section 3.4*).

3.4 RESULTS

This section first discusses the physical structure of the neutrally buoyant hydrothermal plumes and venting features observed at each station, as described by ORP, temperature, and particle (nepheloid turbidity unit, dNTU) anomalies (*section 3.4.1*). Next, the chemical characteristics of the neutrally buoyant plume at each site are described including tdFe, dFe, pFe, tdMn, and dCH_4 (*section 3.4.2*). Additional anomalies in other particulate metals (*see section 3.3.6 for full list*) are discussed as applicable. Finally, the last section describes near-seafloor features, including high temperature venting and low temperature "diffuse" venting. Variables tdFe, tdMn, pFe, dCH_4 and dH_2 are discussed, as well as additional particulate variables as needed (*section 3.4.3*).

Finally, the physical and chemical speciation of Fe is discussed as it relates to the geochemial characteristics of the sampling environments (*section 3.4.4*).

3.4.1 *Physical structure of the neutrally buoyant plume*

Two trace metal rosette casts were performed at each sampling location (Figure 3.1), except at station Micro which only had a single cast. There was high spatial and temporal variability observed in the physical characteristics of the neutrally-buoyant plumes sampled at each station. To address and synthesize this variability, each site and its associated casts are discussed individually in the following section (Figure 3.2).

3.4.1.1 Station Macro

Station Macro was located on-axis at 113° 10' W, 17° 20' S. Two trace metal rosette casts, M21A-14 and M21A-15, were completed 24 hours apart (Figure 3.2A). M21A-14 encountered a large plume stretching from 2,538 m to the seafloor with a single maximum particle anomaly ($dNTU_{max} = 0.04$) at 2,580 m. This plume corresponded with a strong ORP decrease in the depth range of 2,530-2,583 m ($\Delta ORP = -129$) and a temperature anomaly (max +0.1ºC, 25 m above seafloor) from 2,541-2,585 m, suggesting the influence of buoyant higher temperature fluid. Above this plume, there were two smaller particle anomaly maxima ($dNTU_{max} = 0.01, 0.01$) that possibly corresponded to additional neutrally buoyant plumes at 2,438 m and 2,487 m, respectively. The second cast, M21A-15, sampled a small neutrally buoyant plume with a single maximum particle anomaly ($dNTU_{max} = 0.01$) at 2,560 m. A possible second plume ($dNTU_{max} = 0.01$) was located above the first at 2,450 m. No ORP or significant temperature anomalies were found during the second cast.

3.4.1.2 Station *North*

Station North was located on-axis at 113° 8' W, 17° 10' S. Two trace metal rosette casts, M21A-10 and M21A-11, were completed 23 hours apart (Figure 3.2B). M21A-10 sampled a neutrally buoyant plume spanning the depth range of 2,475-2,550 m, with a single particle anomaly maximum ($dNTU_{max} = 0.06$) at 2,540 m. There was a small ORP decrease ($\Delta ORP = -4$) in the plume core. A near seafloor particle anomaly ($dNTU = 0.04$) was found coincident with a strong ORP decrease ($\Delta ORP = -41$) between 2,573 and 2,581 m. This ORP drop corresponded to a near-seafloor (0-10 m) maximum temperature anomaly of +0.09 ºC, and likely captured a buoyant plume. During the second cast, M21A-11, we observed a neutrally buoyant plume stretching from 2,500 m to the seafloor with a single particle anomaly maximum ($dNTU_{max} = 0.03$) at 2,530 m. A dramatic decrease in ORP ($\Delta ORP = -103$) was observed from 2,530 m to the seafloor on the downcast, with a further 31-unit ORP drop as the CTD moved back through the plume to 2,530 m on the upcast. No significant temperature anomaly was associated with cast M21A-11.

3.4.1.3 Station *Lava*

Station Lava was located on-axis at 113° 16' W, 17° 44' S. Two trace metal rosette casts, M21A-21 and M21A-22, were completed 19 hours apart (Figure 3.2C). M21A-21 encountered a large neutrally buoyant plume extending 2,400 m to 2,600 m with maximum particle anomalies ($dNTU_{max} = 0.10, 0.09$) at 2,490 m and 2,535 m, respectively. This cast also detected a near-bottom particle feature ($dNTU_{max} = 0.09$) at 2,620 m. This feature corresponded with a large ORP decrease ($\Delta ORP = -137$) and a temperature anomaly extending up to 2,613 m ($\Delta T_{max} = 0.23$ºC). The second cast, M21A-22, encountered a neutrally buoyant plume extending 2,425-2,555 m with two particle anomaly maxima ($dNTU_{max} = 0.10, 0.11$) at 2,427 m and 2,493 m, respectively. A small ORP drop was detected in the plume (ΔORP = -2) and near the seafloor (ΔORP = -1). There were no significant temperature anomalies detected in M21A-22.

3.4.1.4 Station M*icro*

Station Micro was located on-axis next to station Macro at 113° 10' W, 17° 20' S. One trace metal rosette cast, M21A-16, was taken at this location (Figure 3.2D). A small plume was observed extending 2,400 to 2,480 m with a single maximum particle anomaly (dNTU_{max} = 0.01) at 2,450 m. A deeper secondary plume stretching between 2,450 and 2,590 m was observed with a larger particle maximum (dNTU_{max} = 0.02) at 2,560 m. ORP signal decreases (ΔORP = -8, -26 for the upcast and downcast respectively) were found in the deeper plume. No significant temperature anomalies were observed.

3.4.1.5 Station *Bart*

Station Bart was located on-axis at 113° 15' W, 17° 37' S. Two trace metal rosette casts, M21A-17 and M21A-18, were completed 12.5 hours apart (Figure 3.2E). M21A-17 sampled a single plume extending from 2,425 m to the seafloor, with two particle anomaly maxima (dNTU_{max} = 0.06, 0.05) at 2,458 m and 2,497 m, respectively. No ORP anomalies were observed. Cast M21A-18 encountered a large plume stretching 2,400 m to the seafloor, with a shallow particle anomaly maximum (dNTU_{max} = 0.06) at 2,424 m and a deeper particle maximum (dNTU_{max} = 0.03) at 2,540 m. An ORP drop was observed for the lower particle maximum (ΔORP = -11) on the upcast. No significant temperature anomalies were found on either cast.

3.4.1.6 Station *Bio*

Station Bio was located on-axis at 113° 12' W, 17° 25' S. Two trace metal rosette casts, M21A-12 and M21A-13, were completed 21 hours apart (Figure 3.2F). M21A-12 encountered a large neutrally buoyant plume stretching from 2,260 m to the seafloor with a single particle anomaly maximum ($dNTU_{max}$ = 0.12) at 2,390 m. M21A-13 observed a similar large neutrally buoyant plume extending from 2,300 m to the seafloor. Two particle anomaly maxima ($dNTU_{max}$ = 0.12, 0.08) were located at depths 2,425 m and 2,525 m, respectively. No ORP or significant temperature anomalies were observed on either cast.

3.4.1.7 Station *Flo*

Station Flo was located on-axis at 113° 18' W, 17° 53' S. Two trace metal rosette casts, M21A-19 and M21A-20, were completed 11 hours apart (Figure 3.2G). M21A-19 sampled an asymmetrical plume extending from 2,330 m to the seafloor, with a maximum particle anomaly ($dNTU_{max}$ = 0.03) at 2,587 m. There was a small ORP decrease ($\Delta ORP = -1$) between 2,580 m and the seafloor. The second cast, M21A-20, encountered a plume with two particle anomaly maxima ($dNTU_{max}$ = 0.02, 0.02) at 2,590 and 2,510 m, respectively. The main plume spanned 2,480-2,610 m, but extended to depths as shallow as 2,350 m. No ORP anomalies were detected in M21A-20 and no significant temperature anomalies were detected in either cast.

3.4.1.8 Station *Purple Haze*

Station Purple Haze was located on-axis at 113° 4' W, 16° 51' S. Two trace metal rosette casts, M21A-25 and M21A-26, were completed 12 hours apart (Figure 3.2H). M21A-25 observed a plume stretching from 2,300 to 2,600 m with particle anomaly maxima at 2,400 m ($dNTU_{max}$ = 0.08), 2,475 m ($dNTU_{max}$ = 0.06), and 2,500 m ($dNTU_{max}$ = 0.08). There was a small ORP drop on the downcast between 2,575 m and the seafloor ($\Delta ORP = -1$) and on the upcast between 2,595 and 2,550 m ($\Delta ORP = -4$). No significant temperature anomalies were observed for this cast. M21A-26 encountered a plume stretching from 2,300-2,600 m with a clearly defined plume centered from 2,420-2,480 m and an associated particle anomaly maximum ($dNTU_{max}$ = 0.08) at 2,460 m. No ORP or significant temperature anomalies were observed for this cast.

3.4.1.9 Station *16º 43'*

Station 16º 43' was located on-axis at -113° 3' W, 16° 43' S. Two trace metal rosette casts, M21A-08 and M21A-09, were completed 17 hours apart (Figure 3.2I). M21A-08 encountered a large particle-rich plume stretching 2,370 to 2,540 m with a single maximum particle anomaly (dNTU_{max} = 0.3) at 2,418 m. A gradual decrease in the ORP signal was observed in the plume core (2,400-2,470 m) on both the downcast (ΔORP = -10) and upcast (ΔORP = -21). Cast M21A-09 sampled a more complex plume structure stretching from 2,300 m to the seafloor. There were five particle anomaly maxima at 2,350 (dNTU_{max} = 0.01), 2,410 (dNTU_{max} = 0.03), 2,440 (dNTU_{max} = 0.08), 2,475 (dNTU_{max} = 0.12) and 2,525 m (dNTU_{max} = 0.10). A small ORP signal decrease was encountered in the lower parts of the plume (2,475-2,530 m and 2,510-2,560 m; ΔORP = -2, -5) for the downcast and upcast, respectively. Neither cast observed significant temperature anomalies.

3.4.1.10 Station PJ

Station PJ was the only station that was sampled off axis of the ridge, and it was located 11 km west of station Bio at 113° 23' W, 17° 25' S. Two trace metal rosette casts, M21A-23 and M21A-24, were completed 17 hours apart (Figure 3.2J). M21A-23 encountered a large neutrally buoyant plume extending 2,300-2,700 m with a maximum particle anomaly (dNTU_{max} = 0.08) at 2,500 m depth. M21A-24 encountered a neutrally buoyant plume from 2,300-2,600 m, which was the maximum depth of the cast. The maximum particle anomaly (dNTU_{max} = 0.09) was located at 2,475 m. Neither cast observed ORP or significant temperature anomalies.

3.4.1.11 Repeat occupation of U.S. GEOTRACES (GP16) Station 18

Station 18 was a repeat occupation of US GEOTRACES (GP16) Station 18, located on the ridge axis at 112º 45' W, 14º 59' S. Two trace metal rosette casts, M21A-04 and M21A-05, were completed 15.5 hours apart. M21A-04 encountered a large neutrally buoyant plume stretching from 2,350 m to the seafloor with a single maximum particle anomaly ($dNTU_{max}$ = 0.05) at 2,473 m. M21A-05 observed a similar large neutrally buoyant plume extending from 2,320 m to the seafloor. Two particle anomaly maxima ($dNTU_{max}$ = 0.06, 0.04) were located at 2,406 m and 2,541 m, respectively. No significant temperature or ORP anomalies were observed on either cast.

3.4.2 *Chemical characteristics of the neutrally buoyant plume*

A neutrally buoyant plume was observed at all sampling sites. These plumes were spatially diverse in their vertical structures, chemical make-up, and intensity. To best describe the variability in plume chemistry, on-axis sites were first grouped based on plume intensities into high, medium, and low particle concentration categories as defined by the average $dNTU_{max}$ observed at each site (*section 3.4.1*). In the following sections, the general chemical characteristics (tdFe, dFe, pFe, tdMn, and dCH_4) at the center of the neutrally buoyant plumes are discussed in the context of these groupings (*see section 3.3.8* for sample groupings), as well as any additional chemical features unique to a given site (Supplementary Table 3.2).

The chemistry of the on-axis samples that were grouped as "neutrally buoyant plume" samples was visualized in PCA space using the variables tdMn, dCH_4, tdFe, pCu, pS_{tot}, and H_2 (*section 3.3.8*; Figure 3.3A). The first two principal components (PC1 and PC2) describe 64.4% of the variance in these samples. Samples clustered by site, highlighting the unique chemical characteristics of each plume. The tdMn, dCH_4, and tdFe contributed the most to PC1, while pS_{tot}, H_2, and pCu contributed the most to PC2. The high particle plumes (Lava, Bio and 16°43') all grouped together in PCA space, driven largely by high tdMn, dCH_4, and tdFe concentrations in these neutrally buoyant plumes. The medium particle plumes (Bart and Purple Haze) cluster together, driven by their moderate tdMn, dCH_4 and tdFe concentrations and low pS_{tot}. Two of the lower particle plumes, Micro and Flo, also cluster with Bart and Purple Haze. The other two low-particle plumes, North and Macro, cluster in the upper right corner of the PCA space due to their high pS_{tot} and H_2, and low tdMn, dCH_4, and tdFe concentrations. The neutrally buoyant plume from Station PJ and Station 18 were not included in the PCA because they were very distinct from the on-axis plumes, and likely represent composite plumes from many of the vents in the sampling region (Jenkins et al., 2018; Lupton and Craig, 1981).

3.4.2.1 High particle plumes: Lava, Bio, 16º 43'

Three sites had intense, high particle plumes with $dNTU_{max} > 0.1$, including Lava, Bio and 16º 43' (Figure 3.2). These plumes had the highest plume-core Fe concentrations observed in the dataset, with tdFe concentrations averaging 419 ± 145 nM, 274 ± 42 nM, and 239 ± 62 nM at 16º 43', Bio, and Lava, respectively. Most of the Fe was in the particulate phase (pFe; 479 ± 203 nM 16º 43', 315 ± 66 nM Bio, 227 ± 28 nM Lava), although substantial dFe concentrations were also present in all three plumes (dFe; 71 ± 36 nM 16º 43', 12 ± 10 nM Bio, 29 ± 11 nM Lava; Figure 3.4C, F, I). The three plumes were also characterized by high tdMn concentrations (51 ± 7 nM 16º 43', 53 ± 13 nM Bio, 45 ± 9 nM Lava), and dCH_4 concentrations (dCH_4; 3.7 ± 1.1 nM 16º 43', 4.1 ± 0.4 nM Bio, and 4.7 ± 1.6 nM Lava).

Site 16º 43' had the highest tdFe, pFe and dFe concentrations of the high-particle plumes. This site was also enriched in pS_{tot}, with concentrations ranging from 89-179 nM compared to Bio (29-69 nM) and Lava (58-86 nM). The neutrally buoyant plume at Lava was notable for high concentrations of several other particulate trace elements (Supplementary Table 3.2). These high concentrations were observed in samples from both casts at the site and were likely a result of proximity to the buoyant plume. Bio did not have any notable elemental particulate enrichments and had comparatively low %dFe (dFe = dFe/tdFe × 100; 4 ± 3%) when compared to 16º 43' (16 ± 4%) and Lava (13 ± 5%).

The variance in the three high-particle sites was largely explained by their high dCH_4, tdFe, and tdMn concentrations (PC1, Figure 3.3A). The variance in Lava was driven by pCu (PC2), likely due to the site's proximity to buoyant fluids enriched in minor particulate elements. The vertical separation of the sites along PC2 is primarily due to pS_{tot}, with minor contributions from pCu and dH_2. Bio was accordingly on the bottom in the PCA space with the lowest pS_{tot} concentrations.

3.4.2.2 Medium particle plumes: Bart, Purple Haze

Bart and Purple Haze had medium particle concentrations in the neutrally buoyant plume, with $dNTU_{max}$ of 0.06 and 0.08, respectively. Plume core tdFe concentrations ranged from 7.8-225 nM (Purple Haze) and 95-204 nM (Bart). The dFe concentrations at Purple Haze (11 ± 5 nM) and Bart (9 ± 4 nM) were comparable to those at Bio (12 ± 10 nM) but much lower than dFe concentrations in the other high particle plumes at Lava and 16º 43' (Figure 3.4). The pFe concentrations at Purple Haze (302 ± 81 nM) were comparable to those of the higher particle plumes, although pFe concentrations at Bart (193 ± 66 nM) were somewhat lower (Figure 3.4). The tdMn concentrations were lower than those of the high particle plumes at both Purple Haze (40 ± 6 nM) and Bart (29 ± 8 nM) as were dCH_4 concentrations (2.7 ± 1.0 nM, 2.5 ± 0.7 nM; Purple Haze and Bart, respectively).

Purple Haze was enriched in pS_{tot} (72 ± 38 nM) compared to Bart (24 ± 8 nM) and was comparable to the pS_{tot} at Lava. Both Purple Haze and 16º 43' (*section 3.4.2.1*) showed enrichment in pS_{tot} relative to plumes of similar intensity and were notably the only two sites north of 17º S. Purple Haze was also high in other particulates (Supplementary Table 3.2), suggesting the nearby presence of a vent. Bart showed no notable elemental enrichments or depletions. Both Purple Haze and Bart cluster toward the bottom center of the PCA (Figure 3.3A). The two stations are at similar positions along the PC1 because of their moderate tdMn, tdFe, and dCH_4 concentrations, while Purple Haze falls above Bart on the PC2 axis due to its higher pS_{tot} concentrations.

3.4.2.3 Low particle plumes: Macro, Micro, Flo, North

The neutrally buoyant plumes at Macro, Micro, Flo, and North had relatively low particle concentrations ($dNTU_{max}$ = 0.01, 0.02, 0.02, 0.06, respectively). Plume core tdFe concentrations were similarly low (37-41 nM Macro, 34-110 nM Micro, 74-90 nM Flo, and 45-52 nM North). The dFe concentrations at North (2.1 ± 0.5 nM) and Macro (5.6 ± 0.9 nM) were lower compared to dFe concentrations at other stations with medium or high particle plumes (Figure 3.4). However, dFe concentrations at Micro (38 ± 52 nM) and Flo (13.5 ± 5 nM) were the third and fourth highest observed across all the neutrally buoyant plumes in the dataset (Figure 3.4). The pFe concentrations for Macro (43 ± 20 nM), Micro (68 ± 37 nM), Flo (98 ± 25 nM), and North (56 nM, $n = 1$) were the lowest observed in the dataset (Figure 3.4). The center plume at North only had one particulate sample associated with it, but it was similar, while North had insufficient particulate data to assess. Similarly, the tdMn concentrations at these stations were also the lowest of the neutrally buoyant plumes (6.4 ± 0.75 nM Macro, 15.9 ± 14.9 nM Micro, 25.1 ± 8.5 nM Flo, 13.6 ± 2.4 nM North). The dCH_4 concentrations however, (1.8 ± 0.1 nM Macro, 2.2 ± 0.1 nM Micro, 3 ± 1.6 nM Flo, 2 ± 0.1 nM North), were similar to the concentrations in the medium particle plumes (*section 3.4.2.2*).

The neutrally buoyant plumes at Flo, Micro, and Macro had high dissolved gas concentrations for both dCH_4 (Flo; maximum concentration 4.3 nM) and dH_2 (maximum concentration 67.2 nM at Micro, maximum concentration 9.3 nM at Macro). Macro and North both also had elevated concentrations of other minor particulate elements (Supplementary Table 3.2), likely due to their proximity to buoyant fluids (*sections 3.4.1.1-3.4.1.2*). North also had comparatively low %dFe (5 ± 1%) with respect to the other sites (15 ± 4% Macro, 37 ± 46% Micro, 16 ± 5% Flo).

Macro, Micro, and North all cluster to the far right of the PCA (Figure 3.3A) driven by their low dCH_4, tdMn, and tdFe concentrations. The variance in Flo, however, was more similar to Purple Haze and Bart. The variance in Macro and North was mostly explained by PC2, resulting from high dH_2 and pS_{tot} concentrations (Supplementary Table 3.2). While one sample from Micro did have a high dH_2 concentration (Supplementary Table 3.2), insufficient particulate data prevented inclusion of this sample in the PCA.

3.4.2.4 Off axis: PJ, Station 18

PJ had a large neutrally buoyant plume with a particle intensity similar to the "high-particle" on-axis plumes. The tdFe concentrations in the core of the plume ranged from 238-318 nM and were comparable to on-axis station Bio (227-318 nM) located 11 km east of PJ. The pFe concentrations (830 ± 427 nM; Figure 3.4J) and the tdMn concentrations (65.0 ± 27.5 nM) were the highest observed in the dataset. The dFe concentrations (10.1 ± 5.1 nM) were also similar to Bio (11.5 ± 9.5 nM) and were relatively low considering the intensity of the plume (Figure 3.4). PJ was enriched in dCH_4 (4.3 ± 0.4 nM) with concentrations similar to those in the high particle plumes (*section 3.4.2.1*).

The neutrally buoyant plume at Station 18 was less intense ($dNTU_{max} = 0.06$) than that at PJ. Although concentrations of tdFe were not measured for all samples, tdFe concentrations in the center of the lower plume on cast M21A-05 (86-94 nM) were comparable to sites Micro and

Flo. Concentrations of pFe, dFe and tdMn were measured in all plume core samples (pFe 141 ± 72 nM; dFe 6.4 ± 2.9 nM; tdMn; 19.1 ± 6.4 nM) and were relatively low compared to PJ. The pFe and dFe concentrations at Station 18 were most similar to those at Bart, but tdMn was similar to the neutrally buoyant plumes at Micro and Flo. Neither dCH_4 nor dH_2 were sampled at Station 18.

3.4.3 *Near seafloor features*

Both high-temperature and low-temperature "diffuse" hydrothermal venting systems were encountered in this dataset, and both strongly influenced the near-seafloor chemical signatures we observed. Below, we describe the defining characteristics observed for each type of system as well as site-specific observations for individual venting locations. Diffuse venting (Supplementary Table 3.1) was split into two categories, sulfur-rich (*section 3.4.3.2*) and sulfur-poor (*section 3.4.3.3*) based on the degree of sulfur enrichment in the particulate fraction.

3.4.3.1 High temperature venting

Two high-temperature buoyant plumes were observed near the seafloor and below the neutrally buoyant plume at sites Macro (number of samples, *n* = 4) and Lava (*n* = 3). Both sites had large temperature anomalies (ΔT_{max}; +0.1ºC Macro, +0.2ºC Lava, *sections 3.4.1.1, 3.4.1.3*) with corresponding negative density anomalies. There were large ORP anomalies (ΔORP; -129 Macro, -137 Lava) at both stations as well that coincided with near-seafloor particle anomalies ($dNTU_{max}$= 0.04 Macro, 0.08 Lava). The tdMn concentrations observed in the buoyant plumes at Lava (122-216 nM) and Macro (87-123 nM) were the highest observed in the dataset. Similarly, tdFe at Lava (458-652 nM) and Macro (354-556 nM) were higher in concentration than all other samples except for the center of the neutrally buoyant plume at 16º 43' (518-569 nM). Both buoyant plumes had high pFe concentrations (199-2530 nM Lava; 284-557 nM Macro; Figure

3.4A, C) and were also enriched in several other trace particulate metals (Supplementary Table 3.1).

Both Macro and Lava had high concentrations of dissolved gases, indicative of recent magmatic activity. Macro had higher concentrations of dH_2 (7.4-28.5 nM) compared to Lava (0.7-32.7 nM), while Lava had higher concentrations of dCH_4 (2.1-31.3 nM) than Macro (3-6.3 nM). The dCH_4 measured at Lava is the highest in the dataset by a large margin, and the next highest value (13.3 nM) was measured in a diffuse sample at North. In contrast with dCH_4, dH_2 values of comparable magnitude to those observed here were found elsewhere in the dataset.

3.4.3.2 Diffuse venting: sulfur-rich

Three sulfur-enriched diffuse venting sites were visited, including Flo ($n = 5$), Purple Haze ($n = 3$) and North ($n = 5$; Supplementary Table 3.1). The unique chemistry at each site was visualized using PCA, with background samples plotted for comparison (Figure 3.3B). Variables dH_2, dCH_4, tdMn, tdFe, and pS_{tot} were chosen to characterize the three sites and highlight their features with respect to background samples (*section 3.3.8*). The first two principal components (PC1 and PC2) describe a total of 71.6% of the variance in the dataset. All sites clearly separated from the background samples (Figure 3.3B). The variance in samples at North were largely explained by dCH_4 and tdMn, while the variance in the samples at Flo were largely explained by dH_2 and pS_{tot}. The samples from Purple Haze were somewhat less distinct from the background samples, but the variance in those samples was largely driven by differences in dH_2 and pS_{tot}. Background samples clustered in the upper left corner and the variance was driven by their higher tdFe concentrations, and lower tdMn, pS_{tot}, dH_2 and dCH_4 concentrations.

Each of the sites with high amounts of particulate sulfur had an associated near seafloor ORP anomaly (ΔORP; -1 Flo, -4 Purple Haze, -103 North. North also had a temperature anomaly of +0.09 ºC (*section 3.4.1.2*) that corresponded with a negative density anomaly, suggesting that buoyant fluids were sampled there. All three sites were low in particulates and were low in tdFe (12.6-23.0 nM North, 10.2-35.3 nM Purple Haze, 11.0-34.2 nM Flo). The tdMn was high however, (3.2-45.0 nM North, 2.4-7.6 nM Purple Haze, 3.7-12.8 nM Flo), supporting the hydrothermal origin of the fluids.

Near seafloor samples at Flo, Purple Haze, and North showed elevated pS_{tot} concentrations when compared to deep background samples with similar particle anomalies. Samples collected near the seafloor from Flo (pS_{tot} = 53.6-223.7 nM) and North (pS_{tot} = 38.3-98.2 nM) were the most sulfur enriched, while Purple Haze (pS_{tot}; 18.4-70.8 nM) was slightly lower. By comparison, pS_{tot} in background samples ranged from 15.4-32.6 nM (*n* = 15) with an outlier of 64.4 nM belonging to North. North, Flo, and Purple Haze were also enriched in several other particulate trace metals (Supplementary Table 3.1). Both North and Flo had elevated dissolved gases. Flo had a stronger dH_2 signature (1.8-3.9 nM) than North (1.1-1.8 nM), while North had a stronger dCH_4 signature (2.5-13.3 nM) than Flo (1.2-2.5 nM). Purple Haze was only slightly enriched in dCH_4 (1.2-1.8 nM) compared to background (0.37-2.1 nM, 1.0 ± 0.6 nM *n* = 14; Figure 3.3B).

3.4.3.3 Diffuse venting: sulfur-poor

Near seafloor samples at Bart (*n* = 2), 16º 43 (*n* = 3) and Micro (*n* = 2) did not show the same degree of pS_{tot} enrichment as Flo, Purple Haze and North, but did contain features that suggested an influence from diffuse flow (Supplementary Table 3.1). The chemistry of the three sites were visualized in a third PCA (Figure 3.3C), with background samples for comparison. Similar variables to the sulfur-rich diffuse PCA (dH_2, dCH_4, tdMn, and pS_{tot}) were chosen. However, tdFe was replaced by %dFe (*section 3.3.3*) because it explained more of the variance in samples from 16º43’. The first two principal components described 61.1% of the variance in these samples. The separation between sites from background samples and the diffuse flow samples was also less clear than for the pS_{tot}-enriched sites, suggesting that diffuse flow was weaker or less distinct at Bart, Micro, and 16º43’. Bart and 16º 43’ had no observed ORP anomaly, but Micro had a ΔORP of -26. All three sites were low in particulates ($dNTU_{max}$; Bart 0.01, 16º 43’ 0.00, and Micro 0.01), and had low tdFe (32.2-34.2 nM Bart, 16.8-22.5 nM 16º 43’, 33.4-35.8 nM Micro). The tdMn concentrations were high enough to distinguish these samples from background samples however, with values ranging 9.0-10.6 nM, 3.0-6.9 nM, and 7.4-8.1 nM for Bart, 16º 43’, and Micro, respectively.

There were very few trace elements enriched in the particulate phase for these sites, in contrast with Flo, North, and Purple Haze. The dCH_4 was higher than background concentrations, ranging from 1.5-1.9 nM across the three sites. Micro also had extremely high dH_2 (70.1 nM), the highest in the dataset, while 16º 43’ had more modest concentrations (1.4 nM). The final line of evidence suggesting an influence of diffuse venting on these samples was the %dFe, because we expected diffuse samples to have a greater proportion of Fe in the dissolved phase compared to the particulate phase (Lough et al., 2019). 16º 43’ had particularly high %dFe (29-40%), although Bart and Micro also had elevated values (%dFe; 12-16% and 10%, respectively). Each site separated slightly from background in PCA space, driven by different variables (Figure 3.3C). The variance in samples from 16º43’ was largely driven by the %dFe and the variance in samples from part was largely explained by dCH_4. Micro had slightly elevated dH_2 concentrations that were responsible for explaining most of the variance in those samples. It’s important to note however, that the Micro sample with the highest dH_2 concentration could not be used in this PCA due to lack of particulate data.

3.4.4 *Physical and chemical speciation of dissolved iron*

To understand how vent chemistry influenced the stabilization of dFe, we further explored the physical and chemical speciation of dFe at each site. In this section, we first present the physical speciation of dFe (*section 3.4.4.1*) expressed as %cFe. Next, we describe the dFe-binding organic ligand data (*section 3.4.4.2*), including conditional stability constants ($\log K_{Fe',FeL}^{cond}$) and ligand concentrations (L). The samples had complex speciation that varied widely between type of hydrothermal environment. As a result, both subsections are discussed in the context of the distinct environments that were sampled*,* including the center neutrally buoyant plume, diffuse, and buoyant high temperature samples. However, we combined sampling environments "Deep Background" and "Shallow" into a single "Background" environment throughout section 3.4.4 to increase statistical power. These environments were statistically indistinguishable (Mann–Whitney *U*-Test, $p > 0.35$) for the variables discussed in this section. Off-axis sites PJ and Station 18 are discussed separately from the on-axis sites.

3.4.4.1 Physical speciation of dissolved iron

There was a large colloidal fraction of dFe in all environments sampled (Supplementary Table 3.1Supplementary Table 3.2), particularly in the neutrally buoyant plume (Figure 3.5F). Overall, there was little variability in the colloidal fraction at the center of the neutrally buoyant plume (90 ± 8%, $n = 27$, Figure 3.5F) despite large inter-site differences in dFe concentrations (Figure 3.4, Figure 3.5A; Supplementary Table 3.2) and particle composition (Figure 3.3, Supplementary Table 3.2). Three sites stood out however, including site 16º 43', a high particle plume (*section 3.4.2.1*) with an unusually high colloidal fraction (98 ± 1%) and sites Macro and North with somewhat lower colloidal fractions (80 ± 21% Micro, 75 ± 3% North). Collectively, the center of the neutrally buoyant plume had a significantly higher colloidal fraction than background samples (Mann–Whitney *U*-Test, $p = 0.001$) and diffuse samples (Mann–Whitney *U*-Test, $p = 0.006$). Off-axis, the colloidal fraction for the center of the neutrally buoyant plume at PJ (93 ± 3%, $n = 3$) and Station 18 (92 ± 1%, $n = 4$) were similar to the on-axis neutrally buoyant plumes.

There was much larger variation in the %cFe for diffuse samples (70 ± 35%, $n = 20$) compared to the neutrally buoyant plume samples (Figure 3.5F). The %cFe at sites 16º43, Flo, and Purple Haze were comparable to the neutrally buoyant plume samples (90 ± 2% 16º43’, 90 ±4% Flo, 90 ± 5% Purple Haze), while Bart and Micro had somewhat lower colloidal fractions (84 ± 1% Bart, 81 ± 1% Micro). North was a notable low outlier, with a colloidal fraction averaging just 15 ± 27%. Although North was a large factor in lowering the average %cFe across all of the diffuse samples, removing North from the dataset still results in a significantly smaller colloidal fraction in diffuse samples when compared to the neutrally buoyant plume (Mann–Whitney *U*-Test, $p = 0.03$). The colloidal fraction of diffuse samples was not, however, statistically different from background samples (%cFe Background, 62 ± 37%, $n = 17$, Mann–Whitney *U*-Test, $p = 0.66$).

Of the two buoyant high temperature plumes we sampled, Macro had a very high colloidal fraction (98 ± 1%, $n = 4$) comparable to the neutrally buoyant plume at 16º 43’. Lava however, had a much lower %cFe (88 ± 8%, $n = 3$) that was closer to the average neutrally buoyant plume value and several of the diffuse sites. Notably, the colloidal fraction in the buoyant plume at Lava decreased with height above the seafloor (from 96% to 80%) likely due to dilution with background seawater. The colloidal fraction at Macro, however, remained similar across all four buoyant plume samples.

3.4.4.2 Chemical speciation of dissolved iron

Organic dFe-binding ligands were heterogeneous across the dataset (*n* = 68) varying widely in concentration (0.3-202.2 nM) and binding strength (log$K_{Fe',FeL}^{cond}$, 9.4-12.7; Figure 3.5D-E). On-axis, ligand concentrations were less than dFe in 68% of samples and primarily belonged to the weakest L_3 ligand class (log$K_{Fe',FeL}^{cond}$ < 11; Gledhill and Buck 2012). Off axis, 91% of samples from PJ (*n* = 11) had [L] < [dFe]. At Station 18 however, only 29% of samples (*n* = 7) had dFe in excess of organic ligands.

On-axis, samples from the center of the neutrally buoyant plume (*n* = 11) had large variability in ligand concentrations (7.4 ± 6.8, 1.7-22.6) with 82% of these samples having [L] < [dFe]. The stability constants of these ligands, however, were very similar (10.5 ± 0.4; Grubbs test outlier 11.96, *p* = 0.02) despite the variability in concentrations. Most of the ligands in the neutrally buoyant plume were fairly weak, and primarily in the L_3 class. Only two samples were in the L_2 (12 > log$K_{Fe',FeL}^{cond}$ > 11) class, and none belonged to the strongest L_1 (log$K_{Fe',FeL}^{cond}$ > 12) class (Gledhill and Buck, 2012).

Samples from diffuse vents (*n* = 13) were distinct from the neutrally buoyant plume samples. Unlike the neutrally buoyant plume, ligand concentrations from diffuse sites were fairly constant (2.9 ± 2.0, 0.3-6.7 nM), but with a much wider range in binding constants (log$K_{Fe',FeL}^{cond}$, 11.0 ± 1.0, 9.4-12.7). Indeed, the highest (log$K_{Fe',FeL}^{cond}$ = 12.7) and lowest (log$K_{Fe',FeL}^{cond}$ = 9.4) binding constants of the dataset were both found in diffuse samples from North. Most diffuse samples belonged to the L_3 class, but three samples from North belonged to the L_1 class and one sample each from Bart and Micro were in the L_2 class. Approximately 69% of diffuse samples had [L] < [dFe]. Only three high-temperature buoyant plume samples were analyzed for ligands, all of which were from Lava. Ligand concentrations in the high-temperature buoyant samples were highly variable (4.1-202.2 nM), but the $\log K_{Fe',FeL}^{cond}$ values were remarkably consistent (10.26 ± 0.02). All high-temperature buoyant plume samples had [L] < [dFe].

Background samples differed considerably from hydrothermally-influenced samples. Only one background sample ($n = 9$) had [L] < [dFe], a considerably smaller proportion of samples (11%) compared to diffuse (69%), neutrally buoyant plume (85%) and high temperature buoyant plume samples (100%). Ligand concentrations in background samples (2.4 ± 1.2, 0.8-4.1 nM) were comparable to diffuse samples, but significantly lower than concentrations of ligands in the center of the neutrally buoyant plume (Mann–Whitney *U*-Test, $p = 0.03$). The binding strengths of background samples ($\log K_{Fe',FeL}^{cond}$ 10.93 ± 0.64, 9.96-11.91) however, had a similar range to those in the neutrally buoyant plume and were less variable than the diffuse samples. Ligands measured in background samples belonged to the L_3 ($n = 6$) and L_2 ($n = 3$) classes.

The ligands measured off-axis at PJ were different from those at the on-axis stations. Background samples off-axis had relatively constant ligand concentrations (2.1 ± 0.5 nM, 1.75-2.91 nM, $n = 5$) and stronger binding strengths ($\log K_{Fe',FeL}^{cond}$ 12.0 ± 0.2; Grubbs test outlier 10.0, $p < 0.01$) than on-axis background samples. 80% of background off-axis samples had [L] < [dFe]. Ligand concentrations in the center of the neutrally buoyant plume at PJ (5.4 ± 0.5 nM, n =4) were relatively high, but they had the weakest binding strengths ($\log K_{Fe',FeL}^{cond}$ 10.0 ± 0.0; Grubbs test outlier 11.1, $p < 0.01$) of any sampling environment in the dataset, three of which were L_3 and one of which was L_2. All four PJ center plume samples had [L] < [dFe].

At Station 18 (Figure 3.6) we had samples ($n = 7$) with mild to moderate plume influence. Ligand concentrations averaged 3.2 ± 1.1 nM (1.7-4.89 nM) with a moderate $\log K_{Fe',FeL}^{cond}$ (11.5 ± 0.5, 10.6-12.0). The binding strengths at Station 18 were significantly greater than those found in the neutrally buoyant plume at either Station PJ or the on-axis sites (Mann–Whitney *U*-Test, $p < 0.03$). One sample belonged to the L_1 class, four samples were L_2, and two were L_3. Only one sample had $[L] < [dFe]$.

3.5 DISCUSSION

In this work, we were focused on understanding how the fast-spreading SEPR impacts the stabilization and dispersal of hydrothermal Fe throughout the Pacific Ocean basin. To explore this, we concentrated on the 16.5º-18ºS section of ridge crest that had been previously been shown to host a high density of vents, including many sites with diffuse flow (Auzende et al., 1996; Charlou et al., 1996; Embley et al., 1998; Renard et al., 1985). We hypothesized that these diffuse sites might be playing an important role in the long-range transport of dFe, and thus have an outsized impact on the deep ocean Fe inventory. The high frequency of diffuse venting discovered along this ridge sector in the 1990's led us to return in 2021 with goals to (1) assess the changes in the region from previous expeditions, (2) chemically characterize diffuse flow and improve water column identification of diffuse venting, and (3) examine the contributions of the highly varied venting systems to the stabilization of Fe and the formation of the large hydrothermal plume of dFe observed thousands of kilometers into the Western Pacific basin (Fitzsimmons et al., 2017, 2014; Resing et al., 2015).

3.5.1 *Chemical characteristics of the SEPR over time*

Our main study area (Figure 3.1) was previously explored during three expeditions between 1993 and 1994 (Auzende et al., 1996; Charlou et al., 1996; Embley et al., 1998; Urabe et al., 1995). In November and December of 1993, a joint U.S. Japanese expedition surveyed the 13º30'-18º40' S sector of the SEPR using a combination of tow-yos and vertical CTD casts to characterize the water column (Baker and Urabe, 1996; Feely et al., 1996; Ishibashi et al., 1997; Urabe et al., 1995). That same December, the French NAUDUR expedition conducted 23 dives with submersible *Nautile* between 17º and 19ºS (Auzende et al., 1996; Charlou et al., 1996). Finally, a joint Japanese (Japanese Ridge Flux program) and American (NOAA VENTS program) expedition visited the 17º22'-17º35' S sector of the ridge from September-December 1994 and conducted eight dives with the Japanese submersible *Shinkai 6500* (Embley et al., 1998). The combination of water column and submersible studies revealed a dynamic ridge crest with chemical and geological features that varied widely along the ridge.

The 17ºS-18ºS sector was found to be of particular interest in all three expeditions. Here, the ridge crest is highly inflated and controlled primarily by magmatic rather than tectonic processes (Scheirer and Macdonald, 1993; Urabe et al., 1995). Furthermore, hydrothermal plumes are nearly continuous along this section (Baker and Urabe, 1996; Feely et al., 1996), resulting from the high density of seafloor venting features (Auzende et al., 1996; Embley et al., 1998). Submersible observations confirm that much of the hydrothermal activity in this section is low temperature or diffuse venting (Auzende et al., 1996; Charlou et al., 1996). The high density and diversity of venting systems observed on the ridge in 1993 and 1994 (Figure 3.7D) suggested that extensive hydrothermal activity should still be present thirty years later. However, we expected there to be potentially significant changes in the locations and chemistry of the venting features. The magmatically-driven system along the 16º-18º S sector of the SEPR is characterized by shallow, less stable vents with shorter lifetimes as the magma supply is rapidly exhausted (Baker and Urabe, 1996; Charlou et al., 1996; Sinton et al., 1991). This is a significant departure from the more stable systems along slow-spreading ridges like the Mid Atlantic Ridge, where vents can be stable for tens of thousands of years (Früh-Green et al., 2003). While individual vent sites may fluctuate along the SEPR, the fast-spreading rates results in the highest spatial frequency of hydrothermal activity along any ridge axis in the world (Baker and German, 2004; Beaulieu et al., 2015). The high density of vents along the SEPR may therefore compensate for variability in the location and chemistry of individual sites. Thus, the composite hydrothermal plume originating at the SEPR and extending deep into the Western Pacific Basin (Resing et al., 2015) may be quite temporally stable (Lupton and Jenkins, 2017). In this section we discuss the on-axis neutrally buoyant plumes (*section 3.5.1.1*) and individual seafloor venting features (*section 3.5.1.2*) in the context of the previous work performed in this region.

3.5.1.1 Changes in the neutrally buoyant plume at the SEPR over time

The 1994 expedition to the SEPR observed a nearly continuous neutrally-buoyant plume over the 16.5º-18ºS sector of the ridge crest (Baker and Urabe, 1996). However, the intensity and chemical composition of this plume changed across relatively short spatial scales (Figure 3.7A-C) (Feely et al., 1996; Ishibashi et al., 1997; Urabe et al., 1995). We observed similar spatial heterogeneity along this section of ridge crest. The $dNTU_{max}$ varied from 0.01-0.34 (Figure 3.2) and particulate elemental composition similarly fluctuated between sites (*section 3.4.2*; Figure 3.3). A strong linear correlation between pFe and dNTU at all sites ($R^2 = 0.81$, $n = 55$) suggested that most plume particles were primarily pFe species, in agreement with results from 1994 (Feely et al., 1996). We did not however, observe the previously-recorded dramatic increase in plume intensity south of 17ºS.

Plume intensity remained relatively similar between 1993 and 2021 when considering the entire 16.5º-18ºS section of ridge (Baker and Urabe, 1996; Embley et al., 1998; Feely et al., 1996; Ishibashi et al., 1997). Temperature anomalies (ΔT; 0 - +0.05 ºC) and particle anomalies (dNTU; 0-0.12, outlier cast M21A-08 $dNTU_{max} = 0.34$) in the neutrally buoyant plumes had ranges comparable to previous results (ΔT; 0-0.04 ºC, dNTU 0-0.08) (Feely et al., 1996). The tdMn concentrations were also comparable between our study (5-67 nM) and previous data (5-100 nM; Figure 3.7C) (Ishibashi et al., 1997). These three metrics are good indicators of hydrothermal activity (Charlou et al., 1991; Elderfield and Schultz, 1996), and the similarity in ranges between the two studies suggests that the ridge sector as a whole has retained a comparable degree of venting activity. The large, Fe-rich plumes located at sites 16º43' and Purple Haze were particularly consistent with previous results from the ridge sector north of 17º20'. This agrees with the assessment of Feely et al. (1996) that the hydrothermal activity at these latitudes is highly evolved and therefore more stable.

South of the 17º20' we saw evidence that hydrothermal activity has changed in the past thirty years. We measured far lower dCH_4 concentrations in the neutrally buoyant plume (1.3-6.5 nM) when compared to 1993 (1-40 nM; Figure 3.7B) (Ishibashi et al., 1997). We can infer by the equally high tdMn concentrations (Figure 3.7C) to previous studies that this is not due to less venting, but rather a result of an aging system. Younger vents are more gas rich, while more evolved venting systems are primarily rich in metals (Baker and Urabe, 1996; Charlou et al., 1991; Feely et al., 1994). We found that the sites with the highest dCH_4:tdMn (nM:nM) ratios (North 0.77, 16º 43' 0.53, Purple Haze 0.50, and Micro 0.41), were likely indicative of more vigorous magmatic activity. These dCH_4 enriched systems have moved northwards since 1993 from 17º30-17º45'S to 17º10-17º20'S (Figure 3.7A, Ishibashi et al. 1997). This shift is consistent with the instability of hydrothermal systems on ultrafast spreading ridges (Baker and Urabe, 1996; Charlou et al., 1996) and suggests that the most active part of the ridge has also moved northwards. However, the maximum dCH_4:tdMn measured in this study are slightly lower than the most active systems in 1993 (~1-2; Figure 3.7A; Ishibashi et al. 1997). Furthermore, the higher dCH_4:tdMn ratios in our dataset primarily result from low tdMn rather than high dCH_4. The maximum dCH_4 concentrations in our dataset at North (13.3 nM), Micro (2.2 nM), and Macro (6.3 nM) are low compared to the 1993 dCH_4 maximum (40 nM; Figure 3.7B; Ishibashi et al. 1997). Only one sample from the buoyant plume at Lava (dCH_4 = 31.3 nM) reached concentrations characteristic of the southern portion of the ridge in 1993. The overwhelmingly lower dCH_4 concentrations measured in this study compared to 1993 suggests that this entire section of ridge has aged.

The pS_{tot}:pFe ratios measured throughout the region also support an aged system relative to 1993. The pS_{tot}:pFe ratio is a good indicator of recent magmatic activity, because younger systems will be enriched in sulfur relative to Fe (Feely et al., 1996, 1994; Von Damm et al., 1995). We found that pS_{tot}:pFe (nM:nM) followed a similar north-south spatial pattern as dCH_4:tdMn, with the highest values at Macro (8.2), North (5.7), and Purple Haze (4.4), although with a notably large outlier at Flo (20.4). While the spatial trends between the two variables are similar, we did not see the tightly coupled relationship between pS_{tot}:pFe and dCH_4:tdMn noted in Ishibashi et al. (1997). This may be either a result of an aging system, changes in the way pS_{tot} is measured (Feely et al., 1991), or some other mechanism.

There is some debate on the temporal stability of hydrothermal plumes on this section of the SEPR. Based on pMn comparisons to 1980 (Shimmield and Price, 1988), Feely et al. (1996) suggested that the SEPR plumes are stable over decadal timescales. However, Embley et al. (1998) demonstrated that plume structure can vary significantly on an annual basis, shown by a repeat site comparison at 17º28'S and 17º34' S in 1993 and 1994. While we cannot infer the relative stability of plumes over longer (months-years) timescales from our dataset, we can assess short term (hours-days) variability. We found that plume structures were often temporally unstable over time scales as short as hours (Figure 3.2), likely a result of tidal flow or internal waves (Rudnicki and German, 2002). It is difficult to know if the plume differences observed by Embley et al. (1998) were a function of tidal variation rather than a truly altered plume source. Although on-axis plumes appeared unstable over hourly timescales in our study, the average plume intensity and structure, especially slightly off-axis, may be more stable when averaged over a daily tidal cycle. West of the ridge axis, the neutrally buoyant plumes are likely comprised of several individual plume signals that advected northwestwards from the ridge axis and represent a spatially and temporally averaged hydrothermal signal (Jenkins et al., 2018; Lupton and Craig, 1981). Station PJ, located eleven kilometers west of the ridge axis, and Station 18 sampled by the U.S. GEOTRACES program (Moffett and German, 2018), likely captured this composite plume (Jenkins et al., 2018). We observed that the plume structure and intensity was stable between casts at PJ and plume intensity was stable at Station 18 although the vertical structure was somewhat different from when it was first measured on GEOTRACES (Buck et al., 2018), possibly as a result of shifting tides or currents (Figure 3.6). The stability observed at both stations, though, suggests that off-axis and older plumes may be temporally stable.

Overall, the composite chemical characteristics of the neutrally buoyant plume over the 16.5º-18ºS section of ridge remained very similar to what was observed 30 years ago. The ranges in temperature and particle anomalies, as well as tdMn concentrations were consistent between studies. We also observed a similar degree of plume heterogeneity along the axis that suggests a comparatively diverse and high density of vents as encountered in previous expeditions (Figure 3.7A-C). However, the younger, more magmatically-active vents have shifted northwards when compared to 1994 (Figure 3.7A), and the lower dCH_4 concentrations throughout the survey area (Figure 3.7B) suggests many of the sites have aged over time

3.5.1.2 Changes in near seafloor features over time

Our 16º30-18ºS survey region overlapped with previous submersible expeditions by *Nautile* (17º08'-17º12'S and 17º21'-17º28'S) and *Shinkai* (17º24'-17º35'S; Figure 3.7D) (Auzende et al., 1996; Embley et al., 1998). Using ORP, light-scattering, and temperature sensors on AUV *Sentry*, we were able to identify hydrothermal seafloor features along the full survey section, including those that had been previously explored. Similar to the prior expeditions, most of the venting that we encountered was diffuse, and only four out of forty hydrothermally-active sites identified by *Sentry* could be confirmed to have active high-temperature chimneys (German et al. *in prep*). We also encountered fresh lava flows, a feature that was previously observed at several locations (Auzende et al., 1996; Charlou et al., 1996). While we observed similar hydrothermal features as earlier studies, there was significant variation in the locations (Figure 3.7D). The similarity of venting features suggests that there are characteristic venting environments found along this section of ridge crest, likely a function of the local ridge morphology. The temporal changes in vent location however, may be a feature of unstable venting conditions on an ultrafast, magmatically-controlled spreading center (Baker and Urabe, 1996). These conditions provide for a high spatial density of hydrothermal venting (Baker and German, 2004; Beaulieu et al., 2015), but may result in shorter lifetimes for individual sites.

Several of the venting fields first identified in 1993 and 1994 appear to have been relatively stable over the past thirty years (Figure 3.7D). *Nautile* first identified a large system of diffuse and high temperature flow along the 17º24'-17º28'S sector of the ridge in 1993 (Auzende et al., 1996). *Shinkai* observed a similarly extensive region of hydrothermal activity along the same section in 1994 (Embley et al., 1998), and we presumably encountered the same system near site Bio based on the strong ORP and particle anomalies recorded by *Sentry* (German et al. *in prep*). We also encountered hydrothermal activity near the locations of diffuse systems first documented by *Nautile* at 17º12'S (Auzende et al., 1996) and by *Shinkai* at 17º32'S (Embley et al., 1998), although we did not designate these sites as major stations. These results suggest that some of the hydrothermal features along this portion of ridge crest are stable over decadal timescales. Other hydrothermal features appear to be more short-lived. We did not observe any indication of seafloor hydrothermal activity at 17º22.43'S, a formerly focused flow feature identified in 1993 (Charlou et al., 1996). The large diffuse field at 17º34'S documented in 1994 (Embley et al., 1998) also does not appear active anymore based on the data from *Sentry*. We did, however, identify a few new venting fields in the previously-explored sectors. Site North at 17º10'S was previously identified as having only minimal hydrothermal activity (Charlou et al., 1996), and a second, likely diffuse, site was found at 17º31'S although it was not chosen as a major station. Thus, this section of ridge crest appears to be relatively dynamic, with some temporal variability in sites in addition to the more stable features. We note however, that it is possible we missed some of the previously-documented sites, because indicators of hydrothermal flow can be both subtle and spatially confined.

We were unable to explore all of the hydrothermal features indicated by *Sentry* data, and of the nine on-axis sites we visited, only two were previously explored by *Nautile*, including North and Bio (Figure 3.7D). These sites showed significant changes compared to their first documentation in 1993 (Auzende et al., 1996). North was previously characterized as a mostly inactive field with some diffuse fluids present (Charlou et al., 1996). Our exploration measured a buoyant fluid signal rich in dCH_4 and pS_{tot} (*sections 3.4.2.3, 3.4.3.2*). While metal concentrations were low and characteristic of diffuse flow, the buoyant fluid combined with high dCH_4 and sulfur concentrations suggests fresh hydrothermal activity and a more recent magma intrusion since it was last visited in 1993. Conversely, Bio was similar to when it was last sampled.

Previous reports described a mature biological community and a highly active hydrothermal site with active chimneys, fresh lava, and high gas content (Auzende et al., 1996; Charlou et al., 1996). We similarly saw active chimneys and a robust biological community. However, no fresh lava was observed in the photo surveys by *Sentry*, and dCH_4 concentrations over the site (2-4 nM) were lower than those measured previously (19-43 nM, 17º29'S; Figure 3.7B) (Ishibashi et al., 1997). This suggests that the vent system has either aged and/or has not had a recent eruption. The system appears quite stable however, having been documented first in 1984 by researchers in the submersible *Cyana* (Renard et al., 1985).

While we did not see new lava flows at Bio, we did find fresh lavas further south at the eponymous site Lava (17º44'S). There, we found recent lava engulfing preexisting biological communities, as well as slightly older lava with yellow staining that could be due to biological activity (German et al. *in prep*). The trace metal CTD cast targeting this site captured a large temperature anomaly (ΔT_{max} = +2ºC, 0.34 m above seafloor) that did not extend 10 m above the lava flow. This was similar to the observations of *Nautile*, which encountered a temperature anomaly of +2.5ºC hugging the seafloor 2-3 m above fresh lava at 18º37'S (Auzende et al., 1996). Although *Sentry* photographed an active chimney near Lava (German et al. *in prep*), the temperature anomaly observed in the cast appears to be a result of diffuse flow around the new lava field rather than the chimney. The temperature anomaly did not extend upwards into the water column as would be characteristic of buoyant chimney fluid, although the plume chemistry at the site (Figure 3.3A; Supplementary Table 3.1-Supplementary Table 3.2) appears to be dominated by the nearby chimney.

The chimney found at Lava was one of four we observed via *Sentry* photographic surveys between 16.5º and 18ºS. Two chimneys, located at 17º27'S and 16º53', were not explored in favor of focusing on diffuse sites, and the fourth chimney was located near Bio. Of the two chimneys we explored, we were only able to capture buoyant fluid from Lava as confirmed by the extremely high metal concentrations (*section 3.4.3.1,* Supplementary Table 3.1), and large negative density anomalies. However, we appeared to have captured buoyant fluid from a fifth unidentified chimney near Macro. While we have no photographic evidence, this site had negative density and positive temperature anomalies that extend 40 m above the seafloor, a strong ORP anomaly, and high metal concentrations characteristic of focused high-temperature flow or possible un-focused pervasive high-temperature diffuse venting. Additionally, Macro also had a moderately high dCH_4:tdMn ratio that suggested recent magmatic input (Figure 3.7A). Because *Sentry* had a limited view, it is likely that we missed photographing the feature contributing to this buoyant signal. The frequency with which we documented chimneys was similar to previous results along the ridge. *Nautile* recorded two sites with active chimneys along their 17º-17º12 and 17º20-17º30 surveys (Charlou et al., 1996), *Shinkai* found one chimney along their 17º24'-17º35'S survey (Embley et al., 1998), and we found four chimneys along our 16º30-18ºS survey (Figure 3.7D). Notably, the chimney we identified at 17º27' was not recorded in the previous surveys, although the area was described as hosting diffuse flow (Charlou et al., 1996). We did not encounter the *Nautile*-identified chimney near 17º25.8' nor the small chimney at 17º26.18' located by *Shinkai* (Auzende et al., 1996; Charlou et al., 1996). We did however, encounter water column anomalies characteristic of hydrothermal activity near those sites (German et al. *in prep*).

Comparison between our dataset and the expeditions in 1993 and 1994 indicate that hydrothermal vents along the SEPR share similar features, but change spatially and temporally (Figure 3.7D). Venting was dominated by diffuse flow with occasional instances of fresh lava or high temperature chimneys. Some venting fields, such as that stretching from 17º24' to 17º28'S seemed to be stable over decadal time scales. Others however, appeared to be more ephemeral such as the venting signals that disappeared from 17º22'S and 17º34'S. Even the systems that were more stable, such as those at Bio, exhibited chemical changes as they evolved from younger, gas-rich systems to more metal dominated fluids. Fresh lava flows were similarly transient, erupting sporadically before being rapidly cooled and colonized by microbes (Auzende et al., 1996; Charlou et al., 1996, German et al. *in prep*). Together, these features create a dynamic ridge crest characterized by diffuse venting and a rapidly changing hydrothermal landscape.

3.5.2 *Identifying diffuse systems*

Low-temperature diffuse venting accounts for an estimated 50-90% of hydrothermal flow (German et al., 2016) and up to 90% of axial heat flux (Elderfield and Schultz, 1996). Despite its geochemical importance, defining and locating diffuse flow remains difficult (Baker et al., 2016; Bemis et al., 2012; Chen et al., 2021; Lough et al., 2019). Diffuse venting is broadly classified as low-temperature (< 50 ºC), low-velocity fluids with a decreased metal and particulate content than their high temperature counterparts (Baker et al., 2016; Bemis et al., 2012). These broad metrics unsurprisingly, cause a wide range of chemical and geological variability across diffuse systems (e.g. Bemis et al. 2012 and references therein). Diffuse low-temperature flow has been identified in hydrothermal systems as shimmering water within and above cracked lava and rubble (e.g. Butterfield et al., 2004; Humphris et al., 2002), associated with sulfide mounds (e.g. Tivey and Johnson, 2002), and even in more focused flows associated with "beehive" chimneys (e.g. Tivey, 1995) or lava pillars (e.g. Butterfield et al., 2004). Diffuse venting is usually found in conjunction with higher temperature fields due to the difficulties in locating isolated diffuse systems without strong particle anomalies (Baker et al., 2016; Bemis et al., 2012). However, diffuse venting without associated high temperature features is likely common, particularly on fast to ultrafast spreading ridges (Auzende et al., 1996; Baker et al., 2016; Charlou et al., 1996; Chen et al., 2021).

Recent studies have demonstrated that diffuse fluid is out of redox equilibrium with the surrounding seawater, helping to improve the identification of isolated diffuse systems (Baker et al., 2016; Chen et al., 2021). A study along the 2ºN-5ºS sector of the EPR used towed ORP arrays in conjunction with turbidity sensors to infer locations of diffuse flow sites (Chen et al., 2021). Locations with an ORP anomaly in conjunction with low turbidity were classified as diffuse sites (Chen et al., 2021). However, there were no photographic or additional chemical surveys to confirm the putative diffuse flow. Here, we expand on this by adding photographic surveys using *Sentry* and chemical sampling with CTD casts to confirm putative diffuse sites initially identified by an ORP and turbidity sensor survey. We found that the ORP-turbidity method was excellent at identifying many diffuse sites, but might have missed more subtle sites that were characterized only by chemical anomalies. Here, we discuss the chemical characteristics of the sites associated with an ORP anomaly as well as those without.

Four of the diffuse sites we sampled (Flo, Purple Haze, Micro, and North) showed a near-seafloor ORP anomaly coincident with low particle anomalies. Of the four, Flo, Purple Haze, and North were enriched in pS_{tot} and had high pS_{tot}:pFe ratios (Figure 3.3B; Supplementary Table 3.1). These sites also had tdMn concentrations above background values and high dCH_4:tdMn, suggesting recent volatile-rich magmatic activity. These sites are therefore likely examples of younger diffuse sites. Interestingly, they were found in very different locations along the ridge axis (Figure 3.1). The chemical similarity between these sites despite the spatial separation indicates that similar processes are influencing diffuse venting along the ridge. Despite similarities, each site also retained some distinct chemical features (Figure 3.3B; *sections 3.4.3.2-3.4.3.3*). This is much like the differentiation between high temperature venting systems. High temperature vents are often categorized by their geological setting (Beaulieu et al., 2015), which gives the vent systems certain shared features, although each vent site retains a unique fluid chemistry even when hosted by a similar geological formation (Beaulieu et al., 2015; Von Damm, 1990).

While the combined ORP and particle anomaly method is very useful for identifying diffuse venting, it cannot capture all types of diffuse systems. Diffuse venting can be very subtle, particularly if the flow is low and fluids are cool enough that they do not rise high above the seafloor. In these instances, diffuse systems must be identified either photographically or by additional chemical characterization. Bart and 16º 43' were two such sites in this study. While these sites were originally chosen based on ORP anomalies from a *Sentry* survey, the additional trace metal casts in the area did not encounter any ORP anomalies, suggesting that we were perhaps over a slightly different area or that the sites had high temporal variability. Both sites had low particle anomalies near the seafloor and tdMn concentrations above background (Figure 3.3C). Site 16º 43' was further notable for having a high %dFe (*section 3.4.3.3*). While Bart did not show a high %dFe, samples had comparatively high dCH_4 concentrations relative to background values (Supplementary Table 3.1), suggesting hydrothermal influence on the sample.

Based on our observations, we can make a few recommendations for identifying diffuse systems in the future. We verified based on submersible photography and chemical analysis that the presence of a near seafloor ORP anomaly coincident with low particulate anomalies is an accurate indicator of diffuse hydrothermal flow along the SEPR. Further chemical analysis identified pS_{tot}, dCH_4, dH_2, tdMn, and %dFe as good indicators of diffuse fluids, even in the absence of an ORP signal. We conclude that diffuse venting along the SEPR is abundant, and that it can be readily identified using both sensor and chemical methods. It is likely that these methods can be used to identify diffuse venting along other ridges as well, although the chemical variation between ridge axes cannot be underestimated.

3.5.3 *Stabilization of dissolved iron*

The high density and diversity of diffuse flow systems along this section of ridge likely has a significant impact on the long-range transport of dFe from the EPR. Here, we discuss the implications of the heterogeneity of the neutrally-buoyant plumes and diffuse flow systems along the ridge axis. Ultimately, we find that all systems appear to undergo similar Fe stabilization mechanisms to reach a stable neutrally-buoyant plume that can be observed west of the ridge and into the Pacific Basin.

3.5.3.1 Dissolved iron concentrations exceed those of organic ligands in most samples

The binding of dFe by organic ligands has been hypothesized as a major stabilization mechanism for hydrothermal Fe (Bennett et al., 2008; Buck et al., 2015; Lough et al., 2019; Resing et al., 2015; Sander and Koschinsky, 2011; Tagliabue et al., 2017, 2010). Indeed, studies of organic ligands near vents have consistently found ligands to be a critical contributor to dFe chemistry in these regions (Bennett et al., 2008; Hawkes et al., 2013; Hawkes et al., 2013; Hoffman et al., 2023; Kleint et al., 2016; Wang et al., 2021, 2019). We similarly found organic ligands that varied widely throughout the SEPR study area. Most of the ligands in our study were weaker and belonged to the L_2 ($11 < \log K^{cond}_{FeL,Fe'} < 12$) and L_3 ($\log K^{cond}_{FeL,Fe'} < 11$) operationally defined ligand classes (Gledhill and Buck, 2012). This result is consistent with the relatively weak ligands measured in hydrothermal systems along the East Scotia Ridge, Southwest Indian Ridge and Mariana back-arc, although studies in other hydrothermal systems identified somewhat stronger ligands (Bennett et al., 2008; Hawkes et al., 2013; Hoffman et al., 2023; Kleint et al., 2016; Wang et al., 2021, 2019). Ligand concentrations in our study were highly variable (0.3-202.2 nM), likely related to the wide range of dFe concentrations (0.3-344.5 nM). Previous studies found a strong correlation between the strongest class of ligands (L_1) and dFe concentrations (Buck et al., 2018; Hoffman et al., 2023). While we only had 7 samples that could be classified as L_1 and therefore could not adequately assess the correlation between L_1 concentrations and dFe, we still observed a strong correlation between *total* ligand concentrations and dFe ($R^2 = 0.86$, Figure 3.8A). The slope of this relationship ($m = 0.55$) was considerably lower than the 1:1 L_1:dFe ratio found in previous studies however, likely a result of the weaker ligands sampled in this study and differences in the proximity to vents across previous studies.

A notable feature shared by the majority (39 out of 48) of the hydrothermally-influenced samples was that dFe concentrations exceeded ligand concentrations. This differs from most open ocean environments where [L] is consistently found in excess of [dFe], resulting in up to 99.9% of the dFe pool stabilized by organic ligands (Buck et al., 2018, 2015; Rue and Bruland, 1995). These organic ligands are essential to maintaining water column dFe concentrations above the low Fe(III) inorganic solubility limit (Liu and Millero, 2002). Hydrothermal vents however, expel large quantities of soluble reduced Fe, up to over one million times the concentration in background seawater (Von Damm, 1990). This large excess of Fe in close proximity to hydrothermal vents causes these environments to be one of the few oceanic environments where [dFe] exceeds [L]. Previous ligand studies in hydrothermal systems along the East Scotia Ridge (Hawkes et al., 2013), Southwest Indian Ridge (Wang et al., 2019), Mariana back-arc (Wang et al., 2021) and the MidAtlantic Ridge (Hoffman et al., 2023) found that once ambient [dFe] exceeded ~10 nM (ESR, SWIR, MBA) or ~20 nM (MAR), ligand concentrations were no longer equal to or in excess of dFe. Along the SEPR, however, we found that dFe exceeded ligand concentrations at ambient dFe concentrations as low as 0.5 nM. To explain the unusually low dFe excess threshold, we examined the physical size fractionation of dFe.

The dFe concentrations in excess over L (Figure 3.8B) in our dataset was largely matched by a high colloidal contribution to the dFe pool. In the deep ocean, cFe comprises ~50% of the dFe pool (Fitzsimmons et al., 2015; Roshan et al., 2020). In our samples however, the cFe fraction was much higher, comprising an average of 80% of dFe in the buoyant and neutrally buoyant plume and 60% of dFe in diffuse samples (Figure 3.9). Samples with higher colloidal content were clearly associated with larger disparities between ligand and dFe concentrations, which can be expressed as excess ligand ([eL] = [L] – [dFe]). As the relative contribution of the colloidal fraction to the dFe pool increased, [eL] dropped precipitously (Figure 3.8B). Conversely, when more of the dFe was in the truly soluble fraction (< 80% cFe), most samples had a positive eL, which is more typical for open ocean environments (Buck et al., 2018, 2015).

It is perhaps unsurprising that a large colloidal fraction of dFe was associated with samples in which dFe exceeded ligand concentrations, because inorganic Fe is very insoluble in seawater (Liu and Millero, 2002). Therefore, in the cases where dFe concentrations were high and ligands are in insufficient supply, Fe likely aggregates into colloids or particulates (Lough et al., 2019). Over time, Fe colloids may precipitate further into a particulate phase that is either scavenged or settles to the seafloor. The precipitation process may also eventually bring both ligand concentrations and the fraction of colloidal Fe closer to what is observed in the open ocean. The total amount of ligands available to bind dFe in hydrothermal systems may be limited due to biological constraints. Ligands are produced either actively or passively by the microbial community, likely to maintain dFe in solution at biologically viable concentrations (Christel S. Hassler et al., 2011; Shaked et al., 2020). All of the dFe-binding ligands that have been identified thus far (e.g. siderophores) are ultimately biologically produced, and these ligands have an energetic cost to the cell for their production (Kramer et al., 2019), which likely limits their concentrations to certain thresholds. This, combined with lower cell counts in hydrothermal environments when compared to the surface ocean (Moore et al. *in prep*), likely explains why ligands do not keep pace with dFe concentrations in hydrothermal systems.

3.5.3.2 The role of ligands in the physical and chemical speciation of dissolved iron

Organic ligands are likely playing an important role in the physical partitioning of Fe between the colloidal and soluble phases (Lough et al., 2019), despite the fact that dFe exceeded the ligand concentrations in the majority of our samples (Figure 3.8). Ligands are expected to be particularly important to stabilizing the sFe pool (Lough et al., 2019) because sFe from vents in the form of Fe(II) has a short residence time in oxic seawater and once oxidized is insoluble if not associated with organic ligands (Field and Sherrell, 2000; Liu and Millero, 2002). Although there is evidence for inorganic sFe even in the presence of organic ligands (Wang et al., 2019), in our dataset [L] > [sFe] in 65 out of 68 samples, and thus we would thermodynamically expect that all of the sFe in these samples is associated with organic ligands. If we assume that any remaining ligands not bound to sFe are next complexed to cFe, we can further split the cFe pool into organic colloids (cFe_{org}), which includes ligand-bound cFe, and inorganic colloids (cFe_{inorg}), which includes any remaining dFe that exceeds ligand concentrations. Using these definitions, we can make a mass balance such that dFe = cFe_{org} + cFe_{inorg} + sFe. We assumed all ligands were bound to Fe when [dFe] > [L] due to the rapid formation kinetics of Fe-organic ligand complexes (Rose and Waite, 2003). While it is possible for some ligands to remain unbound in the presence of dFe if some portion of the dFe is unexchangeable with ligands, we do not anticipate this fraction to be major, because the reverse titrations used to calculate [L] for the cases in which [dFe] > [L] also provided an independent estimate of the portion of dFe that was exchangeable with the added organic ligand (Hawkes et al., 2013), and this was always greater than calculated ligand concentrations.

While there is considerable variation in the physical and chemical dFe speciation between individual samples and sites, there were also notable patterns between distinct hydrothermal environments (Figure 3.9). Outside of the plume, the colloidal fraction averaged ~50% of the dFe pool, which is consistent with other studies of background deep ocean water (Fitzsimmons et al., 2015; Roshan et al., 2020). In hydrothermally influenced environments however, most dFe was in the colloidal form. Based on our calculations under the above assumptions, we predict that ~70% of colloidal hydrothermal Fe was associated with organic ligands, with only a small (15-25%) portion of the dFe likely to be inorganic. We predict a considerably higher organic cFe fraction than was measured in the Longqi hydrothermal plume (~14%), but this might be a result of variation in plume sulfur content, such that higher sulfur would lead to more FeS nanoparticle formation and fewer organic colloids (Wang et al., 2019). Notably in the current study, there was virtually no inorganic cFe in the background samples. This implies that cFe_{inorg} is formed close to the vent and is lost from the dFe pool as the plume ages, likely from aggregation and subsequent precipitation. We conclude that organic ligands are important for stabilizing both the soluble and colloidal fractions of dFe in all environments that we studied. The impact of organic ligands on the colloidal pool is of particular interest because little is known about organic colloids (Wells and Goldberg, 1992), particularly in vent environments.

Organic ligands appeared to be important for complexing both colloidal and soluble dFe and thus may be impacting the physical partitioning of dFe, particularly for samples influenced by hydrothermal venting. In on-axis background samples, where ligand concentrations were overwhelmingly in excess of dFe when measured, sFe and dFe have a tight relationship ($R^2 = 0.96$; Figure 3.10), where the sFe averages ~40% of the dFe pool. This consistent relationship implies that most of the dFe is labile and that exchange is occurring between the sFe and cFe phases, resulting in a steady state partitioning of sFe and cFe, which is likely mediated by the organic ligand pool (Fitzsimmons et al., 2015). This contrasts with the hypothesis that dFe concentrations are primarily driven by the cFe pool on top of a fixed background of sFe, and instead supports results from Fitzsimmons et al. (2015) who found a strong steady state relationship governing the 50:50 sFe:cFe ratio of the dFe pool in the deep Atlantic. They posited that active exchange between cFe and sFe via adsorption/desorption or aggregation/disaggregation is responsible for maintaining the near constant percentage of soluble deep Atlantic dFe (Fitzsimmons et al., 2015). Indeed, the average sFe:cFe ratio for background samples along the SEPR is approximately 50:50 (Figure 3.9). In the on-axis neutrally buoyant plume and diffuse venting samples however, the dFe pool no longer appears to be fully exchangeable between the sFe and cFe pools. Indeed, as the influence from hydrothermal fluids grows, dFe becomes increasingly less correlated to sFe, reflected by the progressively lower slopes from background, to the neutrally buoyant plume, to diffuse vent sampling environments (Figure 3.10).

Fitzsimmons et al. (2015) suggested that the lack of a relationship between sFe and dFe results from the inputs of inorganic cFe that cannot exchange with organic ligands and is thus not able to reach a steady state between the sFe and cFe pools. This reflects a lack of steady-state conditions and subsequent deterioration in the sFe and dFe relationship, because most dFe must be labile to exchange between the cFe and sFe pools in order to achieve steady state. Therefore, a non-labile inorganic cFe fraction of dFe (e.g. fresh hydrothermal input) implies that there are non-steady-state processes occurring (e.g. aggregation and precipitation) and that some portion of cFe is in disequilibrium with the in-situ ligand pool. We can test this hypothesis in this dataset by subtracting out the inorganic fraction of the dFe (cFe_{inorg}) and plotting only the ligand-bound, organic fraction of the dFe pool ($dFe_{org} = sFe + cFe_{organic}$). In the neutrally buoyant plume, a significant correlation is observed between dFe_{org} and sFe ($R^2 = 0.46$; Figure 3.10B), and the slope ($m = 0.07$) is similar to the background samples ($m = 0.06$). This implies that only the fraction of dFe that is stabilized by available organic ligands is in steady state and labile to exchange between the sFe and cFe pools, and that this relationship may be relatively constant in a given environment, assuming it is being governed by similar exchange processes (Fitzsimmons et al., 2015). The remaining inorganic colloidal fraction of dFe is likely out of equilibrium with the available ligands and therefore is more likely to undergo rapid transformations that are not mediated by organic ligands. An example of these disequilibrium processes was also seen in the buoyant plume samples, where the buoyant fluids similarly had an inorganic cFe fraction that was not well correlated with dFe (data not plotted, $n = 3$).

Notably, the diffuse samples did not have significant correlation between sFe and dFe, or sFe and dFe_{org}, unlike the neutrally-buoyant plume samples. Interestingly, the lack of a correlation is driven by a few datapoints with anomalously high sFe concentrations at low dFe concentrations (Figure 3.10) and not due to high concentrations of cFe_{inorg}. These samples also had unusually strong ligands. Three of these samples have an average log $K^{cond}_{FeL,Fe'}$ > 12, including the two strongest conditional stability constants measured in the entire dataset (log $K^{cond}_{FeL,Fe'}$ = 12.68 and 12.56). Strong ligands are generally assumed to be siderophores, small dFe-binding molecules produced by microorganisms for facilitating Fe acquisition (Gledhill and Buck, 2012; Kramer et al., 2019). Siderophores, or similarly strong ligands, may disproportionally partition dFe into the soluble phase (Kraemer et al., 2005; Leventhal et al., 2019; Velasquez et al., 2016), which could explain the high sFe concentrations observed here. Indeed, we found relatively high concentrations (1.6-15.8 pM) of siderophores in these samples (Moore et al. *in prep*) that suggests siderophores might have a disproportionate impact on the speciation of dFe in some diffuse environments. Thus, it appears that the type of organic ligands, in addition to the total concentration, influences the partitioning of dFe between the cFe and sFe size fractions.

3.5.3.3 Organic colloids facilitate the stabilization of dissolved iron

Our results offer further insight into some of the hypothesized mechanisms for the long-distance transport of dissolved hydrothermal dFe across the western Pacific Basin. Originating at the SEPR axis, this large plume of dFe stretches over 4,000 km westwards and was studied extensively as part of the U.S. GEOTRACES GP16 transect (Fitzsimmons et al., 2017; Moffett and German, 2018; Resing et al., 2015; Roshan et al., 2020). Based on the size fractionation results, Fitzsimmons et al. (2017) concluded that the colloidal size fraction of dFe was the most important phase at the ridge axis and Roshan et al. (2020) further establish that dFe is primarily in the colloidal size fraction as the plume develops. Our results agree with a predominately colloidal phase at the ridge axis (Figure 3.9), but this study provides additional detailed data on the chemical speciation of this size fraction. Fitzsimmons et al. (2017) hypothesized that most cFe near the ridge axis was inorganic oxyhydroxides, based on a light (-0.19‰) δ^{56}Fe signature, and Roshan et al. (2020) further proposed that this inorganic cFe is gradually transformed into organic cFe as the plume develops. The ligand results of our study however, suggest that the majority of cFe near the ridge axis is likely in an organically-bound phase (Figure 3.9; *section 3.5.3.2*).

Several lines of evidence support the assertion that most of the colloidal fraction is bound to organic ligands in the SEPR region. For instance, imaging of Fe bearing particles in the SEPR plume found that Fe was embedded in an organic matrix (Fitzsimmons et al., 2017; Hoffman et al., 2020, 2018). The colloidal fraction could have a similar organic speciation, particularly because organic colloidal Fe phases have been documented in several oceanic environments (Boye et al., 2010; Cullen et al., 2006; Thuróczy et al., 2010; Wells and Goldberg, 1992). In particles, the organic matrix is thought to slow the settling of inorganic Fe through the water column (Hoffman et al., 2020, 2018) and is used to partially explain the persistence of pFe so far from the ridge crest in the SEPR hydrothermal plume (Fitzsimmons et al., 2017). Similarly, an organic colloidal phase may enable dFe to resist settling or aggregation processes leading to precipitative loss. Although the ability of the organic cFe pool to exchange with sFe is poorly constrained (Lough et al., 2019), the correlation between sFe and dFe_{org} in our data suggest that the constant portion of cFe that remains is stable, and there are sufficient dFe-binding ligands available to suggest that this cFe is indeed organic. An organic cFe phase would be consistent with ligand-mediated reversible scavenging processes governing the Fe dynamics of the SEPR plume. Reversible scavenging has been used to explain the descent of the dFe plume across the basin as a product of adsorption/desorption and aggregation/disaggregation processes

(Fitzsimmons et al., 2017). The organic colloidal fraction may act as a crucial intermediate between the carbon matrix associated pFe fraction and truly soluble organic Fe (Fitzsimmons et al., 2015; Honeyman and Santschi, 1989).

The light isotopic signature of dFe near the ridge axis does not preclude an organic colloidal phase. While organic ligands have been shown to preferentially bind heavier isotopes (Dideriksen et al., 2008; Morgan et al., 2010), these studies focus on siderophores in a model system. Siderophores are the strongest natural Fe-binding ligands identified to date, and are therefore likely to demonstrate the most dramatic size and isotopic fractionation (Morgan et al., 2010). The ligands in our study, however, are primarily weaker L_2 and L_3 type ligands and may be expected to have less fractionation. It is also possible that any organic ligand fractionation signal in the SEPR is obscured by other hydrothermal fractionation factors (Bennett et al., 2009). The isotopic fractionation of dFe near individual vent sites is also still largely unconstrained, so is difficult to predict whether the measured -0.19 δ^{56}Fe along the SEPR is solely a result of inorganic oxyhydroxide particle formation or a combination of several processes or endmembers (Bennett et al., 2009). It is also possible that the light isotopic signature of the dFe source at the ridge crest is still reflecting a heavy fractionation signature, but if the dFe source is very light this instantaneous fractionation when the dFe associates with the available ligands would not be discernable. We therefore conclude that organic ligands, and particularly organic colloids, are the primary mechanism for stabilizing dFe along the SEPR.

A comparison between the southern on-axis sites and older plumes we sampled further north at 9ºN and Station 18 (Figure 3.6) additionally support that organic Fe colloids might be particularly stable as the composite plume develops. Although a large fraction of hydrothermal dFe that is expelled close to the ridge crest binds to available ligands, these ligands rapidly become saturated, leaving the remaining dFe to form inorganic colloids or precipitate. However, as the plume ages and moves off-axis, it appears that these inorganic colloids are quickly removed, while the organic colloidal and soluble fractions remain behind (e.g. Fitzsimmons et al. 2017). Ligand and dFe data from stations further north support this conclusion. We sampled older hydrothermal plumes at Station 18 (aged ~ 1 month) and near 9ºN, which we assume to be similarly aged on the basis its location 100 km west of the ridge axis and low particle intensity ($dNTU_{max} = 0.01$) while we await more precise radium dating. At these stations, we found that 83% of plume samples ($n = 12$) had [L] > [dFe], compared to only 19% of the on-axis, fresher plume samples ($n = 48$). The excess of ligand over dFe in these more aged plumes implies that there are few inorganic colloids present, and that ligands are likely produced over time within the neutrally-buoyant plume (Mellett et al. submitted). It is likely that inorganic colloids have been preferentially removed in the plume while the organic ligand phases are more long-lived. Station PJ was not included as an aged plume in this analysis, because it is likely a relatively young plume based on its high particle intensity ($dNTU_{max} = 0.09$) and large dCH_4 content ($dCH_{4max} = 4.8$ nM), despite its location 11 km west off the ridge axis.

3.5.3.4 Contributions of individual sites to iron stabilization

While there is compelling evidence that the stabilization of dFe along the SEPR is facilitated by organic ligands, the role of different venting environments remain uncertain. Our reoccupation of the composite plume at U.S. GEOTRACES Station 18 suggests that this ~1 month old plume is relatively stable in terms of trace metals (Figure 3.6; dFe_{max} 10-14 nM), despite temporal changes in the locations of individual vent sites and a slight a slightly shallower plume maximum compared to 2013 (Buck et al., 2018; Kipp et al., 2018; Resing et al., 2015). Thus, it is possible that changes in the dFe flux from individual venting locations may not significantly impact the overall flux of stabilized dFe into the western Pacific, provided the net venting output of the ridge crest remains similar over time. This scenario is plausible if we assume a relatively constant average spatial density of hydrothermal sites, maintained by a constant rate of ridge spreading (Baker and German, 2004; Beaulieu et al., 2015). Furthermore, the specific type of vent site does not appear to impact the proportion of dFe stabilized near the source. Proportionally, diffuse vents input more sFe than do the high temperature vents (Figure 3.9), but both systems averaged an equal fraction of organically stabilized dFe (dFe_{org} = sFe + cFe_{org}). The neutrally buoyant plume also contained a similar fraction of dFe_{org} compared to both the diffuse and high temperature vent samples (Figure 3.9), despite representing a more aged signal. The comparable dFe_{org} fraction between the neutrally buoyant plume and younger diffuse and high temperature vent samples implies that dFe is likely stabilized by ligands very close to the vent site, which then remain stable in the older neutrally-buoyant plume. This is consistent with the rapid kinetics of ligand-dFe equilibration (Rose and Waite, 2003), which should occur on the timescale of seconds after leaving the vent, provided sufficient organic ligands are present.

Although the organic fraction of dFe was similar across the different hydrothermal environments, the overall physical speciation of dFe varied among sampling sites. Diffuse venting samples had an sFe fraction that was 2-3 times greater than either the neutrally buoyant or buoyant plume, and was close to the 50:50 sFe:cFe ratio observed in background samples (Figure 3.9). It is possible that the lower metal content of diffuse fluids helps prevent inorganic colloid formation or that the ligands near diffuse vents are disproportionally in the soluble size fraction (e.g. siderophores). The disproportionately high sFe fraction from diffuse vents was not apparent once these fluids were presumably entrained into the neutrally buoyant plume. The elevated fraction of sFe from diffuse vents was likely either diluted with high cFe signatures from nearby buoyant and/or neutrally buoyant plumes or the sFe from diffuse vents aggregated into a colloidal form upon entrainment into the rising plume. Despite changes in the sFe fraction from diffuse sites near the seafloor and into the neutrally buoyant plume, the overall dFe_{org} fraction appeared to be set close to the vent sites and maintained in the neutrally buoyant plume. Inorganic colloidal Fe however, was likely removed from the neutrally buoyant as it aged, a conclusion supported by the nearly entirely organic signal measured at Station 18 (Figure 3.6).

The similarities in the dFe_{org} composition between vent types and the neutrally buoyant plume imply that venting environment does not significantly impact the amount of organic ligands available to stabilize dFe. This differs from previous hypotheses that posited the lower temperatures and higher organic content of diffuse fluids would contribute to greater organic stabilization of dFe than high temperature venting environments (Lough et al., 2019; Sander and Koschinsky, 2011). We, however, find no evidence that diffuse venting is more efficient at stabilizing dFe along the SEPR, in terms of the overall proportion of organically-stabilized dFe in the composite neutrally-buoyant plume. Despite lack of evidence for more *efficient* stabilization, the net stabilized dFe output of all diffuse venting systems may still be greater than that of high temperature systems. Although high temperature vents have higher dFe concentrations, a larger volume of axial hydrothermal flow is estimated to circulate through diffuse vents (Elderfield and Schultz, 1996; German et al., 2016). Therefore, the combined output of all diffuse flow could contribute a larger amount of stabilized Fe to the composite neutrally buoyant plume than the net output of high temperature flow. The high spatial frequency of diffuse venting along the SEPR when compared to high temperature sites (Figure 3.7) suggests that this is a plausible scenario for this study region.

We conclude that organic ligands are a very important mechanism for stabilizing dissolved hydrothermal Fe along the SEPR. A significant fraction of both the soluble and colloidal size fractions of dFe were organically-bound, with higher concentrations of organic cFe than organic sFe. We also found a significant inorganic colloidal fraction over the ridge axis that appeared to be rapidly lost as the plume aged. Finally, although high temperature and diffuse venting had similar proportions of organically-complexed dFe, diffuse venting may ultimately contribute more stabilized Fe to the composite neutrally buoyant plume due to the higher flux of fluids circulating through diffuse systems.

3.6 CONCLUSIONS

The 16-18ºS sector of the SEPR is a dynamic system characterized by diverse hydrothermal venting systems with a high degree of spatial and temporal chemical variability. Low-temperature diffuse venting systems were the main type of vent encountered on the ridge, although several high temperature chimneys and fresh lavas were also found. We were able to successfully locate diffuse systems through a combination of AUV *Sentry*, ORP anomalies and low particle anomalies. We further determined that the best chemical indicators of low temperature venting were enrichments in dCH_4, dH_2, tdMn, %dFe, and pS_{tot}. We suggest these metrics for identifying low temperature systems in the future, particularly when AUV work is not possible.

In addition to examining the overall chemical diversity in venting systems along the SEPR, we specifically examined the stabilization of dFe. Fe in close proximity to vents along the ridge crest was found to have a complex chemical and physical speciation that varied greatly between sampling environments and sites. Most dFe was chemically stabilized by organic Fe-binding ligands that varied greatly in concentration and binding strength. The dFe was predominately in the colloidal fraction, most of which we predict was in the form of organic colloids rather than inorganic nanoparticles. We found that although chemical and physical Fe speciation was spatially and temporally variable along the ridge crest, a stable composite plume forms west of the ridge axis. Organic ligands likely stabilize a large fraction of dFe during the development of the stable plume and thereby help facilitate long distance Fe transport off the ridge and into the ocean interior. We conclude that on-axis Fe stabilization is highly variable and that characterizing the near-vent environment is critical for understanding and predicting the chemical development of young hydrothermal plumes.

3.7 ACKNOWLEDGEMENTS

We thank the Captain and crew of the R/V *Roger Revelle* and the AUV *Sentry* team. This work was supported by NSF-OCE #1756402 to J.A.R., R.M.B. and Edward Baker.

3.8 AUTHOR CONTRIBUTIONS

LM completed the total organic ligand measurements, analyzed and synthesized all of the data and drafted the manuscript. JR and RB helped design the study and draft and edit the manuscript. CG processed AUV *Sentry* data. BS made the sFe and sMn measurements and TW completed shipboard dAl analyses. NB performed shipboard dMn, tdMn, dFe, and tdFe analyses and laboratory suspended particle analyses. CH aided in shipboard sample collection and helped with ligand analyses. TB and AA performed shipboard dCH_4 and dH_2 analyses. PS and MC helped design the study. SW processed the CTD and ORP data.

3.9 FIGURES AND TABLES

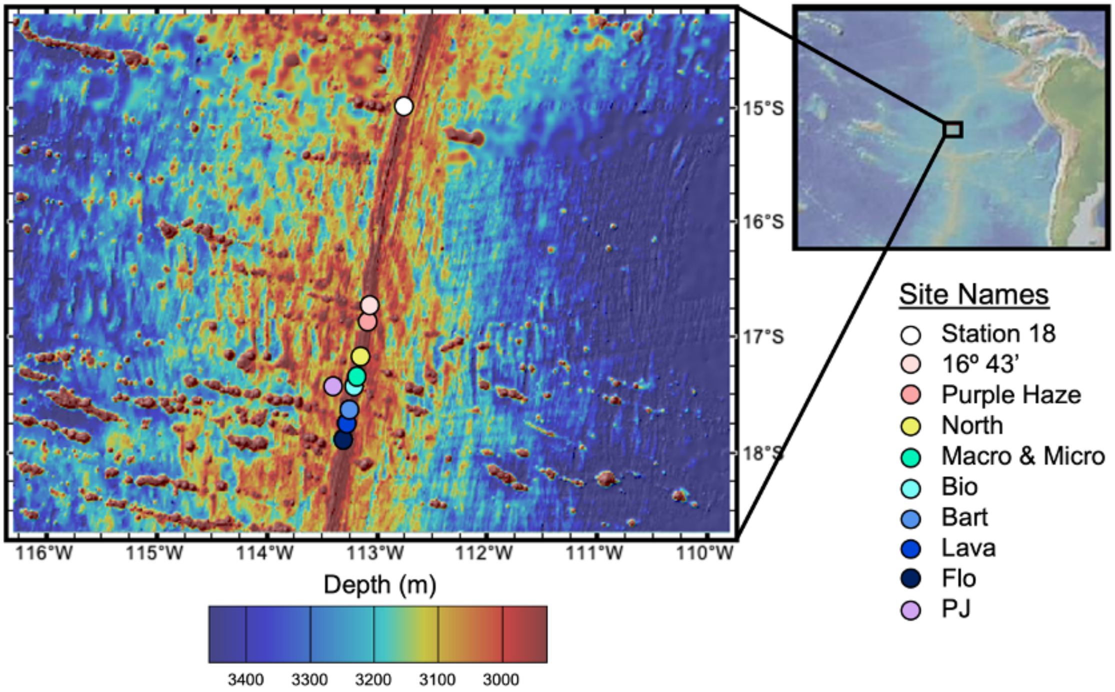

Figure 3.1. Site map.

Left: Station locations along the 16-18ºS sector of the Southern East Pacific Rise (SEPR). Right: Larger area encompassing the SEPR. Map created using GeoMapApp.

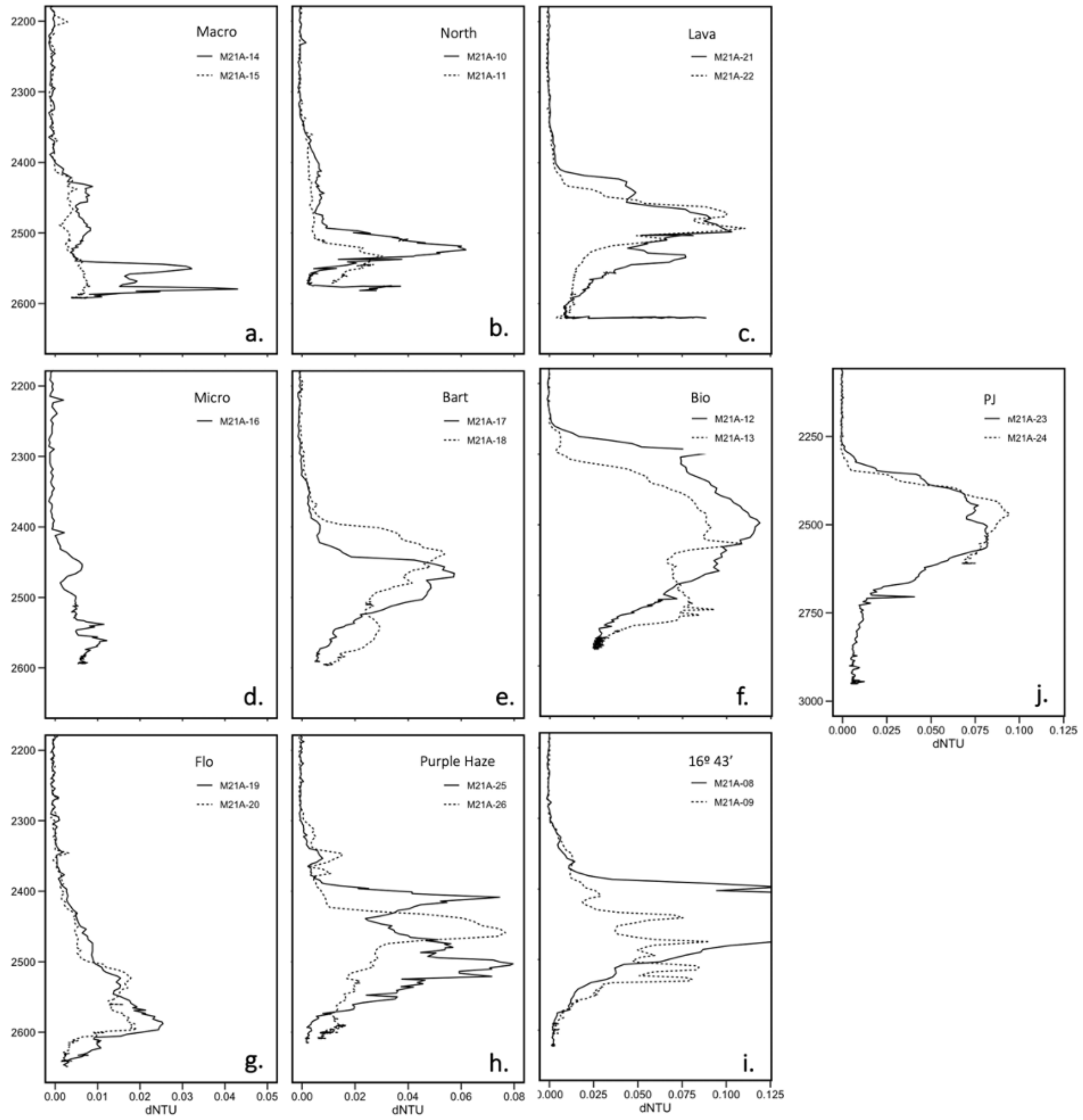

Figure 3.2. Particle anomaly (dNTU) profiles for each station.

A) Macro, B) North, C) Lava, D) Micro, E) Bart, F) Bio, G) Flo, H) Purple Haze, I) 16º 43', and J) PJ. Note the separate depth axis on Station PJ (j). Sites in the first column (panels a, d, g) have an x-axis range from 0-0.05 (unitless). Sites in the second column (panels b, e, h) have an x-axis range of 0-0.08. Sites in the third and fourth columns (panels c, f, i, j) have an x-axis range from 0-0.125. Note that the first row (panels a-c) had samples containing a near seafloor particle feature and a buoyant plume. Solid lines refer to the first cast at a station while dashed lines denote the second cast.

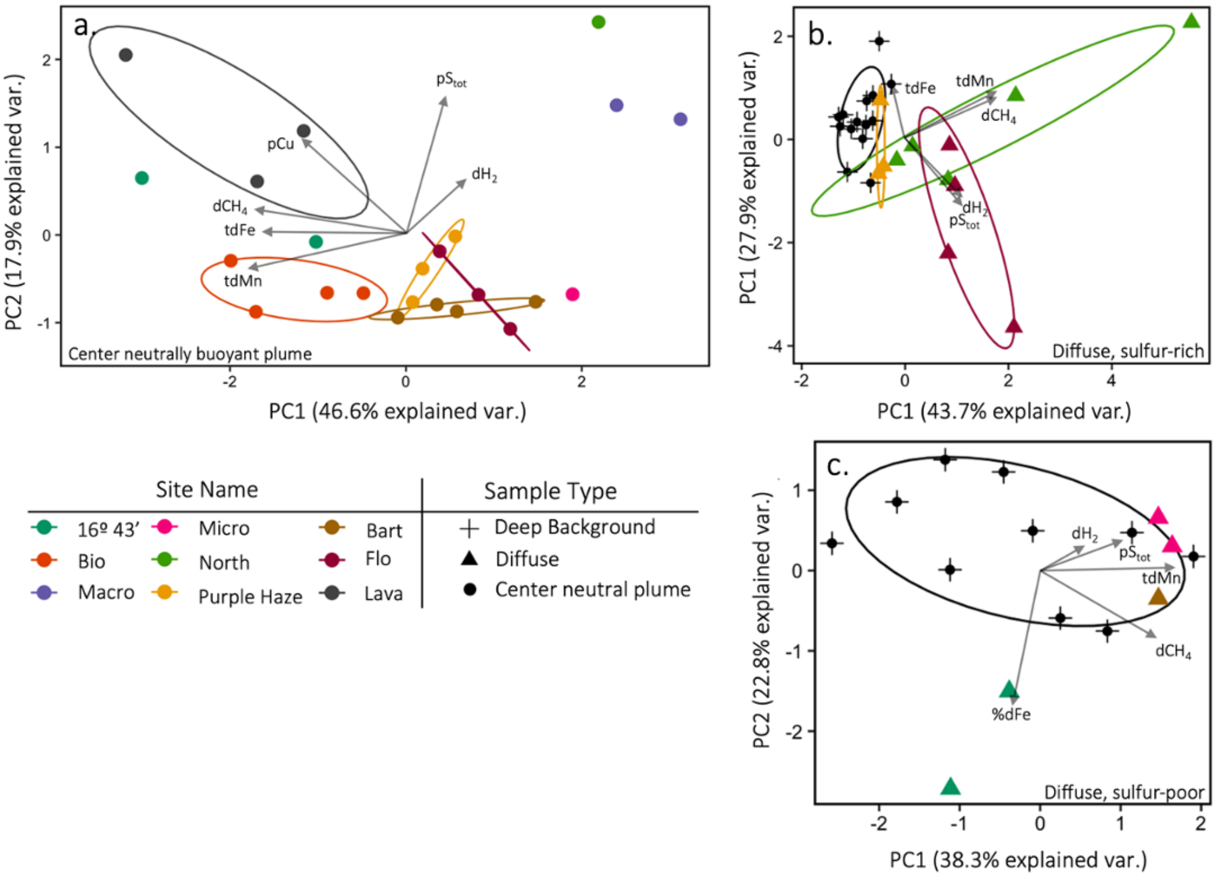

Figure 3.3. Principal Component analyses of sampling sites.

A) The center of the neutrally buoyant plume for on-axis sites. Variables include pCu, dCH_4, tdFe, tdMn, dH_2, and pS_{tot}. The first two principal components (PC1 and PC2), describe 64.4% of the variance in the dataset. The third component, PC3 (not plotted) describes an additional 16.3% of the variance. B) Sulfur-enriched diffuse venting samples compared to background. Variables include dCH_4, tdFe, tdMn, dH_2, and pS_{tot}. The first two principal components, PC1 and PC2 describe 71.6% of the variation in this dataset. The third component, PC3 (not plotted) describes an additional 19.1%. C) Sulfur-poor diffuse venting samples compared to background. Variables include dCH_4, %dFe, tdMn, dH_2, and pS_{tot}. The first two principal components, PC1 and PC2, describe 61.1% of the variation in this dataset. The third component, PC3 (not plotted) describes an additional 21.9%.

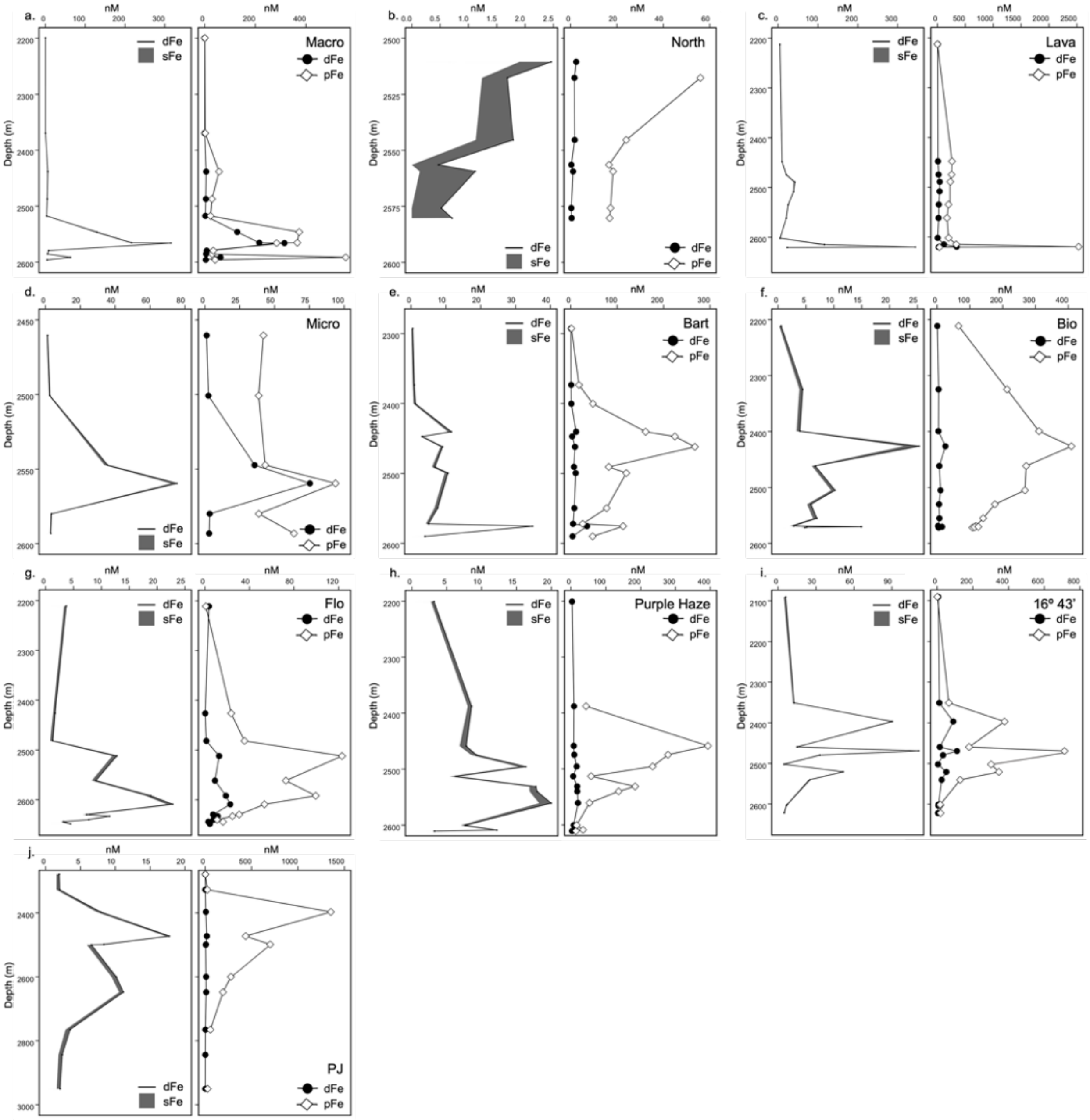

Figure 3.4. Dissolved iron, soluble iron, and particulate iron profiles for each station.

A) Macro, B) North, C) Lava, D) Micro, E) Bart, F) Bio, G) Flo, H) Purple Haze, I) 16º43’ and J) PJ. Note the variation in depth and concentration axes between stations. For each station, the left panel shows the dFe concentration profile with sFe concentrations depicted as the width of the line. Right panels show dFe (solid circles) and pFe (open diamonds).

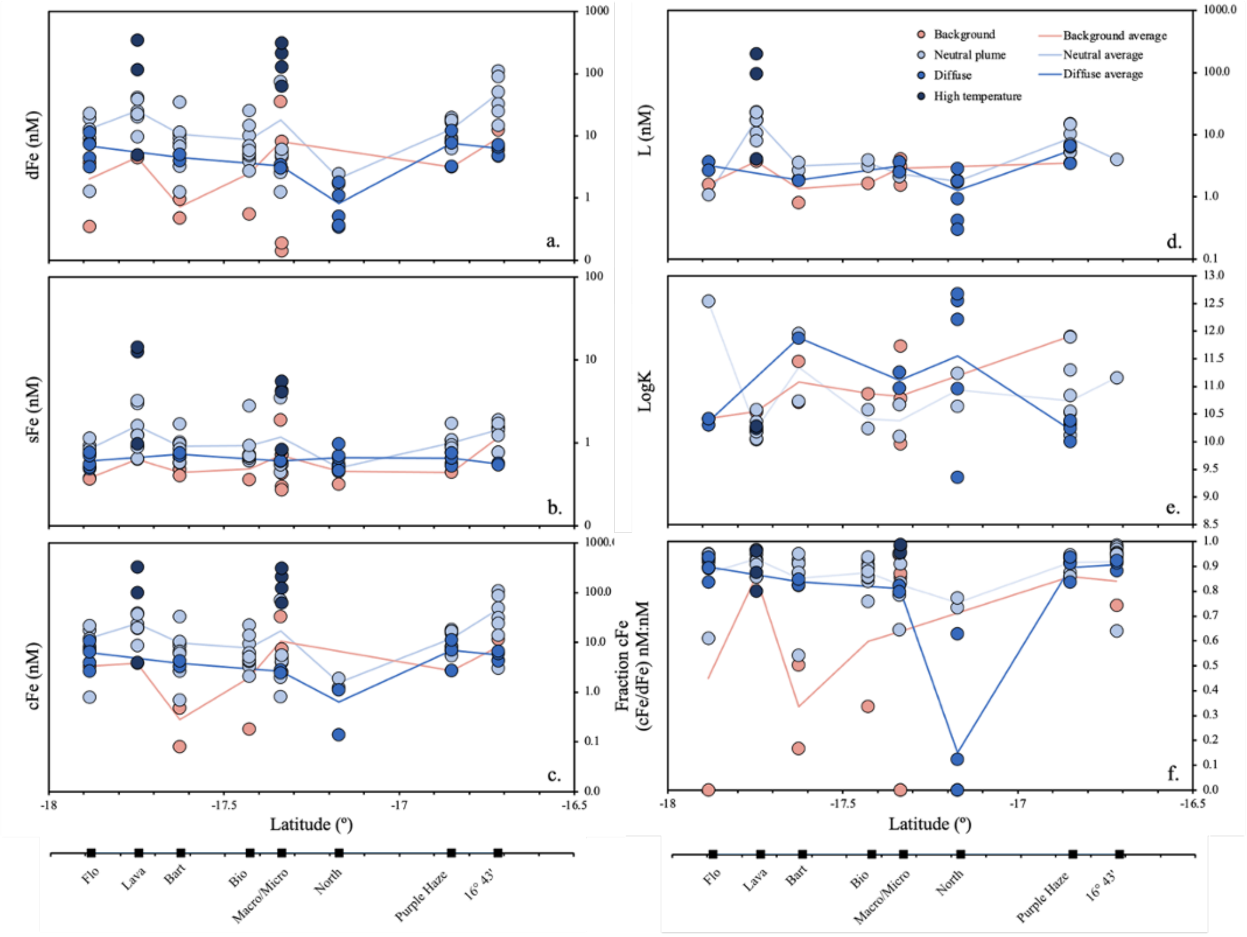

Figure 3.5. Dissolved iron speciation across latitude.

A) Dissolved iron (dFe < 0.2 µm) concentrations, B) soluble iron (sFe < 0.02 µm) concentrations, C) colloidal iron (0.02 µm < cFe < 0.2 µm) concentrations, D) ligand (L) concentrations, E) conditional stability constants ($\log K_{Fe',FeL}^{cond}$), F) fraction colloidal (cFe/dFe) of on-axis stations. Points refer to individual samples and lines depict site-based averages. Sites Macro and Micro were combined due to proximity, and high temperature samples were excluded from averaging due to the low (n = 2) number of sites. Note the y-axes in A-D are logarithmic.

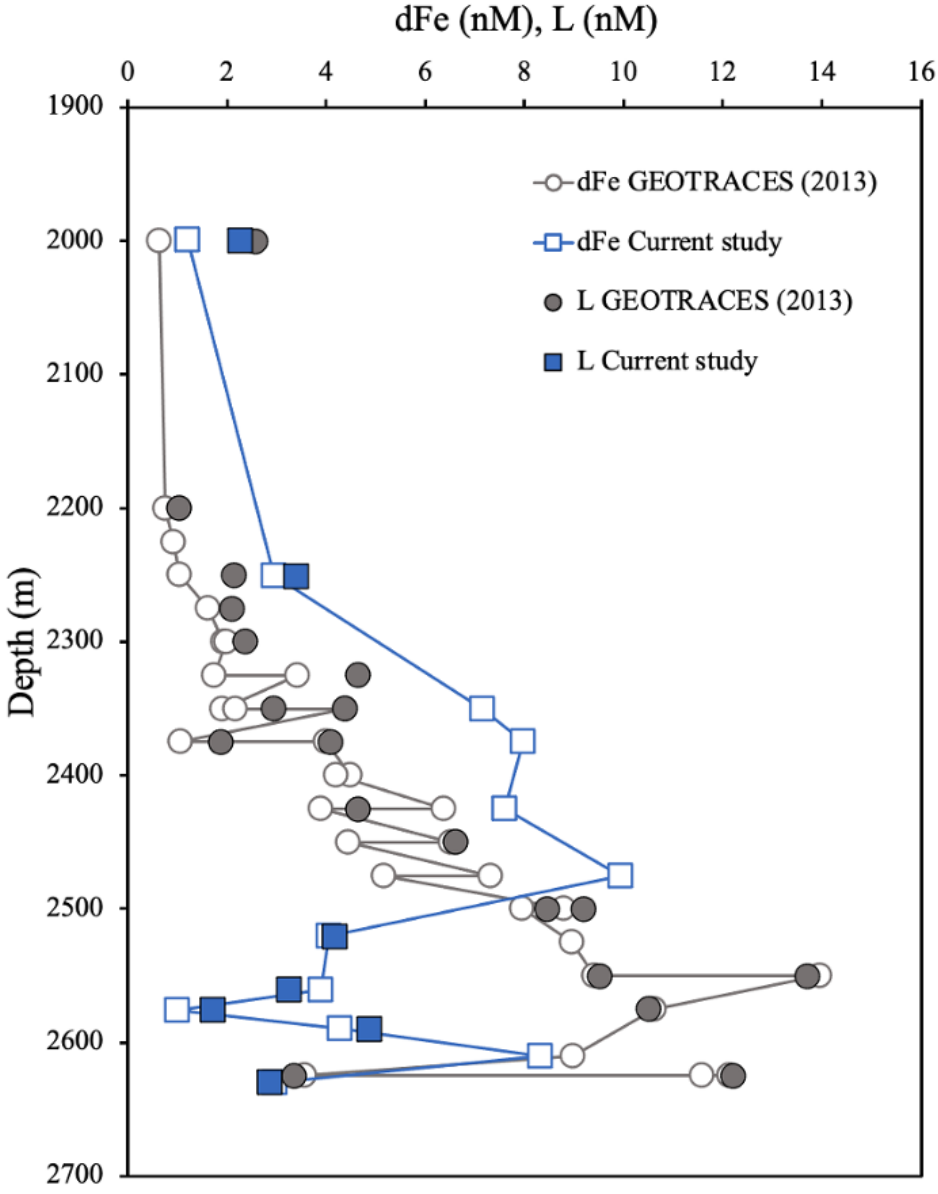

Figure 3.6. Chemical speciation of dissolved iron at repeat occupation of U.S. GEOTRACES Station 18.

Filled symbols refer to dissolved iron concentrations and open symbols refer to total organic iron-binding ligand concentrations. Grey circles refer to data from the prior GEOTRACES occupation in 2013 (Buck et al., 2018) and blue squares refer to the current study.

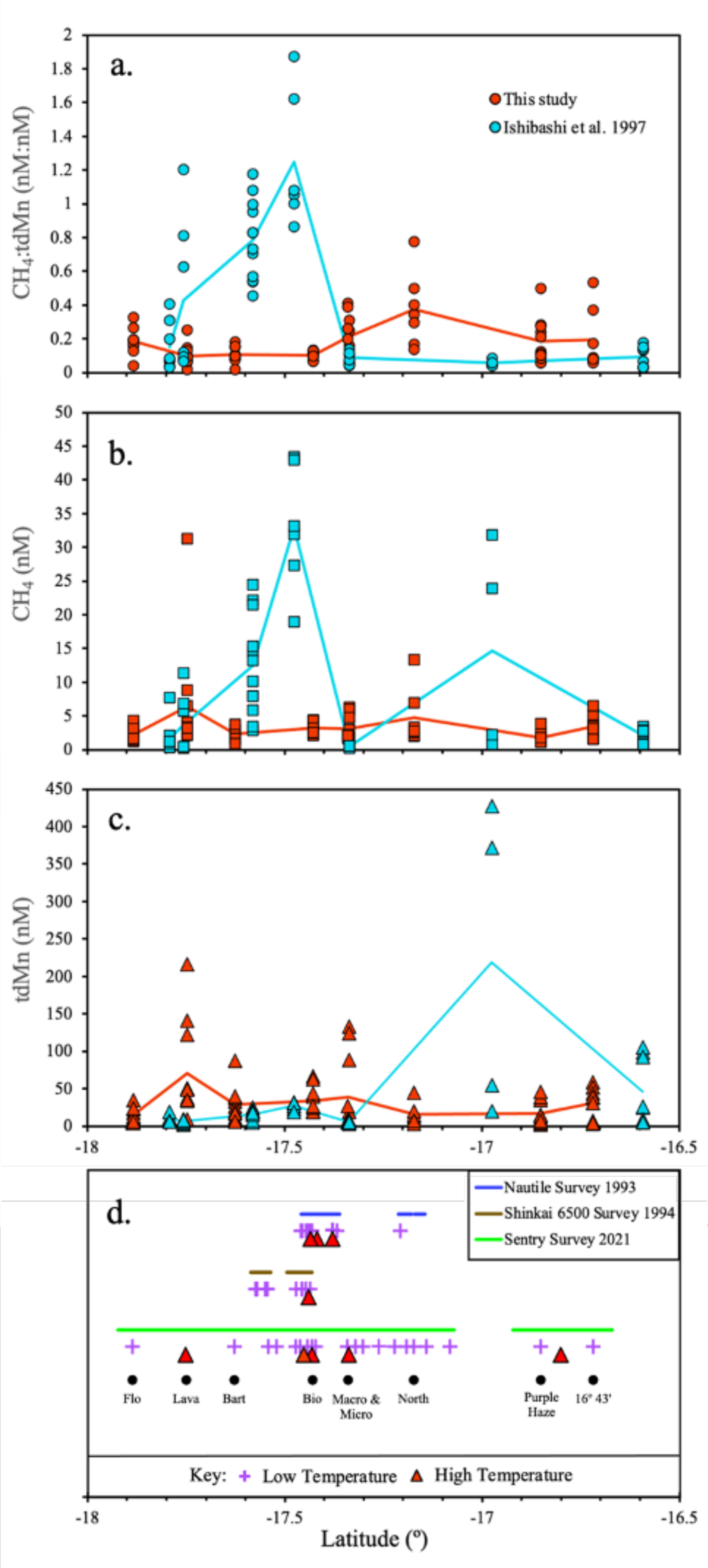

Figure 3.7. Comparison of the current study (red) to 1993 and 1994 surveys.

A) dCH_4:tdMn (nM:nM), B) dCH_4 and C) tdMn with cyan representing Ishibashhi et al. (1997) and red representing this study. Symbols refer to individual samples taken during a CTD cast and lines connect the average value for each CTD station. All samples plotted are those containing hydrothermal influence (neutrally buoyant plume, diffuse, and buoyant). D) Diagram showing study areas and type of hydrothermal activity found along the 16.5-18ºS sector of the SEPR. Blue lines refer to the survey area of the submersible *Nautile* in 1993 (Auzende et al., 1996; Charlou et al., 1996). Brown lines refer to the region surveyed by submersible *Shinkai* 6500 in 1994 (Embley et al., 1998). Green lines are the area surveyed by AUV *Sentry* (German et al., *in prep*) in the current study. Purple plus signs are regions of diffuse hydrothermal activity and red triangles are high temperature hydrothermal vents. Black labeled dots refer to the sites chosen for CTD sampling in the current study.

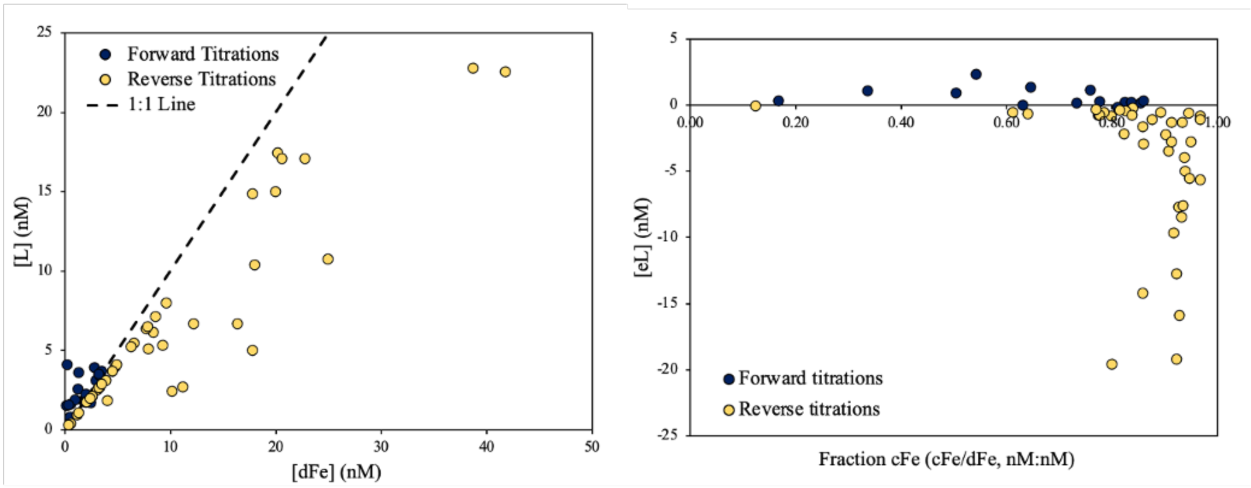

Figure 3.8. Relationships between organic iron-binding ligands and dissolved iron.

A) Ligand concentration ([L]) versus dissolved iron concentration ([dFe]), $R^2 = 0.86$. Dashed line denotes the 1:1 line. B) Excess ligand concentration ([eL] = [L] – [dFe]) versus fraction of the sample in the colloidal phase (Fraction cFe = [cFe]/[dFe]). Yellow dots refer to samples for which a reverse titration was performed, dark blue dots refer to samples run using forward titrat ion.

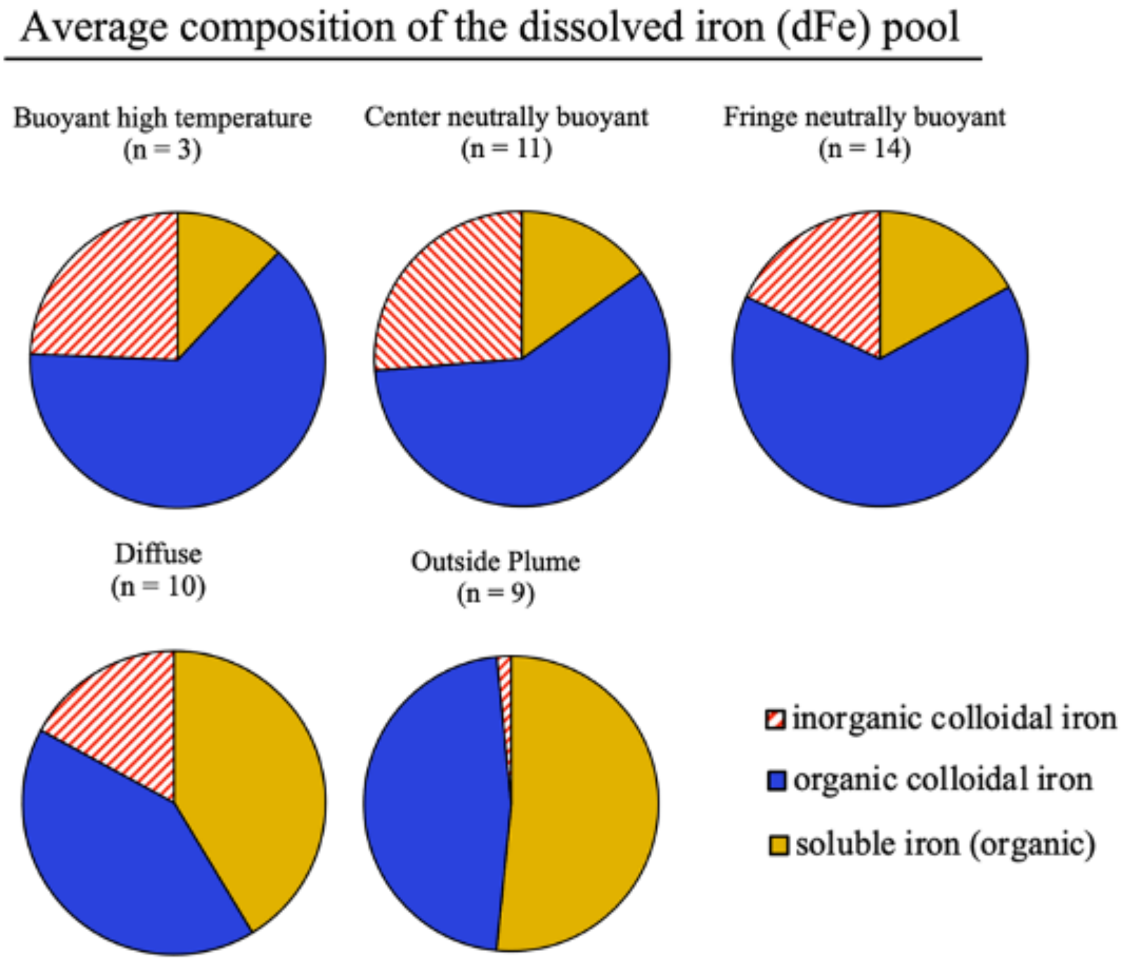

Figure 3.9. Physical speciation of dissolved iron on-axis.

Blue solid refers to organic colloidal iron, gold solid refers to organic soluble iron, red stripes refer to inorganic colloidal iron. Pie size is not scaled. Environments were defined as described in *section 3.3.8*, except "Outside Plume." "Outside Plume" combined "Shallow" and "Deep Background" samples to increase statistical power. Samples where sFe > dFe were considered 100% soluble.

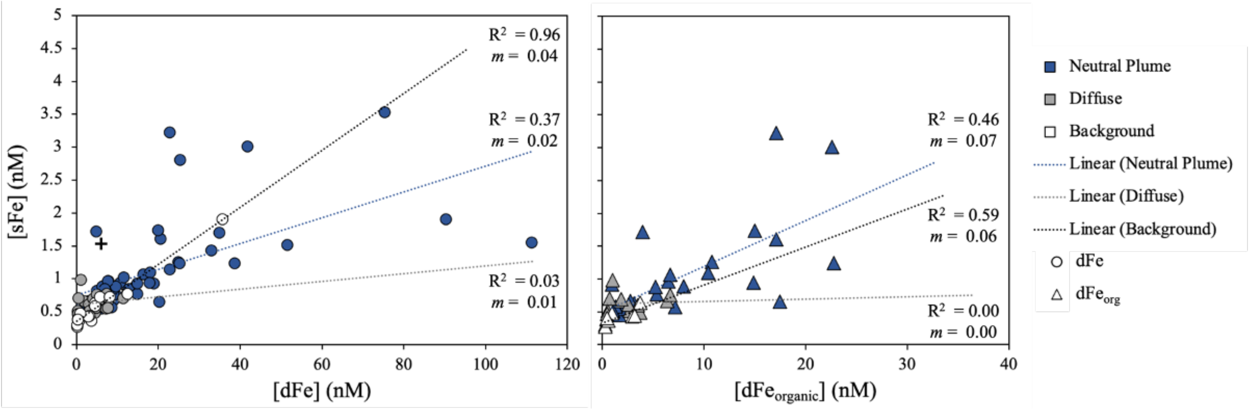

Figure 3.10. Relationships between soluble Fe and dissolved Fe.

Correlations between soluble iron (sFe) and dissolved iron (dFe) in the background (white), the neutrally buoyant plume (blue), and diffuse venting samples (grey). All fits are linear regressions. A) sFe versus dFe. Cross indicates a background sample outlier. B) sFe versus organic dissolved iron ($dFe_{org} = sFe + cFe_{org}$).

3.10 SUPPLEMENTAL FIGURES AND TABLES

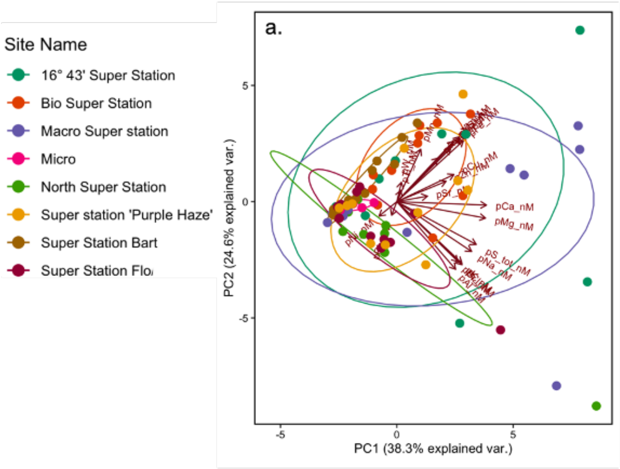

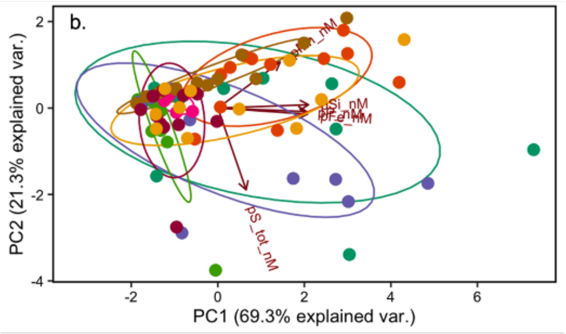

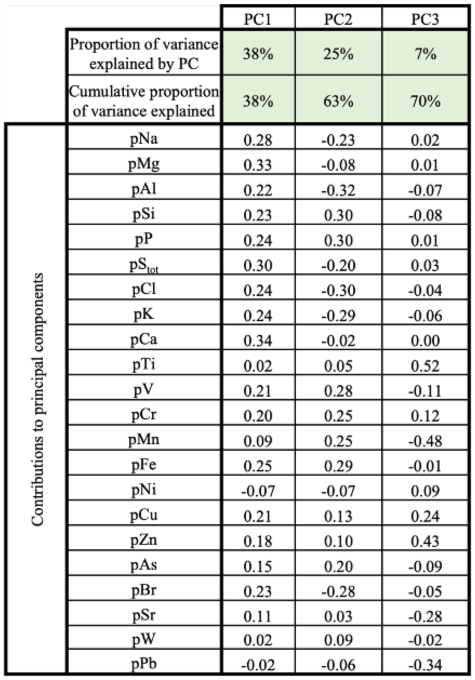

		PC1	PC2	PC3
	Proportion of variance explained by PC	38%	25%	7%
	Cumulative proportion of variance explained	38%	63%	70%
Contributions to principal components	pNa	0.28	-0.23	0.02
	pMg	0.33	-0.08	0.01
	pAl	0.22	-0.32	-0.07
	pSi	0.23	0.30	-0.08
	pP	0.24	0.30	0.01
	pS_{tot}	0.30	-0.20	0.03
	pCl	0.24	-0.30	-0.04
	pK	0.24	-0.29	-0.06
	pCa	0.34	-0.02	0.00
	pTi	0.02	0.05	0.52
	pV	0.21	0.28	-0.11
	pCr	0.20	0.25	0.12
	pMn	0.09	0.25	-0.48
	pFe	0.25	0.29	-0.01
	pNi	-0.07	-0.07	0.09
	pCu	0.21	0.13	0.24
	pZn	0.18	0.10	0.43
	pAs	0.15	0.20	-0.09
	pBr	0.23	-0.28	-0.05
	pSr	0.11	0.03	-0.28
	pW	0.02	0.09	-0.02
	pPb	-0.02	-0.06	-0.34

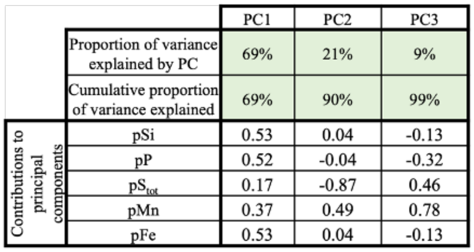

		PC1	PC2	PC3
	Proportion of variance explained by PC	69%	21%	9%
	Cumulative proportion of variance explained	69%	90%	99%
Contributions to principal components	pSi	0.53	0.04	-0.13
	pP	0.52	-0.04	-0.32
	pS_{tot}	0.17	-0.87	0.46
	pMn	0.37	0.49	0.78
	pFe	0.53	0.04	-0.13

Supplementary Figure 3.11. Principal component analysis of particulate variables.

A) All particulate variables (see corresponding table for list). The first two principal components (PC1 and PC2), describe 63% of the variance in the dataset. The third component, PC3 (not plotted) describes an additional 7% of the variance. B) Select particulate variables (see corresponding table for list). The first two principal components (PC1 and PC2), describe 90% of the variance in the dataset. The third component, PC3 (not plotted) describes an additional 9% of the variance. Only the contributions to PC1-PC3 are described in the tables.

Supplementary Table 3.1. Averages, standard deviations, and ranges of key variables for the seafloor features at each station and combined background samples for comparison.

	Deep Background	**Diffuse (sulfur-poor)**			**Diffuse (sulfur-rich)**			**High Temperature**	
	Deep Background	**16º 43'**	**Bart**	**Micro**	**Purple Haze**	**Flo**	**North**	**Macro**	**Lava**
Latitude	16º43'–17º53'	16º43'	17º37'	17º20'	16º51'	17º53'	17º10'	17º20'	17º44'
Depth (m)	2526.57±180.85 2327.61–2950.2	2608.41±11.38 2600.73–2621.48	2580.98±12.59 2572.08–2589.88	2586.55±9.31 2579.97–2593.13	2606.62±5.49 2600.38–2610.71	2639.01±7.77 2629.6–2648.3	2563.46±14.37 2545.36–2580.25	2567.3±18.56 2546.22–2591.46	2612.17±9.24 2601.86–2619.71
Temperature (ºC)	1.85±0.01 1.83–1.87	1.83±0 1.83–1.83	1.84±0 1.84–1.84	1.83±0 1.83–1.83	1.83±0.01 1.83–1.84	1.84±0.01 1.83–1.84	1.85±0.03 1.83–1.89	1.85±0.02 1.83–1.86	1.89±0.05 1.85–1.94
Salinity (PSU)	34.67±0 34.66–34.67	34.68±0 34.68–34.68	34.67±0 34.67–34.67	34.67±0 34.67–34.67	34.68±0 34.68–34.68	34.68±0.01 34.67–34.68	34.67±0 34.67–34.67	34.67±0 34.67–34.68	34.68±0.01 34.67–34.68
Theta	1.66±0.02 1.64–1.71	1.64±0 1.64–1.64	1.65±0 1.65–1.65	1.64±0 1.64–1.64	1.64±0.01 1.64–1.65	1.64±0.01 1.64–1.65	1.66±0.02 1.64–1.7	1.67±0.02 1.64–1.68	1.7±0.05 1.66–1.75
Sigma Theta	27.73±0.01 27.72–27.74	27.74±0 27.74–27.74	27.74±0 27.74–27.74	27.74±0 27.74–27.74	27.74±0 27.74–27.74	27.74±0 27.74–27.74	27.74±0 27.73–27.74	27.74±0 27.74–27.74	27.74±0.01 27.73–27.74
Height above seafloor (m)	169.01±157.49 6.83–673.03	21.08±11.84 7.62–29.92	18.53±12.89 9.41–27.64	14.56±9.91 7.55–21.56	11.65±5.57 7.51–17.99	16.06±7.48 7.16–25.11	18.98±13.12 3.3–35.6	34.9±18.39 11–55.85	15.42±9.23 7.82–25.69
dNTU	0.01±0.01 0–0.01	0±0 0–0	0.01±0 0.01–0.01	0.01±0 0.01–0.01	0±0.01 0–0.01	0±0.01 0–0.01	0.02±0.01 0–0.02	0.02±0.01 0–0.03	0.03±0.03 0.01–0.06
tdFe (nM)	29.09±21.01 0.87–93.43	19.11±3.03 16.79–22.54	33.21±1.43 32.2–34.22	34.62±1.73 33.4–35.84	19.39±13.8 10.18–35.25	22.74±9.62 11.04–34.19	17.59±4.63 12.62–22.99	344.08±191.51 90.97–555.92	405.26±276.91 105.68–651.85
dFe (nM)	6.22±9.49 0.14–35.68	6.24±1.26 4.83–7.27	4.51±0.71 4–5.01	3.25±0.28 3.05–3.45	7.69±4.48 3.23–12.19	6.84±3.22 3.19–11.47	0.83±0.63 0.34–1.8	180.74±109.43 62.74–315.19	155.04±173.18 4.92–344.5
tdMn (nM)	4.73±2.69 0.12–9.75	4.42±1.61 3.03–6.18	9.79±1.17 8.96–10.61	7.22±0.16 7.1–7.33	4.18±2.96 2.41–7.6	8.29±3.45 3.67–12.83	14.79±14.92 2.99–39	80.55±46.92 19.07–133.06	126.1±91.05 28.51–208.76
dMn (nM)	4.07±2.69 0.08–10.27	4.25±2.3 2.46–6.85	8.49±0.76 7.95–9.03	7.75±0.56 7.35–8.14	4.54±2.62 2.07–7.28	7.59±2.97 3.66–10.88	16.37±17.27 3.23–45.08	71.43±63.5 14.23–128.95	154.96±53.24 122.3–216.4
H_2 (nM)	0.83±0.32 0.38–1.3	0.98±0.56 0.58–1.37	1.9 (n=1)	35.35±49.14 0.6–70.1	0.93±0.21 0.7–1.1	2.76±0.75 1.8–3.9	1.48±0.24 1.14–1.8	18±8.62 7.4–28.5	12.7±17.44 0.7–32.7
CH_4 (nM)	0.98±0.6 0.37–2.1	1.56±0.08 1.5–1.61	1.0 (n=1)	1.75±0.21 1.6–1.9	1.4±0.35 1.2–1.8	1.64±0.53 1.2–2.5	5.77±4.57 2.5–13.3	4.98±1.48 3–6.3	14.07±15.3 2.1–31.3
dAl (nM)	6.59±2.57 1.81–9.95	9.1±1.03 8.12–10.17	10.14±1.91 8.79–11.49	9.9±0.02 9.88–9.91	9.61±2.64 6.62–11.61	8.66±0.29 8.3–9.07	9.16±0.59 8.45–9.91	9.4±1.63 7.86–11.66	8.66±0.13 8.58–8.81

Supplementary Table 3.1 *continued*.

	Deep Background	**Diffuse (sulfur-poor)**			**Diffuse (sulfur-rich)**			**High Temperature**	
	Deep Background	**16º 43'**	**Bart**	**Micro**	**Purple Haze**	**Flo**	**North**	**Macro**	**Lava**
sFe (nM)	0.61±0.36 0.3–1.91	0.56±0.01 0.55–0.57	0.73±0.04 0.7–0.76	0.61±0.01 0.6–0.61	0.65±0.12 0.53–0.76	0.61±0.13 0.48–0.77	0.67±0.2 0.47–0.98	3.7±2.02 0.83–5.55	9.31±7.27 0.98–14.35
cFe (nM)	6.16±9.26 0.48–33.78	5.68±1.26 4.27–6.72	3.78±0.67 3.3–4.25	2.64±0.29 2.43–2.84	7.04±4.37 2.7–11.43	6.23±3.13 2.67–10.76	0.64±0.7 0.14–1.13	177.04±108.47 61.91–311.09	145.73±168.43 3.94–331.9
fraction sFe (sFe/dFe; nM:nM)	0.34±0.57 0.05–2.19	0.1±0.02 0.08–0.12	0.16±0.01 0.15–0.17	0.19±0.02 0.17–0.2	0.1±0.05 0.06–0.16	0.1±0.04 0.06–0.16	1.09±0.47 0.37–1.52	0.02±0.01 0.01–0.04	0.12±0.08 0.04–0.2
sMn (nM)	6.33±3.26 0.75–14.77	4.2±0.32 4.02–4.57	9.35±0.18 9.22–9.47	8.9±0.64 8.45–9.35	5.93±2.62 3.56–8.75	6.99±3.5 4.15–11.28	12.08±14.18 4.78–37.42	74.88±50.76 8.74–130.66	174.64±141.79 12.48–275.25
fraction dFe (dFe/tdFe; nM:nM)	0.1±0.05 0.02–0.19	0.33±0.06 0.29–0.4	0.14±0.03 0.12–0.16	0.1±0.01 0.09–0.1	0.42±0.15 0.32–0.6	0.34±0.22 0.19–0.7	0.05±0.03 0.02–0.08	0.58±0.26 0.34–0.89	0.28±0.24 0.05–0.53
Total siderophore (pM)	6.18±5.91 0–18.32	10.05±4.5 7.23–15.23	7.33±1.37 6.37–8.3	14.49±4.08 11.61–17.38	0.96±1.66 0–2.87	3.76±2.47 1.89–7.8	5.4±5.91 1.6–15.81	1.46±1.05 0–2.36	1.56±2.71 0–4.69
ICP Organic Iron Concentrations (pM)	338.64±67.29 220.29–429.24	609.32±44.25 581.32–660.34	551.04±39.14 523.36–578.71	456.19±81.67 398.44–513.94	281.09±60.04 219.65–339.64	295.5±37.55 251.41–355.39	311.12±39.06 260.27–351.93	294.61±60.76 237.4–372.08	231.89±112.19 164.99–361.42
L (nM)	2.14±0.59 1.55–3.1	NA	1.84 (n=1)	3.12±0.82 2.54–3.7	5.5±1.79 3.44–6.68	3.19±0.74 2.66–3.71	1.27±1.08 0.3–2.87	NA	100.81±99.14 4.1–202.22
logK	11.26±0.86 10.05–12.32	NA	11.88 (n=1)	11.12±0.21 10.97–11.26	10.21±0.19 10.01–10.39	10.36±0.08 10.3–10.42	11.56±1.4 9.36–12.68	NA	10.26±0.02 10.24–10.28
eL (nM)	0.35±0.77 -0.58–1.41	NA	-2.16 (n=1)	-0.13±0.54 -0.51–0.25	-2.19±2.97 -5.51–0.21	-0.64±0.16 -0.75–-0.53	0.44±1.17 -0.19–2.53	NA	-54.23±76.83 -142.28–-0.82
alpha	1344.15±1550.71 25.76–4133.56	NA	1399.93 (n=1)	403.01±84.97 342.93–463.09	103.08±64.75 35.28–164.27	72.3±2.72 70.37–74.22	1287.49±1830.91 6.61–4470.67	NA	1770.39±1753.25 78.72–3579.33
number unique siderophores	4.76±1.09 3–6	5.33±0.58 5–6	3.5±0.71 3–4	6±0 6–6	2.67±0.58 2–3	4.8±1.1 3–6	5±1 4–6	4.25±0.96 3–5	4.33±1.53 3–6
pNa (nM)	21.87±34.53 BDL–121.63	4.71±8.15 0–14.12	13.84±2.98 11.73–15.94	BDL	76.38±68.33 BDL–131.71	191.77±135.7 92.47–391.4	46.39±27.06 17.68–79.61	312.66±44.82 273.86–364.41	360.85±171.39 241.73–557.27
pMg (nM)	6.86±4.3 2.59–19.59	4.19±1.34 3.23–5.72	6.47±0.83 5.88–7.05	7.32±5.41 3.49–11.14	13.8±8.06 5.08–20.99	27.45±16.91 14.96–52.41	8.77±3.75 4.34–12.6	77.08±10.18 65.83–86.33	109.8±108.11 40.93–234.41
pAl (nM)	0.22±0.54 BDL–2.01	BDL	BDL	BDL	1.66±1.44 BDL–2.54	3.42±2.06 2.21–6.49	0.86±0.9 BDL–2.12	1.89±0.47 1.56–2.58	1.65±2.86 BDL–4.95

Supplementary Table 3.1 *continued*.

	Deep Background	**Diffuse (sulfur-poor)**			**Diffuse (sulfur-rich)**			**High Temperature**	
	Deep Background	**16º 43'**	**Bart**	**Micro**	**Purple Haze**	**Flo**	**North**	**Macro**	**Lava**
pSi (nM)	7.2±2.67 2.11–12.07	5.29±0.61 4.76–5.95	8.26±2.95 6.17–10.34	11.66±5.01 8.11–15.2	5.54±1.82 4.4–7.64	5.72±0.82 4.91–6.56	5.36±0.58 4.68–6.24	53.54±13.95 39.48–72.72	127.05±164.53 8.84–314.96
pP (nM)	3.95±3.44 BDL–12.22	1.81±0.53 1.32–2.37	7.22±5.99 2.98–11.45	7±2.72 5.07–8.92	1.47±2.54 BDL–4.4	0.79±1.1 BDL–2.34	1.19±0.34 0.9–1.72	90.42±29.05 62.6–131.29	219.23±301.08 BDL–562.52
pS_{tot} (nM)	24.67±11.8 12.55–64.04	19.84±5.18 14.47–24.81	19.78±0.78 19.23–20.33	25.65±8.92 19.34–31.96	47.09±26.55 18.4–70.8	103.24±80.58 53.61–223.67	60.82±25.8 38.28–98.18	148.02±21.38 136.52–180.08	142.26±37.43 99.92–170.96
pS_{NV} (nM)	8.46±11.32 0–46.37	4.49±3.25 2.42–8.24	7.67±0.88 7.04–8.29	2.1±0.46 1.77–2.42	0±0 0–0	78.41±60.49 40.52–168.77	49.71±25.91 25.81–86.89	124.94±44.16 63.22–166.39	113.99±33.03 76.21–137.42
pS_{V} (nM)	15.12±3.07 9.67–21.14	15.35±2.89 12.05–17.43	12.12±1.66 10.94–13.29	23.56±8.46 17.57–29.54	NA	24.83±20.11 13.09–54.9	11.11±0.83 10.36–12.48	32.42±36.47 9.13–74.45	28.28±12.7 18.49–42.63
pCl (nM)	176.88±185.31 21–788	96±42.79 66–145	127.5±6.36 123–132	74±4.24 71–77	558±453.39 61–949	1319±1054.41 650–2893	294±180.48 99–522	1063.75±161.38 910–1253	1377.67±1335.2 457–2909
pK (nM)	3.09±3.18 0.34–13.54	1.67±0.8 1.11–2.59	2.28±0.04 2.25–2.31	1.18±0.13 1.08–1.27	9.27±7.48 1.02–15.62	21.73±17.53 10.59–47.88	5.35±3.34 1.89–9.68	19.65±2.79 17.03–22.71	31.49±18.1 16.27–51.51
pCa (nM)	16.8±4.31 11.87–29.21	13±1.18 11.93–14.26	14.96±4.09 12.07–17.85	23.88±10.08 16.75–31.01	23.89±8.15 14.78–30.47	43.28±28.34 25.57–85.61	17.4±4.23 12.6–22.17	77.33±12.53 61.94–91.88	165.52±147.45 77.28–335.75
pTi (nM)	0.18±0.15 BDL–0.37	0.19±0.06 0.13–0.25	0.32±0.19 0.18–0.45	BDL	0.12±0.21 BDL–0.37	0.13±0.09 BDL–0.19	0.14±0.16 BDL–0.38	0.32±0.08 0.2–0.39	19.29±25.31 0.9–48.16
pV (nM)	0.08±0.1 BDL–0.27	BDL	BDL	BDL	0.07±0.13 BDL–0.22	0.09±0.19 BDL–0.37	0.1±0.1 BDL–0.22	1.28±0.32 0.97–1.71	6.28±5.99 BDL–11.92
pCr (nM)	0.06±0.08 BDL–0.18	0.03±0.05 BDL–0.09	0.06±0.08 BDL–0.11	BDL	BDL	0.14±0.11 BDL–0.27	BDL	0.43±0.18 0.23–0.62	42.75±48.06 3.04–96.18
pMn (nM)	0.82±0.65 0.17–2.81	0.85±0.25 0.61–1.11	1.2±0.23 1.03–1.36	1.18±0.6 0.75–1.6	0.98±0.26 0.75–1.26	0.85±0.09 0.73–0.93	1.07±0.12 0.88–1.19	0.83±0.22 0.62–1.14	112.13±100.13 2.12–197.94
pFe (nM)	30.52±15.2 2.24–65.11	17.59±1.25 16.58–18.99	36.39±15.22 25.63–47.15	51.39±17.89 38.74–64.04	21.63±11.15 14.22–34.46	20.71±8.82 10.98–30.81	18.6±3.11 16.58–24.04	395.21±115.43 284.02–557.34	1023.22±1309.4 199.48–2533.1
pNi (nM)	0.02±0.04 BDL–0.09	BDL	BDL	BDL	BDL	0.01±0.02 BDL–0.04	0.03±0.04 BDL–0.1	BDL	112.63±108.67 BDL–216.86
pCu (nM)	0.21±0.29 BDL–1.27	0.14±0.1 0.07–0.26	0.12±0.08 0.06–0.18	0.25±0.09 0.18–0.31	0.15±0.19 BDL–0.36	0.21±0.17 0.05–0.45	2±1.17 0.07–3.07	2.89±0.56 2.36–3.68	16.44±11.73 3.29–25.82

Supplementary Table 3.1 *continued*.

	Deep Background	**Diffuse (sulfur-poor)**			**Diffuse (sulfur-rich)**			**High Temperature**	
	Deep Background	**16º 43'**	**Bart**	**Micro**	**Purple Haze**	**Flo**	**North**	**Macro**	**Lava**
pZn (nM)	0.1±0.2 BDL–0.8	0.04±0.06 BDL–0.11	0.07±0.09 BDL–0.13	0.16±0.01 0.15–0.16	0.08±0.02 0.06–0.09	0.01±0.03 BDL–0.05	0.05±0.03 BDL–0.07	12.95±3.44 8.32–16.29	18.94±10.45 12–30.95
pAs (nM)	0.06±0.15 BDL–0.59	BDL	0.06±0.08 BDL–0.12	0.05±0.06 BDL–0.09	0.05±0.04 BDL–0.08	0.01±0.03 BDL–0.05	BDL	0.51±0.52 BDL–1.24	1.5±1.58 BDL–3.15
pBr (nM)	0.26±0.61 BDL–2.11	BDL	BDL	BDL	0.97±0.86 BDL–1.65	2.3±1.93 0.92–5.15	0.76±0.89 BDL–2.04	1.97±0.27 1.69–2.33	6.24±4.69 1.09–10.27
pSr (nM)	0.29±0.55 BDL–2.21	0.06±0.05 BDL–0.09	0.11±0 0.11–0.11	0.17±0.03 0.15–0.19	0.21±0.02 0.2–0.23	0.35±0.16 0.24–0.58	1.83±1.78 BDL–4.12	0.96±0.24 0.72–1.26	4.9±2.35 2.63–7.32
pW (nM)	0.01±0.02 BDL–0.05	0.02±0.03 BDL–0.05	BDL	BDL	0.01±0.02 BDL–0.04	BDL	0.01±0.02 BDL–0.05	0.02±0.05 BDL–0.09	BDL
pPb (nM)	0.61±1.23 BDL–3.75	0.02±0.04 BDL–0.07	0.01±0.01 BDL–0.02	0.12±0.06 0.07–0.16	0.04±0.06 BDL–0.11	0.08±0.07 0.02–0.17	1.67±1.3 BDL–3.46	0.06±0.12 BDL–0.23	3.21±4.06 BDL–7.77
pP:pFe ratio (nM:nM)	0.12±0.04 0.07–0.20	0.1±0.03 0.08–0.14	0.18±0.09 0.12–0.24	0.14±0.01 0.13–0.14	0.13 (n=1)	0.05±0.03 0.03–0.08	0.07±0.02 0.04–0.1	0.23±0.01 0.22–0.24	0.25±0.04 0.22–0.28
$\text{tdMn}_{\text{adjusted}}$ (nM)	4.89±2.66 0.12–10.27	4.65±1.98 3.03–6.85	9.82±1.12 9.03–10.61	7.75±0.56 7.35–8.14	4.76±2.63 2.41–7.6	8.65±3.49 3.67–12.83	16.39±17.26 3.23–45.08	91.14±51.71 19.07–133.06	159.91±49.81 122.3–216.4

Stations are grouped by type of feature. Samples that were below detection limit are denoted as “BDL” in the ranges. BDL samples were input as zeros when calculating averages and standard deviations. NA means a sample was not taken. N = 1 indicates that only one sample from that station had that variable measured.

Supplementary Table 3.2. Averages, standard deviations, and ranges of key variables for the center of the neutrally buoyant plume at each station.

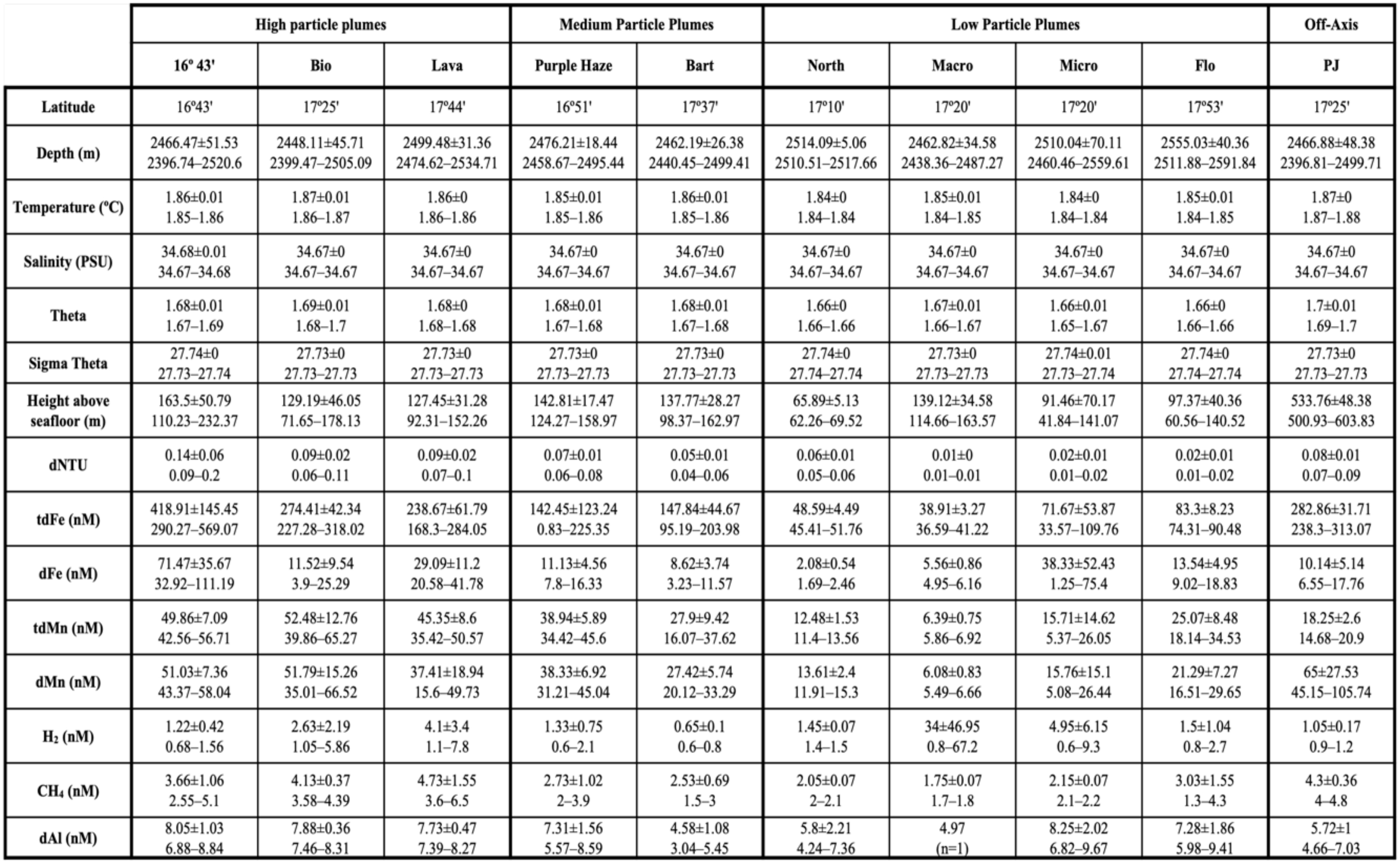

	High particle plumes			**Medium Particle Plumes**		**Low Particle Plumes**				**Off-Axis**
	16º 43'	**Bio**	**Lava**	**Purple Haze**	**Bart**	**North**	**Macro**	**Micro**	**Flo**	**PJ**
Latitude	16º43'	17º25'	17º44'	16º51'	17º37'	17º10'	17º20'	17º20'	17º53'	17º25'
Depth (m)	2466.47±51.53 2396.74–2520.6	2448.11±45.71 2399.47–2505.09	2499.48±31.36 2474.62–2534.71	2476.21±18.44 2458.67–2495.44	2462.19±26.38 2440.45–2499.41	2514.09±5.06 2510.51–2517.66	2462.82±34.58 2438.36–2487.27	2510.04±70.11 2460.46–2559.61	2555.03±40.36 2511.88–2591.84	2466.88±48.38 2396.81–2499.71
Temperature (ºC)	1.86±0.01 1.85–1.86	1.87±0.01 1.86–1.87	1.86±0 1.86–1.86	1.85±0.01 1.85–1.86	1.86±0.01 1.85–1.86	1.84±0 1.84–1.84	1.85±0.01 1.84–1.85	1.84±0 1.84–1.84	1.85±0.01 1.84–1.85	1.87±0 1.87–1.88
Salinity (PSU)	34.68±0.01 34.67–34.68	34.67±0 34.67–34.67	34.67±0 34.67–34.67	34.67±0 34.67–34.67	34.67±0 34.67–34.67	34.67±0 34.67–34.67	34.67±0 34.67–34.67	34.67±0 34.67–34.67	34.67±0 34.67–34.67	34.67±0 34.67–34.67
Theta	1.68±0.01 1.67–1.69	1.69±0.01 1.68–1.7	1.68±0 1.68–1.68	1.68±0.01 1.67–1.68	1.68±0.01 1.67–1.68	1.66±0 1.66–1.66	1.67±0.01 1.66–1.67	1.66±0.01 1.65–1.67	1.66±0 1.66–1.66	1.7±0.01 1.69–1.7
Sigma Theta	27.74±0 27.73–27.74	27.73±0 27.73–27.73	27.73±0 27.73–27.73	27.73±0 27.73–27.73	27.73±0 27.73–27.73	27.74±0 27.74–27.74	27.73±0 27.73–27.73	27.74±0.01 27.73–27.74	27.74±0 27.74–27.74	27.73±0 27.73–27.73
Height above seafloor (m)	163.5±50.79 110.23–232.37	129.19±46.05 71.65–178.13	127.45±31.28 92.31–152.26	142.81±17.47 124.27–158.97	137.77±28.27 98.37–162.97	65.89±5.13 62.26–69.52	139.12±34.58 114.66–163.57	91.46±70.17 41.84–141.07	97.37±40.36 60.56–140.52	533.76±48.38 500.93–603.83
dNTU	0.14±0.06 0.09–0.2	0.09±0.02 0.06–0.11	0.09±0.02 0.07–0.1	0.07±0.01 0.06–0.08	0.05±0.01 0.04–0.06	0.06±0.01 0.05–0.06	0.01±0 0.01–0.01	0.02±0.01 0.01–0.02	0.02±0.01 0.01–0.02	0.08±0.01 0.07–0.09
tdFe (nM)	418.91±145.45 290.27–569.07	274.41±42.34 227.28–318.02	238.67±61.79 168.3–284.05	142.45±123.24 0.83–225.35	147.84±44.67 95.19–203.98	48.59±4.49 45.41–51.76	38.91±3.27 36.59–41.22	71.67±53.87 33.57–109.76	83.3±8.23 74.31–90.48	282.86±31.71 238.3–313.07
dFe (nM)	71.47±35.67 32.92–111.19	11.52±9.54 3.9–25.29	29.09±11.2 20.58–41.78	11.13±4.56 7.8–16.33	8.62±3.74 3.23–11.57	2.08±0.54 1.69–2.46	5.56±0.86 4.95–6.16	38.33±52.43 1.25–75.4	13.54±4.95 9.02–18.83	10.14±5.14 6.55–17.76
tdMn (nM)	49.86±7.09 42.56–56.71	52.48±12.76 39.86–65.27	45.35±8.6 35.42–50.57	38.94±5.89 34.42–45.6	27.9±9.42 16.07–37.62	12.48±1.53 11.4–13.56	6.39±0.75 5.86–6.92	15.71±14.62 5.37–26.05	25.07±8.48 18.14–34.53	18.25±2.6 14.68–20.9
dMn (nM)	51.03±7.36 43.37–58.04	51.79±15.26 35.01–66.52	37.41±18.94 15.6–49.73	38.33±6.92 31.21–45.04	27.42±5.74 20.12–33.29	13.61±2.4 11.91–15.3	6.08±0.83 5.49–6.66	15.76±15.1 5.08–26.44	21.29±7.27 16.51–29.65	65±27.53 45.15–105.74
H_2 (nM)	1.22±0.42 0.68–1.56	2.63±2.19 1.05–5.86	4.1±3.4 1.1–7.8	1.33±0.75 0.6–2.1	0.65±0.1 0.6–0.8	1.45±0.07 1.4–1.5	34±46.95 0.8–67.2	4.95±6.15 0.6–9.3	1.5±1.04 0.8–2.7	1.05±0.17 0.9–1.2
CH_4 (nM)	3.66±1.06 2.55–5.1	4.13±0.37 3.58–4.39	4.73±1.55 3.6–6.5	2.73±1.02 2–3.9	2.53±0.69 1.5–3	2.05±0.07 2–2.1	1.75±0.07 1.7–1.8	2.15±0.07 2.1–2.2	3.03±1.55 1.3–4.3	4.3±0.36 4–4.8
dAl (nM)	8.05±1.03 6.88–8.84	7.88±0.36 7.46–8.31	7.73±0.47 7.39–8.27	7.31±1.56 5.57–8.59	4.58±1.08 3.04–5.45	5.8±2.21 4.24–7.36	4.97 (n=1)	8.25±2.02 6.82–9.67	7.28±1.86 5.98–9.41	5.72±1 4.66–7.03

Supplementary Table 3.2 *continued*.

	High particle plumes			**Medium Particle Plumes**		**Low Particle Plumes**				**Off-Axis**
	16º 43'	**Bio**	**Lava**	**Purple Haze**	**Bart**	**North**	**Macro**	**Micro**	**Flo**	**PJ**
sFe (nM)	1.6±0.21 1.43–1.9	1.2±1.08 0.61–2.81	1.96±0.93 1.26–3.01	0.93±0.15 0.77–1.07	0.8±0.21 0.57–1.02	0.51±0.08 0.45–0.56	0.69±0.19 0.55–0.82	1.99±2.18 0.45–3.53	0.84±0.09 0.75–0.93	0.62±0.03 0.59–0.65
cFe (nM)	69.87±35.56 31.49–109.64	10.32±8.49 3.27–22.48	27.13±10.35 18.97–38.77	10.2±4.47 6.84–15.27	7.82±3.55 2.66–10.55	1.57±0.47 1.24–1.9	4.87±1.05 4.13–5.61	36.34±50.25 0.81–71.87	12.7±4.86 8.27–17.9	9.52±5.16 5.91–17.17
fraction sFe (sFe/dFe; nM:nM)	0.03±0.01 0.01–0.04	0.11±0.04 0.07–0.16	0.07±0.02 0.05–0.08	0.09±0.03 0.07–0.12	0.11±0.05 0.07–0.18	0.25±0.03 0.23–0.27	0.13±0.06 0.09–0.17	0.21±0.22 0.05–0.36	0.07±0.02 0.05–0.08	0.07±0.03 0.03–0.1
sMn (nM)	63.13±18.36 45.17–88.41	50.43±12.73 38.29–61.88	48.21±9.68 37.21–55.46	44.37±7.75 36.1–51.47	25.58±9.89 10.94–31.76	10.27±6.57 5.62–14.91	7.81±0.99 7.11–8.51	15.82±13.42 6.33–25.31	23.88±6.69 18.84–31.47	57.29±6.75 48.1–64.1
fraction dFe (dFe/tdFe; nM:nM)	0.16±0.04 0.11–0.2	0.04±0.03 0.01–0.08	0.13±0.05 0.07–0.16	3.16±5.37 0.04–9.36	0.07±0.04 0.02–0.12	0.05±0.01 0.04–0.05	0.15±0.04 0.12–0.17	0.37±0.46 0.04–0.69	0.16±0.05 0.12–0.22	0.04±0.02 0.02–0.06
Total siderophore (pM)	8.84±7.1 0–16.95	0.56±0.89 0–1.87	2.63±3.39 0.5–6.55	2.31±1.35 1.05–3.74	6.96±4.31 2.16–11.95	1.09±1.53 0–2.17	7.34±0.82 6.76–7.92	21.01±3.85 18.29–23.73	0±0 0–0	2.09±1.61 0–3.63
ICP Organic Iron Concentrations (pM)	261.47±140.75 135.3–416.24	311.71±49.31 259–364.59	321.7±20.89 303.83–344.66	279.37±61.36 208.62–318.12	392.43±176.51 266.38–653.91	341.19±53.82 303.13–379.24	529.18±38.21 502.16–556.2	449.39±82.91 390.77–508.02	238.75±5.02 235.53–244.53	228.09±60.2 167.28–311.16
L (nM)	NA	3.11 (n=1)	16.8±5.92 10.74–22.56	6.17±0.74 5.32–6.69	2.69 (n=1)	1.78±0.1 1.71–1.85	NA	2.60 (n=1)	NA	5.44±0.51 5.03–6.15
logK	NA	10.24 (n=1)	10.2±0.16 10.04–10.36	10.64±0.17 10.53–10.84	11.96 (n=1)	10.94±0.42 10.64–11.24	NA	10.67 (n=1)	NA	10.32±0.52 10.04–11.1
eL (nM)	NA	-0.79 (n=1)	-12.29±8.04 -19.22–-3.47	-4.96±4.26 -9.64–-1.3	-0.54 (n=1)	-0.3±0.64 -0.75–0.16	NA	1.35 (n=1)	NA	-4.7±5.4 -12.73–-1.09
alpha	NA	53.82 (n=1)	301.69±201 118.19–516.52	291.01±150.61 182.02–462.87	2452.27 (n=1)	197.22±172.62 75.16–319.28	NA	121.89 (n=1)	NA	208.19±290.61 55.28–644
number unique siderophores	5.25±0.96 4–6	4.75±1.71 3–7	4±1.73 3–6	4.67±2.08 3–7	3.75±1.71 2–6	4±1.41 3–5	5±1.41 4–6	4±0 4–4	5±1 4–6	5.5±1.91 4–8
pNa (nM)	298.12±263.91 127.86–602.13	41.8±13.43 30.3–58	78.74±70.61 15.66–155.01	173.31±102.92 55.18–243.6	10.48±8.79 0–19.96	691.41 (n=1)	519.18±496.03 168.43–869.92	17.06±24.13 BDL–34.12	54.5±84.13 BDL–151.4	744.49±638.07 137.13–1409.38
pMg (nM)	69.98±30.6 40.8–101.82	31.29±8.23 23.54–42.84	29.95±10.57 18.33–39	48.18±4.23 43.31–50.91	20.77±5.29 13.62–26.33	137.35 (n=1)	61±45.25 29–93	11.26±3.45 8.82–13.7	18.27±13.78 9.62–34.16	176.43±161.05 36.56–352.5
pAl (nM)	2.17±3.76 BDL–6.51	BDL	BDL	1.28±1.11 BDL–1.93	BDL	11.38 (n=1)	5.82±4.6 2.57–9.07	BDL	0.94±1.63 BDL–2.82	BDL

Supplementary Table 3.2 *continued*.

	High particle plumes			**Medium Particle Plumes**		**Low Particle Plumes**				**Off-Axis**
	16º 43'	**Bio**	**Lava**	**Purple Haze**	**Bart**	**North**	**Macro**	**Micro**	**Flo**	**PJ**
pSi (nM)	64.67±29.88 45.44–99.09	52.74±9.16 46.42–65.94	44.31±13.67 28.54–52.82	49.23±15.24 36.68–66.19	34.76±10.64 21.75–46.43	11.1 (n=1)	8.61±4.82 5.2–12.01	13.31±4.28 10.28–16.33	18.41±4.48 14.01–22.97	136.83±78.59 70.17–223.49
pP (nM)	107.1±54.06 73.19–169.44	70.86±14.7 60.85–92.2	59.5±22.76 33.25–73.75	69.84±18 55.57–90.06	43.8±17.08 22.93–62.22	1.08 (n=1)	4.15±5.87 BDL–8.3	11.42±8.97 5.07–17.76	19.57±5.47 13.42–23.89	131.1±155.45 BDL–302.83
$\mathrm{pS_{tot}}$ (nM)	163.04±95.88 89.34–271.44	40.41±19.33 29.25–69.34	72.8±14.13 57.66–85.64	71.88±38.48 31.75–108.46	24.35±7.83 17.04–33.26	317.77 (n=1)	157.54±111.78 78.5–236.58	33.6±11.71 25.32–41.88	35.83±26.01 18.64–65.76	559.71±786.5 64.2–1466.58
$\mathrm{pS_{NV}}$ (nM)	118.05±139.71 0–272.3	22.9±17.93 11.13–49.47	56.03±14.46 40.66–69.35	0±0 0–0	8.01±4.57 4.18–14.62	284.61 (n=1)	129.29±93.27 63.34–195.24	16.82±16.04 5.48–28.16	19.69±22.63 5.37–45.78	0±0 0–0
$\mathrm{pS_{V}}$ (nM)	7.5 (n=1)	17.51±2.22 14.54–19.87	16.77±0.41 16.29–17.01	NA	16.35±4.45 12.4–21.49	33.16 (n=1)	28.26±18.52 15.16–41.35	16.78±4.33 13.72–19.84	16.15±3.46 13.27–19.98	NA
pCl (nM)	1117.67±1424.39 237–2761	171.75±29.39 137–199	675±97.62 563–742	667±444.26 166–1013	87.25±45.71 42–143	3979 (n=1)	2340.5±1911.31 989–3692	90±39.6 62–118	317.67±384.96 51–759	3934±5363.47 507–10115
pK (nM)	19.41±23.51 4.94–46.54	3.81±0.88 2.69–4.58	14.83±2.89 11.55–17.02	13.03±8.81 3.03–19.62	1.98±0.88 0.87–2.9	99.61 (n=1)	38.85±31.42 16.63–61.06	2.71±1.25 1.82–3.59	5.42±6.53 0.79–12.88	68.58±92.05 8.7–174.58
pCa (nM)	80.98±24.64 52.54–95.89	45.98±8.46 39.27–58.04	55.69±13.52 40.33–65.79	52.88±0.43 52.45–53.3	35.95±10.64 22.24–47.95	98.32 (n=1)	59.8±31.4 37.6–82	18.92±0.64 18.47–19.37	27.98±11.92 20.01–41.68	186.21±111.94 65.94–287.36
pTi (nM)	0.28±0.25 BDL–0.45	0.16±0.19 BDL–0.38	11.7±12.9 BDL–25.54	0.26±0.3 BDL–0.59	0.05±0.1 BDL–0.2	BDL	0.09±0.13 BDL–0.18	0.11±0.16 BDL–0.22	0.09±0.16 BDL–0.27	5.18±8.32 BDL–14.78
pV (nM)	1.27±1.05 0.25–2.34	0.98±0.18 0.75–1.14	14.99±18.23 BDL–35.28	1.33±0.3 1.13–1.67	0.66±0.42 0.29–1.21	BDL	0.42±0.11 0.34–0.49	0.15±0.21 BDL–0.29	0.39±0.1 0.3–0.49	2.03±2.37 BDL–4.64
pCr (nM)	0.41±0.43 BDL–0.86	0.3±0.08 0.21–0.39	43.03±11.81 29.71–52.21	0.2±0.22 BDL–0.44	0.19±0.09 0.11–0.32	BDL	0.1±0.13 BDL–0.19	0.06±0.08 BDL–0.12	0.11±0.11 BDL–0.21	0.68±0.69 BDL–1.37
pMn (nM)	2.32±0.79 1.6–3.17	5.32±0.95 4.58–6.7	81.17±14.41 72.81–97.81	4.32±1.73 3.02–6.29	4.92±1.71 2.97–7.12	2.12 (n=1)	1.41±0.65 0.95–1.87	0.94±0.23 0.77–1.1	1.07±0.13 0.97–1.22	12.19±4.71 9.47–17.63
pFe (nM)	478.7±203.59 345.72–713.07	315.11±66 267.98–409.75	226.78±28.17 197.32–253.46	302.08±81.81 234.61–393.07	193.17±65.54 119.75–267.39	55.97 (n=1)	42.9±19.73 28.95–56.85	67.92±36.57 42.06–93.78	98.44±25.19 72.72–123.07	829.89±472.37 436.13–1353.64
pNi (nM)	BDL	BDL	95.54±10.46 83.76–103.72	BDL	BDL	BDL	BDL	0.11±0.05 0.07–0.14	BDL	BDL
pCu (nM)	2.88±0.89 2.26–3.9	1.27±1.05 0.62–2.84	13.03±4.33 8.22–16.63	0.78±0.14 0.62–0.87	0.52±0.02 0.49–0.54	1.14 (n=1)	0.19±0.02 0.17–0.2	0.9±1.16 0.08–1.72	0.24±0.05 0.18–0.27	3.5±2.42 1–5.83

Supplementary Table 3.2 *continued*.

	High particle plumes			**Medium Particle Plumes**		**Low Particle Plumes**				**Off-Axis**
	16º 43'	**Bio**	**Lava**	**Purple Haze**	**Bart**	**North**	**Macro**	**Micro**	**Flo**	**PJ**
pZn (nM)	0.98±0.33 0.79–1.36	0.29±0.28 0.12–0.7	3±2.83 BDL–5.63	0.21±0.03 0.19–0.24	0.23±0.03 0.2–0.26	BDL	BDL	0.5±0.49 0.15–0.85	0.16±0.02 0.15–0.18	0.35±0.37 BDL–0.73
pAs (nM)	0.71±0.32 0.48–1.07	0.34±0.28 BDL–0.58	0.46±0.8 BDL–1.38	0.43±0.11 0.31–0.52	0.31±0.21 BDL–0.48	BDL	0.06±0.08 BDL–0.12	0.24±0.16 0.13–0.35	0.14±0.08 0.06–0.22	0.97±1.42 BDL–2.6
pBr (nM)	2±2.69 0.37–5.11	0.21±0.26 BDL–0.54	1.73±1.66 BDL–3.31	1.14±0.94 0.07–1.8	0.03±0.05 BDL–0.1	5.15 (n=1)	4.47±4.26 1.45–7.48	0.87±1.23 BDL–1.74	0.4±0.69 BDL–1.19	5.53±7.26 0.46–13.84
pSr (nM)	1.13±0.34 0.78–1.45	1.03±0.51 0.56–1.64	3.45±3.51 BDL–7.01	0.81±0.07 0.75–0.89	0.49±0.13 0.3–0.6	1.13 (n=1)	0.63±0.42 0.33–0.93	0.28±0.06 0.23–0.32	0.24±0.12 0.15–0.37	4.09±3.96 0.85–8.51
pW (nM)	BDL	0.01±0.03 BDL–0.05	0.35±0.61 BDL–1.06	BDL	0.06±0.05 BDL–0.13	BDL	BDL	BDL	0.04±0.04 BDL–0.08	BDL
pPb (nM)	0.05±0.06 BDL–0.11	0.26±0.37 BDL–0.81	3.46±1.31 2.31–4.88	0.07±0.04 0.03–0.11	0.1±0.13 BDL–0.3	2.59 (n=1)	0.03±0.04 BDL–0.05	BDL	0.01±0.01 BDL–0.02	0.16±0.16 BDL–0.31
pP:pFe ratio (nM:nM)	0.22±0.02 0.19–0.24	0.22±0 0.22–0.23	0.26±0.08 0.17–0.32	0.23±0 0.23–0.24	0.22±0.02 0.19–0.24	0.02 (n=1)	0.15 (n=1)	0.16±0.05 0.12–0.19	0.2±0.02 0.18–0.21	0.22±0.01 0.21–0.22
$tdMn_{adjusted}$ (nM)	51.03±7.36 43.37–58.04	53.11±13.48 39.86–66.52	45.35±8.6 35.42–50.57	39.59±5.64 34.42–45.6	29.11±7.68 20.12–37.62	13.61±2.4 11.91–15.3	6.39±0.75 5.86–6.92	15.91±14.9 5.37–26.44	25.07±8.48 18.14–34.53	65±27.53 45.15–105.74

Stations are grouped by plume intensity (left: high particles, middle: medium particles, right: low particles, far right: off axis. Samples that were below detection limit are denoted as “BDL” in the ranges. BDL samples were input as zeros when calculating averages and standard deviations. NA means a sample was not taken. N = 1 indicates that only one sample from that station had that variable measured.

Chapter 4. SIDEROPHORES ARE UBIQUITOUS IN HYDROTHERMAL SYSTEMS ALONG THE SOUTHERN EAST PACIFIC RISE AND CONTRIBUTE TO IRON STABILIZATION NEAR THE RIDGE CREST

*This chapter will be submitted to a journal with the following author list. See 4.8 for detailed author contributions.

Laura E. Moore, Randelle M. Bundy, Joseph A. Resing, Peter N. Sedwick, Jiwoon Park, Bettina M. Sohst, Nathaniel J. Buck, Dylan Vecchione, Robert M. Morris

4.1 ABSTRACT

Siderophores are low molecular weight, iron-binding ligands produced by microbes to obtain scarce iron resources. Despite their critical importance to microbial iron acquisition, oceanic siderophore studies are sparse and primarily focus on the surface and mesopelagic ocean. Here, we quantify and identify siderophores in diverse hydrothermal venting systems below 2,200 m along the 16º-18ºS sector of the Southern East Pacific Rise (SEPR). Siderophore concentrations ranged from 0-41 pM and were ubiquitous throughout the dataset, which is the first evidence for widespread siderophore production in deep ocean environments. We identified eight unique siderophores that were commonly detected in multiple hydrothermal environments and across large dissolved iron gradients (0.5-345 nM). Several of these siderophores, including hyalachelin A and talarazine C, have not previously been detected in the ocean. We additionally assessed the impacts of siderophores on the total iron-binding ligand pool, and for the first time demonstrate that siderophores contribute significantly to the total iron-binding ligand pool, elevating the

average binding strength and enhancing the complexation capacity of the entire ligand pool. We propose that despite the low concentrations, the strong iron-binding properties of siderophores may have a disproportionate impact on local iron stabilization in hydrothermal environments, with potential impacts on long-term iron stability in the neutrally-buoyant plume.

4.2 INTRODUCTION

Iron (Fe) is an essential nutrient for life in the ocean, facilitating key cellular processes such as DNA synthesis, nitrogen fixation, and cellular respiration (Morel and Price, 2003). However, oceanic dissolved Fe (dFe) concentrations are very low (Moore et al., 2013; Tagliabue et al., 2017), and only a small fraction of the total Fe pool is accessible to marine microorganisms (Christel S. Hassler et al., 2011; Lis et al., 2015; Rich and Morel, 1990; Shaked et al., 2020). The dFe pool (< 0.2 μm) is considered the most biologically labile (Morel et al., 2008), but inorganic dFe solubility in seawater is quite small (~0.02 nM) (Liu and Millero, 2002) and several orders of magnitude lower than the concentrations required for sustaining phytoplankton growth (Johnson et al., 1997; Moore et al., 2013). Instead, dFe is primarily stabilized by organic dFe-binding ligands that bind more than 99% of the dFe throughout much of the ocean (Gledhill and Buck, 2012; Gledhill and van den Berg, 1994; Rue and Bruland, 1995). These organic ligands are a heterogeneous mixture of biologically-produced compounds that help maintain dFe in seawater at concentrations above the inorganic solubility limit (Gledhill and Buck, 2012; Hunter and Boyd, 2007). As a result, characterizing the organic dFe-binding ligands in seawater is essential to understanding Fe biogeochemistry, particularly with regards to bioavailability and stability of dFe.

Most organic ligand studies focus on bulk electrochemical measurements that determine the concentration and average binding strengths of the ligand pool (Buck et al., 2015, 2012;

Bundy et al., 2015; Gerringa et al., 2015; Gledhill and van den Berg, 1994). These studies have found that ligand concentrations exceed dFe in most of the ocean, except in areas of extremely high Fe concentrations (dFe > 10 nM) such as in hydrothermal vents (Buck et al., 2015, 2018; Hawkes et al., 2013; Kleint et al., 2016). While electrochemical methods thus confirm the ubiquity of organic ligands and recognize their importance as a dFe stabilization mechanism, these methods cannot identify the specific types of dFe-binding molecules present beyond operational definitions based on dFe binding strength (Bundy et al., 2015; Gledhill and Buck, 2012; Hunter and Boyd, 2007). Electrochemical methods can also be used to measure specific classes of ligands such as humic-like substances and exopolysaccharides (C. S. Hassler et al., 2011; Laglera et al., 2007; Norman et al., 2015). However, these studies are somewhat limited in that the ligand classifications from these methods are still operational and do not allow for the identification of specific compounds. More recent ligand identification studies use mass spectrometry to identify known and unknown dFe-binding compounds by molecular weight. These studies focus largely on identifying siderophores (Boiteau et al., 2019; Bundy et al., 2018; Mawji et al., 2008; Park et al., 2023), low molecular weight dFe-binding ligands produced by microbes to obtain scarce or inaccessible Fe resources (Kramer et al., 2019; Neilands, 1981).

Siderophores have the strongest dFe-binding constants of any natural molecule identified to date, with conditional stability constants ($K_{FeL,Fe'}^{cond}$) ranging from 12-14.5 (Bundy et al., 2018; Witter et al., 2000a). The unusually high binding constants help siderophore-producing microbes to maintain competitive advantage over their neighbors by sequestering Fe from organisms without the necessary receptors to take up the siderophore complex (Kramer et al., 2019). While over 500 siderophores have been identified to date, most were isolated from terrestrial bacterial and fungal cultures (Hider and Kong, 2010; Sandy and Butler, 2009). There are still relatively few studies of oceanic siderophores (Boiteau et al., 2016a, 2019; Bundy et al., 2018; Mawji et al., 2008, 2011; Park et al., 2023; Vraspir and Butler, 2009), but most have noted the importance of siderophores in Fe cycling. Siderophores are thought to have important impacts on both the physical and chemical speciation of Fe in the ocean (Bundy et al., 2015; Kraemer et al., 2005; Kügler et al., 2020; Manck et al., 2022; Vraspir and Butler, 2009). Hydrophilic siderophores are small and polar, and therefore likely primarily reside in the dissolved and perhaps even the soluble (< 0.02 µm) phase. Amphiphilic siderophores however, contain a fatty acid tail that could anchor the Fe-binding head group to a cell membrane or a particle (Martinez et al., 2003), and thus some siderophores could also be found in the particulate phase (> 0.2 µm). Siderophores have also been shown to be used by heterotrophic bacteria to transform particulate Fe (pFe) in dust, solubilizing the Fe into the dissolved phase (Kraemer et al., 2005; Manck et al., 2022). Chemically, the extremely high binding constants associated with siderophores suggest that they may disproportionately impact Fe complexation and could be important for overall Fe stabilization in the water column depending on their concentrations in the ligand pool (Buck et al., 2018; Bundy et al., 2018; Tagliabue et al., 2017; Vraspir and Butler, 2009).

Despite the importance of siderophores to oceanic Fe biogeochemistry, measurements are still sparse. The majority of the measurements thus far have been focused on the upper and mesopelagic ocean (< 1,500 m) (Boiteau et al., 2016a, 2019; Bundy et al., 2018; Park et al., 2023), but very few studies have examined deeper regions, where sedimentary and hydrothermal Fe sources are prominent and Fe concentrations are elevated relative to surface waters (Hoffman et al., 2023; Hunter and Boyd, 2007; Tagliabue et al., 2014). The importance of siderophores in the deep ocean has previously been assumed to be negligible, since they are largely used by bacteria to facilitate Fe uptake when Fe is scarce (Leventhal et al., 2019). However, active uptake of siderophore-bound Fe in the upper mesopelagic (Bundy et al. 2022), the presence of siderophores in high Fe coastal benthic boundary layers (Boiteau et al., 2019) and oxygen minimum zones (Moore et al., 2021) suggests that siderophore Fe acquisition might be a common strategy throughout the water column. Indeed, a laboratory study using a model heterotrophic bacteria showed that the siderophore petrobactin was being used in order to make refractory sources of Fe such as pFe more accessible (Manck et al., 2022). Thus, siderophores might also be important in the deep ocean despite higher Fe concentrations, if only a portion of this Fe pool is biologically accessible for uptake.

Hydrothermal vents are one such high Fe environment where siderophore production and uptake might be influential to Fe cycling. Although hydrothermal venting inputs Fe at high concentrations, up to over 1 million times that of background seawater (Von Damm, 1990), not all of this Fe is readily accessible. Much of the Fe is immediately precipitated from hydrothermal fluids upon contact with oxic seawater (Mottl and McConachy, 1990), and the remaining dFe is likely primarily in the colloidal size fraction ($0.02\ \mu m < cFe < 0.2\ \mu m$) (Fitzsimmons et al., 2017; Gartman et al., 2014; Moore et al. *in prep;* Yücel et al., 2011). Colloidal Fe is less bioavailable than truly soluble Fe, particularly if the colloids are inorganic (Chen et al., 2003; Morel et al., 2008; Wang and Dei, 2003). Thus, siderophores' production may be triggered in hydrothermal environments to access more refractory colloidal or particulate Fe pools, despite ostensibly high Fe concentrations. Indeed, a study at Guaymas Basin hydrothermal field found that bacterial transcripts corresponding to siderophore uptake, regulation, and synthesis comprise ~50% of all Fe-uptake system transcripts (Li et al., 2014). A more recent study focusing on the Mid-Atlantic Ridge also identified siderophores at several hydrothermal sites (Hoffman et al., 2023), and electrochemical results from the GEOTRACES GP16 transect indicated particularly strong ligands near the hydrothermally-active Southern East Pacific Rise (SEPR), which could be a sign of local siderophore production (Buck et al., 2018; Vraspir and Butler, 2009). The presence of siderophores in hydrothermal systems might therefore be an essential Fe uptake and stabilization mechanism near vents, with possible long-term impacts on dFe transport away from the immediate vent vicinity.

To explore the impact of siderophores in hydrothermal settings, we sampled hydrothermal systems along the ultrafast spreading SEPR. The SEPR has the highest spatial frequency of hydrothermal venting of any ridge system in the world and hosts a diverse array of venting sites (Auzende et al., 1996; Beaulieu et al., 2015; Charlou et al., 1996; Moore et al. *in prep*). The site variability allows us to examine siderophore impact on Fe biogeochemistry under different hydrothermal conditions and across a wider range of Fe concentrations than has previously been examined. Furthermore, the SEPR produces a large plume of stabilized dFe that extends over 4,000 km westwards into the Pacific Basin (Fitzsimmons et al., 2017; Moffett and German, 2018; Resing et al., 2015), making it critical to understand Fe biogeochemistry at its source on the ridge axis.

In this study, we identified and quantified siderophores in diverse hydrothermal vent systems along the SEPR. We examined site and environmental variation in siderophore identity and concentration, and compared siderophore distributions to bacterial cell counts to assess the relationship between siderophores and the in-situ microbial community. Additionally, we discuss the role of siderophores in altering the physical and chemical speciation of Fe and speculate on siderophore contribution to the stabilization of dFe as the neutrally-buoyant plume ages. Finally, we compared siderophore concentrations to electrochemical measurements of the total organic ligand pool and find for the first time in any region studied so far, that siderophores are disproportionate contributors to the overall Fe-binding capacity of the ligand pool in hydrothermal systems.

4.3 METHODS

4.3.1 *Seawater collection*

Samples were collected on the R/V *Roger Revelle* during the 18 September – 6 November 2021 PLUME RAIDERS cruise (RR2106). The main study area was located along the 16-18ºS sector of the Southern East Pacific Rise (SEPR, Figure 4.1), with an additional crossover station at U.S. GEOTRACES GP16 Station 18 (15ºS). Seawater was collected on the U.S. GEOTRACES trace metal rosette (Cutter and Bruland, 2012) equipped with 12 L Teflon-coated GO-Flo bottles (General Oceanics). The rosette was additionally outfitted with a miniature autonomous plume recorder (MAPR) from the National Oceanic and Atmospheric Administration Pacific Marine Environmental Laboratory (NOAA-PMEL) equipped with oxidation reduction potential (ORP) and light scattering sensors, and an ultra-short baseline (USBL) transponder to ensure precise site location during repeat casts. To ensure adequate volumes of seawater were obtained for sample analysis, two bottles were tripped at every depth. Samples for total dissolvable Fe and manganese (tdFe and tdMn), dissolved Fe and Mn (dFe and dMn), and soluble Fe (sFe) were collected from even numbered bottles, while total organic dFe-binding ligand and siderophore samples were collected from odd numbered bottles. The GEOTRACES cookbook protocols (Cutter and Bruland, 2012) were followed for all sampling and cleaning procedures and all subsampling was performed in a Class-100 clean container.

Samples for tdFe, tdMn, dFe, dMn, sFe, organic ligands, and siderophores were filtered under pressure (10 psi, High Efficiency Particulate Air (HEPA) filtered) through a 0.2 µm polyethersulfone (Supor) membrane filter (Acropak 200 capsule filter, Pall corporation). Filters were cleaned with dilute ultrapure HCl (Trace Metal Grade, Fisher Scientific) before use and rinsed with sample prior to subsample collection. The tdFe, tdMn, dFe, and dMn samples were collected into 100 mL acid-washed low-density polyethylene (LDPE) bottles then acidified with 0.5 mL sub-boiled quartz-distilled 6 N HCl (Optima, Fisher Scientific) to pH 1.7 within one hour of sampling. Organic ligand samples were collected into acid-washed 500 mL fluorinated high-density polyethylene (FLPE) bottles and stored frozen (-20ºC). The sFe samples were collected in 125 mL acid washed bottles prior to a second filtration step through a 0.02 µm syringe filter (Anotop filter, Ussher et al., 2010), then acidified to pH 1.7 within one hour of sampling and stored in 60 mL LDPE bottles. Siderophore samples were collected into 4 L acid-washed polycarbonate bottles and extracted onboard within 5 hours of sampling (*section 4.3.4*). Unfiltered samples for tdMn and tdFe analyses were collected into 125 mL acid-washed LDPE bottles and acidified to pH 1.7 within one hour of sampling.

Samples for bacterial abundance were taken from the standard CTD rosette and fixed with 0.25% glutaraldehyde. Samples were stained with SYBR Green I (Invitrogen, Carlsbad, CA) diluted in TRIS buffer for a final concentration of 1/2000 then analyzed on a Easyflow Guava flow cytometer as described in Spietz et al. (2019).

4.3.2 *Iron and manganese analyses*

All samples for tdFe, dFe, tdMn, and dMn were analyzed shipboard within 6-8 hours of sample collection using Flow Injection Analysis (FIA). The dFe, tdFe, dMn, and tdMn samples were measured using direct injection FIA with spectrophotometric detection modified from (Measures et al., 1995) and detailed in (Sedwick et al., 2008) for Fe and from (Resing and Mottl, 1992) for Mn. Detection limits for Mn and Fe were 1 nM and 1.5 nM, respectively. The sFe samples were analyzed using a sector-field inductively coupled plasma mass spectrometer (Element XR, Thermo Fisher Scientific) with an in-line separation-preconcentration system (SeaFAST, SP3, Elemental Scientific) at Old Dominion University. To ensure method accuracy, SAFe D2 and GEOTRACES GSP seawater consensus materials were analyzed and are reported elsewhere (Moore et al. *in prep*). The detection limit was 0.15 nM Fe. The colloidal fraction (0.02-0.2 µm) of Fe was calculated by difference from measurements of dFe and sFe (cFe = dFe-sFe). In a few cases, sFe > dFe, likely as a result of the more sensitive ICP-MS method when compared to FIA. For these cases, all dFe was assumed to be soluble. The percentage of dFe in the soluble fraction was then calculated as %sFe = 100 × sFe/dFe with the remaining percentage as the colloidal contribution (%cFe = 100 – %sFe). Similarly, the percentage of the tdFe pool in the dissolved fraction was calculated as %dFe = 100 × dFe/tdFe.

4.3.3 *Organic iron-binding ligands*

The total pool of dFe-binding organic ligands were measured using competitive ligand exchange adsorptive cathodic stripping voltammetry (CLE-ACSV) (Abualhaija and van den Berg, 2014; Hawkes et al., 2013; Rue and Bruland, 1995). Methods are described in detail elsewhere (Moore et al. *in prep*), but are briefly as follows. All analyses were performed on a controlled growth mercury drop electrode (CGME, Bioanalytical Systems Incorporated) equipped with a platinum auxiliary electrode and an Ag/AgCl reference electrode. Samples for which dFe concentrations were less than 10 nM were first analyzed using a forward titration method (Abualhaija and van den Berg, 2014; Rue and Bruland, 1995) in differential pulse stripping voltammetry mode with 5 µM salicyladoxime as the analytical window. For those samples in which forward titrations showed no curvature or when dFe > 10 nM, reverse titrations were performed (Hawkes et al., 2013) with 1-nitroso-2-naphthol (NN) as the competing ligand and analyzed using linear sweep voltammetry. All peak heights were obtained using ECD-Soft and ligand concentrations and binding strengths were calculated using ProMCC (Omanović et al., 2015) for forward titrations and code from Hawkes et al. (2013) for the reverse titrations. Data from forward and reverse titrations could be accurately compared (Moore et al. *in prep*) and as such are pooled in the following sections.

4.3.4 *Siderophore analyses*

At sea, four liters of 0.2 µm filtered seawater (Acropak 200, Pall Corporation) were collected for siderophore analyses. Prior to solid phase extraction, columns were activated with 2 column volumes of ultrapure methanol (Fisher, Optima grade) and rinsed with 2 column volumes of ultrapure Milli-Q water. Filtered seawater samples were then pumped continuously (~15-18 mL min^{-1}) onto a Bond Elut solid phase extraction column (1g ENV, 6 mL, Agilent Technologies). After solid phase extraction, columns were again rinsed with at least 2 column volumes of Milli-Q water to flush remaining sea salts then stored frozen at -20ºC prior to analysis. In the laboratory, columns were thawed in the dark at room temperature and then rinsed with 2 column volumes of Milli-Q water to remove any additional salts. Columns were then eluted with 12 mL ultrapure methanol into 15 mL acid-washed and methanol-rinsed falcon tubes. Eluent was then concentrated to ~0.5 mL on a vacuum concentrator with a refrigerated vapor trap (SpeedVac, Thermo Scientific) and transferred to clean 2 mL low density polyethylene vials. Extracts were weighed to determine exact volumes then frozen at -20ºC until analysis.

Samples were analyzed using liquid chromatography (LC) coupled to an inductively coupled plasma mass spectrometer (ICP-MS) and an electrospray ionization mass spectrometer (ESI-MS). For each analysis, 100 µL of sample was combined with a spike of 15 µL of 5 µM cyanocobalamin internal standard then injected and separated using a Dionex 3000 LC system equipped with a ZORBAX-SB C18 trap column (0.5x35 mm, 3.5µm, Agilent technologies) and a ZORBBAX-SB C18 working column (0.5x150 mm, 5 µm, Agilent technologies) after the method of (Li et al., 2021). For each sample, a 62.5 µL injection was loaded onto the trap column at 25 µL/min with a 5-minute isocratic elution of solvent C (5% Optima methanol in 95% Milli-Q water, with 5 mM ammonium formate). Samples were then separated on working column using a flow rate of 40 µL/min at 30ºC beginning with a 5-minute isocratic elution of 95% solvent A (Milli-Q water with 5 mM ammonium formate) and 5% solvent B (Optima methanol with 5 mM ammonium formate buffer) followed by a 20 minute gradient from 95% solvent A to 90% solvent B, then a 10-minute isocratic elution at 90% solvent B, followed by a 5 minute gradient from 90% solvent B to 95% solvent B, then a 5-minute isocratic elution at 95% solvent B and a 13 minute conditioning step at 5% solvent B prior to the next injection. The same chromatography structure was used for both LC-ICP-MS and LC-ESI-MS (Boiteau et al., 2016a; Bundy et al., 2018; Park et al., 2023).

Samples were introduced from the LC to the ICP-MS (iCAP-RQ; Thermo Scientific) via a PFA-ST nebulizer (Elemental Scientific) and spray chamber cooled to 2.7ºC. The ICP-MS was equipped with platinum sample and skimmer cones and a 10% oxygen flow was added to the sample chamber to prevent organic matter precipitation on the cones. Analyses were made in kinetic energy discrimination (KED) mode with a helium collision flow rate of 4.0-4.2 mL/min. ^{56}Fe peaks were identified using an in-house R code with a peak threshold of 700 counts above the large background of non-chromatographically resolved dFe-binding organic matter (Figure 4.4A). All identified ^{56}Fe peaks were considered putative siderophores. The large "background" of unresolved dFe-binding organic matter was also quantified and used to estimate the Fe-binding ligand extraction efficiency by comparing the result to CLE-ACSV ligand concentrations (*section 4.3.3*). We operationally defined this mixture as "humic-like" based on its similarity to a Suwannee River Humic Acid standard analyzed under the same instrument conditions. Putative siderophore and humic-like substances concentrations were calculated using a standard curve of ferrioxamine E (25-200 nM) (Boiteau et al., 2016a; Bundy et al., 2018; Park et al., 2023). A 50 nM ferrioxamine E standard followed by a MilliQ blank were analyzed every six samples to adjust for instrument drift and ensure minimal carryover between samples.

To identify putative siderophores, samples were then analyzed using ESI-MS with an Orbitrap (Q-Exactive HF, Thermo Scientific) under the following settings: 3.5 kV spray voltage, 320ºC capillary temperature, 90ºC auxiliary gas heater temperature, S-lens RF level 65, 16 sheath gas, 3 auxiliary gas, and 1 sweep gas (arbitrary units). MS^1 scans were collected in positive mode with a 120,000 mass resolution, a 200-2000 *m/z* range, 1E6 AGC target, and a 100 ms maximum injection times. MS^2 scans were taken in data dependent mode with a 30,000 mass resolution, 2E4 AGC target, 1.0 *m/z* isolation window, 100 ms maximum injection time and a 35% collision energy. An inclusion list of known *m/z* of 530 siderophores was used for MS^2 data collection. Resultant scan data were converted into open source mzXML format using MS Convert (Proteowizard). Data were processed using in-house R-scripts using the XCMS (Boiteau et al., 2016a; Bundy et al., 2018) and RaMS package (Kumler and Ingalls, 2022). Processing was performed using a targeted approach of the 530-siderophore inclusion list, and siderophores were identified using the exact *m/z* matches of known siderophores from MS^1 (± 0.005 Da) and further identified with associated MS^2. This process generated a list of 25 putative siderophores totaling 1,022 features across the 125 samples.

To increase confidence in the putative siderophore list, select samples were brought to the National High Field Magnetic Lab to examine on the 21 Tesla Fourier Transform-Ion Cyclotron Resonance-Mass Spectrometer (FT-ICR-MS, Brüker) (Hendrickson et al., 2015). Samples were introduced to the FT-ICR-MS using the facility's Dionex 3000 LC system under the conditions described earlier with a few small changes. Due to a smaller required injection volume (25 µL), samples were further concentrated on the vacuum concentrator and were prepared by spiking 30 µL of sample with 5µL of 2.5µM cyanocobalamin standard. Additionally, the trap column could not be connected, so samples were immediately sent to the working column and the 5-minute trap column loading step was eliminated from the chromatography. The FT-ICR-MS was run under the following settings: 3.5k spray voltage, 350ºC capillary temperature, 75ºC auxiliary gas heater temperature, S-lens RF level 40, 15 sheath gas, 5 auxiliary gas, and 0 sweep gas. MS^1 scans were collected in positive mode with a 600,000 mass resolution, a 230-1450 *m/z* range, 1E6 AGC target, and a 500 ms maximum inject time. An inclusion list of only the 25 putative siderophores resulting from the Orbitrap analyses was applied. Samples were analyzed directly in Thermo Fisher's XCalibur software. Under the higher resolution of the FT-ICR-MS, only compounds with exact *m/z* within ± 0.0002 Da of known siderophores could be reasonably included. Only 11 of the original 25 putative siderophores fit this criterion, totaling 606 features across the 125 samples. The 11 remaining compounds were then further checked for reasonability of retention times and carbon series, resulting in a final list of 8 putative siderophores, totaling 561 features across the dataset. MS^1 scans from FT-ICR-MS analyses were aligned with Orbitrap scans using the internal standard cyanocobalamin peaks.

Following the FT-ICR-MS analyses, the ESI-MS data was filtered to include only the 8 putative siderophore identities determined reasonable under the stricter *m/z* and carbon series criteria. These ESI-MS data were then used to assign confidence levels to the remaining 561 features associated with the 8 putative siderophores using a combination of MS^1 and MS^2 scans. Although all features associated with the 8 putative siderophores were considered high confidence due to the more rigorous *m/z* criteria provided by FT-ICR analysis, individual confidence levels were assigned to features based on Park et al. (2023), previously modified from (Sumner et al., 2007) to maintain consistency with other siderophore studies. Level one confidence was assigned to peaks with at least one of the 5 most abundant fragments in the MS^2 scan matching literature spectra (55 compounds). Level two confidence was assigned to peaks that had retention time within ± 30 seconds and *m/z* within ± 0.0015 Da of a level one peak in another sample (12 compounds). Level three confidence was assigned to peaks with at least one of the 5 most abundant fragments in the MS^2 scan matching in-silico fragmentation predictions (CFMID and MetFrag; 96 compounds). Level four confidence was assigned to either features with a *m/z* within ± 0.0015 Da and a retention time within ± 30 seconds of a level three feature in another sample (excepting broad peak hyalachelin where criterion was ± 90 seconds) or features belonging to putative siderophores with no associated MS^2 data or no fragments matching literature spectra (398 compounds). Scans were aligned between samples using internal standard cyanocobalamin peaks.

For each sample, MS^1 scans from the ESI-MS were aligned with the ^{56}Fe trace from the ICP-MS using the internal standard cyanocobalamin. Peaks within ± 15 seconds were considered a match and the ^{56}Fe peak areas were used to quantify the putative siderophores identified using ESI-MS. 37 features could be matched to a ^{56}Fe peak.

4.4 RESULTS

This section first defines the different types of environments that were sampled along the axis and characterizes the samples found at each cast site accordingly (*section 4.4.1*). Refer to Moore et al. (*in prep*) for a more detailed discussion of the sampling designations. Flow cytometry results of bacterial cell counts are then presented (*section 4.4.2*), followed by the physical and chemical speciation of Fe, including size fractionation and organic dFe-binding ligand data (*section 4.4.3*). Finally, a summary of the concentration and identities of siderophores found in the dataset (*section 4.4.4*) is presented.

4.4.1 *Oceanographic setting*

Ten sites were visited between 16ºS and 18ºS near the SEPR ultrafast spreading center (Figure 4.1D). Nine of these sites were located on-axis, while PJ was located 11 km off-axis west of Bio to examine the development of the distal plume. An additional station, Station 18, was also sampled slightly outside this section of ridge crest at 15ºS. This station was revisited from a previous U.S. GEOTRACES GP16 expedition as an example of an aged composite plume (Kipp et al., 2018; Moffett and German, 2018). Sites along the main study region were chosen to capture a wide range of hydrothermal environments including high-temperature venting, low-temperature "diffuse" venting, and sites containing a neutrally buoyant plume (Table 4.1). Criteria for environmental designations and sample classifications are presented in detail elsewhere (Moore et al. *in prep*), but are briefly as follows. High-particle environments, including high temperature venting and the neutrally buoyant plume, were defined using a combination of particle anomalies (dNTU) and principal component analysis of select chemical variables that were found to contribute the most to the variance between samples and stations. These variables included total particulate sulfur (pS_{tot}), particulate copper (pCu), dissolved hydrogen (dH_2), dissolved methane (dCH_4), tdFe and tdMn. Low-particle environments, including diffuse vents and deep background seawater, were similarly classified using principal component analysis, although pCu was removed as a variable. Deep background samples were those considered to have minimal hydrothermal influence, although the pervasiveness of hydrothermal activity along this ridge largely prevents true on-axis background samples (Moore et al. *in prep*).

The sampling sites along axis exhibited a high degree of spatial and temporal variability (Figure 4.1A-C, Moore et al. *in prep*). A neutrally buoyant plume overlayed all sampling sites, although it varied widely in intensity and vertical extent (Figure 4.1A-B). Near the seafloor, sites Flo, Bart, North, Purple Haze, and 16°43' had evidence of diffuse flow, while sites Lava and Macro showed evidence of high-temperature flow (Moore et al. *in prep*). Sites North, Macro, and Lava were particularly notable for their large near seafloor ORP anomalies, suggesting very fresh hydrothermal fluid (Figure 4.1C). Sites PJ and Station 18 did not have associated near-seafloor anomalies, but did contain well-defined neutrally buoyant plumes.

4.4.2 *Flow cytometry*

Flow cytometry samples (Figure 4.2G) were taken using the standard CTD rosette on separate casts from the trace metal and ligand samples. As a result, the flow cytometry dataset has a different spatial coverage than the samples that were obtained from the trace metal rosette. 42 of the 64 total flow cytometry samples were aligned with samples from the trace metal rosette based on depth and tdFe and dMn concentrations. Only samples for which the percent error was less than 50% between the measured concentrations of tdFe and dMn in the standard and trace metal rosettes at comparable depths were considered a reasonable match. For Station 18, tdMn was evaluated instead of dMn because dMn was not measured on the Station 18 flow cytometry cast. Depths and dNTU values were also compared to ensure similar plume environments were matched between samples and casts.

The flow cytometry dataset was classified into broad environmental groups, including the neutrally buoyant plume, background, buoyant fluid, and non-buoyant near seafloor samples.

Bacterial cell abundances were highest in the neutrally buoyant plume (5.4 x 10^4 ± 3.3 x 10^4 cell/mL) and buoyant fluid (4.6 x 10^4 ± 1.6 x 10^4 cells/mL), both of which had significantly greater cell counts (Mann–Whitney *U*-Test, $p < 0.02$) than the background (2.0 x 10^4 ± 5.4 x 10^3 cells/mL) and near seafloor samples (2.6 x 10^4 ± 8.0 x 10^3 cells/mL). Cell counts in samples from the neutrally buoyant plume at PJ were not significantly different from the on-axis neutrally buoyant plume samples (Mann–Whitney *U*-Test, $p = 0.53$). However, cell counts in the neutrally buoyant plume from Station 18 (8.5 x 10^4 ± 2.2 x 10^4 cells/mL) were significantly higher than those from the on-axis neutrally buoyant plume (Mann–Whitney *U*-Test, $p = 0.02$).

4.4.3 *Physical and chemical iron speciation*

There was large variability in dFe and pFe concentrations that could be attributed to the diversity and density of vent sites along the ridge axis and their heterogeneous contributions to the overlying neutrally buoyant plume (Figure 4.1A-C). The pFe concentrations (Figure 4.2A) ranged from 199.5-2533.1 nM in high temperature sites ($n = 7$), 11.0-64.0 nM ($n = 19$) in diffuse sites, and 29.0-713.1 nM ($n = 25$) in the center of the neutrally buoyant plume across all on-axis sites. The pFe concentrations in the neutrally buoyant plume at PJ (192.1-1353.6 nM, $n = 5$) and Station 18 (40.0-211.3 nM, $n = 9$) were in a similar range to those of the on-axis plumes. However, pFe concentrations at Station 18 were somewhat lower than those at PJ.

The dFe concentrations (Figure 4.2B) were also highly variable, ranging from 4.9-344.5 nM ($n = 7$) in high-temperature samples, 0.3-12.2 nM ($n = 20$) in low temperature samples, and 1.3-111.2 nM ($n = 27$) in the center of the on-axis neutrally buoyant plume. The dFe concentrations at PJ (6.6-17.8 nM, $n = 5$) and Station 18 (1.0-1.9 nM, $n = 9$) were within the range of dFe measured in the on-axis neutrally buoyant plumes, although dFe concentrations at Station 18 were generally low.

The majority of the dFe was in the colloidal fraction (Figure 4.2C). On-axis, cFe contributed 84 ± 38% (*n* = 96) of dFe with the remaining fraction as sFe. The colloidal fraction varied between environments however, comprising only 70 ± 35% of dFe (*n* = 20) in diffuse samples compared to 90 ± 8% of dFe (*n* = 27) in the center of the on-axis neutrally buoyant plume and 94 ± 7% of dFe (*n* = 7) in high-temperature samples. The colloidal fraction of dFe in the neutrally buoyant plume at PJ was high (92 ± 2%, *n* = 5) compared to Station 18 (88 ± 4%, *n* = 9), although both stations had similar values to the on-axis plumes.

Dissolved organic Fe-binding ligand concentrations (L, Figure 4.2F) and average conditional stability constants (log $K_{FeL,Fe'}^{cond}$, Figure 4.2G) also showed a high degree of variation. On axis, ligand concentrations ranged from 4-202 nM in high temperature samples (*n* = 3), 0.3-6.7 nM in low temperature samples (*n* = 13), and 1.7-22.6 nM in the center of the neutrally-buoyant plume (*n* = 10). The $K_{FeL,Fe'}^{cond}$values also encompassed a wide range, spanning the three operational ligand strength classifications including L_1 ($12 < K_{FeL,Fe'}^{cond}$), L_2 ($11< K_{FeL,Fe'}^{cond} < 12$), and L_3 ($K_{FeL,Fe'}^{cond} < 11$) (Gledhill and Buck, 2012). High-temperature samples only included L_3 ligands ($10.2 < \log K_{FeL,Fe'}^{cond} < 10.3$), while samples from low-temperature ($9.4 < \log K_{FeL,Fe'}^{cond} < 12.7$) and the center neutrally buoyant plume ($10.0 < \log K_{FeL,Fe'}^{cond} < 12.0$) environments spanned the full L_1-L_3 operational ligand class range. The neutrally buoyant plumes at PJ and Station 18 had similar ligand concentrations (PJ = 2.4-6.2 nM, Station 18 = 1.7-4.9 nM) and conditional stability constants (PJ = 10.0-11.1, Station 18 = 10.6-12.0) as the on-axis neutrally buoyant plumes.

4.4.4 *Siderophore distributions*

4.4.4.1 Siderophore concentrations

Total dissolved siderophore concentrations varied considerably in samples collected on-axis (Figure 4.2H). Dissolved siderophore concentrations ranged from 0-41 pM with an average of 4.7 ± 5.1 pM in all on-axis samples ($n = 101$). Average siderophore concentrations did not differ significantly (Mann–Whitney *U*-Test, $p > 0.05$) between most sampling environments despite significant differences in dFe and pFe. The exception was for high temperature samples (average total siderophore concentrations = 1.5 ± 1.7 pM), which had significantly lower siderophore concentrations (Mann–Whitney *U*-Test, $p < 0.03$) than either diffuse samples (6.1 ± 5.3 pM) or background samples (5.7 ± 6.0 pM). The neutrally buoyant plume samples exhibited the highest variation in siderophore concentration, averaging 4.9 ± 7.1 pM.

Differences in siderophore concentrations were primarily driven by site rather than vent environment (Figure 4.2E). For example, siderophore concentrations at Micro (19.5 ± 12.4 pM) were significantly higher than any other site (Mann–Whitney *U*-Test, $p < 0.03$). Siderophore concentrations at Bart (5.2 ± 3.4 pM) and 16°43’ (7.9 ± 5.8 pM) were only significantly higher (Mann–Whitney *U*-Test, $p < 0.03$) than Bio (2.1 ± 2.1 pM), Lava (2.3 ± 2.3 pM), and Purple Haze (1.6 ± 1.7 pM). Purple Haze had the lowest average siderophore concentrations in the dataset, significantly lower (Mann–Whitney *U*-Test, $p < 0.04$) than those at Micro, Bart, 16°43’, North (4.9 ± 4.7 pM), and Macro (5.2 ± 5.3 pM). Siderophore concentrations at Bio, Macro, Lava, North, and Flo (4.4 ± 5.0 pM) were statistically indistinguishable ($p > 0.05$). Siderophore concentrations at PJ (2.1 ± 1.8 pM) were significantly lower than those measured at Micro, Bart, and 16° 43’ although siderophore concentrations at Station 18 (6.0 ± 10.4 pM) were only significantly less than Micro (Mann–Whitney *U*-Test, $p < 0.02$).

4.4.4.2 Siderophore identities

Eight unique siderophores were detected with high confidence (Levels 1-4; *section 4.3.4*) in the dataset (Figure 4.3-Figure 4.4). Of these, tenacibactin C, synechobactin C11, and hyalachelin A were found most often (in 100%, 98% and 86% of samples (*n* = 125), respectively). These siderophores were ubiquitous, and showed no specific pattern with environment or site, and were found exclusively in their apo, or Fe-free form. A fourth siderophore, acremonpeptide B was also identified exclusively in the apo form. Like the other apo siderophores, acremonpeptide B was not unique to certain environments or sites, although it was found less frequently (35% of samples).

In addition to this suite of Fe-free siderophores, several Fe-bound siderophores were detected including oxahomorhizoferrin, avenic acid, and aspergillic acid. Unlike the apo siderophores, the Fe-bound siderophores had specific patterns with site and/or vent environments. Oxahomorhizoferrin was the most frequently observed Fe-bound siderophore, and was detected in 54% of samples. Oxahomorhizoferrin was particularly prevalent in the low-temperature environment, detected in 75% of those samples (*n* = 20), and at sites 16°43’, North, Flo, Bio, and Station 18. Avenic acid was detected in 41% of samples, and was primarily found at sites 16º43’, PJ, and Station 18. Although avenic acid was detected across several environments, it was particularly prevalent in the deep background, found in 71% of background samples (*n* = 17). Aspergillic acid was detected less often (31% of samples) but was identified most often at sites Bio and Flo. Fe-talarazine was also detected infrequently, identified in only 7 samples across the dataset (Figure 4.3).

4.5 DISCUSSION

4.5.1 *Siderophore distributions*

This dataset greatly expands existing siderophore distribution data beyond the more extensively studied upper ocean (< 1,500 m; (Boiteau et al., 2016a, 2019; Bundy et al., 2018; Mawji et al., 2011; Moore et al., 2021; Park et al., 2023) and extends the measurements into the higher-Fe deep ocean (2,200 – 2,650 m). Siderophores were detected in every sample, with an average concentration of 4.9 ± 6.4 pM (0-41 pM) across all sites. These results are comparable to and often exceed siderophore concentrations that have been measured in the upper ocean (< 400 m, 3.4 ± 4.3 pM, 0-21.1 pM, Park et al., 2023). Unlike the surface ocean however, we sampled across a much larger dFe gradient, ranging from < 1 nM to 345 nM, which is over 1000x more concentrated than typical surface ocean measurements (0.1-1 nM) (Hatta et al., 2015; Park et al., 2023). The percentage of dFe bound to siderophores was therefore smaller in this dataset ([siderophore]/[dFe] × 100 = 0.24 ± 0.72%, range 0 - 4.9%) when compared to the surface ocean (average 2.4 ± 5.4%, range 0 – 30%; Park et al., 2023). However, this is likely a low estimate of siderophore impact because the solid phase extraction method used to concentrate siderophores only captured 11.9 ± 13.0% (0.1 - 86.7%, $n = 62$) of the total Fe-binding ligands measured in this dataset (Moore et al. *in prep*). The ~10% extraction efficiency typical for this method (Bundy et al., 2018) makes it likely that siderophore concentrations are consistently underestimated.

We were able to quantify a total of 321 discrete ^{56}Fe peaks above the large complex background of uncharacterized Fe-binding organic ligands present at each site (Figure 4.4A). However, only 37 of these ^{56}Fe peaks could be identified with high confidence using ESI-MS and the remaining unidentified peaks from ICP-MS were classified as putative siderophores. Because all known siderophores bind a single Fe atom (Hider and Kong, 2010), ^{56}Fe peaks representing putative siderophores can be quantified and translated into the siderophore concentrations reported here. However, siderophores identified using ESI-MS without a corresponding ICP-MS ^{56}Fe peak cannot be accurately quantified. Ionization efficiencies vary widely by compound in ESI-MS, and very few (< 10) siderophores are commercially available for use as standards. Thus, the putative siderophores we quantify via ICP-MS (Figure 4.2E) and the siderophores we qualitatively identified with high confidence in the ESI-MS (Figure 4.4) represent different but overlapping pools.

We found many more putative siderophores by ICP-MS than were identified by ESI-MS. Although we performed a wide targeted search for 530 known siderophores using ESI-MS, it is highly likely that deep sea and hydrothermal microbial communities produce suites of novel siderophores that have not yet been molecularly characterized. These unknown compounds may therefore manifest as unidentified putative siderophores in the ^{56}Fe ICP-MS trace. Future work may be able to use untargeted mass spectrometry strategies to identify these compounds (e.g. Baars et al., 2014). However, previous studies using this strategy have relied on natural abundance Fe isotope patterns to identify compounds (e.g. Boiteau et al., 2019; Boiteau and Repeta, 2015; Velasquez et al., 2011, 2016). In this dataset, complex isotope fractionation by hydrothermal processes (Bennett et al., 2009) or siderophore complexation (Morgan et al., 2010) may complicate the use of the natural abundance method.

The presence of so many unidentified putative siderophore peaks cannot, however, explain why so few of the ESI-MS identified peaks appear on the ^{56}Fe ICP trace. The mismatch is instead largely because most siderophore peaks identified by ESI-MS in this dataset (71%) were in their Fe-free, or apo form. It is unclear why so many of the detected siderophores were Fe-free. These compounds may naturally be Fe-free in the samples, but it could also be a result of Fe-loss during sample processing or ionization. Interestingly, 34 apo-form peaks (18 synechobactin C11 and 16 tenacibactin C) identified by ESI-MS could be matched to Fe peaks in the ICP-MS dataset. This could occur if the corresponding Fe-bound form of the siderophore was also present and detected via ICP-MS, but was too low in concentration for ESI-MS detection. Only three Fe-bound siderophores detected by ESI-MS (1 aspergillic acid and 2 oxahomorhizoferrin) were successfully matched to peaks in the ^{56}Fe ICP-MS trace. It is likely that the large background of uncharacterized Fe-binding organic compounds masks individual peak signals in the ^{56}Fe ICP-MS trace, preventing further matches to the ESI-MS peaks.

4.5.2 *Environmental and regional provenance of siderophores*

The suite of siderophores identified in this dataset was notably different from what has been documented in most previous siderophore studies to date (Boiteau et al., 2016a, 2019; Bundy et al., 2018; Mawji et al., 2008; Moore et al., 2021; Park et al., 2023; Velasquez et al., 2011). Indeed, all compounds identified in this study except one have either never been detected in the ocean before or have only been found in the single other hydrothermal siderophore study (Hoffman et al., 2023). Synechobactin C11, detected in nearly every sample in this dataset, was the sole exception. Synechobactins were first structurally characterized in a *Synechococcus sp.* PCC P7002 culture, originally isolated from marine mud (Ito and Butler, 2005). Since then, six variants of synechobactin have been identified and detected in several oceanic environments (Boiteau and Repeta, 2015), including the surface Pacific (< 150 m) (Bundy et al., 2018; Park et al., 2023), an oxygen deficient zone (Moore et al., 2021), a nepheloid layer along the California Current (Boiteau et al., 2019), and Broken Spur hydrothermal field on the Mid-Atlantic Ridge (Hoffman et al., 2023). Several of these environments share key characteristics with the sampling locations in this study, so the ubiquitous presence of synechobactin C11 in our dataset is perhaps unsurprising. Both the Broken Spur hydrothermal field and the nepheloid layer in the California Current have high concentrations of dFe (1-21 nM and 10-17, nM respectively) that are within the range of several hydrothermal environments sampled in this study (Boiteau et al., 2019; Hoffman et al., 2023). Conversely, the oxygen deficient zone study found synechobactins C9 and C10 in an environment with a lower dFe range (1-5 nM) (Moore et al., 2021), which was similar to many background samples in this dataset. It has also been proposed that synechobactins might be more common in the deep ocean (Boiteau et al., 2019), where they are not subject to photodegradation.

The other siderophores in this dataset showed a high degree of similarity to those identified in hydrothermal systems along the Mid-Atlantic Ridge (Hoffman et al., 2023). Common siderophores in our dataset, including acremonpeptide B, avenic acid, oxahomorhizoferrin, and aspergillic acid were also detected along the Mid-Atlantic Ridge. Additionally, members of the tenacibactin siderophore family were found in both studies, although the variants differed slightly (e.g. tenacibactin B vs. tenacibactin C). Only hyalachelin A and talarazine C were unique to the SEPR, and of these hyalachelin alone was widespread. The high degree of similarity in siderophores between the two ridge systems suggests an overlap in microbial community taxonomy or similarly evolved Fe acquisition strategies for hydrothermal bacteria. Notably, both tenacibactins and acremonpeptide B were originally isolated from marine cultures, a marine bacterium *Tenacibaculum* sp. A4K-17 (Jang et al., 2007) and marine fungus *Acremonium persicinum* SCSIO 115 (Luo et al., 2019), respectively.

Most siderophores isolated from marine bacteria are amphiphilic (Sandy and Butler, 2009), containing a polar head group with one or more fatty-acid side chains that can be tethered to the cell membrane (Martinez et al., 2003) to prevent diffusive loss of the siderophore in the dilute marine environment (Vraspir and Butler, 2009). This contrasts with terrestrial systems, where hydrophilic and non-amphiphilic siderophores are more common (Sandy and Butler, 2009). Nevertheless, seven of the eight siderophores identified in this study were hydrophilic (Figure 4.4C-G). A hydrophilic suite of siderophores is consistent, however, with previous work that found a greater abundance of hydrophilic siderophores in Fe-rich coastal regions while amphiphilic siderophores were more strongly associated with lower Fe systems (Boiteau et al., 2016a). The prevalence of hydrophilic siderophores in the SEPR samples suggests that diffusive loss of siderophores may not be a critical cost to microbial communities living in hydrothermal environments, especially considering that hydrophilic siderophores appear to have the advantage of possessing stronger Fe-binding constants when compared to their amphiphilic counterparts (Bundy et al., 2018). Stronger binding constants may be particularly beneficial in the high-particle environments of hydrothermal systems, in which siderophores with particularly strong binding constants may be capable of solubilizing Fe from particles (Kraemer et al., 2005; Manck et al., 2022). While hydrophilic siderophores were overwhelmingly the most common type of siderophore encountered along the SEPR, accounting for 78% of the identified features, only 62% of identified features in hydrothermal samples along the Mid-Atlantic Ridge were hydrophilic (Hoffman et al., 2023). Therefore, despite similarities in siderophore identities between the two ridge sectors, there is a larger preference for hydrophilic siderophores along the SEPR.

In addition to varied hydrophilicity, the eight siderophores identified in this study had diverse Fe-binding functional groups including five hydroxamate siderophores (Figure 4.4C-E, H and talarazine c), two carboxylate siderophores (Figure 4.4F-G), and one mixed-group compound (Figure 4.4I). Hydroxamate siderophores are the most common siderophore identified in the ocean to date (e.g. ferrioxamines and amphibactins) (Boiteau et al., 2019; Bundy et al., 2018; Park et al., 2023), and they were found in every sample in this dataset, with no pattern based on site or environment. However, the two carboxylate compounds, avenic acid and oxahomorhizoferrin, were associated primarily with background and low-temperature venting environments, respectively. This is consistent with siderophore results from the Mid-Atlantic Ridge (Hoffman et al., 2023) in which carboxylate compounds were primarily identified in low-temperature venting environments. Carboxylate siderophores therefore seem to be a preferred microbial Fe-acquisition strategy under the low-Fe conditions in background and low-temperature environments, particularly in comparison to their high-Fe neutrally buoyant and buoyant plume counterparts. Carboxylate siderophores are also far more prevalent in the hydrothermal datasets than the surface ocean (Boiteau et al., 2019; Bundy et al., 2018; Park et al., 2023), possibly due to their photo reactivity. Carboxylate siderophores readily photolyze, weakening their Fe-binding capacities in the sunlit surface ocean (Barbeau et al., 2001; Butler et al., 2021; Vraspir and Butler, 2009). In the deep ocean however, these siderophores will be far more stable, perhaps contributing to their greater prevalence in the hydrothermal datasets.

4.5.3 *Siderophores and the in-situ microbial community*

The high concentrations of siderophores measured in this dataset suggest that siderophores are an important microbial Fe acquisition strategy throughout the deep ocean, independent of dFe concentration or amount of hydrothermal influence. Indeed, there were no significant differences in siderophore concentrations between diffuse, neutrally-buoyant plume, and background samples (*section 4.4.4.1*). This suggests that in-situ dFe concentration is not the only driver of siderophore concentration despite its role in the regulation of siderophore biosynthesis pathways (Miethke and Marahiel, 2007; Troxell and Hassan, 2013). This observation was also noted across a dFe gradient in the upper ocean of the North Pacific, where no correlation between siderophore and dFe concentrations was observed (Park et al., 2023). Thus, siderophore production is likely a common microbial Fe acquisition strategy across many oceanic environments spanning a large range of dFe concentrations (Boiteau et al., 2019; Bundy et al., 2018; Li et al., 2014; Moore et al., 2021; Park et al., 2023). Indeed, (Garber et al., 2020) examined metagenomes from marine organisms across the surface, deep ocean, and groundwater environments and found siderophore biosynthesis pathways in all marine environments examined.

Siderophore concentrations varied more significantly between stations than between environments defined by hydrothermal influence (*section 4.4.4.1)*. This suggests that the variation in siderophore concentration may be the result of factors other than dFe, such as changes in the microbial community. Sites Micro, 16º 43' and Bart had the highest average siderophore concentrations of the dataset (Micro 19.5 ± 12.4 pM, 16º43' 7.9 ± 5.8 pM, Bart 5.2 ± 3.4 pM) when averaged across the full cast (2,200 m – seafloor). While these sites were neither chemically similar nor co-located, all three sites were associated with low-temperature venting in their deepest samples (*section 4.4.1*, Moore et al. *in prep*). Low-temperature venting has been shown to support robust and diverse biological communities with connections to the subseafloor (Butterfield et al., 2004; Früh-Green et al., 2022; Opatkiewicz et al., 2009; Perner et al., 2010). These communities have higher bacterial abundances than background seawater or high-temperature fluids (Butterfield et al., 2004), which could lead to greater local siderophore production. Additionally, entrainment of bacteria present near low-temperature vents into the neutrally buoyant plume (e.g. Jackson et al., 2010) could potentially stimulate siderophore production shallower in the water column.

While average cell abundances in low-temperature samples ($3.2 \times 10^4 \pm 7.0 \times 10^3$ cells/mL, $n = 10$) were higher than those in the background ($2.1 \times 10^4 \pm 5.7 \times 10^3$ cells/mL, $n = 4$, Mann–Whitney U-Test, $p = 0.08$), cell abundances in low-temperature samples were significantly less (Mann–Whitney U-Test, $p < 0.002$) than those in the center of the neutrally buoyant plume ($6.1 \times 10^4 \pm 2.4 \times 10^4$ cells/mL, $n = 14$). Furthermore, there was no correlation between cell abundances and siderophore concentrations for any site or environment in this dataset. As a result, increased microbial activity associated with low-temperature venting cannot adequately explain the unusually high siderophore concentrations observed throughout the deep water column at Micro, 16º43’, and Bart.

This result does not however, preclude a microbial explanation for the high siderophore concentrations at these sites, or conversely, the very low siderophore concentrations at a different low-temperature site, Purple Haze (1.6 ± 1.7 pM). Distinct community structures could result in variable rates of siderophore production or different compounds being produced. Microbial communities in low-temperature venting habitats exhibit large spatial variability, even within the same venting site (Fortunato et al., 2018; Perner et al., 2010), and vent chemistry has a large impact on microbial community structure and metabolism (Früh-Green et al., 2022). Additionally, siderophores may be cycled rapidly in a microbial community (Bundy et al. 2023), leading to only small measurable quantities of siderophores in the dissolved phase that are largely independent of total bacteria abundances. Finally, the flow cytometry and siderophore measurements were taken from separate sampling casts. As a result, only 42 of the 125 siderophore samples could be matched to flow cytometry data, and it is likely that different communities were sampled on each cast due to the high temporal variability of on-axis hydrothermal activity.

Determining the distribution of siderophore identities is particularly important because siderophores are microbially-produced and can be tied back to the specific communities that produced them (e.g. Park et al., 2023). Siderophores thus provide insight into the Fe acquisition strategies of the microbial community, particularly if siderophore uptake and biosynthesis genes are known (Garber et al., 2020; Li et al., 2014; Park et al., 2023). While genomic data is not yet available for our dataset, previous taxonomic (Zeng et al., 2021 and references therein) and genomic results (Connell et al., 2009; Homann et al., 2009; Li et al., 2014) from a diverse array of venting systems suggest that siderophores are a common Fe acquisition strategy in hydrothermal systems. For instance, work identifying Fe uptake and storage genes in bacterial communities from Guaymas Basin show ample evidence for both siderophore production and siderophore transport in that hydrothermal system (Li et al., 2014). On a broader level, taxonomic results for a diverse array of venting systems consistently identify clades of bacteria and fungi that contain known siderophore-producers (Burgaud et al., 2009; Connell et al., 2009; Zeng et al., 2021; Zhou et al., 2022).

Many of the siderophore-producing clades identified previously in hydrothermal systems (Zeng et al., 2021) contain bacteria known to produce the siderophores identified in our dataset. Myxococcales, for instance, are frequently a component of hydrothermal microbial communities (Li et al., 2014; Zhou et al., 2022) and contain members capable of producing hyalachelin A (Nadmid et al., 2014), one of the most common siderophores observed in our dataset. Similarly, Flavobacteria have been identified in vent sites, members from which the siderophore tenacibactin C has been isolated (Hoffman et al., 2023; Jang et al., 2007; Li et al., 2014).

Interestingly, several of the identified siderophores, including aspergillic acid, talarazine C, oxahomorhizoferrin, and acremonpeptide B, were first isolated from fungi. Fungal production of siderophores near hydrothermal systems has precedent, having been documented in fungal isolates from Vailulu'u Seamount in Samoa, although they have not been structurally characterized (Connell et al., 2009). Additionally, several fungal strains belonging to the siderophore-producing orders Eurotiales and Hypocreales were previously identified in hydrothermal systems, including members of Hypocreales at site Elsa along the Northern East Pacific Rise 13ºN (Burgaud et al., 2009). Members of Hypocreales have been shown to produce acremonpeptide B (Luo et al., 2019), while members of Eurotiales have been associated with the production of aspergillic acid (Lebar et al., 2018) and talarazine C (Kalansuriya et al., 2017). Indeed, members of the Aspergillius genus, the main genus associated with aspergillic acid producers (Lebar et al., 2018), have been identified in hydrothermal systems (Pang et al., 2020) as have members of the Acremonium genus, the primary genus associated with acremonpeptide production (Le Calvez et al., 2009). This raises the intriguing possibility for fungi to be impacting Fe speciation in hydrothermal vents. The producers of these compounds are not, however, limited to fungi because siderophores are frequently identified in very different organisms than those from which they were first isolated. Several siderophores originally isolated from fungi (e.g. ferrichromes) have later been shown to be biosynthesized by marine bacteria, and this may be the case here (e.g. Winkelmann and Braun, 1981). Several of the siderophores identified in this study have not yet been isolated from members of clades found near hydrothermal vents. These include oxahomorhizoferrin, avenic acid, and synechobactin C11, first isolated from Mucorales fungi (Drechsel et al., 1995), plant root washings (Tsednee et al., 2012), and cyanobacteria (Ito and Butler, 2005), respectively. It is possible that these clades haven't been identified yet or are being produced by different organisms from which they were first isolated.

Identifying siderophores in such a high Fe environment and finding siderophores that have never been found in the ocean before is an exciting result, and points to unique processes occurring in hydrothermal systems with respect to Fe cycling. The measured concentrations of siderophores in this study likely only offer a snapshot in time of multiple complex processes, and yet the concentration of siderophores in this dataset were on par and exceeded those from surface ocean studies (Boiteau et al., 2016a, 2019; Bundy et al., 2018; Park et al., 2023). It is also notable that bacteria abundances in the hydrothermal samples were an order of magnitude lower (~$1\text{x}10^4$-$1\text{x}10^5$ cells/mL) than those in the surface ocean ($\geq 1\text{x}10^6$ cells/mL) (Park et al., 2023). This suggests that deep sea microbial communities either produce more siderophores on a per cell basis than surface communities, or that siderophores are cycled less rapidly, yielding larger standing stocks of dissolved siderophores. Regardless, the high siderophore concentrations relative to bacteria abundances are compelling, and highlight the importance of siderophores as a microbial Fe uptake strategy in hydrothermal environments and the deep ocean.

4.5.4 *The role of siderophores in the physical and chemical speciation of dissolved iron*

The dFe concentrations in this study span a much larger range (0-345 nM) than most siderophore studies performed in the low Fe surface ocean (< 0.5 nM). Despite this, siderophore concentrations were comparable between the two environments, which is incongruous with the expectation of siderophore production mechanics. Siderophore production is regulated by cellular Fe concentrations such that siderophore synthesis is downregulated under Fe replete conditions (Miethke and Marahiel, 2007; Troxell and Hassan, 2013). Therefore, the ubiquity of siderophores in this study, even in the high Fe concentrations found in hydrothermal plumes, is unanticipated and suggests a few possible explanations. The first is that Fe requirements may be exceptionally high for microorganisms in hydrothermal environments, necessitating the need for competitive Fe acquisition. However, the competition for Fe by bacteria is somewhat unlikely in our dataset, given the relatively low abundances of bacteria. A second possibility is that despite high dFe concentrations, most of the dFe in hydrothermal plumes is not readily accessible, necessitating siderophore production to obtain scarce bioavailable Fe resources. Size fractionation data of the dFe pool supports this second explanation.

Most samples in this dataset are considered Fe replete from a microbial standpoint based on dFe concentrations alone (21.6 ± 51.9 nM, $n = 109$). However, the size fractionation data suggests that much of this dFe may not be microbially accessible. The dFe pool can be divided into the sFe, which is considered the most biologically labile source of Fe (Morel et al., 2008), and cFe, which is anticipated to be somewhat less bioavailable (Chen et al., 2003; Rich and Morel, 1990). Along the SEPR, cFe dominated the dFe pool, accounting for 82 ± 23% ($n = 107$) of dFe (Figure 4.2C). The remaining sFe averaged only 18% or 1.22 ± 1.91 nM. The low proportion of the more labile sFe pool relative to cFe might help explain the presence of siderophores in the ostensibly Fe-rich hydrothermal environments. Bacteria may only have access to a very small proportion of the dFe pool, necessitating siderophore production to maintain an adequate bioavailable Fe fraction.

The cFe pool is unlikely to be entirely inaccessible to microbial uptake though. Indeed, studies from the same region estimate that approximately 70% of cFe is organic (Moore et al. *in prep*), thereby enhancing its lability (Chen et al., 2003). Organic cFe is still considered less bioavailable than sFe (Chen et al., 2003; Morel et al., 2008), so siderophore production may be an essential strategy for accessing organic cFe. Model marine heterotrophic bacteria have been shown to use siderophores to transform otherwise refractory Fe pools into more accessible forms, including cFe (Manck et al., 2022). In the high colloidal and particulate Fe environments of hydrothermal systems, siderophores could be used to maintain an adequate sFe fraction by solubilizing the larger cFe or pFe fractions. The small, hydrophilic siderophores identified in this study (Figure 4.4C-G) support this explanation because they are likely components of the sFe pool. Furthermore, when compared to the surface ocean, the cFe fraction in this dataset is much larger (%cFe; surface Pacific ~50%, >2000 m SEPR 82%) (Roshan et al., 2020). This results in more comparable sFe concentrations between the surface (0.1-0.3 nM; Roshan et al., 2020) and deep ocean environments (sFe; ~1 nM). Thus, it is possible that the similar siderophore concentrations between the surface and deep ocean are helping to maintain a relatively steady consistent bioavailable sFe pool.

4.5.5 *Siderophores and the bulk ligand pool*

In addition to potentially stabilizing a consistent concentration of sFe, siderophores also have a measurable impact on the total organic Fe-binding ligand pool. Organic Fe-binding ligands are the primary Fe stabilization mechanism in much of the ocean, maintaining dFe concentrations above the small (~0.02 nM) inorganic solubility limit (Gledhill and Buck, 2012; Gledhill and van den Berg, 1994; Liu and Millero, 2002; Rue and Bruland, 1995). The organic ligands are heterogeneous and span both the soluble and colloidal size fractions as a function of their relative sizes and polarities (Boye et al., 2010; Gledhill and Buck, 2012). In hydrothermal systems however, inputs of Fe up to one million times more concentrated than background seawater (Von Damm, 1990) outpace available organic ligands, even when in-situ microbial production of ligands is considered. As a result, only a fraction of dFe is bound to organic ligands while the remainder is likely stabilized as inorganic colloids (Fitzsimmons et al., 2017; Moore et al. *in prep*). In this dataset, organic ligands stabilized an average of 83 ± 17% (46-100%, *n* = 13) of dFe in low-temperature hydrothermal samples and 70 ± 22% (41-100%, *n* = 11) of dFe in neutrally buoyant plume samples. In on-axis background samples where dFe was lower in concentration, an average of 98 ± 5% of dFe (83-100%, $n = 9$) was bound to organic ligands. Notably, organic ligands stabilized ~100% of sFe regardless of environment.

Siderophores account for only a small fraction of this total ligand pool (0-1.9%, $n = 63$). However, the extremely high Fe affinities of siderophores (log $K_{FeL,Fe'}^{cond} > 12$) have long been hypothesized to disproportionately impact the average binding strength of the entire organic ligand pool, particularly in the case where the other ligands present are relatively weak (Bundy et al., 2014; Gledhill and Buck, 2012; Vraspir and Butler, 2009). A major limitation that can obscure the connection between siderophore concentrations and the bulk ligand pool though, is the low efficiency of the solid phase extraction method. Solid phase extraction only captures a fraction of the total dFe-binding organic ligands detected using bulk electrochemistry methods (Bundy et al., 2018), or approximately 10.4 ± 8.4% (< 0.1%-35.3%, Grubbs Test outliers 44.6%, 86.8%, $p < 0.005$, $n = 64$) of total ligands for this dataset. Despite this limitation, we present for the first time a positive correlation between the relative contribution of siderophores to the total ligand pool (siderophore:L) and the average conditional stability constant of the total ligand pool (log $K_{FeL,Fe'}^{cond}$, Figure 4.5). This correlation suggests that siderophores meaningfully impact the total Fe-binding ligand pool in hydrothermal samples from the SEPR.

The correlations between siderophore:L and log $K_{FeL,Fe'}^{cond}$ are best explained by logarithmic fits. This is consistent with a log-scaling binding constant and with a theoretical maximum of siderophore Fe-binding constants that might be observed in the environment. The strongest siderophores documented to date have conditional stability constants of ~14 (Bundy et al., 2018), and thus we would expect average binding constants of the heterogeneous ligand mixtures in environmental samples to be below that limit. A notable feature of these trends, though, is that they differ between sampling environment and are only significant for hydrothermally-influenced samples. The variation in correlation is likely because the average strength of the ligand pool also depends largely on the composition of other, non-siderophore ligands. The ligand composition is expected to change between environments in response to variables such as microbial community or chemical composition (Boiteau et al., 2019; Gledhill and Buck, 2012; Moore et al., 2021). These environmental changes are likely particularly dramatic in the highly variable vent settings. With this in mind, the correlation for the low-temperature venting environment has a comparatively small slope with respect to the neutrally buoyant plume environment. This might be explained by the presence of strong non-siderophore ligands such that siderophore contributions do not disproportionately impact the overall log $K_{FeL,Fe'}^{cond}$ of the ligand pool as significantly, similar to what has been observed in surface waters (Bundy et al., 2018). Alternatively, the siderophores present in low-temperature settings might be weaker and therefore not exert as large an impact on log $K_{FeL,Fe'}^{cond}$. We observed some slight differences in siderophore composition between environments that could affect log $K_{FeL,Fe'}^{cond}$, but the Fe-binding strengths of the siderophores identified along the SEPR are unknown. The low-temperature vents do, however, have different chemistry (e.g. lower metal concentrations) than high-temperature venting or neutrally buoyant plumes in this study region (Moore et al. *in prep*), which could impact the correlation between L:siderophore and log $K_{FeL,Fe'}^{cond}$.

Samples from the neutrally buoyant plume had a much steeper relationship between L:siderophore and log $K_{FeL,Fe'}^{cond}$ than samples from low-temperature sites, suggesting that siderophores have a greater measurable impact on total average log $K_{FeL,Fe'}^{cond}$ in the neutrally buoyant plume. This is likely a result of the comparatively weaker overall ligand pool found in the neutrally buoyant plume. The environmental variability in correlation suggests that the impact of siderophores on the associated bulk ligand pool greatly depends on the other, non-siderophore ligands in the samples. The presence of siderophores should generally increase the average log $K_{FeL,Fe'}^{cond}$ measured by voltammetry, but the influence of siderophores on the overall Fe-binding capacity of the ligand pool might not be as significant in environments where other non-siderophore strong ligands are present, such as in the surface ocean. However, it appears that siderophores contribute meaningfully to the average Fe-binding capacity of the ligand pool in hydrothermal systems despite their relatively small total concentrations.

4.5.6 *Siderophores and iron transport*

Siderophores are a small but integral component of the organic Fe-binding ligand pool in our dataset, which is important when considering the stability and longevity of Fe in these systems. In this study, the ratio of siderophore concentrations to total ligand concentrations was directly related to the average log $K_{FeL,Fe'}^{cond}$ of the organic Fe-binding ligand pool, suggesting that siderophores play an outsized role in complexing Fe in low-temperature and neutrally buoyant plume environments. Increased stabilization capacity of the ligand pool in plumes along the ridge crest may in turn allow a greater proportion of hydrothermal Fe to persist in the dissolved phase and resist precipitative loss during plume advection.

We examined off-axis station PJ and a composite on-axis plume at Station 18 (previously recorded aged ~ 1 month; Kipp et al., 2018) to determine how siderophores and organic Fe-binding ligands might impact stabilization during plume development. Interestingly, the siderophores identified at these sites were the same as those found throughout the fresher, on-axis plumes (Figure 4.3), and the siderophore concentrations were also very similar (younger plumes 4.7 ± 5.1 pM, Station 18 & PJ, 4.0 ± 7.4 pM). This similarity could arise from a few possible scenarios: (1) The microbial communities and amount of siderophore production are similar between the fresh and aged composite plumes, or (2) The siderophores are produced by bacteria at the ridge axis and advected westward with the plume, independent of further microbial production within the aging plume. Option (2) is less likely because recent evidence suggests that siderophores are rapidly cycled in microbial communities. Park et al. (2023) found that transcripts for siderophore uptake were highly active in microbial communities in the surface Pacific (< 500 m), suggesting that siderophores are quickly assimilated into local bacteria. Indeed, Bundy et al. (2023) measured turnover rates of Fe-siderophore complexes on the order of 10 days to months. Thus, siderophores may accumulate in the young plume, but are unlikely to advect over long distances without significant turnover or additional microbial synthesis. Option (1) is far more likely because despite large chemical changes during the evolution of the neutrally buoyant plume, most of the plume microbial community is entrained from background seawater (Dick and Tebo, 2010; German et al., 2010; Lesniewski et al., 2012). Thus, the microbial community and its associated siderophores may remain similar as the plume ages. The large overlap in siderophores detected in the background and neutrally buoyant plume supports this explanation. However, microbial cell abundances were far higher in the neutrally buoyant plume than background seawater (e.g. Dick and Tebo, 2010; German et al., 2010, current study). It is possible that microbes are taking advantage of the additional chemical resources provided by the plume and altering their metabolisms accordingly (e.g. Anantharaman et al., 2013). It remains unknown if siderophore production is impacted by this process, but siderophores have been proposed to be an essential mechanism for solubilizing hydrothermal metals and thereby facilitating microbial access to Fe in the neutrally buoyant plume (Dick, 2019; Li et al., 2014).

Siderophores may also help maintain a consistent sFe fraction as the plume develops (A. J.M. Lough et al., 2019). Station PJ showed evidence of precipitative Fe loss in the center of the plume based on decreases in the dFe fraction (%dFe) compared to on-axis sites (off-axis 4% ± 2% $n = 3$, on-axis 10% ± 6% $n = 25$, Mann–Whitney *U*-Test, $p = 0.072$). However, the sFe fraction (%sFe) at PJ remained similar to the on-axis stations (PJ 7% ± 3% n = 3, on-axis 10% ± 6% $n = 26$, Mann–Whitney *U*-Test, $p = 0.47$). A stable sFe fraction as the plume ages has also been recorded in a plume over the Mid-Cayman Rise (A. J.M. Lough et al., 2019). The consistent sFe fraction as the plume ages, along with similar siderophore compositions and concentrations between the fresher and more developed hydrothermal plumes, suggest that siderophores occupy a critical role throughout the lifetime of the plume and possibly help facilitate long-distance dFe transport away from the ridge axis.

4.6 CONCLUSIONS

We found that siderophores were ubiquitous throughout diverse hydrothermal systems and chemical gradients along the 16-18ºS sector of the SEPR. These siderophores were similar in concentration to those found in surface ocean environments, suggesting that siderophores are an essential microbial Fe acquisition strategy in hydrothermal systems. The identified siderophores represent a diverse array of structures, many of which have never been encountered in the ocean before. We suggest that in the high-Fe environments of hydrothermal vents, siderophores may be utilized to transform biologically inaccessible Fe pools into a more bioavailable form, possibly via an Fe solubilization mechanism. By comparing siderophore concentrations to electrochemical measurements of the entire Fe-binding organic ligand pool, we were able to demonstrate for the first time that an increasing siderophore fraction (siderophore: ligand) results in a higher average binding strength of the total ligand pool. We conclude that siderophores likely have a disproportionate impact on Fe stabilization in these systems, and that siderophore-mediated stabilization of Fe may be an important process throughout the development of the neutrally buoyant plume.

4.7 ACKNOWLEDGEMENTS

We thank the Captain and crew of the R/V *Roger Revelle* and the AUV *Sentry* team. Thank you to Laura Carlson and Lydia Babcock-Adams for technical support with data acquisition on the Q-Exactive and 21T ICR-MS, respectively, and Patrick Monreal for work in siderophore analysis code updates. This work was supported by NSF-OCE #1756402 to J.A.R., R.M.B and Edward Baker, and by the NHMFL P20222 to R.M.B. and Jiwoon Park. *A portion of this work was performed at the National High Magnetic Field Laboratory, which is supported by National Science Foundation Division of Materials Research and Division of Chemistry through DMR-2128556 and the State of Florida.*

4.8 AUTHOR CONTRIBUTIONS

LM completed all siderophore analyses and drafted the manuscript. RB and JR helped to design the study and edit the manuscript. PS helped design the study. JP assisted in siderophore analyses. BS performed sFe and sMn analyses. NB performed shipboard dMn, tdMn, dFe, and dFe analyses and laboratory suspended particle analyses. DV and RM coordinated and performed flow cytometry analyses.

4.9 FIGURES AND TABLES

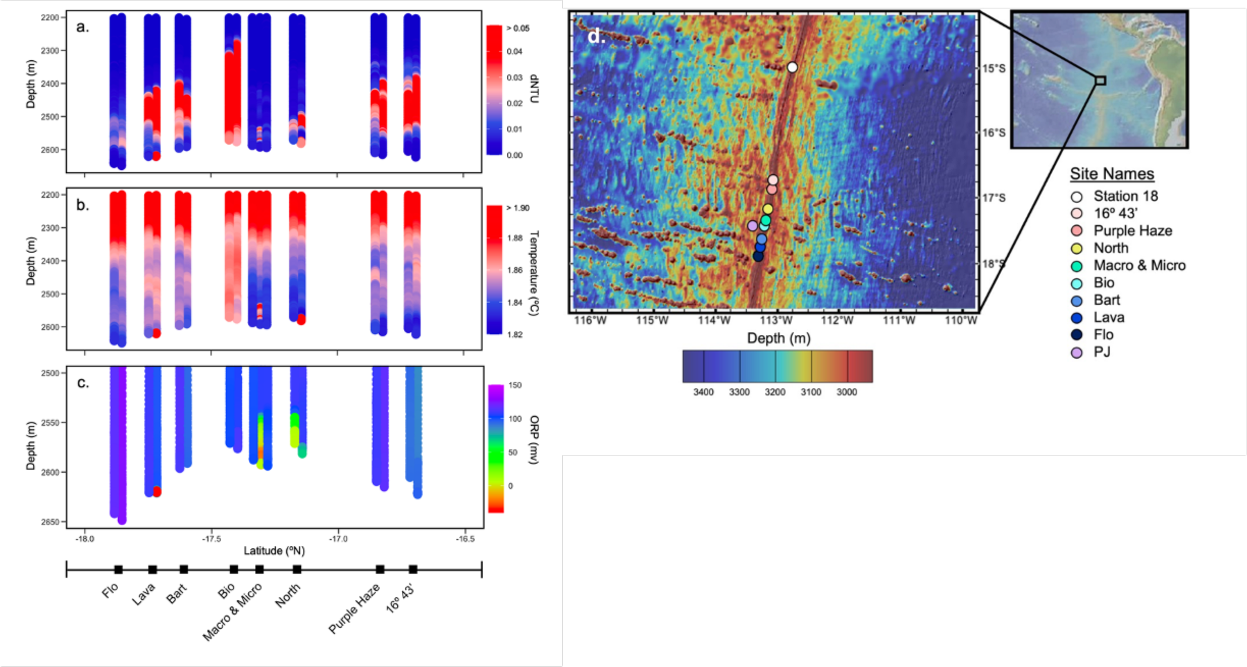

Figure 4.1. Station map and physical characteristics.

A) Particle anomaly (dNTU), B) temperature, and C) oxidation reduction potential (ORP) collected from CTD casts. D) Site map of stations included in panels A-C, plus off-axis sites Station 18 and PJ. The bar below panels A-C indicates site names and casts at the same site are offset slightly to show inter-cast variation.

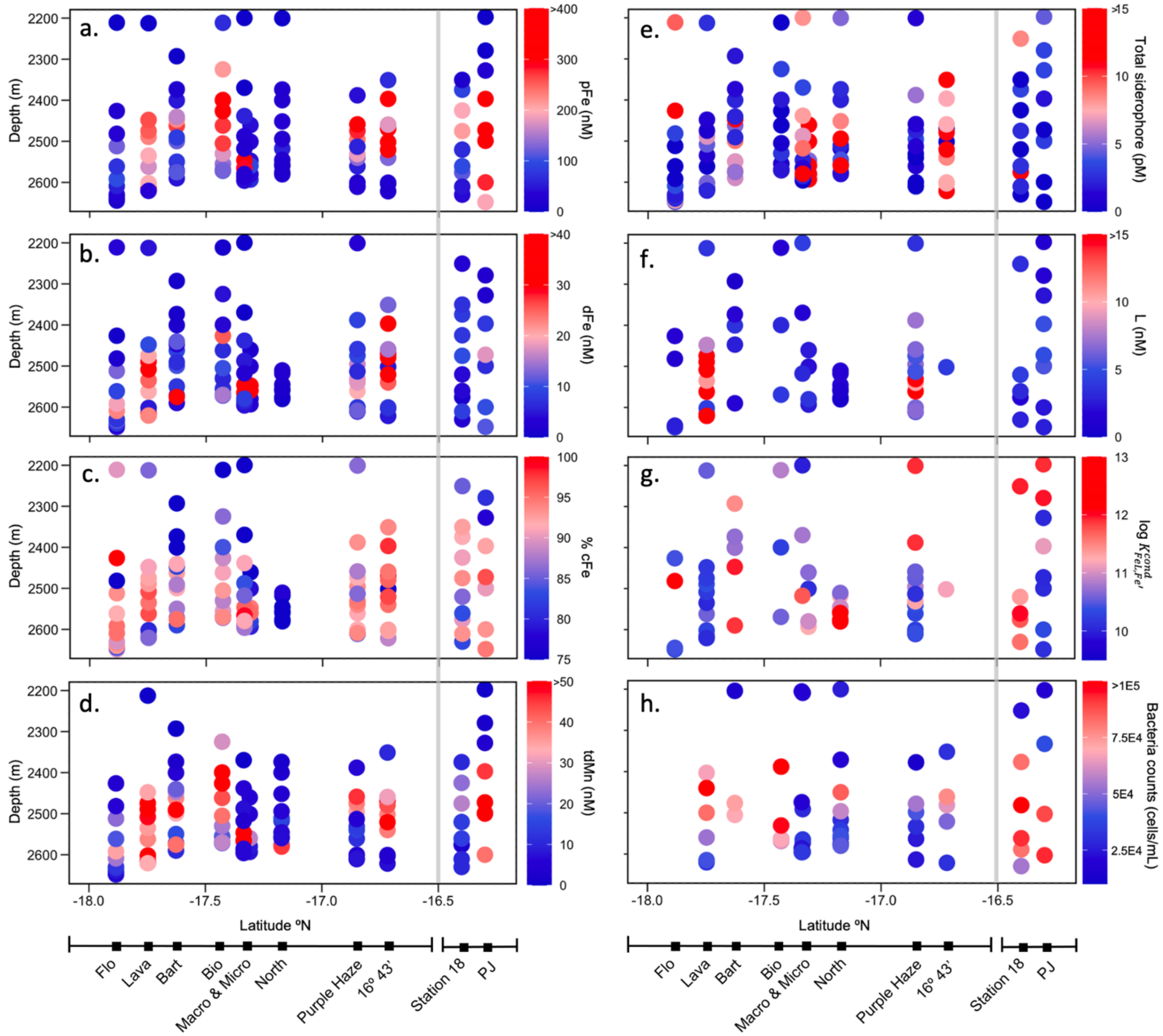

Figure 4.2. Chemical and biological parameters for all sampling sites.

A) particulate iron (pFe) concentrations, B) dissolved iron (dFe) concentrations, C) percentage of dFe in the colloidal fraction (%cFe = 100 X cFe/dFe), D) total dissolvable manganese (tdMn) concentrations, E) total siderophore concentrations, F) total ligand concentrations, G) organic Fe-binding ligand conditional stability constants (log $K^{cond}_{FeL,Fe'}$), and H) bacteria cell counts. Grey bar separates the on-axis sites in the main 16.5º-18ºS study region (left) and sites PJ and Station 18 (right). PJ is located 11 km west of the axis at 17.4ºS and Station 18 is located on-axis at 15.0ºS.

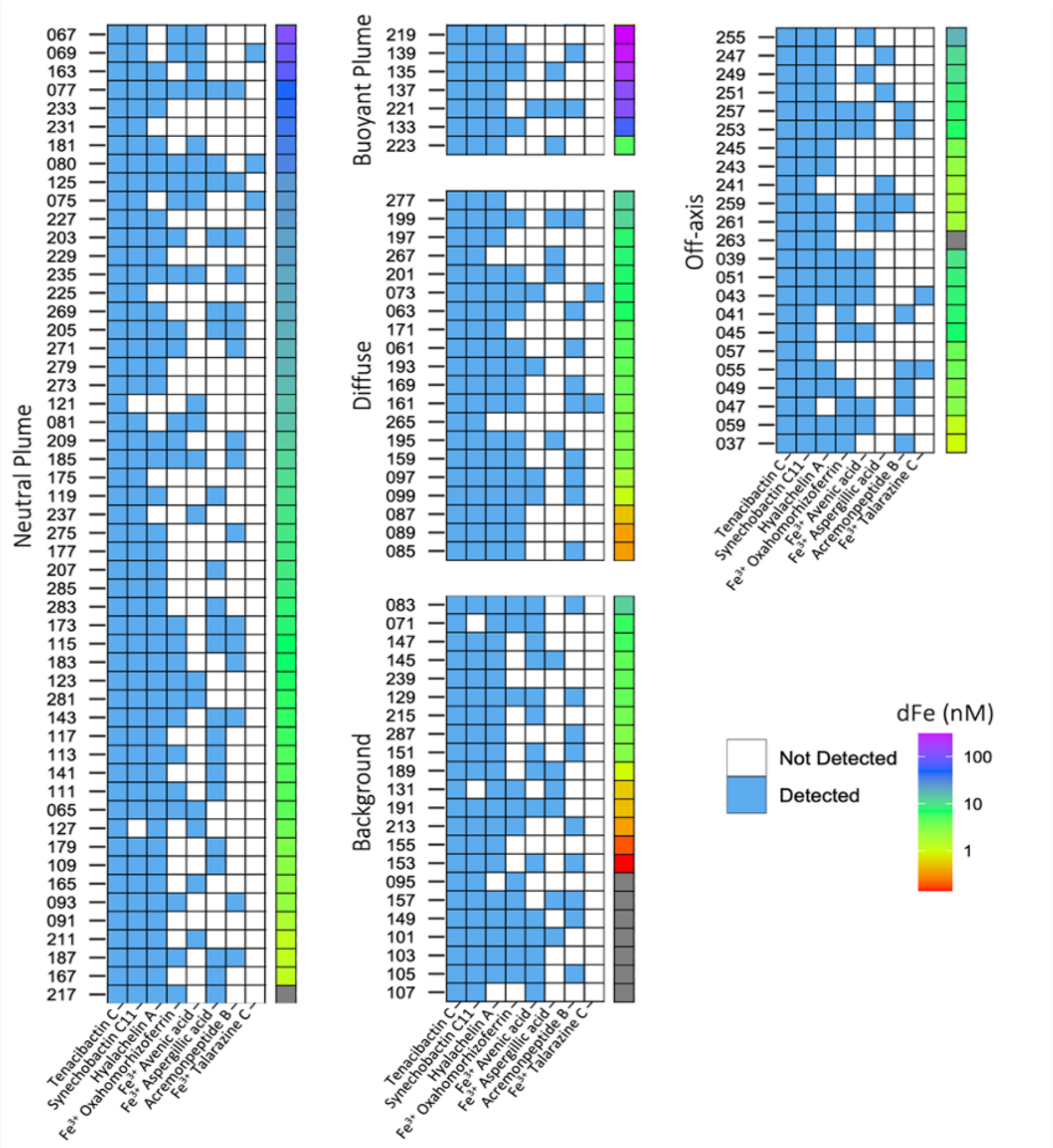

Figure 4.3. Siderophore identification results.

Data are grouped by sampling environment. The eight highest confidence siderophores (Levels 1-4) are listed across the base of the plot with blue tiles indicating detection in that sample. Color bar refers to dissolved iron (dFe) concentration.

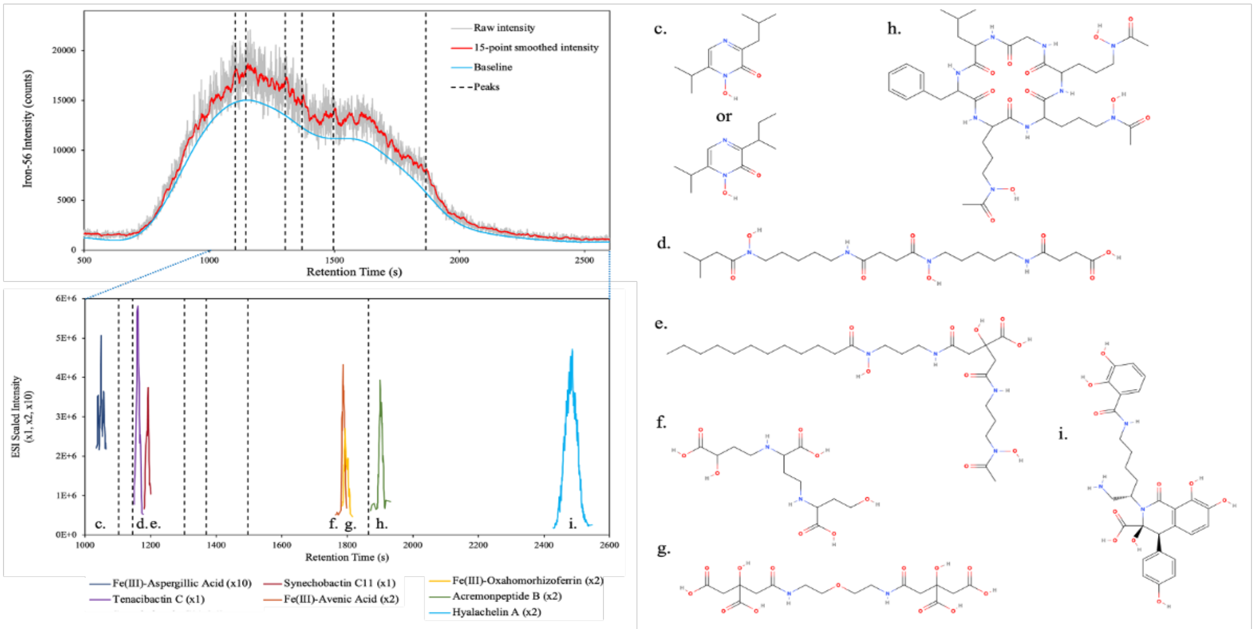

Figure 4.4. Siderophore identification and quantification.

A) ^{56}Fe trace from ICP-MS. Peaks are denoted as vertical dashed lines. B) Scaled ion intensities from ESI-MS for the seven most abundant siderophores detected in the dataset. Scale factors are expressed in the legend. Letters refer to siderophore structures C-G at right. All data shown except peak c are from sample 077, which was from the center of the neutrally buoyant plume at site 16º 43'. Peak c is from sample 109, taken from the edge of the neutrally buoyant plume at site Bio. C-G) Siderophore structures including C) aspergillic acid, D) tenacibactin C, E) synechobactin C11, F) avenic acid, G) oxahomorhizoferrin, H) acremonpeptide B, and I) hyalachelin A.

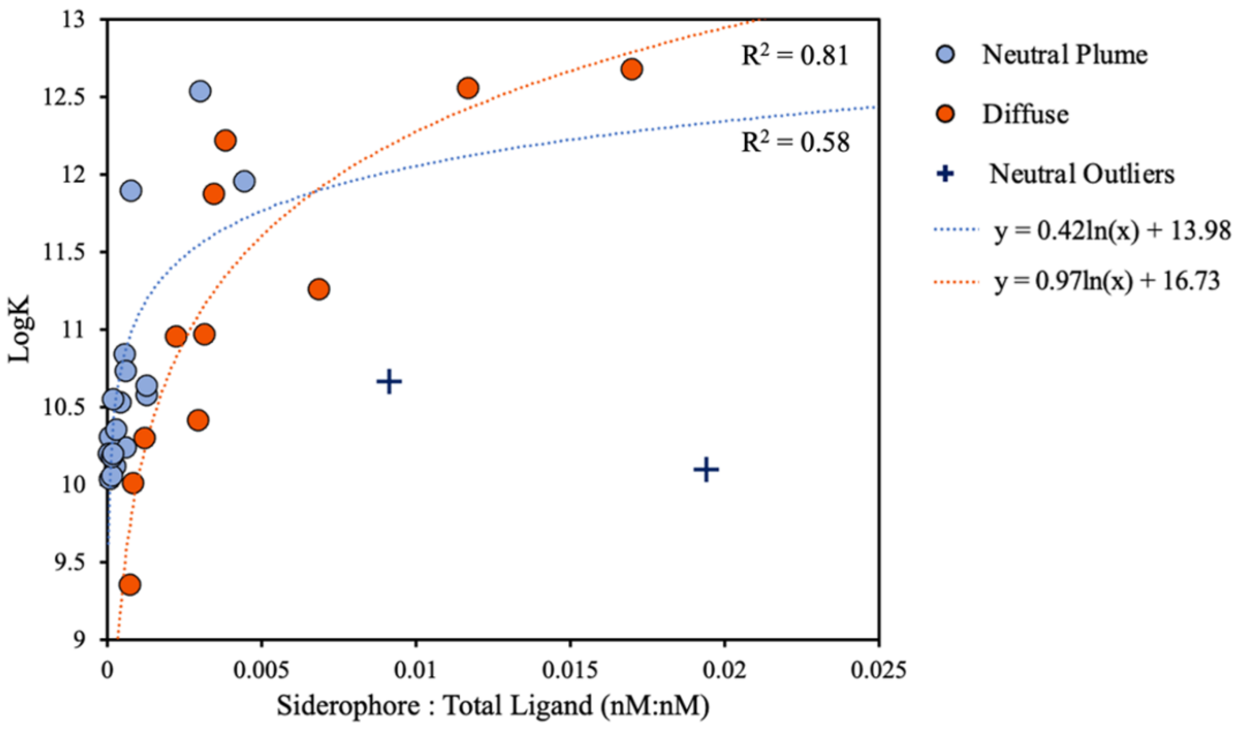

Figure 4.5. Correlation between average ligand binding strength (log $K_{FeL,Fe'}^{cond}$) and siderophore contribution to the total iron-binding organic ligand pool, [siderophore]:[L]. Colors refer to sampling environment and plus signs refer to outlier belonging to the neutrally buoyant plume at Micro. Both fits are logarithmic.

Table 4.1. Summary of sampling environments by site.

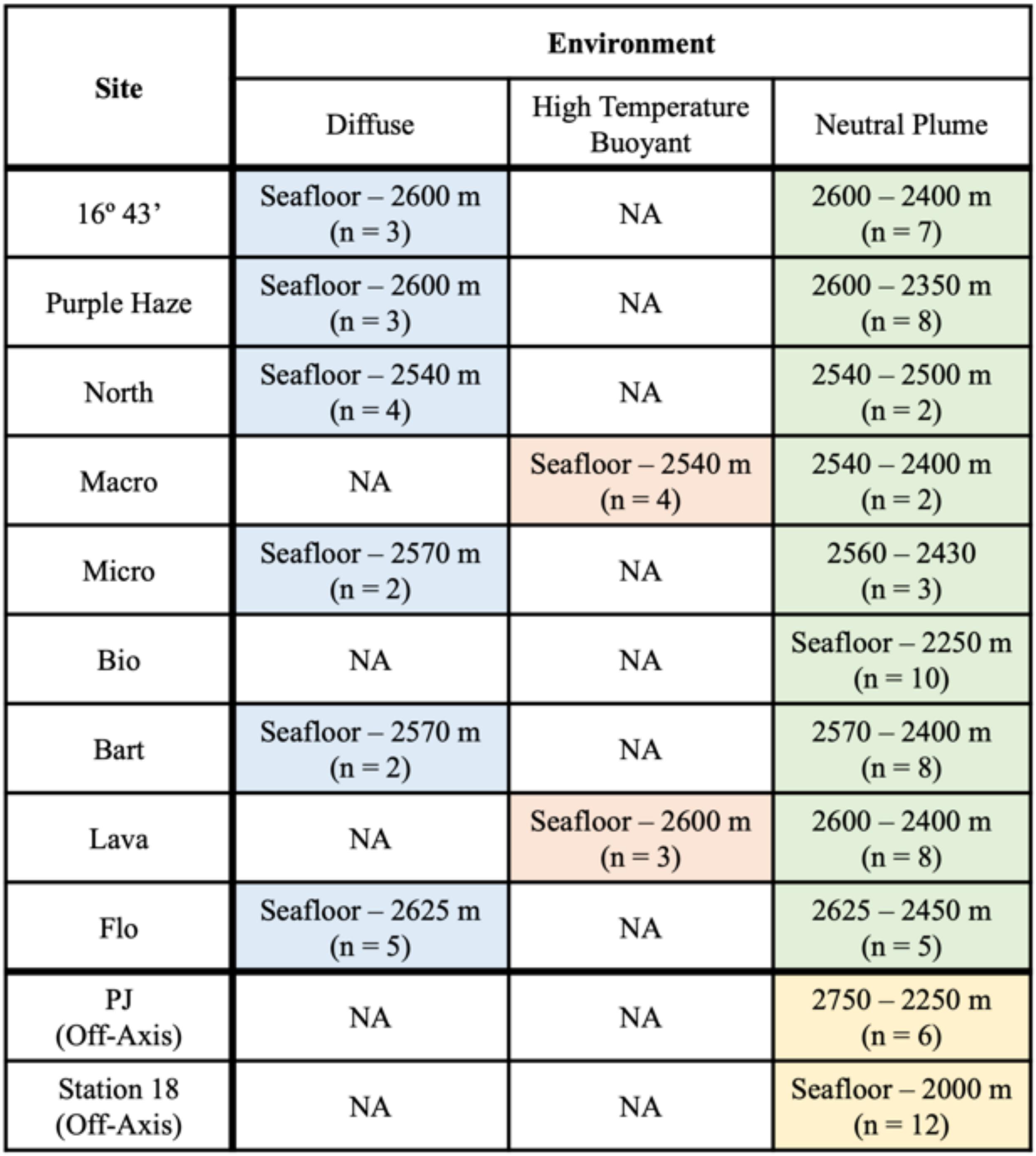

Site	Environment		
	Diffuse	High Temperature Buoyant	Neutral Plume
16º 43’	Seafloor – 2600 m (n = 3)	NA	2600 – 2400 m (n = 7)
Purple Haze	Seafloor – 2600 m (n = 3)	NA	2600 – 2350 m (n = 8)
North	Seafloor – 2540 m (n = 4)	NA	2540 – 2500 m (n = 2)
Macro	NA	Seafloor – 2540 m (n = 4)	2540 – 2400 m (n = 2)
Micro	Seafloor – 2570 m (n = 2)	NA	2560 – 2430 (n = 3)
Bio	NA	NA	Seafloor – 2250 m (n = 10)
Bart	Seafloor – 2570 m (n = 2)	NA	2570 – 2400 m (n = 8)
Lava	NA	Seafloor – 2600 m (n = 3)	2600 – 2400 m (n = 8)
Flo	Seafloor – 2625 m (n = 5)	NA	2625 – 2450 m (n = 5)
PJ (Off-Axis)	NA	NA	2750 – 2250 m (n = 6)
Station 18 (Off-Axis)	NA	NA	Seafloor – 2000 m (n = 12)

The “n” refers to the number of samples in each category. NA indicates the environment was not encountered at that site.

Chapter 5. CONCLUSIONS

Iron (Fe) is an essential nutrient for the oceanic microbial community, and is responsible for facilitating critical cellular processes such as respiration, photosynthesis, and nitrogen fixation (Morel and Price, 2003). Dissolved Fe (dFe) is the most biologically labile form of Fe in the ocean (Morel et al., 2008), and most of this Fe (> 99%) is chemically stabilized by a heterogeneous pool organic Fe-binding ligands (Gledhill and Buck, 2012; Gledhill and van den Berg, 1994; Rue and Bruland, 1995). The concentrations and identities of these ligands exert key controls over the stability, bioavailability and biogeochemical cycling of Fe. Indeed, modeling studies have demonstrated that doubling the ligand concentration in the ocean has a greater impact on total primary productivity than increasing Fe sources alone (Tagliabue et al., 2014). Thus, measuring the quantities and diversity of organic Fe-binding ligands is essential for understanding the Fe biogeochemical cycle and the resulting impacts on CO_2 uptake, primary productivity, and climate (Moore et al., 2013; Tagliabue et al., 2017, 2014).

Despite the widely acknowledged role of ligands in mediating Fe cycling, there are critical gaps in ligand characterization studies. While electrochemical measurements of Fe-binding ligands such as competitive ligand exchange-adsorptive cathodic stripping voltammetry (CLE-ACSV) are widespread (Caprara et al., 2016), studies have focused primarily on the open ocean and often lack detail in important environments near Fe sources such as continental margins and hydrothermal vents (Buck et al., 2018, 2015; Gerringa et al., 2015). Studies using liquid chromatography-mass spectrometry (LC-MS) techniques to identify specific ligands are even more limited, and are largely confined to the surface and mesopelagic ocean (>1,500 m) (Boiteau et al., 2019, 2016a; Bundy et al., 2018; Mawji et al., 2011, 2008; Park et al., 2023; Velasquez et al., 2011). These LC-MS studies primarily focus on identifying siderophores, small

Fe-binding molecules produced specifically for microbial Fe acquisition, because they are thought to disproportionately impact dFe bioavailability relative to the larger ligand pool (Bundy et al., 2018, 2015; Gledhill and Buck, 2012; Vraspir and Butler, 2009). However, siderophore identification studies are rarely combined with CLE-ACSV measurements of the total ligand pool (Bundy et al., 2018), thereby limiting the scope of interpretation.

This thesis addresses the environmental gap in ligand measurements by expanding studies into the Eastern Tropical North Pacific Oxygen Deficient Zone (ETNP ODZ) near the Mexican margin and into diverse hydrothermal venting systems along the 16-18ºS sector of the Southern East Pacific Rise (SEPR). The novel combined application of CLE-ACSV measurements of the total ligand pool and LC-MS siderophore identification analyses offers unprecedented insight into the impact of ligand composition and concentration on dFe speciation and transport in these regions. Furthermore, this thesis presents the largest siderophore dataset to date and identifies siderophores for the first time in an ODZ and in high Fe hydrothermal vent systems. This thesis adds significant contributions of ligand concentration and identity data in understudied Fe-rich environments to the existing body of work and paves the way for future studies using combined CLE-ACSV and LC-MS techniques.

Chapter 2 expanded Fe-binding ligand characterization studies into the ETNP ODZ to test the hypothesis that organic ligands contribute significantly to the stabilization and transport of Fe in an ODZ margin. Ligands within the ODZ were found to be stronger and in higher concentrations than those in the surrounding oxygenated waters, and siderophores were identified for the first time within the bounds of an ODZ. Ligand results were incorporated into a 1-dimensional model demonstrating that organic ligands help facilitate Fe transport along an inshore-offshore transect. This represents one of the first studies to combine siderophore and bulk ligand measurements and demonstrates the critical role of organic ligands in mediating Fe stabilization near a Fe-rich margin and within the oxygen-poor redox conditions of an ODZ.

Chapter 3 explored the spatial and temporal chemical variability in hydrothermal venting sites along the 16-18ºS sector of the SEPR, an ultrafast spreading ridge with the highest spatial frequency of hydrothermal vent systems in the world (Beaulieu et al., 2015). This chapter tested the hypothesis that organic Fe-binding ligands stabilize significant amounts of hydrothermal dFe along the ridge crest. CLE-ACSV analyses revealed that organic ligands were the primary stabilization mechanism for hydrothermal dFe across a diverse array of venting systems and dFe concentrations. Ligands were found to be particularly important to the stabilization of colloidal Fe ($0.02 < \text{cFe} < 0.2$ μm) and had an essential role in mediating the physical partitioning of dFe between the soluble Fe ($\text{sFe} < 0.02$ μm) and cFe pools. Ligands were also hypothesized to be a critical stabilization mechanism that allows transport of dFe away from the ridge axis and into the ocean interior. This study is the first comprehensive ligand study of multiple venting systems along a ridge crest and one of the few that combine dFe size fractionation and ligand data.

Chapter 4 quantified and identified siderophores along the SEPR using LC-MS to test the hypothesis that siderophores are an important component of the Fe-binding ligand pool near hydrothermal vents and potentially a key Fe-acquisition strategy for local microbial communities. Siderophore presence was ubiquitous across diverse physical and chemical gradients in venting systems, and eight unique siderophore structures were identified with widespread distribution across the dataset. Combining siderophore concentration data with CLE-ACSV results from Chapter 3 revealed the measurable impact of siderophores on the average Fe-binding strength of the ligand pool. This confirmed for the first time the long-held hypothesis that siderophores contribute meaningfully, and possibly disproportionally, to the total Fe-binding ligand pool despite low individual siderophore concentrations. This study represents the largest siderophore dataset to date and is among the first siderophore characterization studies in the deep ocean.

This thesis applied a novel combination of LC-MS and CLE-ACSV approaches to characterize ligands near understudied Fe sources to the deep Pacific Ocean. Future work could extend the application of these techniques to other hydrothermally active regions and continental margins to examine the impact of ligands on Fe stabilization in response to diverse chemical regimes. Further work identifying siderophores in a wider range of oceanic environments would also be invaluable, because the diversity of siderophores in the ocean is not well understood. This endeavor would be improved by use of an untargeted LC-MS approach that could be used to identify novel siderophores, which may be unique to individual environments. Finally, by extensively characterizing Fe-binding ligands near Fe sources, this work provides a basis for future modeling studies that require better constraints on ligand parameters near these understudied regions. Overall, this thesis expanded the coverage of both the total ligand pool and siderophore studies into critical regions of the deep ocean. CLE-ACSV and LC-MS techniques were combined for one of the first times, offering unprecedented insights into Fe-binding ligand dynamics in these regions and paving the way for future studies using these complementary ligand measurement methods.

BIBLIOGRAPHY

Abualhaija, M.M., van den Berg, C.M.G., 2014. Chemical speciation of iron in seawater using catalytic cathodic stripping voltammetry with ligand competition against salicylaldoxime. Mar. Chem. 164, 60–74. https://doi.org/10.1016/j.marchem.2014.06.005

Anantharaman, K., Breier, J.A., Sheik, C.S., Dick, G.J., 2013. Evidence for hydrogen oxidation and metabolic plasticity in widespread deep-sea sulfur-oxidizing bacteria. Proc. Natl. Acad. Sci. U. S. A. 110, 330–335. https://doi.org/10.1073/pnas.1215340110

Ardiningsih, I., Seyitmuhammedov, K., Sander, S.G., Stirling, C.H., Reichart, G.J., Arrigo, K.R., Gerringa, L.J.A., Middag, R., 2021. Fe-binding organic ligands in coastal and frontal regions of the western Antarctic Peninsula. Biogeosciences 18, 4587–4601. https://doi.org/10.5194/bg-18-4587-2021

Armstrong, F.A.J., Stearns, C.R., Strickland, J.D.H., 1967. The measurement of upwelling and subsequent biological process by means of the Technicon Autoanalyzer® and associated equipment. Deep. Res. Oceanogr. Abstr. 14, 381–389. https://doi.org/10.1016/0011-7471(67)90082-4

Auzende, J.M., Ballu, V., Batiza, R., Bideau, D., Charlou, J.L., Cormier, M.H., Fouquet, Y., Geistdoerfer, P., Lagabrielle, Y., Sinton, J., Spadea, P., 1996. Recent tectonic, magmatic, and hydrothermal activity on the East Pacific Rise between 17^{o}S and 19^{a}S: Submersible observations. J. Geophys. Res. 101.

Baars, O., Morel, F.M.M., Perlman, D.H., 2014. ChelomEx: Isotope-assisted discovery of metal chelates in complex media using high-resolution LC-MS. Anal. Chem. 86, 11298–11305. https://doi.org/10.1021/ac503000e

Baakza, A., Vala, A.K., Dave, B.P., Dube, H.C., 2004. A comparative study of siderophore production by fungi from marine and terrestrial habitats. J. Exp. Mar. Bio. Ecol. 311, 1–9. https://doi.org/10.1016/j.jembe.2003.12.028

Baker, E.T., 1997. MAPR: A new instrument for hydrothermal plume mapping. RIDGE events 8, 23–25.

Baker, E.T., German, C.R., 2004. On the global distribution of hydrothermal vent fields. Mid-Ocean Ridges Hydrothermal Interact. Between Lithosph. Ocean. Geophys. Monogr. Ser. 148, 245–266.

Baker, E.T., Resing, J.A., Haymon, R.M., Tunnicliffe, V., Lavelle, J.W., Martinez, F., Ferrini, V., Walker, S.L., Nakamura, K., 2016. How many vent fields? New estimates of vent field populations on ocean ridges from precise mapping of hydrothermal discharge locations. Earth Planet. Sci. Lett. 449, 186–196. https://doi.org/10.1016/j.epsl.2016.05.031

Baker, E.T., Urabe, T., 1996. Extensive distribution of hydrothermal plumes along the superfast spreading East Pacific Rise, 13°30′-18°40′S. J. Geophys. Res. B Solid Earth 101, 8685–8695. https://doi.org/10.1029/95jb03746

Barbeau, K., Rue, E.L., Bruland, K.W., Butler, A., 2001. Photochemical cycling of iron in the surface ocean mediated by microbial iron(III)-binding ligands. Nature 413, 409–413.

Baumberger, T., Lilley, M.D., Resing, J.A., Lupton, J.E., Baker, E.T., Butterfield, D.A., Olson, E.J., Früh-Green, G.L., 2014. Understanding a submarine eruption through time series hydrothermal plume sampling of dissolved and particulate constituents: West Mata, 2008–2012. Geochemistry, Geophys. Geosystems 15, 4631–4650. https://doi.org/10.1002/2014GC005460.Received

Beaulieu, S.E., Baker, E.T., German, C.R., 2015. Where are the undiscovered hydrothermal vents on oceanic spreading ridges? Deep. Res. Part II Top. Stud. Oceanogr. 121, 202–212.

https://doi.org/10.1016/j.dsr2.2015.05.001

Bemis, K., Lowell, R.P., Farough, A., 2012. Diffuse flow: On and Around Hydrothermal Vents. Oceanography 25, 182–191.

Bennett, S.A., Achterberg, E.P., Connelly, D.P., Statham, P.J., Fones, G.R., German, C.R., 2008. The distribution and stabilisation of dissolved Fe in deep-sea hydrothermal plumes. Earth Planet. Sci. Lett. 270, 157–167. https://doi.org/10.1016/j.epsl.2008.01.048

Bennett, S.A., Rouxel, O., Schmidt, K., Garbe-Schönberg, D., Statham, P.J., German, C.R., 2009. Iron isotope fractionation in a buoyant hydrothermal plume, 5°S Mid-Atlantic Ridge. Geochim. Cosmochim. Acta 73, 5619–5634. https://doi.org/10.1016/j.gca.2009.06.027

Boiteau, R.M., Fitzsimmons, J.N., Repeta, D.J., Boyle, E.A., 2013. Detection of iron ligands in seawater and marine cyanobacteria cultures by high-performance liquid chromatography-inductively coupled plasma-mass spectrometry. Anal. Chem. 85, 4357–4362. https://doi.org/10.1021/ac3034568

Boiteau, R.M., Mende, D.R., Hawco, N.J., McIlvin, M.R., Fitzsimmons, J.N., Saito, M.A., Sedwick, P.N., Delong, E.F., Repeta, D.J., 2016. Siderophore-based microbial adaptations to iron scarcity across the eastern Pacific Ocean. Proc. Natl. Acad. Sci. U. S. A. 113, 14237–14242. https://doi.org/10.1073/pnas.1608594113

Boiteau, R.M., Repeta, D.J., 2015. An extended siderophore suite from Synechococcus sp. PCC 7002 revealed by LC-ICPMS-ESIMS. Metallomics 7, 877–884. https://doi.org/10.1039/c5mt00005j

Boiteau, R.M., Till, C.P., Coale, T.H., Fitzsimmons, J.N., Bruland, K.W., Repeta, D.J., 2019. Patterns of iron and siderophore distributions across the California Current System. Limnol. Oceanogr. 64, 376–389. https://doi.org/10.1002/lno.11046

Boyd, P.W., Ellwood, M.J., 2010. The biogeochemical cycle of iron in the ocean. Nat. Geosci. 3, 675–682. https://doi.org/10.1038/ngeo964

Boye, M., Nishioka, J., Croot, P., Laan, P., Timmermans, K.R., Strass, V.H., Takeda, S., de Baar, H.J.W., 2010. Significant portion of dissolved organic Fe complexes in fact is Fe colloids. Mar. Chem. 122, 20–27. https://doi.org/10.1016/j.marchem.2010.09.001

Buck, K.N., Gerringa, L.J.A., Rijkenberg, M.J.A., 2016. An intercomparison of dissolved iron speciation at the Bermuda Atlantic Time-series Study (BATS) site: Results from GEOTRACES crossover station A. Front. Mar. Sci. 3, 1–14. https://doi.org/10.3389/fmars.2016.00262

Buck, K.N., Moffett, J., Barbeau, K.A., Bundy, R.M., Kondo, Y., Wu, J., 2012. The organic complexation of iron and copper: An intercomparison of competitive ligand exchange-adsorptive cathodic stripping voltammetry (CLE-ACSV) techniques. Limnol. Oceanogr. Methods 10, 496–515. https://doi.org/10.4319/lom.2012.10.496

Buck, K.N., Sedwick, P.N., Sohst, B., Carlson, C.A., 2018. Organic complexation of iron in the eastern tropical South Pacific: Results from US GEOTRACES Eastern Pacific Zonal Transect (GEOTRACES cruise GP16). Mar. Chem. 201, 229–241. https://doi.org/10.1016/j.marchem.2017.11.007

Buck, K.N., Sohst, B., Sedwick, P.N., 2015. The organic complexation of dissolved iron along the U.S. GEOTRACES (GA03) North Atlantic Section. Deep. Res. Part II Top. Stud. Oceanogr. 116, 152–165. https://doi.org/10.1016/j.dsr2.2014.11.016

Buck, N.J., Barrett, P.M., Morton, P.L., Landing, W.M., Resing, J.A., 2021. Energy dispersive X-ray fluorescence methodology and analysis of suspended particulate matter in seawater for trace element compositions and an intercomparison with high-resolution inductively coupled plasma-mass spectrometry. Limnol. Oceanogr. Methods 19, 401–415. https://doi.org/10.1002/lom3.10433

Bundy, R.M., Abdulla, H.A.N., Hatcher, P.G., Biller, D. V., Buck, K.N., Barbeau, K.A., 2015. Iron-binding ligands and humic substances in the San Francisco Bay estuary and estuarine-influenced shelf regions of coastal California. Mar. Chem. 173, 183–194. https://doi.org/10.1016/j.marchem.2014.11.005

Bundy, R.M., Biller, D. V., Buck, K.N., Bruland, K.W., Barbeau, K.A., 2014. Distinct pools of dissolved iron-binding ligands in the surface and benthic boundary layer of the California current. Limnol. Oceanogr. 59, 769–787. https://doi.org/10.4319/lo.2014.59.3.0769

Bundy, R.M., Boiteau, R.M., McLean, C., Turk-Kubo, K.A., McIlvin, M.R., Saito, M.A., Van Mooy, B.A.S., Repeta, D.J., 2018. Distinct siderophores contribute to iron cycling in the mesopelagic at station ALOHA. Front. Mar. Sci. 5, 1–15. https://doi.org/10.3389/fmars.2018.00061

Burgaud, G., Le Calvez, T., Arzur, D., Vandenkoornhuyse, P., Barbier, G., 2009. Diversity of culturable marine filamentous fungi from deep-sea hydrothermal vents. Environ. Microbiol. 11, 1588–1600. https://doi.org/10.1111/j.1462-2920.2009.01886.x

Butler, A., Harder, T., Ostrowski, A.D., Carrano, C.J., 2021. Photoactive siderophores: Structure, function and biology. J. Inorg. Biochem. 221, 111457. https://doi.org/10.1016/j.jinorgbio.2021.111457

Butterfield, D.A., Roe, K.K., Lilley, M.D., Huber, J.A., Baross, J.A., Embley, R.W., Massoth, G.J., 2004. Mixing, reaction and microbial activity in the sub-seafloor revealed by temporal and spatial variation in diffuse flow vents at axial volcano. Geophys. Monogr. Ser. 144, 269–289. https://doi.org/10.1029/144GM17

Caprara, S., Buck, K.N., Gerringa, L.J.A., Rijkenberg, M.J.A., Monticelli, D., 2016. A compilation of iron speciation data for open oceanic waters. Front. Mar. Sci. 3, 1–7. https://doi.org/10.3389/fmars.2016.00221

Charlou, J.L., Bougault, H., Appriou, P., Nelsen, T., Rona, P., 1991. Different TDM/CH4 hydrothermal plume signatures: TAG site at 26°N and serpentinized ultrabasic diapir at 15°05′N on the Mid-Atlantic Ridge. Geochim. Cosmochim. Acta 55, 3209–3222. https://doi.org/10.1016/0016-7037(91)90484-M

Charlou, J.L., Fouquet, Y., Donval, J.P., Auzende, J.M., Jean-Baptiste, P., Stievenard, M., Michel, S., 1996. Mineral and gas chemistry of hydrothermal fluids on an ultrafast spreading ridge: East Pacific Rise, 17° to 19°S (Naudur cruise, 1993) phase separation processes controlled by volcanic and tectonic activity. J. Geophys. Res. B Solid Earth 101, 15899–15919. https://doi.org/10.1029/96jb00880

Chen, M., Dei, R.C.H., Wang, W.X., Guo, L., 2003. Marine diatom uptake of iron bound with natural colloids of different origins. Mar. Chem. 81, 177–189. https://doi.org/10.1016/S0304-4203(03)00032-X

Chen, S., Tao, C., German, C.R., 2021. Abundance of low-temperature axial venting at the equatorial East Pacific Rise. Deep. Res. Part I Oceanogr. Res. Pap. 167. https://doi.org/10.1016/j.dsr.2020.103426

Connell, L., Barrett, A., Templeton, A., Staudigel, H., 2009. Fungal diversity associated with an active deep sea volcano: Vailulu’u seamount, Samoa. Geomicrobiol. J. 26, 597–605. https://doi.org/10.1080/01490450903316174

Croot, P.L., Heller, M.I., Wuttig, K., 2019. Redox Processes Impacting the Flux of Iron(II) from Shelf Sediments to the OMZ along the Peruvian Shelf. ACS Earth Sp. Chem. 3, 537–549.

https://doi.org/10.1021/acsearthspacechem.8b00203

Crosby, H.A., Roden, E.E., Johnson, C.M., Beard, B.L., 2007. The mechanisms of iron isotope fractionation produced during dissimilatory Fe(III) reduction by Shewanella putrefaciens and Geobacter sulfurreducens. Geobiology 5, 169–189. https://doi.org/10.1111/j.1472-4669.2007.00103.x

Cullen, J.T., Bergquist, B.A., Moffett, J.W., 2006. Thermodynamic characterization of the partitioning of iron between soluble and colloidal species in the Atlantic Ocean. Mar. Chem. 98, 295–303. https://doi.org/10.1016/j.marchem.2005.10.007

Cutter, G., Casciotti, K., Croot, P., Geibert, W., Heimbürger, L.-E., Lohan, M., Planquette, H., van de Flierdt, T., 2017. Sampling and Sample-handling Protocols for GEOTRACES Cruises. Version 3, August 2017. 139pp. & Appendices. https://doi.org/http://dx.doi.org/10.25607/OBP-2

Cutter, G.A., Bruland, K.W., 2012. Rapid and noncontaminating sampling system for trace elements in global ocean surveys. Limnol. Oceanogr. Methods 10, 425–436. https://doi.org/10.4319/lom.2012.10.425

Dick, G.J., 2019. The microbiomes of deep-sea hydrothermal vents: distributed globally, shaped locally. Nat. Rev. Microbiol. 17, 271–283. https://doi.org/10.1038/s41579-019-0160-2

Dick, G.J., Tebo, B.M., 2010. Microbial diversity and biogeochemistry of the Guaymas Basin deep-sea hydrothermal plume. Environ. Microbiol. 12, 1334–1347. https://doi.org/10.1111/j.1462-2920.2010.02177.x

Dideriksen, K., Baker, J.A., Stipp, S.L.S., 2008. Equilibrium Fe isotope fractionation between inorganic aqueous Fe(III) and the siderophore complex, Fe(III)-desferrioxamine B. Earth Planet. Sci. Lett. 269, 280–290. https://doi.org/10.1016/j.epsl.2008.02.022

Drechsel, H., Tschierske, M., Thieken, A., Jung, G., Zähner, H., Winkelmann, G., 1995. The carboxylate type siderophore rhizoferrin and its analogs produced by directed fermentation. J. Ind. Microbiol. 14, 105–112. https://doi.org/10.1007/BF01569891

Elderfield, H., Schultz, A., 1996. Mid-ocean ridge hydrothermal fluxes and the chemical composition of the ocean. Annu. Rev. Earth Planet. Sci. 24, 191–224. https://doi.org/10.1146/annurev.earth.24.1.191

Elrod, V.A., Berelson, W.M., Coale, K.H., Johnson, K.S., 2004. The flux of iron from continental shelf sediments: A missing source for global budgets. Geophys. Res. Lett. 31, 2–5. https://doi.org/10.1029/2004GL020216

Embley, R.W., Lupton, J.E., Massoth, G., Urabe, T., Tunnicliffe, V., Butterfield, D.A., Shibata, T., Okano, O., Kinoshita, M., Fujioka, K., 1998. Geological, chemical, and biological evidence for recent volcanism at 17.5°S: East Pacific Rise. Earth Planet. Sci. Lett. 163, 131–147. https://doi.org/10.1016/S0012-821X(98)00181-2

Emerson, D., Fleming, E.J., McBeth, J.M., 2010. Iron-oxidizing bacteria: An environmental and genomic perspective. Annu. Rev. Microbiol. 64, 561–583. https://doi.org/10.1146/annurev.micro.112408.134208

Feely, R.A., Baker, E.T., Marumo, K., Urabe, T., Ishibashi, J., Gendron, J., Lebon, G.T., Okamura, K., 1996. Hydrothermal plume particles and dissolved phosphate over the superfast-spreading southern East Pacific Rise. Geochim. Cosmochim. Acta 60, 2297–2323. https://doi.org/10.1016/0016-7037(96)00099-3

Feely, R.A., Gendron, J.F., Baker, E.T., 1994. TH6 " ~ I 128, 19–36.

Feely, R.A., Massoth, G.J., Lebon, G.T., 1991. Sampling of marine particulate matter and analysis by X-ray fluorescence spectrometry. Washingt. DC Am. Geophys. Union Geophys.

Monogr. Ser. 63 251–257.

Field, M.P., Sherrell, R.M., 2000. Dissolved and particulate Fe in a hydrothermal plume at 9°45′N, East Pacific Rise: Slow Fe(II) oxidation kinetics in Pacific plumes. Geochim. Cosmochim. Acta 64, 619–628. https://doi.org/10.1016/s0016-7037(99)00333-6

Fiedler, P.C., Talley, L.D., 2006. Hydrography of the eastern tropical Pacific: A review. Prog. Oceanogr. 69, 143–180. https://doi.org/10.1016/j.pocean.2006.03.008

Fitzsimmons, J.N., Boyle, E.A., Jenkins, W.J., 2014. Distal transport of dissolved hydrothermal iron in the deep South Pacific Ocean. Proc. Natl. Acad. Sci. U. S. A. 111, 16654–16661. https://doi.org/10.1073/pnas.1418778111

Fitzsimmons, J.N., Carrasco, G.G., Wu, J., Roshan, S., Hatta, M., Measures, C.I., Conway, T.M., John, S.G., Boyle, E.A., 2015. Partitioning of dissolved iron and iron isotopes into soluble and colloidal phases along the GA03 GEOTRACES North Atlantic Transect. Deep. Res. Part II Top. Stud. Oceanogr. 116, 130–151. https://doi.org/10.1016/j.dsr2.2014.11.014

Fitzsimmons, J.N., John, S.G., Marsay, C.M., Hoffman, C.L., Nicholas, S.L., Toner, B.M., German, C.R., Sherrell, R.M., 2017. Iron persistence in a distal hydrothermal plume supported by dissolved-particulate exchange. Nat. Geosci. 10, 195–201. https://doi.org/10.1038/ngeo2900

Fortunato, C.S., Larson, B., Butterfield, D.A., Huber, J.A., 2018. Spatially distinct, temporally stable microbial populations mediate biogeochemical cycling at and below the seafloor in hydrothermal vent fluids. Environ. Microbiol. 20, 769–784. https://doi.org/10.1111/1462-2920.14011

Früh-Green, G.L., Kelley, D.S., Bernasconi, S.M., Karson, J.A., Ludwig, K.A., Butterfield, D.A., Boschi, C., Proskurowski, G., 2003. 30,000 Years of Hydrothermal Vent Field. Science (80-

.). 301, 495–498.

Früh-Green, G.L., Kelley, D.S., Lilley, M.D., Cannat, M., Chavagnac, V., Baross, J.A., 2022. Diversity of magmatism, hydrothermal processes and microbial interactions at mid-ocean ridges. Nat. Rev. Earth Environ. 3, 852–871. https://doi.org/10.1038/s43017-022-00364-y

Garber, A.I., Nealson, K.H., Okamoto, A., McAllister, S.M., Chan, C.S., Barco, R.A., Merino, N., 2020. FeGenie: A Comprehensive Tool for the Identification of Iron Genes and Iron Gene Neighborhoods in Genome and Metagenome Assemblies. Front. Microbiol. 11, 1–23. https://doi.org/10.3389/fmicb.2020.00037

Gartman, A., Findlay, A.J., 2020. Impacts of hydrothermal plume processes on oceanic metal cycles and transport. Nat. Geosci. 13, 396–402. https://doi.org/10.1038/s41561-020-0579-0

Gartman, A., Findlay, A.J., Luther, G.W., 2014. Nanoparticulate pyrite and other nanoparticles are a widespread component of hydrothermal vent black smoker emissions. Chem. Geol. 366, 32–41. https://doi.org/10.1016/j.chemgeo.2013.12.013

German, C.R., Bowen, A., Coleman, M.L., Honig, D.L., Huber, J.A., Jakuba, M. V., Kinsey, J.C., Kurz, M.D., Leroy, S., McDermott, J.M., De Mercier Lépinay, B., Nakamura, K., Seewald, J.S., Smith, J.L., Sylva, S.P., Van Dover, C.L., Whitcomb, L.L., Yoerger, D.R., 2010. Diverse styles of submarine venting on the ultraslow spreading Mid-Cayman Rise. Proc. Natl. Acad. Sci. U. S. A. 107, 14020–14025. https://doi.org/10.1073/pnas.1009205107

German, C.R., Casciotti, K.A., Dutay, J.C., Heimbürger, L.E., Jenkins, W.J., Measures, C.I., Mills, R.A., Obata, H., Schlitzer, R., Tagliabue, A., Turner, D.R., Whitby, H., 2016. Hydrothermal impacts on trace element and isotope ocean biogeochemistry. Philos. Trans. R. Soc. A Math. Phys. Eng. Sci. 374, 0–2. https://doi.org/10.1098/rsta.2016.0035

Gerringa, L.J.A., Blain, S., Laan, P., Sarthou, G., Veldhuis, M.J.W., Brussaard, C.P.D., Viollier, E., Timmermans, K.R., 2008. Fe-binding dissolved organic ligands near the Kerguelen Archipelago in the Southern Ocean (Indian sector). Deep. Res. Part II Top. Stud. Oceanogr. 55, 606–621. https://doi.org/10.1016/j.dsr2.2007.12.007

Gerringa, L.J.A., Rijkenberg, M.J.A., Schoemann, V., Laan, P., de Baar, H.J.W., 2015. Organic complexation of iron in the West Atlantic Ocean. Mar. Chem. 177, 434–446. https://doi.org/10.1016/j.marchem.2015.04.007

Glass, J.B., Kretz, C.B., Ganesh, S., Ranjan, P., Seston, S.L., Buck, K.N., Landing, W.M., Morton, P.L., Moffett, J.W., Giovannoni, S.J., Vergin, K.L., Stewart, F.J., 2015. Meta-omic signatures of microbial metal and nitrogen cycling in marine oxygen minimum zones. Front. Microbiol. 6, 1–13. https://doi.org/10.3389/fmicb.2015.00998

Gledhill, M., Buck, K.N., 2012. The organic complexation of iron in the marine environment: A review. Front. Microbiol. 3, 1–17. https://doi.org/10.3389/fmicb.2012.00069

Gledhill, M., van den Berg, C.M.G., 1994. Determination of complexation of iron(III) with natural organic complexing ligands in seawater using cathodic stripping voltammetry. Mar. Chem. 47, 41–54. https://doi.org/10.1016/0304-4203(94)90012-4

Granger, J., Price, N.M., 1999. The importance of siderophores in iron nutrition of heterotrophic marine bacteria. Limnol. Oceanogr. 44, 541–555. https://doi.org/10.4319/lo.1999.44.3.0541

Guerinot, M. Lou, 1994. Microbial Iron Transport. Annu. Rev. Microbiol. 48, 743–772.

Hassler, C. S., Alasonati, E., Mancuso Nichols, C.A., Slaveykova, V.I., 2011. Exopolysaccharides produced by bacteria isolated from the pelagic Southern Ocean - Role in Fe binding, chemical reactivity, and bioavailability. Mar. Chem. 123, 88–98. https://doi.org/10.1016/j.marchem.2010.10.003

Hassler, C.S., Schoemann, V., Nichols, C.M., Butler, E.C.V., Boyd, P.W., 2011. Saccharides enhance iron bioavailability to southern ocean phytoplankton. Proc. Natl. Acad. Sci. U. S. A. 108, 1076–1081. https://doi.org/10.1073/pnas.1010963108

Hatta, M., Measures, C.I., Wu, J., Roshan, S., Fitzsimmons, J.N., Sedwick, P., Morton, P., 2015. An overview of dissolved Fe and Mn distributions during the 2010-2011 U.S. GEOTRACES north Atlantic cruises: GEOTRACES GA03. Deep. Res. Part II Top. Stud. Oceanogr. 116, 117–129. https://doi.org/10.1016/j.dsr2.2014.07.005

Hawkes, J. A., Connelly, D.P., Gledhill, M., Achterberg, E.P., 2013. The stabilisation and transportation of dissolved iron from high temperature hydrothermal vent systems. Earth Planet. Sci. Lett. 375, 280–290. https://doi.org/10.1016/j.epsl.2013.05.047

Hawkes, J.A., Gledhill, M., Connelly, D.P., Achterberg, E.P., 2013. Characterisation of iron binding ligands in seawater by reverse titration. Anal. Chim. Acta 766, 53–60. https://doi.org/10.1016/j.aca.2012.12.048

Heller, M.I., Lam, P.J., Moffett, J.W., Till, C.P., Lee, J.M., Toner, B.M., Marcus, M.A., 2017. Accumulation of Fe oxyhydroxides in the Peruvian oxygen deficient zone implies non-oxygen dependent Fe oxidation. Geochim. Cosmochim. Acta 211, 174–193. https://doi.org/10.1016/j.gca.2017.05.019

Hendrickson, C.L., Quinn, J.P., Kaiser, N.K., Smith, D.F., Blakney, G.T., Chen, T., Marshall, A.G., Weisbrod, C.R., Beu, S.C., 2015. 21 Tesla Fourier Transform Ion Cyclotron Resonance Mass Spectrometer: A National Resource for Ultrahigh Resolution Mass Analysis. J. Am. Soc. Mass Spectrom. 26, 1626–1632. https://doi.org/10.1007/s13361-015-1182-2

Hider, R.C., Kong, X., 2010. Chemistry and biology of siderophores. Nat. Prod. Reports 27, 637–657. https://doi.org/10.1039/b906679a

Hoffman, C.L., Monreal, P.J., Albers, J.B., Lough, A.J.M., Santoro, A.E., Mellett, T., Buck, K.N., Tagliabue, A., Lohan, M.C., Joseph A. Resing, 2023. Microbial siderophore production is tightly coupled to iron in hydrothermal plumes. bioRxiv.

Hoffman, C.L., Nicholas, S.L., Ohnemus, D.C., Fitzsimmons, J.N., Sherrell, R.M., German, C.R., Heller, M.I., Lee, J. mi, Lam, P.J., Toner, B.M., 2018. Near-field iron and carbon chemistry of non-buoyant hydrothermal plume particles, Southern East Pacific Rise 15°S. Mar. Chem. 201, 183–197. https://doi.org/10.1016/j.marchem.2018.01.011

Hoffman, C.L., Schladweiler, C.S., Seaton, N.C.A., Nicholas, S.L., Fitzsimmons, J.N., Sherrell, R.M., German, C.R., Lam, P.J., Toner, B.M., 2020. Diagnostic Morphology and Solid-State Chemical Speciation of Hydrothermally Derived Particulate Fe in a Long-Range Dispersing Plume. ACS Earth Sp. Chem. 4, 1831–1842. https://doi.org/10.1021/acsearthspacechem.0c00067

Holyńska, B., Bisiniek, K., 1976. Determination of trace amounts of metals in salline water by energy-dispersive XRF (with the NaDDTC preconcentration). J. Radioanal. Chem. 31, 159–166. https://doi.org/10.1007/BF02516475

Homann, V. V., Sandy, M., Tincu, J.A., Templeton, A.S., Tebo, B.M., Butler, A., 2009. Loihichelins A-F, a suite of amphiphilic siderophores produced by the marine bacterium halomonas LOB-5. J. Nat. Prod. 72, 884–888. https://doi.org/10.1021/np800640h

Honeyman, B.D., Santschi, P.H., 1989. A Brownian-pumping model for oceanic trace metal scavenging: evidence from Th isotopes. J. Mar. Res. 47, 951–992. https://doi.org/10.1357/002224089785076091

Hopkinson, B.M., Barbeau, K.A., 2007. Organic and redox speciation of iron in the eastern tropical North Pacific suboxic zone. Mar. Chem. 106, 2–17.

https://doi.org/10.1016/j.marchem.2006.02.008

Horak, R.E.A., Ruef, W., Ward, B.B., Devol, A.H., 2016. Expansion of denitrification and anoxia in the eastern tropical North Pacific from 1972 to 2012. Geophys. Res. Lett. 43, 5252–5260. https://doi.org/10.1002/2016GL068871

Humphris, S.E., Fornari, D.J., Scheirer, D.S., German, C.R., Parson, L.M., 2002. Geotectonic setting of hydrothermal activity on the summit of Lucky Strike Seamount (37°17′N, Mid-Atlantic Ridge). Geochemistry, Geophys. Geosystems 3, 1–25. https://doi.org/10.1029/2001gc000284

Hunter, K.A., Boyd, P.W., 2007. Iron-binding ligands and their role in the ocean biogeochemistry of iron. Environ. Chem. 4, 221–232. https://doi.org/10.1071/EN07012

Hutchins, D.A., Hare, C.E., Weaver, R.S., Zhang, Y., Firme, G.F., DiTullio, G.R., Alm, M.B., Riseman, S.F., Maucher, J.M., Geesey, M.E., Trick, C.G., Smith, G.J., Rue, E.L., Conn, J., Bruland, K.W., 2002. Phytoplankton iron limitation in the Humboldt Current and Peru Upwelling. Limnol. Oceanogr. 47, 997–1011. https://doi.org/10.4319/lo.2002.47.4.0997

Ishibashi, J., Wakita, H., Okamura, K., Nakayama, E., Feely, R.A., Lebon, G.T., Baker, E.T., Marumo, K., 1997. Hydrothermal methane and manganese variation in the plume over the superfast-spreading southern East Pacific Rise. Geochim. Cosmochim. Acta 61, 485–500. https://doi.org/10.1016/S0016-7037(96)00304-3

Ito, Y., Butler, A., 2005. Structure of synechobactins, new siderophores of the marine cyanobacterium Synechococcus sp. PCC 7002. Limnol. Oceanogr. 50, 1918–1923. https://doi.org/10.4319/lo.2005.50.6.1918

Jackson, P.R., Ledwell, J.R., Thurnherr, A.M., 2010. Dispersion of a tracer on the East Pacific Rise (9°N to 10°N), including the influence of hydrothermal plumes. Deep. Res. Part I

Oceanogr. Res. Pap. 57, 37–52. https://doi.org/10.1016/j.dsr.2009.10.011

Jang, J.H., Kanoh, K., Adachi, K., Matsuda, S., Shizuri, Y., 2007. Tenacibactins A-D, hydroxamate siderophores from a marine-derived bacterium, Tenacibaculum sp. A4K-17. J. Nat. Prod. 70, 563–566. https://doi.org/10.1021/np060502b

Jenkins, W.J., Lott, D.E., German, C.R., Cahill, K.L., Goudreau, J., Longworth, B., 2018. The deep distributions of helium isotopes, radiocarbon, and noble gases along the U.S. GEOTRACES East Pacific Zonal Transect (GP16). Mar. Chem. 201, 167–182. https://doi.org/10.1016/j.marchem.2017.03.009

Johnson, K., Elrod, V., Fitzwater, S., Plant, J., Landing, M., Edward, B., Bergquist, B., Bruland, K., Aguilar-Islas, A., Buck, K., Lohan, M., Smith, G.J., Sohst, B., Coale, K., Gordon, M., Tanner, S., Measures, C., Moffett, J., Barbeau, K., King, A., Bowie, A., Chase, Z., Cullen, J., Laan, P., Landing, W., Mendez, J., Milne, A., Obata, H., Doi, T., Ossiander, L., Sarthou, G., Sedwick, P., Van den Berg, S., Laglera-Baquer, L., Wu, J., Cai, Y., 2007. Developing standards for dissolved iron in seawater. Eos (Washington. DC). 88, 131–132.

Johnson, K.S., Chavez, F.P., Friederich, G.E., 1999. Continental-shelf sediment as a primary source of iron for coastal phytoplankton. Nature 398, 697–700. https://doi.org/10.1038/19511

Johnson, K.S., Gordon, R.M., Coale, K.H., 1997. What controls dissolved iron in the world ocean? Mar. Chem. 57, 137–161.

Kalansuriya, P., Quezada, M., Espósito, B.P., Capon, R.J., 2017. Talarazines A-E: Noncytotoxic Iron(III) Chelators from an Australian Mud Dauber Wasp-Associated Fungus, Talaromyces sp. (CMB-W045). J. Nat. Prod. 80, 609–615. https://doi.org/10.1021/acs.jnatprod.6b00889

Kelley, D.S., Lilley, M.D., Lupton, J.E., Olson, E.J., 1998. Enriched H2, CH4, 3He concentrations in hydrothermal plumes associated with the 1996 Gorda Ridge eruptive event. Deep. Res. Part II Top. Stud. Oceanogr. 45, 2665–2682. https://doi.org/10.1016/S0967-0645(98)00088-5

King, D.W., Lounsbury, H.A., Millero, F.J., 1995. Rates and Mechanism of Fe(II) Oxidation at Nanomolar Total Iron Concentrations. Environ. Sci. Technol. 29, 818–824. https://doi.org/10.1021/es00003a033

Kipp, L.E., Sanial, V., Henderson, P.B., van Beek, P., Reyss, J.L., Hammond, D.E., Moore, W.S., Charette, M.A., 2018. Radium isotopes as tracers of hydrothermal inputs and neutrally buoyant plume dynamics in the deep ocean. Mar. Chem. 201, 51–65. https://doi.org/10.1016/j.marchem.2017.06.011

Klar, J.K., Schlosser, C., Milton, J.A., Woodward, E.M.S., Lacan, F., Parkinson, I.J., Achterberg, E.P., James, R.H., 2018. Sources of dissolved iron to oxygen minimum zone waters on the Senegalese continental margin in the tropical North Atlantic Ocean: Insights from iron isotopes. Geochim. Cosmochim. Acta 236, 60–78. https://doi.org/10.1016/j.gca.2018.02.031

Kleint, C., Hawkes, J.A., Sander, S.G., Koschinsky, A., 2016. Voltammetric investigation of hydrothermal iron speciation. Front. Mar. Sci. 3, 1–11. https://doi.org/10.3389/fmars.2016.00075

Kondo, Y., Moffett, J.W., 2015. Iron redox cycling and subsurface offshore transport in the eastern tropical South Pacific oxygen minimum zone. Mar. Chem. 168, 95–103. https://doi.org/http://dx.doi.org/10.1016/j.marchem.2014.11.007

Kondo, Y., Moffett, J.W., 2013. Dissolved Fe(II) in the Arabian Sea oxygen minimum zone and western tropical Indian Ocean during the inter-monsoon period. Deep. Res. Part I Oceanogr.

Res. Pap. 73, 73–83. https://doi.org/10.1016/j.dsr.2012.11.014

Kraemer, S.M., 2004. Iron oxide dissolution and solubility in the presence of siderophores. Aquat. Sci. 66, 3–18. https://doi.org/10.1007/s00027-003-0690-5

Kraemer, S.M., Butler, A., Borer, P., Cervini-Silva, J., 2005. Siderophores and the dissolution of iron-bearing minerals in marine systems. Rev. Mineral. Geochemistry 59, 53–84. https://doi.org/10.2138/rmg.2005.59.4

Kramer, J., Özkaya, Ö., Kümmerli, R., 2019. Bacterial siderophores in community and host interactions. Nat. Rev. Microbiol. 18, 152–163. https://doi.org/10.1038/s41579-019-0284-4

Kügler, S., Cooper, R.E., Boessneck, J., Küsel, K., Wichard, T., 2020. Rhizobactin B is the preferred siderophore by a novel Pseudomonas isolate to obtain iron from dissolved organic matter in peatlands. BioMetals 33, 415–433. https://doi.org/10.1007/s10534-020-00258-w

Kumler, W., Ingalls, A.E., 2022. Tidy Data Neatly Resolves Mass-Spectrometry's Ragged Arrays. R J. 14, 193–202. https://doi.org/10.32614/RJ-2022-050

Laglera, L.M., Battaglia, G., van den Berg, C.M.G., 2007. Determination of humic substances in natural waters by cathodic stripping voltammetry of their complexes with iron. Anal. Chim. Acta 599, 58–66. https://doi.org/10.1016/j.aca.2007.07.059

Laglera, L.M., Battaglia, G., van den Berg, C.M.G., 2011. Effect of humic substances on the iron speciation in natural waters by CLE/CSV. Mar. Chem. 127, 134–143. https://doi.org/10.1016/j.marchem.2011.09.003

Laglera, L.M., Filella, M., 2015. The relevance of ligand exchange kinetics in the measurement of iron speciation by CLE-AdCSV in seawater. Mar. Chem. 173, 100–113. https://doi.org/10.1016/j.marchem.2014.09.005

Lam, P.J., Bishop, J.K.B., 2008. The continental margin is a key source of iron to the HNLC

North Pacific Ocean. Geophys. Res. Lett. 35, 1–5. https://doi.org/10.1029/2008GL033294

Lam, P.J., Bishop, J.K.B., Henning, C.C., Marcus, M.A., Waychunas, G.A., Fung, I.Y., 2006. Wintertime phytoplankton bloom in the subarctic Pacific supported by continental margin iron. Global Biogeochem. Cycles 20, 1–12. https://doi.org/10.1029/2005GB002557

Lam, P.J., Heller, M.I., Lerner, P.E., Moffett, J.W., Buck, K.N., 2020. Unexpected Source and Transport of Iron from the Deep Peru Margin. ACS Earth Sp. Chem. 4, 977–992. https://doi.org/10.1021/acsearthspacechem.0c00066

Le Calvez, T., Burgaud, G., Mahé, S., Barbier, G., Vandenkoornhuyse, P., 2009. Fungal diversity in deep-sea hydrothermal ecosystems. Appl. Environ. Microbiol. 75, 6415–6421. https://doi.org/10.1128/AEM.00653-09

Lebar, M.D., Cary, J.W., Majumdar, R., Carter-Wientjes, C.H., Mack, B.M., Wei, Q., Uka, V., De Saeger, S., Diana Di Mavungu, J., 2018. Identification and functional analysis of the aspergillic acid gene cluster in Aspergillus flavus. Fungal Genet. Biol. 116, 14–23. https://doi.org/10.1016/j.fgb.2018.04.009

Lee, J.M., Boyle, E.A., Echegoyen-Sanz, Y., Fitzsimmons, J.N., Zhang, R., Kayser, R.A., 2011. Analysis of trace metals (Cu, Cd, Pb, and Fe) in seawater using single batch nitrilotriacetate resin extraction and isotope dilution inductively coupled plasma mass spectrometry. Anal. Chim. Acta 686, 93–101. https://doi.org/10.1016/j.aca.2010.11.052

Lesniewski, R.A., Jain, S., Anantharaman, K., Schloss, P.D., Dick, G.J., 2012. The metatranscriptome of a deep-sea hydrothermal plume is dominated by water column methanotrophs and lithotrophs. ISME J. 6, 2257–2268. https://doi.org/10.1038/ismej.2012.63

Leventhal, G.E., Ackermann, M., Schiessl, K.T., 2019. Why microbes secrete molecules to modify their environment: The case of iron-chelating siderophores. J. R. Soc. Interface 16. https://doi.org/10.1098/rsif.2018.0674

Li, J., Boiteau, R.M., Babcock-Adams, L., Acker, M., Song, Z., McIlvin, M.R., Repeta, D.J., 2021. Element-Selective Targeting of Nutrient Metabolites in Environmental Samples by Inductively Coupled Plasma Mass Spectrometry and Electrospray Ionization Mass Spectrometry. Front. Mar. Sci. 8, 1–15. https://doi.org/10.3389/fmars.2021.630494

Li, M., Toner, B.M., Baker, B.J., Breier, J.A., Sheik, C.S., Dick, G.J., 2014. Microbial iron uptake as a mechanism for dispersing iron from deep-sea hydrothermal vents. Nat. Commun. 5, 1–8. https://doi.org/10.1038/ncomms4192

Lis, H., Shaked, Y., Kranzler, C., Keren, N., Morel, F.M.M., 2015. Iron bioavailability to phytoplankton: An empirical approach. ISME J. 9, 1003–1013. https://doi.org/10.1038/ismej.2014.199

Liu, X., Millero, F.J., 2002. The solubility of iron in seawater. Mar. Chem. 77, 43–54. https://doi.org/10.1016/S0304-4203(01)00074-3

Lohan, M.C., Bruland, K.W., 2008. Elevated Fe(II) and dissolved Fe in hypoxic shelf waters off Oregon and Washington: An enhanced source of iron to coastal upwelling regimes. Environ. Sci. Technol. 42, 6462–6468. https://doi.org/10.1021/es800144j

Lohan, M.C., Crawford, D.W., Purdie, D.A., Statham, P.J., 2005. Iron and zinc enrichments in the northeastern subarctic Pacific: Ligand production and zinc availability in response to phytoplankton growth. Limnol. Oceanogr. 50, 1427–1437. https://doi.org/10.4319/lo.2005.50.5.1427

Lough, A.J.M., Connelly, D.P., Homoky, W.B., Hawkes, J.A., Chavagnac, V., Castillo, A., Kazemian, M., Nakamura, K.I., Araki, T., Kaulich, B., Mills, R.A., 2019. Diffuse hydrothermal venting: A hidden source of iron to the oceans. Front. Mar. Sci. 6, 1–14. https://doi.org/10.3389/fmars.2019.00329

Lough, A. J.M., Homoky, W.B., Connelly, D.P., Comer-Warner, S.A., Nakamura, K., Abyaneh, M.K., Kaulich, B., Mills, R.A., 2019. Soluble iron conservation and colloidal iron dynamics in a hydrothermal plume. Chem. Geol. 511, 225–237. https://doi.org/10.1016/j.chemgeo.2019.01.001

Luo, M., Zang, R., Wang, X., Chen, Z., Song, X., Ju, J., Huang, H., 2019. Natural Hydroxamate-Containing Siderophore Acremonpeptides A-D and an Aluminum Complex of Acremonpeptide D from the Marine-Derived Acremonium persicinum SCSIO 115. J. Nat. Prod. 82, 2594–2600. https://doi.org/10.1021/acs.jnatprod.9b00545

Lupton, J.E., Craig, H., 1981. A Major Helium-3 Source at 15^{o}S on the East Pacific Rise. Science (80-.). 214, 13–18.

Lupton, J.E., Jenkins, W.J., 2017. Geochemistry, Geophysics, Geosystems. Geochemistry, Geophys. Geosystems 18, 1810–1823. https://doi.org/10.1002/2017GC006848.Received

Manck, L.E., Park, J., Tully, B.J., Poire, A.M., Bundy, R.M., Dupont, C.L., Barbeau, K.A., 2022. Petrobactin, a siderophore produced by Alteromonas, mediates community iron acquisition in the global ocean. ISME J. 16, 358–369. https://doi.org/10.1038/s41396-021-01065-y

Margolskee, A., Frenzel, H., Emerson, S., Deutsch, C., 2019. Ventilation Pathways for the North Pacific Oxygen Deficient Zone. Global Biogeochem. Cycles 33, 875–890. https://doi.org/10.1029/2018GB006149

Martinez, J.S., Carter-Franklin, J.N., Mann, E.L., Martin, J.D., Haygood, M.G., Butler, A., 2003. Structure and membrane affinity of a suite of amphiphilic siderophores produced by a marine bacterium. Proc. Natl. Acad. Sci. U. S. A. 100, 3754–3759.

https://doi.org/10.1073/pnas.0637444100

Maßmig, M., Lüdke, J., Krahmann, G., Engel, A., 2020. Bacterial degradation activity in the eastern tropical South Pacific oxygen minimum zone. Biogeosciences 17, 215–230. https://doi.org/10.5194/bg-17-215-2020

Mawji, E., Gledhill, M., Milton, J.A., Tarran, G.A., Ussher, S., Thompson, A., Wolff, G.A., Worsfold, P.J., Achterberg, E.P., 2008. Hydroxamate siderophores: Occurrence and importance in the Atlantic Ocean. Environ. Sci. Technol. 42, 8675–8680. https://doi.org/10.1021/es801884r

Mawji, E., Gledhill, M., Milton, J.A., Zubkov, M. V., Thompson, A., Wolff, G.A., Achterberg, E.P., 2011. Production of siderophore type chelates in Atlantic Ocean waters enriched with different carbon and nitrogen sources. Mar. Chem. 124, 90–99. https://doi.org/10.1016/j.marchem.2010.12.005

McCormack, P., Worsfold, P.J., Gledhill, M., 2003. Separation and detection of siderophores produced by marine bacterioplankton using high-performance liquid chromatography with electrospray ionization mass spectrometry. Anal. Chem. 75, 2647–2652. https://doi.org/10.1021/ac0340105

Measures, C.I., Yuan, J., Resing, J.A., 1995. Determination of iron in seawater by flow injection analysis using in-line preconcentration and spectrophotometric detection. Mar. Chem. 50, 3–12. https://doi.org/10.1016/0304-4203(95)00022-J

Miethke, M., Marahiel, M.A., 2007. Siderophore-Based Iron Acquisition and Pathogen Control. Microbiol. Mol. Biol. Rev. 71, 413–451. https://doi.org/10.1128/MMBR.00012-07

Millero, F.J., Sotolongo, S., Izaguirre, M., 1987. Oxidation kinetics of Fe (II) in sea water. Geochim. Cosmochim. Acta 51, 793–801.

Millero, F.J., Yao, W., Aicher, J., 1995. The speciation of Fe(II) and Fe(III) in natural waters. Mar. Chem. 50, 21–39. https://doi.org/10.1016/0304-4203(95)00024-L

Moffett, J.W., German, C.R., 2018. The U.S.GEOTRACES Eastern Tropical Pacific Transect (GP16). Mar. Chem. 201, 1–5. https://doi.org/10.1016/j.marchem.2017.12.001

Moffett, J.W., Goepfert, T.J., Naqvi, S.W.A., 2007. Reduced iron associated with secondary nitrite maxima in the Arabian Sea. Deep. Res. Part I Oceanogr. Res. Pap. 54, 1341–1349. https://doi.org/10.1016/j.dsr.2007.04.004

Moore, C.M., Mills, M.M., Arrigo, K.R., Berman-Frank, I., Bopp, L., Boyd, P.W., Galbraith, E.D., Geider, R.J., Guieu, C., Jaccard, S.L., Jickells, T.D., La Roche, J., Lenton, T.M., Mahowald, N.M., Marañón, E., Marinov, I., Moore, J.K., Nakatsuka, T., Oschlies, A., Saito, M.A., Thingstad, T.F., Tsuda, A., Ulloa, O., 2013. Processes and patterns of oceanic nutrient limitation. Nat. Geosci. 6, 701–710. https://doi.org/10.1038/ngeo1765

Moore, L.E., Heller, M.I., Barbeau, K.A., Moffett, J.W., Bundy, R.M., 2021. Organic complexation of iron by strong ligands and siderophores in the eastern tropical North Pacific oxygen deficient zone. Mar. Chem. 236, 104021.

Morel, F.M.M., Kustka, A.B., Shaked, Y., 2008. The role of unchelated Fe in the iron nutrition of phytoplankton. Limnol. Oceanogr. 53, 400–404. https://doi.org/10.4319/lo.2008.53.1.0400

Morel, F.M.M., Price, N.M., 2003. The biogeochemical cycles of trace metals in the oceans. Science (80-.). 300, 944–947. https://doi.org/10.1126/science.1083545

Morgan, J.L.L., Wasylenki, L.E., Nuester, J., Anbar, A.D., 2010. Fe isotope fractionation during equilibration of Fe-organic complexes. Environ. Sci. Technol. 44, 6095–6101. https://doi.org/10.1021/es100906z

Mottl, M.J., McConachy, T.F., 1990. Chemical processes in buoyant hydrothermal plumes on the East Pacific Rise near 21°N. Geochim. Cosmochim. Acta 54, 1911–1927. https://doi.org/10.1016/0016-7037(90)90261-I

Nadmid, S., Plaza, A., Lauro, G., Garcia, R., Bifulco, G., Müller, R., 2014. Hyalachelins A-C, unusual siderophores isolated from the terrestrial myxobacterium hyalangium minutum. Org. Lett. 16, 4130–4133. https://doi.org/10.1021/ol501826a

Neilands, J.B., 1981. Microbial iron compounds. Annu. Rev. Biochem. 50, 715–731. https://doi.org/10.1146/annurev.bi.50.070181.003435

Norman, L., Worms, I.A.M., Angles, E., Bowie, A.R., Nichols, C.M., Ninh Pham, A., Slaveykova, V.I., Townsend, A.T., David Waite, T., Hassler, C.S., 2015. The role of bacterial and algal exopolymeric substances in iron chemistry. Mar. Chem. 173, 148–161. https://doi.org/10.1016/j.marchem.2015.03.015

Omanović, D., Garnier, C., Pižeta, I., 2015. ProMCC: An all-in-one tool for trace metal complexation studies. Mar. Chem. 173, 25–39. https://doi.org/10.1016/j.marchem.2014.10.011

Opatkiewicz, A.D., Butterfield, D.A., Baross, J.A., 2009. Individual hydrothermal vents at Axial Seamount harbor distinct subseafloor microbial communities. FEMS Microbiol. Ecol. 70, 413–424. https://doi.org/10.1111/j.1574-6941.2009.00747.x

Ottley, C.J., Davison, W., Edmunds, W.M., 1997. Chemical catalysis of nitrate reduction by iron(II). Geochim. Cosmochim. Acta 61, 1819–1828. https://doi.org/10.1016/S0016-7037(97)00058-6

Pang, K.L., Chiang, M.W.L., Guo, S.Y., Shih, C.Y., Dahms, H.U., Hwang, J.S., Cha, H.J., 2020. Growth study under combined effects of temperature, pH and salinity and transcriptome analysis revealed adaptations of Aspergillus terreus NTOU4989 to the extreme conditions at Kueishan Island Hydrothermal Vent Field, Taiwan. PLoS One 15, 1–24. https://doi.org/10.1371/journal.pone.0233621

Park, J., Durham, B.P., Key, R.S., Groussman, R.D., Bartolek, Z., Pinedo-Gonzalez, P., Hawco, N.J., John, S.G., Carlson, M.C.G., Lindell, D., Juranek, L.W., Ferrón, S., Ribalet, F., Armbrust, E.V., Ingalls, A.E., Bundy, R.M., 2023. Siderophore production and utilization by marine bacteria in the North Pacific Ocean. Limnol. Oceanogr. 1636–1653. https://doi.org/10.1002/lno.12373

Perner, M., Petersen, J.M., Zielinski, F., Gennerich, H.H., Seifert, R., 2010. Geochemical constraints on the diversity and activity of H 2-oxidizing microorganisms in diffuse hydrothermal fluids from a basalt- and an ultramafic-hosted vent. FEMS Microbiol. Ecol. 74, 55–71. https://doi.org/10.1111/j.1574-6941.2010.00940.x

Pižeta, I., Sander, S.G., Hudson, R.J.M., Omanović, D., Baars, O., Barbeau, K.A., Buck, K.N., Bundy, R.M., Carrasco, G., Croot, P.L., Garnier, C., Gerringa, L.J.A., Gledhill, M., Hirose, K., Kondo, Y., Laglera, L.M., Nuester, J., Rijkenberg, M.J.A., Takeda, S., Twining, B.S., Wells, M., 2015. Interpretation of complexometric titration data: An intercomparison of methods for estimating models of trace metal complexation by natural organic ligands. Mar. Chem. 173, 3–24. https://doi.org/10.1016/j.marchem.2015.03.006

Renard, V., Hekinian, R., Francheteau, J., Ballard, R.D., Backer, H., 1985. Submersible observations at the axis of the ultra-fast-spreading East Pacific Rise (17°30′ to 21°30′S). Earth Planet. Sci. Lett. 75, 339–353. https://doi.org/10.1016/0012-821X(85)90178-5

Resing, J.A., Mottl, M.J., 1992. Determination of manganese in seawater using flow injection analysis with on-line preconcentration and spectrophotometric detection. Anal. Chem. 64, 2682–2687.

Resing, J.A., Sedwick, P.N., German, C.R., Jenkins, W.J., Moffett, J.W., Sohst, B.M., Tagliabue, A., 2015. Basin-scale transport of hydrothermal dissolved metals across the South Pacific Ocean. Nature 523, 200–203. https://doi.org/10.1038/nature14577

Revsbech, N.P., Larsen, L.H., Gundersen, J., Dalsgaard, T., Ulloa, O., Thamdrup, B., 2009. Determination of ultra-low oxygen concentrations in oxygen minimum zones by the STOX sensor. Limnol. Oceanogr. Methods 7, 371–381. https://doi.org/10.4319/lom.2009.7.371

Revsbech, N.P., Thamdrup, B., Dalsgaard, T., Canfield, D.E., 2011. Construction of STOX oxygen sensors and their application for determination of O2 concentrations in oxygen minimum zones. Methods Enzymol. 486, 325–341. https://doi.org/10.1016/B978-0-12-381294-0.00014-6

Rich, H.W., Morel, F.M.M., 1990. Availability of well-defined iron colloids to the marine diatom Thalassiosira weissflogii. Limnol. Oceanogr. 35, 652–662. https://doi.org/10.4319/lo.1990.35.3.0652

Rose, A.L., Waite, T.D., 2003. Predicting iron speciation in coastal waters from the kinetics of sunlight-mediated iron redox cycling. Aquat. Sci. 65, 375–383. https://doi.org/10.1007/s00027-003-0676-3

Roshan, S., DeVries, T., Wu, J., John, S., Weber, T., 2020. Reversible scavenging traps hydrothermal iron in the deep ocean. Earth Planet. Sci. Lett. 542, 116297. https://doi.org/10.1016/j.epsl.2020.116297

Rudnicki, M.D., German, C.R., 2002. Temporal variability of the hydrothermal plume above the Kairei vent field, 25°S, Central Indian Ridge. Geochemistry, Geophys. Geosystems 3, XXX–XXX. https://doi.org/10.1029/2001gc000240

Rue, E.L., Bruland, K.W., 1995. Complexation of iron(III) by natural organic ligands in the Central North Pacific as determined by a new competitive ligand equilibration/adsorptive cathodic stripping voltammetric method. Mar. Chem. 50, 117–138. https://doi.org/10.1016/0304-4203(95)00031-L

Saito, M.A., Mcilvin, M.R., Moran, D.M., Santoro, A.E., Dupont, C.L., Rafter, P.A., Saunders, J.K., Kaul, D., Lamborg, C.H., Westley, M., Valois, F., Waterbury, J.B., 2020. Abundant nitrite-oxidizing metalloenzymes in the mesopelagic zone of the tropical Pacific Ocean. Nat. Geosci. 13. https://doi.org/10.1038/s41561-020-0565-6

Sander, S.G., Koschinsky, A., 2011. Metal flux from hydrothermal vents increased by organic complexation. Nat. Geosci. 4, 145–150. https://doi.org/10.1038/ngeo1088

Sandy, M., Butler, A., 2009. Microbial iron acquisition: Marine and terrestrial siderophores. Chem. Rev. 109, 4580–4595. https://doi.org/10.1021/cr9002787

Scheirer, D.S., Macdonald, K.C., 1993. Variation in cross-sectional area of the axial ridge along the East Pacific Rise: Evidence for the magmatic budget of a fast spreading center. J. Geophys. Res. Solid Earth. 98, 7871–7885.

Scholz, F., Löscher, C.R., Fiskal, A., Sommer, S., Hensen, C., Lomnitz, U., Wuttig, K., Göttlicher, J., Kossel, E., Steininger, R., Canfield, D.E., 2016. Nitrate-dependent iron oxidation limits iron transport in anoxic ocean regions. Earth Planet. Sci. Lett. 454, 272–281. https://doi.org/10.1016/j.epsl.2016.09.025

Sedwick, P.N., Bowie, A.R., Trull, T.W., 2008. Dissolved iron in the Australian sector of the Southern Ocean (CLIVAR SR3 section): Meridional and seasonal trends. Deep. Res. Part I Oceanogr. Res. Pap. 55, 911–925. https://doi.org/10.1016/j.dsr.2008.03.011

Shaked, Y., Buck, K.N., Mellett, T., Maldonado, M.T., 2020. Insights into the bioavailability of oceanic dissolved Fe from phytoplankton uptake kinetics. ISME J. https://doi.org/10.1038/s41396-020-0597-3

Shimmield, G.B., Price, N.B., 1988. The scavenging of U,230Th and 231Pa during pulsed hydrothermal activity at 20°S, East Pacific Rise. Geochim. Cosmochim. Acta 52, 669–677. https://doi.org/10.1016/0016-7037(88)90329-8

Sinton, J.M., Smaglik, S.M., Mahoney, J.J., Macdonald, K.C., 1991. Magmatic processes at superfast spreading mid-ocean ridges: glass compositional variations along the East Pacific Rise 13°-23°S. J. Geophys. Res. 96, 6133–6155. https://doi.org/10.1029/90JB02454

Spietz, R.L., Lundeen, R.A., Zhao, X., Nicastro, D., Ingalls, A.E., Morris, R.M., 2019. Heterotrophic carbon metabolism and energy acquisition in Candidatus Thioglobus singularis strain PS1, a member of the SUP05 clade of marine Gammaproteobacteria. Environ. Microbiol. 21, 2391–2401. https://doi.org/10.1111/1462-2920.14623

Sumner, L.W., Amberg, A., Barrett, D., Beale, M.H., Beger, R., Daykin, C.A., Fan, T.W.M., Fiehn, O., Goodacre, R., Griffin, J.L., Hankemeier, T., Hardy, N., Harnly, J., Higashi, R., Kopka, J., Lane, A.N., Lindon, J.C., Marriott, P., Nicholls, A.W., Reily, M.D., Thaden, J.J., Viant, M.R., 2007. Proposed minimum reporting standards for chemical analysis: Chemical Analysis Working Group (CAWG) Metabolomics Standards Initiative (MSI). Metabolomics 3, 211–221. https://doi.org/10.1007/s11306-007-0082-2

Tagliabue, A., Aumont, O., Bopp, L., 2014. The Impact of Different External Sources of Iron on the Global Carbon Cycle. Geophys. Res. Lett. 318, 920–926. https://doi.org/10.1002/2013GL059059.Received

Tagliabue, A., Aumont, O., DeAth, R., Dunne, J.P., Dutkiewicz, S., Galbraith, E., Misumi, K., Moore, J.K., Ridgwell, A., Sherman, E., Stock, C., Vichi, M., Völker, C., Yool, A., 2016.

How well do global ocean biogeochemistry models simulate dissolved iron distributions. Global Biogeochem. Cycles 30, 149–174. https://doi.org/10.1002/2015GB005289.Received

Tagliabue, A., Bopp, L., Dutay, J.C., Bowie, A.R., Chever, F., Jean-Baptiste, P., Bucciarelli, E., Lannuzel, D., Remenyi, T., Sarthou, G., Aumont, O., Gehlen, M., Jeandel, C., 2010. Hydrothermal contribution to the oceanic dissolved iron inventory. Nat. Geosci. 3, 252–256. https://doi.org/10.1038/ngeo818

Tagliabue, A., Bowie, A.R., Boyd, P.W., Buck, K.N., Johnson, K.S., Saito, M.A., 2017. The integral role of iron in ocean biogeochemistry. Nature 543, 51–59. https://doi.org/10.1038/nature21058

Tagliabue, A., Resing, J., 2016. Impact of hydrothermalism on the ocean iron cycle. Philos. Trans. R. Soc. A Math. Phys. Eng. Sci. 374. https://doi.org/10.1098/rsta.2015.0291

Thamdrup, B., 2000. Bacterial manganese and iron reduction in aquatic sediments, in: Advances in Microbial Ecology. pp. 41–84.

Thuróczy, C.E., Gerringa, L.J.A., Klunder, M.B., Middag, R., Laan, P., Timmermans, K.R., de Baar, H.J.W., 2010. Speciation of Fe in the Eastern North Atlantic Ocean. Deep. Res. Part I Oceanogr. Res. Pap. 57, 1444–1453. https://doi.org/10.1016/j.dsr.2010.08.004

Tiano, L., Garcia-Robledo, E., Dalsgaard, T., Devol, A.H., Ward, B.B., Ulloa, O., Canfield, D.E., Peter Revsbech, N., 2014. Oxygen distribution and aerobic respiration in the north and south eastern tropical Pacific oxygen minimum zones. Deep. Res. Part I Oceanogr. Res. Pap. 94, 173–183. https://doi.org/10.1016/j.dsr.2014.10.001

Tivey, M.A., Johnson, P.H., 2002. Crustal magnetization reveals subsurface structure of Juan de Fuca Ridge hydrothermal vent fields. Geology 30, 979–982. https://doi.org/10.1130/0091-7613(2002)030<0979:CMRSSO>2.0.CO;2

Tivey, M.K., 2007. Generation of seafloor hydrothermal vent fluids and associated mineral deposits. Oceanography 20, 50–65. https://doi.org/10.5670/oceanog.2007.80

Tivey, M.K., 1995. Modeling chimney growth and associated fluid flow at seafloor hydrothermal vent sites. Geophys. Monogr. Ser. 91, 158–177. https://doi.org/10.1029/GM091p0158

Tortell, P.D., Maldonado, M.T., Price, N.M., 1996. The role of heterotrophic bacteria in iron-limited ocean ecosystems. Nature 383, 330–332. https://doi.org/10.1038/383330a0

Troxell, B., Hassan, H.M., 2013. Transcriptional regulation by Ferric Uptake Regulator (Fur) in pathogenic bacteria. Front. Cell. Infect. Microbiol. 4, 1–13. https://doi.org/10.3389/fcimb.2013.00059

Tsednee, M., Mak, Y.W., Chen, Y.R., Yeh, K.C., 2012. A sensitive LC-ESI-Q-TOF-MS method reveals novel phytosiderophores and phytosiderophore-iron complexes in barley. New Phytol. 195, 951–961. https://doi.org/10.1111/j.1469-8137.2012.04206.x

Turner, D.R., Whitfield, M., Dickson, A.G., 1981. The equilibrium speciation of dissolved components in freshwater and sea water at 25°C and 1 atm pressure. Geochim. Cosmochim. Acta 45, 855–881. https://doi.org/10.1016/0016-7037(81)90115-0

United Nations Educational Scientific and Cultural Organization, 1994. Protocols for the Joint Global Ocean Flux Study (JGOFS) Core Measurements. New York.

Urabe, T., Baker, E.T., Ishibashi, J., Feely, R.A., Marumo, K., Massoth, G.J., Maruyama, A., Shitashima, K., Okamura, K., Lupton, J.E., Sonoda, A., Yamazaki, T., Aoki, M., Gendron, J., Greene, R., Kaiho, Y., Kisimoto, K., Lebon, G., Matsumoto, T., Nakamura, K., Nishizawa, A., Okano, O., Paradis, G., Roe, K., Shibata, T., Tennant, D., Vance, T., Walker, S.L., Yabuki, T., Ytow, N., 1995. The effect of magmatic activity on hydrothermal venting along the superfast-spreading east pacific rise. Science (80-.). 269, 1092–1095.

https://doi.org/10.1126/science.269.5227.1092

Ussher, S.J., Achterberg, E.P., Sarthou, G., Laan, P., de Baar, H.J.W., Worsfold, P.J., 2010. Distribution of size fractionated dissolved iron in the Canary Basin. Mar. Environ. Res. 70, 46–55. https://doi.org/10.1016/j.marenvres.2010.03.001

Van de Vossenberg, J., Woebken, D., Maalcke, W.J., Wessels, H.J.C.T., Dutilh, B.E., Kartal, B., Janssen-Megens, E.M., Roeselers, G., Yan, J., Speth, D., Gloerich, J., Geerts, W., Van der Biezen, E., Pluk, W., Francoijs, K.J., Russ, L., Lam, P., Malfatti, S.A., Tringe, S.G., Haaijer, S.C.M., Op den Camp, H.J.M., Stunnenberg, H.G., Amann, R., Kuypers, M.M.M., Jetten, M.S.M., 2013. The metagenome of the marine anammox bacterium "Candidatus Scalindua profunda" illustrates the versatility of this globally important nitrogen cycle bacterium. Environ. Microbiol. 15, 1275–1289. https://doi.org/10.1111/j.1462-2920.2012.02774.x

Vedamati, J., Goepfert, T., Moffett, J.W., 2014. Iron speciation in the eastern tropical south pacific oxygen minimum zone off peru. Limnol. Oceanogr. 59, 1945–1957. https://doi.org/10.4319/lo.2014.59.6.1945

Velasquez, I., Nunn, B.L., Ibisanmi, E., Goodlett, D.R., Hunter, K.A., Sander, S.G., 2011. Detection of hydroxamate siderophores in coastal and Sub-Antarctic waters off the South Eastern Coast of New Zealand. Mar. Chem. 126, 97–107. https://doi.org/10.1016/j.marchem.2011.04.003

Velasquez, I.B., Ibisanmi, E., Maas, E.W., Boyd, P.W., Nodder, S., Sander, S.G., 2016. Ferrioxamine siderophores detected amongst iron binding ligands produced during the remineralization of marine particles. Front. Mar. Sci. 3, 1–14. https://doi.org/10.3389/fmars.2016.00172

Völker, C., Tagliabue, A., 2015. Modeling organic iron-binding ligands in a three-dimensional biogeochemical ocean model. Mar. Chem. 173, 67–77. https://doi.org/10.1016/j.marchem.2014.11.008

Von Damm, K.L., 1990. Seafloor hydrothermal activity: black smoker chemistry and chimneys. Annu. Rev. Earth Planet. Sci. 18, 173–204. https://doi.org/10.1146/annurev.ea.18.050190.001133

Von Damm, K.L., Oosting, S.E., Kozlowski, R., Buttermore, L.G., Colodner, D.C., Edmonds, H.N., Edmond, J.M., Grebmeier, J.M., 1995. Evolution of East Pacific rise hydrothermal vent fluids following a volcanic erruption. Nature 375, 47–50.

Vraspir, J.M., Butler, A., 2009. Chemistry of marine ligands and siderophores. Ann. Rev. Mar. Sci. 1, 43–63. https://doi.org/10.1146/annurev.marine.010908.163712

Wang, H., Resing, J.A., Yan, Q., Buck, N.J., Michael, S.M., Zhou, H., Liu, M., Walker, S.L., Yang, Q., Ji, F., 2021. The characteristics of Fe speciation and Fe-binding ligands in the Mariana back-arc hydrothermal plumes. Geochim. Cosmochim. Acta 292, 24–36. https://doi.org/10.1016/j.gca.2020.09.016

Wang, H., Yan, Q., Yang, Q., Ji, F., Wong, K.H., Zhou, H., 2019. The Size Fractionation and Speciation of Iron in the Longqi Hydrothermal Plumes on the Southwest Indian Ridge. J. Geophys. Res. Ocean. 124, 4029–4043. https://doi.org/10.1029/2018JC014713

Wang, W.X., Dei, R.C.H., 2003. Bioavailability of iron complexed with organic colloids to the cyanobacteria Synechococcus and Trichodesmium. Aquat. Microb. Ecol. 33, 247–259. https://doi.org/10.3354/ame033247

Wells, M.L., Goldberg, E.D., 1992. Marine submicron particles. Mar. Chem. 40, 5–18. https://doi.org/10.1016/0304-4203(92)90045-C

Winkelmann, G., Braun, V., 1981. Stereoselective recognition of ferrichrome by fungi and bacteria. FEMS Microbiol. Lett. 11, 237–241. https://doi.org/10.1111/j.1574-6968.1981.tb06972.x

Witter, A.E., Hutchins, D.A., Butler, A., Luther, G.W., 2000. Determination of conditional stability constants and kinetic constants for strong model Fe-binding ligands in seawater. Mar. Chem. 69, 1–17. https://doi.org/10.1016/S0304-4203(99)00087-0

Witter, A.E., Lewis, B.L., Luther, G.W., 2000. Iron speciation in the Arabian Sea. Deep. Res. Part II Top. Stud. Oceanogr. 47, 1517–1539. https://doi.org/10.1016/S0967-0645(99)00152-6

Yücel, M., Gartman, A., Chan, C.S., Luther, G.W., 2011. Hydrothermal vents as a kinetically stable source of iron-sulphide-bearing nanoparticles to the ocean. Nat. Geosci. 4, 367–371. https://doi.org/10.1038/ngeo1148

Zeng, X., Alain, K., Shao, Z., 2021. Microorganisms from deep-sea hydrothermal vents. Mar. Life Sci. Technol. 3, 204–230. https://doi.org/10.1007/s42995-020-00086-4

Zhou, Z., St. John, E., Anantharaman, K., Reysenbach, A.L., 2022. Global patterns of diversity and metabolism of microbial communities in deep-sea hydrothermal vent deposits. Microbiome 10, 1–22. https://doi.org/10.1186/s40168-022-01424-7